Gradient-based optimization in nonlinear structural dynamics

Dou, Suguang; Jensen, Jakob Søndergaard

Publication date:
2015

Document Version
Publisher's PDF, also known as Version of record

Gradient-based optimization in nonlinear structural dynamics

PhD Thesis

$$(EIv'')''=q-\rho A\ddot{v}$$

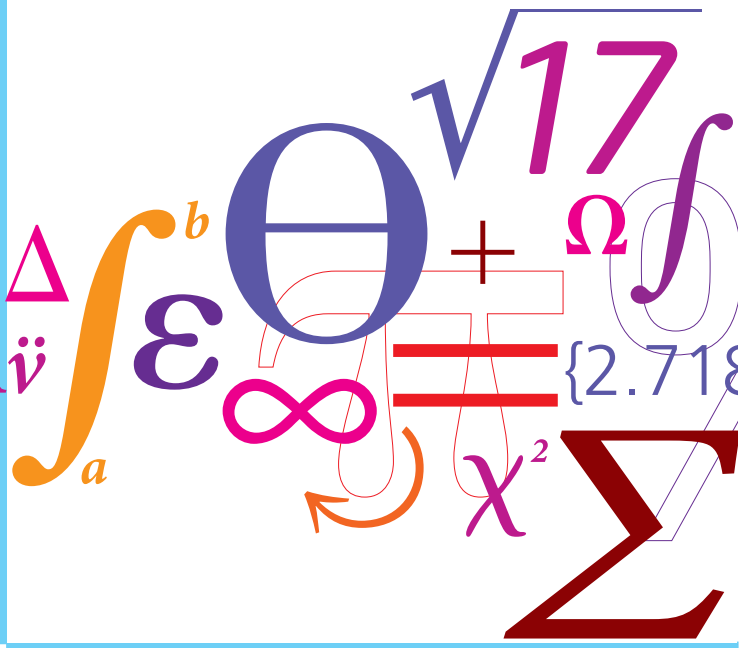

Suguang Dou
DCAMM Special Report No. S184
April 2015

DTU Mechanical Engineering
Department of Mechanical Engineering

Gradient-based optimization in nonlinear structural dynamics

by

Suguang Dou

DEPT. OF MECHANICAL ENGINEERING
Solid Mechanics

TECHNICAL UNIVERSITY OF DENMARK

Title of the thesis:
Gradient-based optimization in nonlinear structural dynamics

Ph.D. student:
Suguang Dou
E-mail: sudou@mek.dtu.dk
E-mail: dousuguang@gmail.com

Address:
Section of Solid Mechanics
Department of Mechanical Engineering
Technical University of Denmark
Nils Koppels Allé, Building 404
2800 Kgs. Lyngby
Denmark

Supervisor:
Jakob Søndergaard Jensen
E-mail: json@elektro.dtu.dk

Address:
CAMM – Centre for Acoustic-Mechanical Micro Systems
Department of Electrical Engineering
Technical University of Denmark
Nils Koppels Allé, Building 352
2800 Kgs. Lyngby
Denmark

Preface

This thesis is submitted in partial fulfillment of the requirements for obtaining the Ph.D. degree in mechanical engineering at the Technical University of Denmark (DTU). The Ph.D. project was funded by European Research Council (ERC) through the project "Integrated Analysis & Design in Nonlinear Dynamics (INNODYN) ". The project was carried out in Department of Mechanical Engineering at DTU from May 1st, 2012 to April 30th, 2015. Professor Dr. techn. Jakob Søndergaard Jensen was the supervisor on the project. Part of the work was carried out during a five-month visit to Professor Dr. Steven W. Shaw and his research group at Michigan State University (MSU), United States.

First and foremost, I would like to thank my supervisor for his inspiring and valuable support during the project. I am also grateful to Professor Steven Shaw and his Ph.D. student B. Scott Strachan for the productive collaboration. Further thanks are given to Professor Gaëtan Kerschen at University of Liège, Belgium, Professor Cyril Touzé at ENSTA-ParisTech, France, and Professor Steven Shaw, for the CISM course "Modal Analysis of Nonlinear Mechanical Systems", held at Udine, Italy, 2012. Additional thanks are given to Associate Professor Silvan Schmid and Ph.D. student Maksymilian Kurek in Department of Micro- and Nanotechnology at DTU for their active help in fabrication and tests of the optimized micro-mechanical structures.

I would like to thank my colleagues in TopOpt Group and in Department of Mechanical Engineering at DTU. They have created a cheerful and inspiring working environment. Special thanks to Gerda Helene Fogt for the great help in many aspects. I also wish to thank my colleagues in Department of Mechanical Engineering at MSU for creating a friendly and welcoming atmosphere.

Last but not the least, I wish to thank my family for their support and understanding, in particular, to my wife, Fangxing Tian, for her love and thoughtfulness.

Lyngby, April 2015

Suguang Dou

Resumé (in Danish)

Ikke-lineariteter i mekaniske strukturer kan give anledning til rige dynamiske effekter. På det seneste har ikke-lineær dynamik i mikromekaniske strukturer bidraget til udviklingen af nye Mikro-Elektro-Mekaniske Systemer (MEMS), for eksempel til "atomic force" mikroskopi, passive frekvensdelere, frekvens stabilisatorer, og resonator gyroskoper. For at muliggøre design og optimering af disse strukturer, er det nødvendigt at udvide de eksisterende optimeringsmetoder, der typisk er baseret på lineær dynamik, til at tage de ikke-lineære dynamiske effekter med i betragtning.

I denne afhandling er der udviklet en metode til at modellere, analysere, karakterisere og optimere strukturer på basis af deres ikke-lineær dynamiske opførsel. Modelleringen baserer sig på ikke-lineær finite element analyse og den ikke-lineære frekvensrespons og ikke-lineære svingningsformer er beregnet ved hjælp af en harmonisk balance metode med højere ordens harmoniske komponenter medtaget. I karakteriseringen er ikke-lineære modale koblingskoefficienter beregnet direkte ud fra den ikke-lineære finite element model. Dette har resulteret i udviklingen af en ny klasse af optimeringsproblemer. Den gradientbaserede optimering er udført ved hjælp følsomhedsanalyse baseret på den adjungerede metode, som er specielt velegnet til storskala optimeringsproblemer. Anvendeligheden af den udviklede metode er eksemplificeret ved optimeringen af plane rammekonstruktioner. Arbejdet har vist følgende resultater: amplitude og frekvens af den ikke-lineære resonante respons kan effektivt optimeres; superharmoniske resonanser kan undertrykkes eller forstærkes; Ikke–lineære karakteristika (hård/blød ikke linearitet) kan kvalitativt manipuleres; og en størrelsesordens forbedring af væsentlige modale koblingskoefficienter kan opnås.

Undersøgelsen har vist lovende mulige applikationer inden for ikke-lineære mikromekaniske resonatorer. Dette baner også vejen for topologioptimering af deres komplekse ikke-lineære dynamik.

Abstract

The intrinsic nonlinearity of mechanical structures can give rise to rich nonlinear dynamics. Recently, nonlinear dynamics of micro-mechanical structures have contributed to developing new Micro-Electro-Mechanical Systems (MEMS), for example, atomic force microscope, passive frequency divider, frequency stabilization, and disk resonator gyroscope. For advanced design of these structures, it is of considerable value to extend current optimization in linear structural dynamics into nonlinear structural dynamics.

In this thesis, we present a framework for modelling, analysis, characterization, and optimization of nonlinear structural dynamics. In the modelling, nonlinear finite elements are used. In the analysis, nonlinear frequency response and nonlinear normal modes are calculated based on a harmonic balance method with higher-order harmonics. In the characterization, nonlinear modal coupling coefficients are calculated directly from a nonlinear finite element model. Based on the analysis and the characterization, a new class of optimization problems is studied. In the optimization, design sensitivity analysis is performed by using the adjoint method which is suitable for large-scale structural optimization. The optimization procedure is exemplified by the design of plane frame structures. The work has demonstrated the following results: the amplitude and the frequency of nonlinear resonance peak can be effectively optimized; the super-harmonic resonances can be either suppressed or enhanced; the hardening/softening behavior can be qualitatively changed; and an order-of-magnitude improvement of some essential modal coupling coefficients can be achieved.

The study has shown promising applications in nonlinear micro-mechanical resonators. It also paves the way for topology optimization of complex nonlinear dynamics.

Publications

The following publications are part of the thesis

[P1] S. Dou, J. S. Jensen, Optimization of nonlinear structural resonance using the incremental harmonic balance method, *Journal of Sound and Vibration*, **334**, 239-254, 2015.

[P2] S. Dou, B. S. Strachan, S. W. Shaw and J. S. Jensen, Structural optimization for nonlinear dynamic response. (To appear in the "A field guide to nonlinearity in structural dynamics" issue of Philosophical Transactions A)

[P3] S. Dou, J. S. Jensen, Optimization of hardening/softening behavior of plane frame structures using nonlinear normal modes. (Submitted for journal publication)

[P4] S. Dou, J. S. Jensen, Optimal design of hardening and softening resonances of plane frame structures. Abstract presented at the 8th European Nonlinear Dynamics Conference, Vienna, Austria, 2014.

[P5] S. Dou, J. S. Jensen, Analytical sensitivity analysis and topology optimization of nonlinear resonant structures with hardening and softening behavior. Abstract presented at the 17th U.S. National Congress on Theoretical and Applied Mechanics, East Lansing, Michigan, United States, 2014.

Contents

Chapter 1
Introduction

The study in this Ph.D. project was an attempt to connect the two fields: nonlinear dynamics and structural optimization. For an integrated analysis and optimization of nonlinear dynamics, finite element models form an ideal bridge, see Fig. 1.1. Based on nonlinear finite element models, we developed a convenient framework for modeling, analysis, characterization and optimization of nonlinear structural dynamics. By using the new framework, complex nonlinear dynamics are systematically optimized by using gradient-based structural optimization. It is particularly suitable for tailoring the intrinsic nonlinearity of mechanical structures. A promising application of the framework is characterization and optimal design of nonlinear micro-mechanical resonators used in Micro-Electro-Mechanical Systems (MEMS).

1.1 Motivation and goals

The intrinsic nonlinearity of mechanical systems can give rise to rich nonlinear dynamics. As a first example, consider the nonlinear transverse vibration of a clamped-clamped beam. Since the movement at the ends is restricted, its

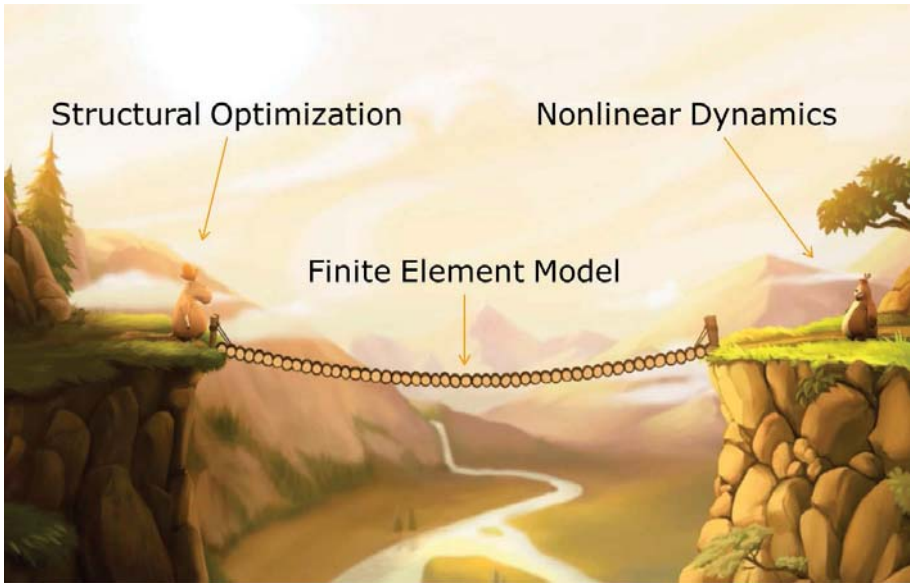

Figure 1.1 Finite element models form a bridge between the two fields: nonlinear dynamics and structural optimization. The image is the courtesy of Ting Chian Tey.

transverse vibration produces midplane stretching. Therefore the transverse and the longitudinal vibration are obviously coupled. Further, midplane stretching causes hardening behavior of the system. Surprisingly, the transverse and the longitudinal vibration are separate in the linear structural dynamics and it follows that the hardening behavior is missed. This simple example shows that linear structural dynamics are approximation of the underlying nonlinear structural dynamics.

For general introductions of nonlinear dynamics in continuum structures, the reader can refer to many textbooks, e.g., Nayfeh and Mook (1979); Thomsen (1997, 2003); Nayfeh et al. (2004); Lacarbonara and Verlag. (2013). Below, we briefly introduce the nonlinear dynamics involved in the Ph.D. project and relevant applications in nonlinear micro-mechanical and nano-mechanical resonators. A comprehensive review of nonlinear micro- and nano-resonators can be found in (Lifshitz and Cross, 2008; Rhoads et al., 2010).

Hardening/softening behavior

The first fundamental feature of nonlinear systems is hardening/softening behavior, see, e.g., Touzé et al. (2004); Lacarbonara and Yabuno (2006). For a hardening/softening behavior, the resonance frequency increases/decreases with the amplitude. The hardening/softening behavior has contributed to broadband nonlinear micro-mechanical resonators (Cho et al., 2010; Hajati and Kim, 2011; Elshurafa et al., 2011), nonlinear atomic force microscopy (Cho et al., 2012b) and nonlinear oscillator with substantially lower phase noise (Villanueva et al., 2013).

Recently, researchers have started to explore the possibility of tailoring the intrinsically geometric nonlinearity for targeted hardening/softening behavior, see, e.g., Cho et al. (2012a); Dai et al. (2012); Jeong et al. (2014). Particularly, Cho et al. (2012a) achieved hardening or softening behavior by changing the orientation of a nano-tube that connects two cantilever structures (Fig. 1.2). In the Ph.D. project, one of our goals is to systematically optimize the hardening/softening behavior by tailoring geometric nonlinearity.

Nonlinear modal interaction

Another extremely useful feature of nonlinear systems is nonlinear modal interaction, or nonlinear mode coupling. For general introductions, the reader can refer to Nayfeh (2000). For a single clamped-clamped beam, Westra et al. (2010) demonstrated that nonlinear modal interaction enables one flexural mode to be used a self-detector for the amplitude of another mode; Matheny et al. (2013) reported that nonlinear mode coupling allows accurate experimental characterization of nonlinearities in MEMS. For complex structures, nonlinear modal interaction has contributed to micro-resonators based on internal resonance (Vyas et al., 2008, 2009), passive frequency divider (Strachan et al., 2013; Qalandar et al.,

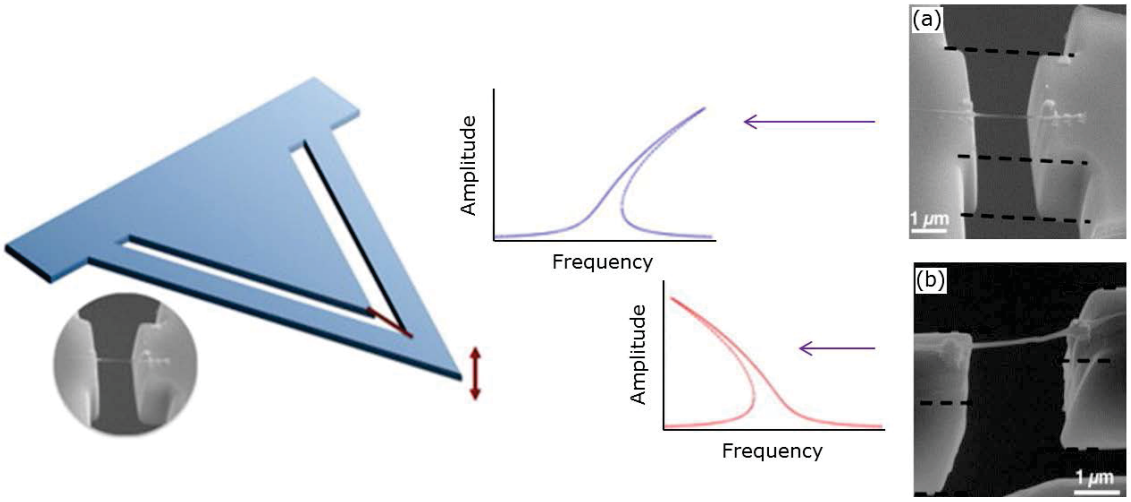

Figure 1.2 A cantilever system with hardening/softening behavior originated from a nano-tube. Figure taken from Cho et al. (2012a).

2014), frequency stabilization (Antonio et al., 2012), multi-harmonic atomic force microscopy (Pettit et al., 2015), and disk resonator gyroscope with self-induced parametric amplification (Nitzan et al., 2015).

From the point of view of structural optimization, Tripathi and Bajaj (2013, 2014) presented two procedures to synthesize families of structures with two commensurable natural frequencies (such as 1:2 or 1:3 relations). In the Ph.D. project, we investigated systematic optimization of the essential modal coupling effects in a T-shaped frequency divider. The T-shaped frequency divider is inspired by the micro-mechanical frequency divider shown in Fig 1.3 Strachan et al. (2013); Qalandar et al. (2014).

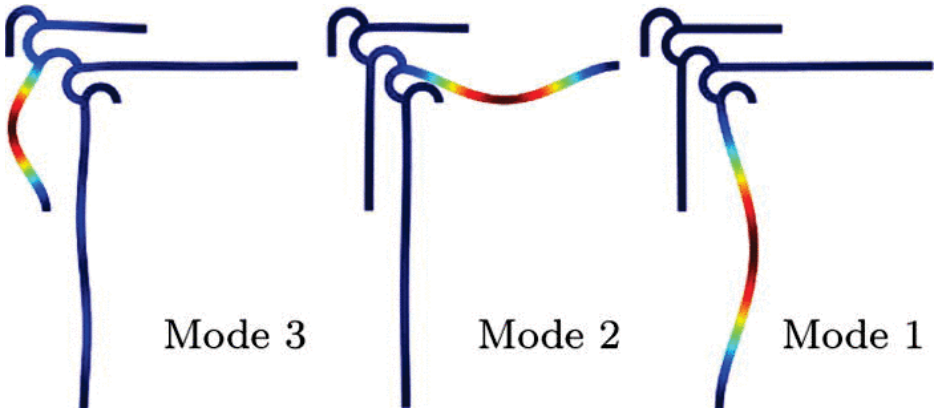

Figure 1.3 The first three vibrational modes of a micro-mechanical frequency divider using resonance cascade from a COMSOL finite element model. The eigenfrequencies of the three modes are tuned such that $\omega_3 \approx 2\omega_2 \approx 4\omega_1$. Figure taken from Qalandar et al. (2014).

Superharmonic resonances

In the Ph.D. project, we also studied the systematic optimization of super-harmonic resonances. In superharmonic resonances, the nonlinear system may generate a significant higher-order harmonic along with the fundamental harmonic, see, e.g., Nayfeh and Mook (1979); Thomsen (1997). The frequency of the higher-order harmonic is an integer multiple of the fundamental frequency. Its applications in nonlinear micro-mechanical resonators have been investigated by Abdel-Rahman and Nayfeh (2003); Nayfeh and Younis (2005); Kacem et al. (2012); Ishinabe et al. (2012); Younesian et al. (2014).

1.2 Current development in nonlinear dynamics

Many concepts and methods are developed for modeling and analysis of complex nonlinear dynamics in mechanical structures. Most existing work are based on analytical modeling and analysis. The analytical approaches are suitable for uniform beams, plates and shells. For the analysis of practical structures, the concepts and numerical methods that can be conveniently combined with finite element models have been developed. Below, we briefly introduce the concepts and numerical methods used in the thesis for the analysis of nonlinear dynamics.

The first concept is nonlinear frequency response. It can be viewed as a nonlinear counterpart of linear frequency response function. It is useful to reveal the nonlinear forced resonances, for example, primary resonances, internal resonances, and superharmonic resonances. The second concept is nonlinear normal mode (NNM). NNM is a nonlinear analogy of the linear normal mode (LNM), see, e.g., Kerschen et al. (2009); Peeters et al. (2009). It provides a systematic way to investigate frequency-energy dependence, which reveals hardening/softening behavior of nonlinear systems, and modal interaction with internal resonance. For a complete and thorough overview of NNM, the reader can refer to (Kerschen, 2014). The third concept is normal form. For general introductions of normal form theory, the reader can refer to many textbooks, e.g., Guckenheimer and Holmes (1983); Wiggins (2003). For mechanical systems with polynomial-type nonlinearity, an explicit link between normal form and NNM was shown by Touzé (2014).

In company with the three concepts, two numerical methods are adopted in our study. The first numerical method is the harmonic balance method (HBM) with higher-order harmonics, see, e.g., Leung and Fung (1989, 1990); Leung (1992); Lewandowski (1992, 1994, 1997); Ribeiro and Petyt (1999); Chen et al. (2001); LaBryer and Attar (2010); Detroux et al. (2014, 2015). It is a natural extension of the harmonic balance method used in linear structural dynamics. Its developments in the past years coincided with the developments of NNM and nonlinear frequency response. The other numerical method is the explicit calculation of nonlinear modal coupling coefficients, see, e.g., Lazarus et al. (2012); Touzé

et al. (2014); Dou et al. (2015). It is suitable for nonlinear finite element models with polynomial-type nonlinearity. Based on the modal coupling coefficients, the normal form linked to normal normal mode can be constructed, see, e.g., Touzé et al. (2004); Touzé and Amabili (2006). For its application in nonlinear micromechanical resonators, we refer to this method as the characterization theory.

These concepts and methods have promoted the use of finite element models in nonlinear dynamics, and consequently paved the way for the study in the thesis. Particularly, the concept of NNM plays a central role. Both the nonlinear frequency response and the normal form can be linked to NNM.

1.3 Gradient-based structural optimization

Gradient-based structural optimization is a powerful tool in design optimization (Choi and Kim, 2006; Bendsøe and Sigmund, 2003). Its basic idea is to improve the targeted performance by manipulating the geometry of structure, i.e., the distribution of material.

Fig 1.4 summarizes current structural optimization in linear structural dynamics. Mechanical structures are modelled by using linear finite elements. The dynamic features are presented by linear frequency response and linear normal modes. The primary optimization problems are with respect to dynamic compliance, eigenvalues and eigenvectors. The sensitivity analysis is calculated by using the adjoint method (Tortorelli and Michaleris, 1994). The design optimization could be shape optimization and topology optimization, see, e.g., Olhoff and Du (2014a,b); Tsai and Cheng (2013).

In nonlinear structural dynamics, gradient-based optimization has been applied to optimize nonlinear transient responses (Jensen and Lazarov, 2008; Kim and Park, 2010; Lee and Park, 2015), and eigenfrequencies of deformed structures with geometrical nonlinearity (Yoon, 2010). Recently, researchers are interested in structural optimization of nonlinear periodic responses (Stanford et al., 2010; Stanford and Beran, 2012; Stanford et al., 2013). Particularly, Petrov (2011) investigated the optimization for tuning nonlinear resonance peak by tracking the maximum amplitude. For internal resonances, Pedersen (2005) and Tripathi and Bajaj (2013, 2014) investigated structural optimization of internal resonance based on the integer relations between the eigenfrequencies.

The contribution of this thesis is a new framework for gradient-based structural optimization in nonlinear structural dynamics, see Fig. 1.5. It forms a nonlinear counterpart of the framework in linear structural dynamics. This thesis highlights that the new framework in nonlinear structural dynamics is convenient for integrated analysis and optimization of complex nonlinear dynamics in mechanical systems.

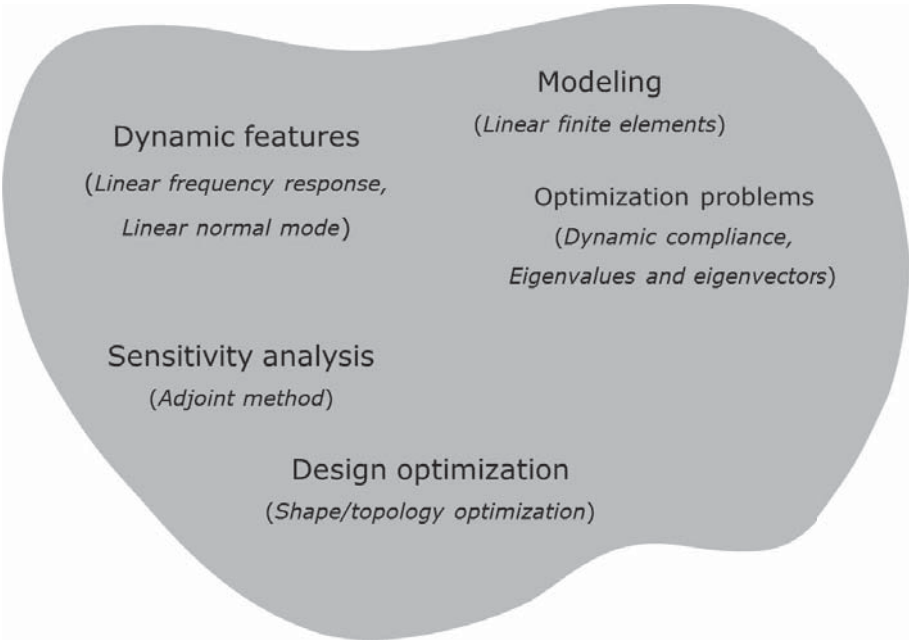

Figure 1.4 A framework for gradient-based optimization in linear structural dynamics.

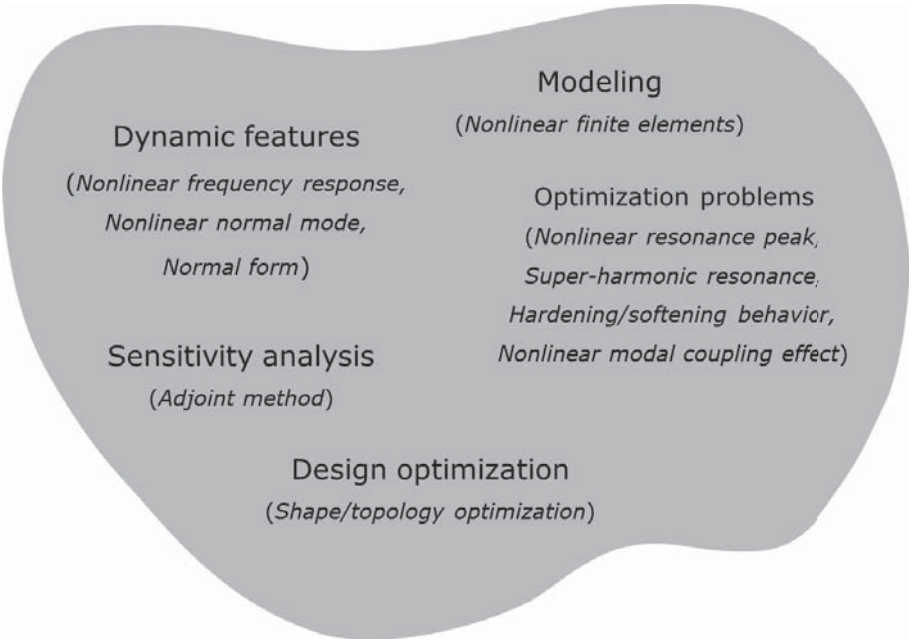

Figure 1.5 A framework for gradient-based optimization in nonlinear structural dynamics.

1.4 Structure of the thesis

This thesis is a summary of the work done during the Ph.D. study. It gives an overview of the main results presented in the five publications [P1]-[P5]. The following is a description of the chapters in the thesis:

- Chapter 1 describes the background and motivation for this Ph.D. project. It also introduces the relevant concepts and methods in nonlinear dynamics and provides an overview of the work in the thesis.
- Chapter 2 is devoted to the methods for modeling, analysis and characterization. First, finite element models with geometric nonlinearity are introduced. Then, we describe computation of nonlinear frequency response and nonlinear normal mode by using the harmonic balance method. Last, we present the explicit calculation of modal coupling coefficients and a brief introduction of normal form linked to nonlinear normal modes. This chapter is the basis for the following optimization problems.
- Chapter 3 introduces advanced optimization of nonlinear resonance peak. A nonlinear resonance peak analysis is first introduced. Next, the optimization problem is formulated based on the resonance condition and the design sensitivity analysis is derived by using the adjoint method. Finally, the optimization examples are offered with respect to the amplitude of nonlinear resonance peak, and the hardening/softening behavior.
- Chapter 4 presents an approach for optimizing the superharmonic resonance. It starts with a brief discussion of superharmonic resonance. Then the optimization problem is formulated based on a prescribed frequency relation. Optimization examples includes superharmonic resonances of order-3 and order-2.
- Chapter 5 is devoted to optimization of nonlinear normal mode. For illustration, a simple example for demonstrating nonlinear normal mode is first discussed. The optimization problem is formulated based on a proper normalization of nonlinear normal mode. The optimization procedure is exemplified by tuning the hardening/softening behavior of plane frame structures.
- Chapter 6 describes how to optimize nonlinear dynamics by using modal coupling coefficients and normal form coefficients. A general optimization problem is first formulated and the design sensitivity analysis is derived. Then, two specific optimization problems are defined for a single-mode resonator and a coupled-mode resonator with 2:1 internal resonance. Finally, case studies involving nonlinear MEMS resonators are offered.
- Chapter 7 summarizes the work and provides suggestions for future work.

Chapter 2
Methods for modelling, analysis and characterization

This chapter presents an overview of the computational methods adopted and developed in the thesis for modelling, analysis and characterization of nonlinear dynamics. In the modelling, finite element models with geometric nonlinearity are introduced. In the analysis, a harmonic balance method with higher-order harmonics is used to compute nonlinear frequency response and nonlinear normal modes (NNMs) (Kerschen et al., 2009; Peeters et al., 2009). In the characterization, a constructive method is used to calculate nonlinear modal coupling coefficients from a finite element model with polynomial-type nonlinearity (Lazarus et al., 2012; Touzé et al., 2014; Dou et al., 2015). Based on the modal coupling coefficients, the normal form coefficients can be further constructed (Touzé et al., 2004; Touzé and Amabili, 2006).

2.1 The method of finite element (FEM)

The method of finite element has become the most frequently applied numerical method in computational mechanics. Its numerical implementation involves discretization of continuum structure, evaluation of element-wise quantities, construction of global quantities and analysis of the equations of motion. For general introductions, the reader can refer to many textbooks, e.g., Cook et al. (2007)

In the thesis, we focus on finite elements with geometric nonlinearity, also known as kinematic nonlinearity. In the following, beam elements and continuum (solid) elements with geometric nonlinearity are discussed. In these elements, geometric nonlinearity is introduced by using a nonlinear strain-displacement relation, which gives an improved measure of the strain in deformed structure.

One of the two kinds of beam elements used in the thesis is based on the Euler-Bernoulli beam theory in conjunction with nonlinearity arising from midplane stretching, see, e.g., Chen et al. (2001); Wriggers (2008). Its strain measures for axial strain ϵ and curvature κ are written as

$$\epsilon = \frac{\partial u}{\partial x} + \frac{1}{2}\left(\frac{\partial v}{\partial x}\right)^2, \ \kappa = \frac{\partial^2 v}{\partial x^2} \tag{2.1}$$

where u denotes the longitudinal displacement, and v denotes the transverse displacement, see Fig. 2.1. The quadratic term in the axial strain denotes the midplane stretching effect. This kind of beam element can be applied to beam structures whose nonlinearity is dictated by the effect of midplane stretching. For beams with large motion, this kind of beam element may give inaccurate,

or even erroneous prediction. In the thesis, this kind of beam element is used for clamped-clamped beams ([P1];[P2]), and a T-shaped frequency divider with three ends clamped ([P2]).

The other kind of beam element used in the thesis is based on the *geometrically exact* theory, see, e.g., Wriggers (2008). It has only one restriction in derivation, i.e., the classical assumption of plane cross sections, and no approximations of trigonometric functions are made. It therefore is applicable for beam structures with large motion. For a shear elastic beam element, its nonlinear strain measures for axial strain ϵ, shear strain γ and curvature κ can be expressed as

$$\begin{aligned} \epsilon &= \left(1 + \frac{\partial u}{\partial x}\right)\cos\varphi + \frac{\partial v}{\partial x}\sin\varphi - 1 \\ \gamma &= \frac{\partial v}{\partial x}\cos\varphi - \left(1 + \frac{\partial u}{\partial x}\right)\sin\varphi \\ \kappa &= \frac{\partial \varphi}{\partial x} \end{aligned} \tag{2.2}$$

where u is the longitudinal displacement, v is the transverse displacement and φ is the rotation, see Fig. 2.1. It can be viewed as an extension of the classical Timoshenko beam theory. In the thesis, the "geometrically exact" beam element is used for a three-beam $\sqcap$-shaped frame structure ([P3];[P4]), and a three-beam H-shaped frame structure ([P3]).

For continuum (solid) finite elements, the geometric nonlinearity can be taken into account by using Green strain, which offers a rotation-independent measure of the deformation, see., e.g., Krenk (2009). For a two-dimensional continuum

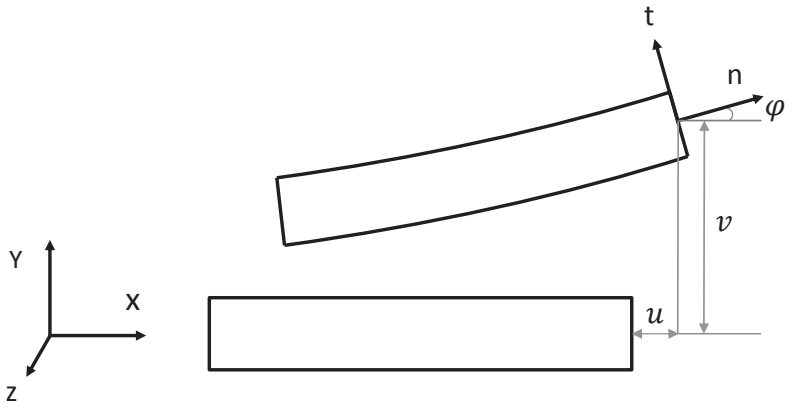

Figure 2.1 Schematic representation of a two-dimensional beam element.

finite element, its strain measure by using Green strain is written as

$$\begin{aligned}\epsilon_{xx} &= \frac{\partial u}{\partial x} + \frac{1}{2}\left(\frac{\partial u}{\partial x}\right)^2 + \frac{1}{2}\left(\frac{\partial v}{\partial x}\right)^2 \\ \epsilon_{yy} &= \frac{\partial v}{\partial y} + \frac{1}{2}\left(\frac{\partial u}{\partial y}\right)^2 + \frac{1}{2}\left(\frac{\partial v}{\partial y}\right)^2 \\ 2\epsilon_{xy} &= \frac{\partial u}{\partial y} + \frac{\partial v}{\partial x} + \frac{\partial u}{\partial x}\frac{\partial u}{\partial y} + \frac{\partial v}{\partial x}\frac{\partial v}{\partial y}\end{aligned} \tag{2.3}$$

The two-dimensional continuum element is used for a clamped-clamped two-dimensional continuum structure ([P5]).

By using the aforementioned nonlinear strain measures and assuming a linear constitutive relation for the material, the equations of motion for a finite element model with geometric nonlinearity can be written as

$$\mathbf{M}\ddot{\mathbf{q}} + \mathbf{C}\dot{\mathbf{q}} + \mathbf{g}(\mathbf{q}) = \mathbf{f} \tag{2.4}$$

where $\mathbf{M}$ is the symmetric and positive-definite mass matrix, $\mathbf{C}$ is the linear damping matrix, $\mathbf{g}(\mathbf{q})$ denotes the nonlinear displacement-dependent internal force, and $\mathbf{f}$ describes the external load. Since Eq. (2.4) is nonlinear, its numerical analysis often requires the Jacobian matrix of the nonlinear internal force, also known as the tangent stiffness matrix, i.e.

$$\mathbf{K}_T(\mathbf{q}) = \frac{\partial \mathbf{g}(\mathbf{q})}{\partial \mathbf{q}} \tag{2.5}$$

When the displacements are zeros, i.e., $\mathbf{q} = \mathbf{0}$, the tangent stiffness matrix reduces to the linear stiffness matrix. For clarity, the linear stiffness matrix is denoted by $\mathbf{K}_L$ in the thesis.

It is noted that the strain measures in Eqs. (2.1) and (2.3) lead to quadratic and cubic nonlinearity in the resulting finite element model; the strain measures in Eq. (2.2) lead to trigonometric nonlinearity in the resulting finite element model.

In the following two sections, the method of finite element is combined with a harmonic balance method with higher-order harmonics to analyze nonlinear frequency response and nonlinear normal modes, and a constructive method for explicit calculation of modal coupling coefficients and normal form coefficients, respectively.

2.2 Harmonic balance method (HBM)

Harmonic balance method with higher-order harmonics, also known as higher-order harmonic balance method, is one of the efficient methods for computation of time-periodic response of nonlinear mechanical systems, including forced

steady-state response linked to nonlinear frequency response, and free time-periodic response linked to nonlinear normal modes. Based on the work of Chen et al. (2001), a slightly modified derivation is used in [P1] to highlight the governing equation in frequency domain and the pre-computation that can simplify the numerical implementation. In [P3], it is further combined with the alternating frequency/time domain method (AFT) (Cameron and Griffin, 1989) for handling complex nonlinearity, e.g., trigonometric nonlinearity in Eq. (2.3).

The derivation starts with the equations of motion in Eq. (2.4). First, a new time scale τ is introduced such that $\tau = \omega t$, where ω is the angular frequency of time-periodic response. Consequently, Eq. (2.4) can be rewritten as

$$\omega^2 \mathbf{M}\mathbf{q}'' + \omega \mathbf{C}\mathbf{q}' + \mathbf{g}(\mathbf{q}) = \mathbf{f} \tag{2.6}$$

where the prime indicates the differentiation with respect to the new time scale τ. Then, the time-periodic system response, e.g., displacement, is expanded into Fourier series with higher-order harmonics as

$$q_i(\tau) = a_0 + \sum_{n=1}^{N_H} (a_{in} cos(n\tau) + b_{in} sin(n\tau)) \tag{2.7}$$

where i denotes the ith degree of freedom, N_H is the highest order of retained harmonics. For convenience, the Fourier expansion can also be written in matrix form as

$$q_i(\tau) = \mathbf{C_s}\,\overline{\mathbf{q}}_i, \quad \overline{\mathbf{q}}_i = [a_{i0}, a_{i1}, \ldots, a_{iN_H}, b_{i0}, \ldots, b_{iN_H}]^T \tag{2.8}$$

where $\mathbf{C_s}$ denotes a Fourier basis consisting of sines and cosines, $\overline{\mathbf{q}}_i$ denotes the Fourier coefficients of $q_i(\tau)$ projected on $\mathbf{C_s}$. Further, the Fourier expansion of the displacements of all degrees of freedom can be written as

$$\mathbf{q}(\tau) = \mathbf{S}\overline{\mathbf{q}}, \quad \overline{\mathbf{q}} = [\overline{\mathbf{q}}_1^T, \ldots, \overline{\mathbf{q}}_{N_D}^T]^T \tag{2.9}$$

where $\mathbf{S}$ denotes a set of Fourier bases, i.e., $\mathbf{S} = \mathrm{diag}(\mathbf{C_s}, \ldots, \mathbf{C_s})$, and N_D is the number of degrees of freedom. By substituting Eq. (2.9) into Eq. (2.6), we obtain

$$\omega^2 \mathbf{M}\mathbf{S}''\overline{\mathbf{q}} + \omega \mathbf{C}\mathbf{S}'\overline{\mathbf{q}} + \mathbf{g}(\mathbf{S}\overline{\mathbf{q}}) = \mathbf{f} \tag{2.10}$$

Finally, the Galerkin method is applied by projecting Eq. (2.10) onto $\mathbf{S}$ and performing integration from 0 to 2π. This leads to the governing equation of nonlinear frequency response below.

2.2.1 Computation of nonlinear frequency response [P1]

The governing equation of nonlinear frequency response is written as

$$\omega^2\, \overline{\mathbf{M}}\, \overline{\mathbf{q}} + \omega\, \overline{\mathbf{C}}\, \overline{\mathbf{q}} + \overline{\mathbf{g}}(\overline{\mathbf{q}}) = \overline{\mathbf{f}} \tag{2.11}$$

where the barred quantities $\overline{\mathbf{M}}$, $\overline{\mathbf{C}}$, $\overline{\mathbf{g}}$ and $\overline{\mathbf{f}}$ are given as

$$\begin{aligned} \overline{\mathbf{M}} &= \frac{1}{2\pi}\int_0^{2\pi} \mathbf{S}^T \mathbf{M}\, \mathbf{S}'' \mathrm{d}\tau, \quad \overline{\mathbf{C}} = \frac{1}{2\pi}\int_0^{2\pi} \mathbf{S}^T \mathbf{C}\, \mathbf{S}' \mathrm{d}\tau \\ \overline{\mathbf{g}} &= \frac{1}{2\pi}\int_0^{2\pi} \mathbf{S}^T \mathbf{g}\, \mathrm{d}\tau, \quad \overline{\mathbf{f}} = \frac{1}{2\pi}\int_0^{2\pi} \mathbf{S}^T \mathbf{f}\, \mathrm{d}\tau \end{aligned} \tag{2.12}$$

Note that Eq. (2.11) is nonlinear and needs to be solved by using iterative methods (e.g., Newton-Raphson method). For numerical implementation, the incremental form of Eq. (2.11) is derived as

$$\left(\omega^2 \overline{\mathbf{M}} + \omega \overline{\mathbf{C}} + \overline{\mathbf{K}}_T(\overline{\mathbf{q}})\right) \Delta\overline{\mathbf{q}} + \left(2\,\omega \overline{\mathbf{M}}\,\overline{\mathbf{q}} + \overline{\mathbf{C}}\,\overline{\mathbf{q}}\right) \Delta\omega = \overline{\mathbf{r}} \tag{2.13}$$

where the barred quantities $\overline{\mathbf{K}}_T(\overline{\mathbf{q}})$ and $\overline{\mathbf{r}}$ are given as

$$\begin{aligned} \overline{\mathbf{K}}_T(\overline{\mathbf{q}}) &= \frac{\partial \overline{\mathbf{g}}}{\partial \overline{\mathbf{q}}} = \frac{1}{2\pi}\int_0^{2\pi} \mathbf{S}^T \frac{\partial \mathbf{g}}{\partial \mathbf{q}} \frac{\partial \mathbf{q}}{\partial \overline{\mathbf{q}}} \mathrm{d}\tau = \frac{1}{2\pi}\int_0^{2\pi} \mathbf{S}^T \mathbf{K}_T\, \mathbf{S}\, \mathrm{d}\tau, \\ \overline{\mathbf{r}} &= \overline{\mathbf{f}} - \left(\omega^2 \overline{\mathbf{M}}\,\overline{\mathbf{q}} + \omega \overline{\mathbf{C}}\,\overline{\mathbf{q}} + \overline{\mathbf{g}}(\overline{\mathbf{q}})\right) \end{aligned} \tag{2.14}$$

In computation of nonlinear frequency response, Eq. (2.11) is solved for a range of frequencies. It is noted that in linear frequency response, the response is a single-valued function of frequency. In contrast, nonlinear frequency response could be a multi-valued function of frequency, particularly, near resonances. Due to this distinct nature of nonlinear frequency response, path following and continuation approaches are often used. These approaches are discussed in Section 2.2.5.

2.2.2 Computation of nonlinear normal modes [P3]

As a nonlinear analogy of linear normal modes, nonlinear normal modes reveal the conservative dynamics of the mechanical systems, i.e. without the effects of dissipation and load. By removing the damping term and the load term from Eq. (2.11), the governing equation of nonlinear normal modes is written as

$$\omega^2 \overline{\mathbf{M}}\,\overline{\mathbf{q}} + \overline{\mathbf{g}}(\overline{\mathbf{q}}) = 0 \tag{2.15}$$

where ω represents the angular frequency of a nonlinear normal mode. For numerical implementation, the incremental form of Eq. (2.15) is derived as

$$\left(\omega^2 \overline{\mathbf{M}} + \overline{\mathbf{K}}_T(\overline{\mathbf{q}})\right) \Delta\overline{\mathbf{q}} + \left(2\,\omega \overline{\mathbf{M}}\,\overline{\mathbf{q}}\right) \Delta\omega = \overline{\mathbf{r}} \tag{2.16}$$

where the residue vector $\overline{\mathbf{r}}$ is given as

$$\overline{\mathbf{r}} = -\left(\omega^2 \overline{\mathbf{M}}\,\overline{\mathbf{q}} + \overline{\mathbf{g}}(\overline{\mathbf{q}})\right) \tag{2.17}$$

An ideal starting point in computation of nonlinear normal modes is continuation of time-periodic response in the neighborhood of linear normal modes, i.e., $\omega \approx \omega_p$, where ω_p is the eigenfrequency of pth linear normal mode. The resulting nonlinear normal modes have a clear relation with the linear normal modes, i.e. a linear normal mode corresponds to a family of nonlinear normal modes. As the system energy increases, ω could be larger or smaller than ω_p, which reveals hardening/softening behavior. As the system energy continues to increase, nonlinear normal modes with internal resonances could be observed. The computation procedure is further discussed in Section 2.2.5 and demonstrated in Chapter 5.

2.2.3 Construction of frequency-domain quantities

Below, the approach for constructing the barred quantities $\overline{\mathbf{M}}$, $\overline{\mathbf{C}}$, $\overline{\mathbf{g}}$, $\overline{\mathbf{f}}$ and $\overline{\mathbf{K}}_T$ are discussed. First, four matrices are defined as

$$\begin{aligned}
\mathbf{H}^{(0)} &= \frac{1}{2\pi}\int_0^{2\pi} \mathbf{C}_S^T \mathbf{C}_S''\, d\tau,\ \mathbf{H}^{(1)} = \frac{1}{2\pi}\int_0^{2\pi} \mathbf{C}_S^T \mathbf{C}_S'\, d\tau \\
\mathbf{H}^{(2)} &= \frac{1}{2\pi}\int_0^{2\pi} \mathbf{C}_S^T \mathbf{C}_S\, d\tau,\ \mathbf{H}^{(3)}_{mnl} = \frac{1}{2\pi}\int_0^{2\pi} \mathbf{C}_S(m)\mathbf{C}_S(n)\mathbf{C}_S(l)\, d\tau
\end{aligned} \tag{2.18}$$

where the subscripts $m, n, l = 1, 2, \ldots, 2N_H + 1$. Since these matrices only depend on the Fourier basis $\mathbf{C}_S$ defined in Eq. (2.8), they can be precomputed. Their explicit expressions and sample codes written in MATLAB are given in Appendix A. Once these matrices are evaluated, the barred quantities are constructed as

$$\begin{aligned}
\overline{\mathbf{M}} &= \begin{bmatrix} \mathbf{H}^{(0)}\mathbf{M}_{11} & \cdots & \mathbf{H}^{(0)}\mathbf{M}_{1\mathrm{d}} \\ \vdots & \ddots & \vdots \\ \mathbf{H}^{(0)}\mathbf{M}_{\mathrm{d}1} & \cdots & \mathbf{H}^{(0)}\mathbf{M}_{\mathrm{dd}} \end{bmatrix}, \quad \overline{\mathbf{g}} = \begin{bmatrix} \mathbf{H}^{(2)}\mathcal{F}(\mathbf{g}_1) \\ \vdots \\ \mathbf{H}^{(2)}\mathcal{F}(\mathbf{g}_\mathrm{d}) \end{bmatrix} \\
\overline{\mathbf{C}} &= \begin{bmatrix} \mathbf{H}^{(1)}\mathbf{C}_{11} & \cdots & \mathbf{H}^{(1)}\mathbf{C}_{1\mathrm{d}} \\ \vdots & & \vdots \\ \mathbf{H}^{(1)}\mathbf{C}_{\mathrm{d}1} & \cdots & \mathbf{H}^{(1)}\mathbf{C}_{\mathrm{dd}} \end{bmatrix}, \quad \overline{\mathbf{f}} = \begin{bmatrix} \mathbf{H}^{(2)}\mathcal{F}(\mathbf{f}_1) \\ \vdots \\ \mathbf{H}^{(2)}\mathcal{F}(\mathbf{f}_\mathrm{d}) \end{bmatrix} \\
\overline{\mathbf{K}}_T &= \begin{bmatrix} \sum_l \mathbf{H}_l^{(3)}(\mathcal{F}(\mathbf{K}_{T11}))_l & \cdots & \sum_l \mathbf{H}_l^{(3)}(\mathcal{F}(\mathbf{K}_{T1\mathrm{d}}))_l \\ \vdots & \ddots & \vdots \\ \sum_l \mathbf{H}_l^{(3)}(\mathcal{F}(\mathbf{K}_{T\mathrm{d}1}))_l & \cdots & \sum_l \mathbf{H}_l^{(3)}(\mathcal{F}(\mathbf{K}_{T\mathrm{dd}}))_l \end{bmatrix}
\end{aligned} \tag{2.19}$$

where "$\mathcal{F}(\ )$" denotes Fourier expansion and yields a vector collecting Fourier coefficients in the same order as in Eq. (2.8), and the subscripts $(1, \ldots, d)$ denote the degrees of freedom and $d = N_D$.

It can be seen that there is a mapping relation from one entry in finite element matrix, e.g., $\mathbf{M}_{11}$, to one block in the augmented matrix, e.g., $\mathbf{H}^{(0)}\mathbf{M}_{11}$. For

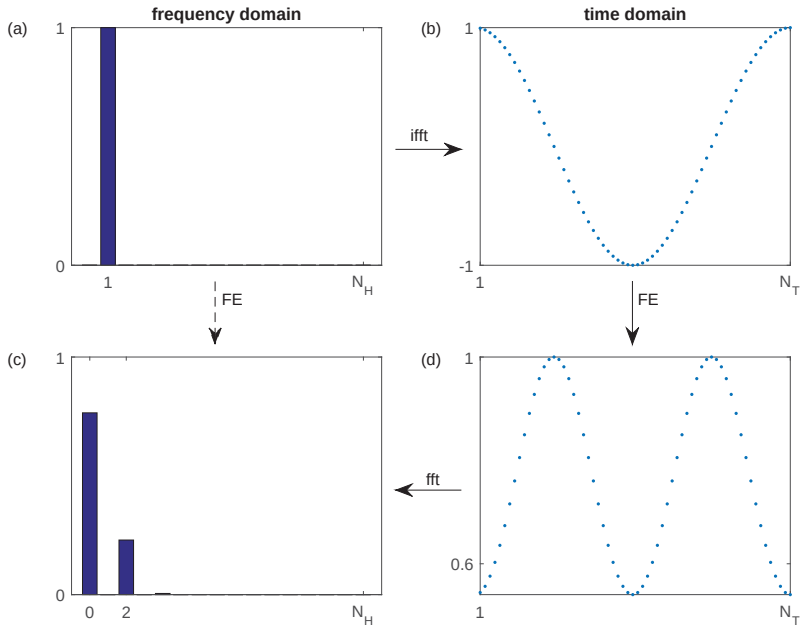

Figure 2.2 Illustration of the two approaches in evaluation of the Fourier coefficients of a nonlinear function. The arrow with dashed line indicates the analytical approach in the frequency domain, and the arrow with solid line indicates the alternating frequency/domain method.

nonlinear internal force and tangent stiffness, this mapping relation is slightly complex. For illustration, take $\mathbf{g}(i) = q_i^3$ as an example. Its tangent stiffness is written as $\mathbf{K}_T(i,i) = 3q_i^2$. In the mapping relation, $\mathbf{g}(i)$ is mapped to the product of $\mathbf{H}^{(2)}$ and $\mathcal{F}(q_i^3)$, and $\mathbf{K}_T(i,i)$ is mapped to $\sum_l \mathbf{H}_l^{(3)}\mathbf{k}_l$, where $\mathbf{k} = \mathcal{F}(3q_i^2)$, $\mathbf{H}_l^{(3)}$ is a two-dimensional matrix extracted from $\mathbf{H}^{(3)}$ with l denoting the third dimension. Once $\mathcal{F}(q_i^3)$ and $\mathcal{F}(3q_i^2)$ are known, the mapping relation can be applied. Below, approaches for evaluating the Fourier coefficients of a nonlinear function, e.g., $\mathcal{F}(q_i^3)$ and $\mathcal{F}(3q_i^2)$ in the example, are discussed.

For a large-scale finite element model with geometric nonlinearity, the mapping relation can be performed on the element-wise quantities (e.g., $\mathbf{M}^e$, $\mathbf{C}^e$, $\mathbf{g}^e$, $\mathbf{K}_T^e$). The resulting augmented element-wise quantities are assembled into global quantities by matching the location of corresponding Fourier coefficients. Sample codes written in MATLAB are offered in Appendix A for both global implementation and element-wise implementation.

2.2.4 Evaluation of Fourier coefficients of nonlinearity

Two approaches for evaluating the Fourier coefficients of a nonlinear function are illustrated in Fig. (2.2), including an analytical approach in the frequency domain, and an alternating frequency/time domain approach.

For the analytical approach in the frequency domain, the Fourier coefficients of a nonlinear function can be obtained by substituting the given Fourier series of its variables into its expression, expanding the expression into a new Fourier series, and extracting the resulting Fourier coefficients. This approach is suitable for polynomial-type nonlinearity. For its application in finite element models, it needs to be implemented in an automatic manner. First, a recursive way is used to calculate the Fourier coefficients of a higher-order polynomial function. For example, once $\overline{\mathbf{q}}_i$ in Eq. (2.8) is given, $\mathcal{F}(q_i^2)$ can be computed, and $\mathcal{F}(q_i^3)$ can be calculated from $\mathcal{F}(q_i^2)$ and $\overline{\mathbf{q}}_i$. Following this reasoning and considering multiple variables, the basic operation is to evaluate $\mathcal{F}(q_i q_j)$ from $\overline{\mathbf{q}}_i$ and $\overline{\mathbf{q}}_j$, see, e.g., Raghothama and Narayanan (1999, 2000). Further, this approach requires extraction of the coefficients of polynomials. Take $c_1 q_i + c_2 q_i^2 + c_3 q_i^3$ as an example. Its Fourier coefficients are calculated as $\mathcal{F}(c_1 q_i + c_2 q_i^2 + c_3 q_i^3) = c_1 \mathcal{F}(q_i) + c_2 \mathcal{F}(q_i^2) + c_3 \mathcal{F}(q_i^3)$, where c_1, c_2 and c_3 are extracted in a symbolic calculation. This approach can be applied to finite element models with geometric nonlinearity defined by strain measures in quadratic form, see, e.g., Eqs. (2.1) and (2.3). Its drawback is the complex procedure in numerical implementation.

The second approach is called the alternating frequency/time domain method (AFT) (Cameron and Griffin, 1989). Instead of evaluating nonlinearity in frequency domain, AFT takes the ease of evaluating nonlinearity in time domain. Take $\mathcal{F}(q_i^2)$ as an example. First, $\overline{\mathbf{q}}_i$ is transformed into a time sequence in the time domain with N_T time points by using the inverse Fourier transform. Then, q_i^2 is evaluated at each time point and generates a new time sequence. Finally, $\mathcal{F}(q_i^2)$ is evaluated from the generated time sequence of q_i^2 by using the direct Fourier transform. It is noted that the inverse and the direct Fourier transforms can also be conveniently realized by using two matrices $\mathbf{W}_{\text{ifft}}$ and $\mathbf{W}_{\text{fft}}$ written as ([P3])

$$\mathbf{W}_{\text{ifft}} = \begin{bmatrix} 1 & \cos\tau_1 & \dots & \cos(N_H\tau_1) & \sin\tau_1 & \dots & \sin(N_H\tau_1) \\ \vdots & \vdots & & \vdots & \vdots & & \vdots \\ 1 & \cos\tau_{N_T} & \dots & \cos(N_H\tau_{N_T}) & \sin\tau_{N_T} & \dots & \sin(N_H\tau_{N_T}) \end{bmatrix} \tag{2.20}$$

$$\mathbf{W}_{\text{fft}} = \frac{2}{N_T} \begin{bmatrix} \frac{1}{2} & \cos\tau_1 & \dots & \cos(N_H\tau_1) & \sin\tau_1 & \dots & \sin(N_H\tau_1) \\ \vdots & \vdots & & \vdots & \vdots & & \vdots \\ \frac{1}{2} & \cos\tau_{N_T} & \dots & \cos(N_H\tau_{N_T}) & \sin\tau_{N_T} & \dots & \sin(N_H\tau_{N_T}) \end{bmatrix}^T \tag{2.21}$$

For its application in a finite element model, it involves N_T sets of internal force vectors and tangent stiffness matrices. To save the memory used in computation, an element-wise implementation is used, see Appendix A. The advantages of the method are the general applicability and the simplicity in numerical implementation.

2.2.5 Analysis and continuation approaches

Path following and continuation approaches play a significant role in numerical computation of nonlinear frequency response and nonlinear normal modes. Below, general and specialized continuation approaches are discussed.

For general continuation approaches, one continuation step can be divided into two sub-steps: a prediction and an iteratively correction. Didier et al. (2013) summarized the three most classical predictors (secant method, tangent method and Lagrange polynomials) and the three most classical correctors (arc-length method, pseudo arc-length method, and Moore-Penrose method). A combination of tangent predictor and Moore-Penrose corrector can be found in (Detroux et al., 2014).

In this study we used the combination of cubic polynomial predictor and arc-length corrector. The arc-length method used in the study is formulated as

$$\beta \left(\frac{\omega - \omega_0}{\omega_0} \right)^2 + \left(\frac{\|\bar{\mathbf{q}} - \bar{\mathbf{q}}_0\|}{\|\bar{\mathbf{q}}_0\|} \right)^2 = (\Delta s)^2 \tag{2.22}$$

where β is a scaling factor and Δs controls the step size. For details, the reader can refer to [P1] and Cheung et al. (1990); Leung and Chui (1995). To start the polynomial prediction, several initial steps are required. For computation of nonlinear frequency response, these initial steps are obtained by using simple frequency increment method. For computation of nonlinear normal modes, these initial steps are generated by using the amplitude increment method discussed below.

Besides general continuation approaches, a set of specialized continuation approaches are studied and developed. These approaches are suitable to compute nonlinear frequency response and nonlinear normal modes with a specific feature.

In computation of nonlinear frequency response, we proposed a special nonlinear resonance peak analysis (Dou and Jensen, 2015) based on phase lag quadrature criterion (Peeters et al., 2011a,b), where the continuation is performed by using load increment method, see Section 3.1. This continuation approach is convenient for evaluating the nonlinear resonance peak at a specific load level.

In computation of nonlinear normal modes with hardening/softening behavior, the continuation can be performed with respect to reference amplitude, e.g., a_{i1}, or the energy of the whole system, see Section 5.1. We refer to these methods as amplitude increment method and energy increment method, respectively. These two continuation approaches are useful for computation of nonlinear normal modes at a specific amplitude or energy.

2.3 Explicit calculation of modal coupling coefficients

This section presents one method for explicit calculation of modal coupling coefficients for mechanical structures with geometric nonlinearity (Lazarus et al.,

2012; Touzé et al., 2014; Dou et al., 2015). These modal coupling coefficients can be used to further construct the normal form coefficients for a given resonance condition (Touzé et al., 2004; Touzé and Amabili, 2006). It is particularly useful for characterization and optimal design of the nonlinear modal coupling effects in micro-mechanical resonators.

2.3.1 Derivation of modal coupling coefficients [P2]

In [P2], the modal coupling coefficients are derived based on explicit modal expansion of the Hamiltonian of the nonlinear finite element model. For completeness, it is presented below.

With finite element discretization of a mechanical structure with geometric nonlinearity, the Hamiltonian for the system, i.e. the sum of kinetic energy T and potential energy U, can be expressed as

$$\mathcal{H} = T + U = \frac{1}{2}\dot{\mathbf{u}}^T\mathbf{M}\dot{\mathbf{u}} + \sum_{e=1}^{N_e}\frac{1}{2}\int_{V_e}\boldsymbol{\epsilon}^T\boldsymbol{\sigma}\ dV \tag{2.23}$$

where $\mathbf{M}$ is the mass matrix of the finite element model, $\mathbf{u}$ is the global vector of nodal displacements, $\boldsymbol{\epsilon}$ and $\boldsymbol{\sigma}$ are element-wise vectors of strain and stress components, respectively, and V_e indicates the volume of the eth element. Assuming a linear strain-stress relation, the potential energy U can be written as

$$U = \sum_{e=1}^{N_e}\frac{1}{2}\int_{V_e}\boldsymbol{\epsilon}^T\boldsymbol{\sigma}\ dV = \sum_{e=1}^{N_e}\frac{1}{2}\int_{V_e}\boldsymbol{\epsilon}^T\mathbb{C}\,\boldsymbol{\epsilon}\ dV \tag{2.24}$$

where $\mathbb{C}$ is a symmetric constitutive matrix. We may now divide the strain into a linear and nonlinear part as

$$\boldsymbol{\epsilon} = \mathbf{B}_0\,\mathbf{u}^e + \frac{1}{2}\,\mathbf{B}_1(\mathbf{u}^e)\,\mathbf{u}^e \tag{2.25}$$

where $\mathbf{B}_0$ is the linear strain-displacement matrix and $\mathbf{B}_1(\mathbf{u}^e)$ is a function of the element-wise vector of nodal displacements $\mathbf{u}^e$. Substituting Eq. (2.25) into Eq. (2.24) and using the symmetry of $\mathbb{C}$, the potential energy U can be divided into three parts as

$$\begin{aligned}
U^{(2)} &= \sum_{e=1}^{N_e}\frac{1}{2}\int_{V_e}(\mathbf{u}^e)^T\,\mathbf{B}_0^T\,\mathbb{C}\,\mathbf{B}_0\,\mathbf{u}^e\ dV,\\
U^{(3)} &= \sum_{e=1}^{N_e}\frac{1}{2}\int_{V_e}(\mathbf{u}^e)^T\,\mathbf{B}_0^T\,\mathbb{C}\,\left(\mathbf{B}_1(\mathbf{u}^e)\right)\,\mathbf{u}^e\ dV\\
U^{(4)} &= \sum_{e=1}^{N_e}\frac{1}{8}\int_{V_e}(\mathbf{u}^e)^T\,\left(\mathbf{B}_1(\mathbf{u}^e)\right)^T\,\mathbb{C}\,\left(\mathbf{B}_1(\mathbf{u}^e)\right)\,\mathbf{u}^e\ dV
\end{aligned} \tag{2.26}$$

The next step is to perform explicit modal expansion of the Hamiltonian of the system. A natural basis for modal expansion is using linear normal modes solved from the linear eigenvalue problem

$$(\omega^2 \mathbf{M} - \mathbf{K}_L)\mathbf{\Phi} = \mathbf{0} \tag{2.27}$$

where $\mathbf{K}_L$ is the linear stiffness matrix. The resulting eigenfrequencies and eigenvectors are denoted as $(\omega_p,\ \mathbf{\Phi}_p)$, and the eigenvectors are normalized with respect to mass matrix such that $\mathbf{\Phi}_p^T \mathbf{M} \mathbf{\Phi}_p = 1$ and $\mathbf{\Phi}_p^T \mathbf{K}_L \mathbf{\Phi}_p = \omega_p^2$. By using the linear eigenvectors, the element-wise nodal displacements can be expressed as a superposition of N_m linear modes as

$$\mathbf{u}^e = \sum_{p=1}^{N_m} q_p \, \mathbf{\Phi}_p^e \tag{2.28}$$

where $\mathbf{u}^e$ is the nodal displacements of the eth element , q_p is the modal coordinate and $\mathbf{\Phi}_p^e$ is the element-wise mode shape vector extracted from the global vector. Substituting Eq. (2.28) into Eq. (2.26), we obtain the strain energy expressed in terms of mode shapes and modal coordinates as

$$\begin{aligned} U^{(2)} &= \sum_{i=1}^{N_m} \sum_{j=1}^{N_m} \alpha_{ij}^{(2)} \ q_i \ q_j \\ U^{(3)} &= \sum_{i=1}^{N_m} \sum_{j=1}^{N_m} \sum_{k=1}^{N_m} \alpha_{ijk}^{(3)} \ q_i \ q_j \ q_k \\ U^{(4)} &= \sum_{i=1}^{N_m} \sum_{j=1}^{N_m} \sum_{k=1}^{N_m} \sum_{l=1}^{N_m} \alpha_{ijkl}^{(4)} \ q_i \ q_j \ q_k \ q_l \end{aligned} \tag{2.29}$$

where the modal coupling coefficients, $\alpha_{ij}^{(2)}$, $\alpha_{ijk}^{(3)}$ and $\alpha_{ijkl}^{(4)}$, are explicitly expressed as

$$\begin{aligned} \alpha_{ij}^{(2)} &= \sum_{e=1}^{N_e} \frac{1}{2} \int_{V_e} (\mathbf{\Phi}_i^e)^T \, \mathbf{B}_0^T \, \mathbb{C} \, \mathbf{B}_0 \, \mathbf{\Phi}_j^e \ dV \\ \alpha_{ijk}^{(3)} &= \sum_{e=1}^{N_e} \frac{1}{2} \int_{V_e} (\mathbf{\Phi}_i^e)^T \, \mathbf{B}_0^T \, \mathbb{C} \left(\mathbf{B}_1(\mathbf{\Phi}_j^e) \right) \mathbf{\Phi}_k^e \ dV \\ \alpha_{ijkl}^{(4)} &= \sum_{e=1}^{N_e} \frac{1}{8} \int_{V_e} (\mathbf{\Phi}_i^e)^T \, \left(\mathbf{B}_1(\mathbf{\Phi}_j^e) \right)^T \, \mathbb{C} \, \left(\mathbf{B}_1(\mathbf{\Phi}_k^e) \right) \, \mathbf{\Phi}_l^e \ dV \end{aligned} \tag{2.30}$$

Since we use the linear normal modes normalized with respect to the mass matrix, we have $\alpha_{ij}^{(2)} = 0$ for $i \neq j$ and $\alpha_{ii}^{(2)} = \omega_i^2/2$. With these modal coupling

coefficients, we can now write the Hamiltonian for the system in Eq. (2.23) in modal coordinates (q_i, p_i) (where $p_i = \dot{q}_i$) as

$$\mathcal{H} = \sum_{i=1}^{N_m} \left(\frac{1}{2} p_i^2 + \frac{1}{2} \omega_i^2 q_i^2 \right) + \sum_{i=1}^{N_m} \sum_{j=1}^{N_m} \sum_{k=1}^{N_m} \alpha_{ijk}^{(3)} \, q_i \, q_j \, q_k + \sum_{i=1}^{N_m} \sum_{j=1}^{N_m} \sum_{k=1}^{N_m} \sum_{l=1}^{N_m} \alpha_{ijkl}^{(4)} \, q_i \, q_j \, q_k \, q_l \tag{2.31}$$

where the relation $\frac{1}{2} p_i^2 = \frac{1}{2} (p_i \mathbf{\Phi}_i)^T \mathbf{M} (p_i \mathbf{\Phi}_i)$ has been used. With the Hamiltonian of the system, it is straightforward to derive a set of ordinary differential equations in modal coordinates as

$$\ddot{q}_p + 2\xi_p \omega_p \dot{q}_p + \omega_p^2 q_p + \sum_{i=1}^{N_m} \sum_{j=1}^{N_m} g_{ij}^p \, q_i \, q_j + \sum_{i=1}^{N_m} \sum_{j=1}^{N_m} \sum_{k=1}^{N_m} h_{ijk}^p \, q_i \, q_j \, q_k = f_p(t) \tag{2.32}$$

where $p = 1, \ldots, N_m$, q_p is the modal coordinate corresponding to $\mathbf{\Phi}_p$, and we have introduced the modal force f_p obtained from a projection of the load vector $\mathbf{f}$ in the full finite element model onto the pth mode, i.e., $f_p = \mathbf{\Phi}_p^T \mathbf{f}$, as well as modal damping ratios (damping as a ratio of critical damping) expressed as ξ_p. The modal coupling coefficients g_{ij}^p and h_{ijk}^p are

$$\begin{aligned} g_{ij}^p &= \alpha_{pij}^{(3)} + \alpha_{ipj}^{(3)} + \alpha_{ijp}^{(3)} \\ h_{ijk}^p &= \alpha_{pijk}^{(4)} + \alpha_{ipjk}^{(4)} + \alpha_{ijpk}^{(4)} + \alpha_{ijkp}^{(4)} \end{aligned} \tag{2.33}$$

It is noted that the differential equation representation of Eq. (2.32) with the modal coupling coefficients in Eq. (2.33) is equivalent to the formulation obtained using the principle of virtual work in a previous study by Touzé et al. (2014).

2.3.2 Derivation of normal form coefficients

One application of the modal coupling coefficients is to predict the type of nonlinearity, i.e., hardening/softening behavior. For a symmetrical mechanical structure like a clamped-clamped beam, its hardening/softening behavior can be well predicted with its dynamics projected onto a linear normal mode.

For asymmetrical mechanical structures like arches and shells, projecting its dynamics onto a linear normal mode may lead to inaccurate or even erroneous prediction of the type of nonlinearity. To correctly predict its hardening/softening behavior, one can use a number of linear normal modes, or alternatively project its dynamics onto a single nonlinear normal mode. The latter can be achieved by using the theory of normal form linked to nonlinear normal modes. In the theory of normal form, modal coordinates (q_p, p_p) can be transformed into the *curved*, normal coordinates (R_p, S_p) (where $S_p = \dot{R}_p$) through a nonlinear

transformation of coordinates, written in general form as

$$\begin{aligned} q_p &= R_p + \mathcal{P}_p(R_i, S_j) \\ p_p &= S_p + \mathcal{Q}_p(R_i, S_j) \end{aligned} \tag{2.34}$$

For details concerning the nonlinear transformation and the resulting normal form, the reader can refer to Touzé et al. (2004); Touzé and Amabili (2006). It is noted that normal form coefficients are explicit functions of modal coupling coefficients.

Based on the modal coupling coefficients and the normal form coefficients, an efficient optimization for nonlinear dynamic response is developed and discussed in Chapter 6. Examples are offered for tuning the hardening/softening behavior of a single-mode resonator, and tuning the essential modal coupling effect of a coupled-mode resonator with 2:1 internal resonance, e.g., a T-shaped frequency divider.

Chapter 3
Optimization of nonlinear resonance peak

This chapter presents a gradient-based optimization method for tuning nonlinear resonance peak. First, an efficient nonlinear resonance peak analysis is proposed based on the phase lag quadrature criterion (Peeters et al., 2011a,b). Then, a general optimization problem is formulated for tuning nonlinear resonance peak, and the design sensitivity analysis is derived by using a specialized adjoint method. Finally, the optimization procedure is exemplified by tuning the amplitude and the hardening/softening behavior of nonlinear resonance peak, respectively.

3.1 Nonlinear resonance peak analysis [P1]

The proposed nonlinear resonance peak analysis is inspired by the phase lag quadrature criterion. This criterion was previously used in dynamic tests of nonlinear normal modes in mechanical structures, see Peeters et al. (2011a,b). According to phase lag quadrature criterion, when a structure with well separated modes vibrates close to the nonlinear resonance peak, the time-periodic response of displacement crosses a phase lag of 90 degrees with respect to the harmonic loads. A physical interpretation of the phase lag quadrature criterion is that the external load compensates for the dissipation in the system.

For nonlinear vibrations, the phase lag criterion can be defined for each harmonic. When the periodic load is written as a combination of sine series

$$f_i = \sum_{n=1}^{N_H} f_{in}^s \sin(n\omega t) \tag{3.1}$$

the nonlinear response fulfilling the phase lag quadrature criterion writes

$$q_i = \sum_{n=1}^{N_H} a_{in} \cos(n\omega t) \tag{3.2}$$

where i denotes the degree of freedom, q denotes the displacement. Note that in the response the coefficients of all sine terms become zero. In the proposed nonlinear resonance peak analysis, it only requires one Fourier coefficient in the response to be zero, i.e.

$$b_{i1} = 0 \tag{3.3}$$

where the subscript i denotes one selected degree of freedom, and the subscript 1 indicates the fundamental harmonic. By setting b_{i1} to zero, the increments of the

other Fourier coefficients and the frequency are solved, and continuation is performed by using incremental load steps to obtain the response at specified load levels. For a clamped-clamped beam shown in Fig. 3.1, its nonlinear frequency response and the "path" of the proposed nonlinear resonance peak analysis are displayed in Figure 3.2.

It is noted that the "path" of nonlinear resonance peak analysis consists of nonlinear resonance peaks for a range of load levels. So we also refer to this "path" as the "backbone" of the nonlinear resonance.

3.2 Formulation of optimization problem

Based on the phase-lag quadrature criterion and by assuming that the external excitation is a pure sine series, a specific formulation for optimizing the nonlinear resonance peak is formulated as

$$\begin{aligned} \min_{\rho_e} \;& c(\overline{\mathbf{q}}(\rho_e), \omega(\rho_e), \omega_p(\rho_e)) \\ \text{s.t. :} \;& \omega^2 \overline{\mathbf{M}}\,\overline{\mathbf{q}} + \omega\,\overline{\mathbf{C}}\,\overline{\mathbf{q}} + \overline{\mathbf{g}} = \overline{\mathbf{f}} \\ & b_{i1} = 0 \text{ (phase condition)} \end{aligned} \tag{3.4}$$

where "s.t." stands for "subject to", $e = 1, \ldots, N_e$ and N_e denoting the number of elements, ρ_e are the normalized design variables used in the optimization to control the geometric dimension of each beam element, and ω_p is the eigenfrequency of the pth linear normal mode associated with the nonlinear resonance.

The design sensitivity analysis is derived by using the adjoint method with two adjoint variables. To derive the adjoint sensitivity analysis, the objective function can be rewritten with the governing equation of the equilibrium state and the phase condition as

$$c = c(\overline{\mathbf{q}}, \omega, \omega_p) + \boldsymbol{\lambda}_1 \left(\omega^2 \overline{\mathbf{M}}\,\overline{\mathbf{q}} + \omega\,\overline{\mathbf{C}}\,\overline{\mathbf{q}} + \overline{\mathbf{g}} - \overline{\mathbf{f}} \right) + \lambda_2\, b_{i1} \tag{3.5}$$

Next, the differentiation of the augmented objective function with respect to the design variables yields

$$\begin{aligned} \frac{\mathrm{d}c}{\mathrm{d}\rho_e} = & \left[\frac{\partial c}{\partial \overline{\mathbf{q}}^T} + \boldsymbol{\lambda}_1^T \left(\omega^2 \overline{\mathbf{M}} + \omega\,\overline{\mathbf{C}} + \overline{\mathbf{K}}_T \right) + \lambda_2 \frac{\partial b_{i1}}{\partial \overline{\mathbf{q}}^T} \right] \frac{\mathrm{d}\overline{\mathbf{q}}}{\mathrm{d}\rho_e} + \\ & \left[\frac{\partial c}{\partial \omega} + \boldsymbol{\lambda}_1^T \left(2\,\omega\,\overline{\mathbf{M}}\,\overline{\mathbf{q}} + \overline{\mathbf{C}}\,\overline{\mathbf{q}} \right) \right] \frac{\mathrm{d}\omega}{\mathrm{d}\rho_e} + \frac{\partial c}{\partial \omega_p} \frac{\mathrm{d}\omega_p}{\mathrm{d}\rho_e} \\ & \boldsymbol{\lambda}_1^T \left(\omega^2 \frac{\partial \overline{\mathbf{M}}}{\partial \rho_e}\,\overline{\mathbf{q}} + \omega \frac{\partial \overline{\mathbf{C}}}{\partial \rho_e}\,\overline{\mathbf{q}} + \frac{\partial \overline{\mathbf{g}}}{\partial \rho_e} \right) \end{aligned} \tag{3.6}$$

Note b_{i1} is one entry in the global vector $\overline{\mathbf{q}}$, and thus $\partial b_{i1}/\partial \overline{\mathbf{q}}$ is a unit vector with all zeros except the n-th entry whose value is one, where $n = (i-1)(2N_H+1) +$

$N_H + 2$. For convenience, $\partial b_{i1}/\partial \overline{\mathbf{q}}$ is denoted as $\mathbf{I}_n$. Then, the values of the adjoint variables are selected such that the expressions in the two brackets in front of $\mathrm{d}\overline{\mathbf{q}}/\mathrm{d}\rho_e$ and $\mathrm{d}\omega/\mathrm{d}\rho_e$ vanish simultaneously. This avoids the direct computation of the first-order sensitivities of the response, which are computationally expensive, and leads to the so-called adjoint equation as

$$\begin{aligned} \frac{\partial c}{\partial \overline{\mathbf{q}}^T} + \boldsymbol{\lambda}_1^T \left(\omega^2 \overline{\mathbf{M}} + \omega \overline{\mathbf{C}} + \overline{\mathbf{K}}_T\right) + \lambda_2 \mathbf{I}_n^T &= \mathbf{0} \\ \frac{\partial c}{\partial \omega} \ + \boldsymbol{\lambda}_1^T \left(2\,\omega \overline{\mathbf{M}}\,\overline{\mathbf{q}} + \overline{\mathbf{C}}\,\overline{\mathbf{q}}\right) &= 0 \end{aligned} \tag{3.7}$$

and the sensitivity of c with respect to ρ_e is in simple form as

$$\frac{\mathrm{d}c}{\mathrm{d}\rho_e} = \boldsymbol{\lambda}_1^T \left(\omega^2 \frac{\partial \overline{\mathbf{M}}}{\partial \rho_e}\,\overline{\mathbf{q}} + \omega \frac{\partial \overline{\mathbf{C}}}{\partial \rho_e}\,\overline{\mathbf{q}} + \frac{\partial \overline{\mathbf{g}}}{\partial \rho_e}\right) + \frac{\partial c}{\partial \omega_p}\frac{\mathrm{d}\omega_p}{\mathrm{d}\rho_e} \tag{3.8}$$

For the convenience in numerical implementation, the adjoint equation is rewritten in matrix form as

$$\begin{bmatrix} \left(\omega^2\overline{\mathbf{M}}+\omega\overline{\mathbf{C}}+\overline{\mathbf{K}}_T\right)^T & \mathbf{I}_n \\ \left(2\,\omega\,\overline{\mathbf{M}}\,\overline{\mathbf{q}} + \overline{\mathbf{C}}\,\overline{\mathbf{q}}\right)^T & \mathbf{0} \end{bmatrix} \begin{bmatrix} \boldsymbol{\lambda}_1 \\ \lambda_2 \end{bmatrix} = - \begin{bmatrix} \dfrac{\partial c}{\partial \overline{\mathbf{q}}} \\ \dfrac{\partial c}{\partial \omega} \end{bmatrix} \tag{3.9}$$

In practical applications, one interesting objective function could be to minimize (or alternatively maximize) the vibration amplitude at the resonance condition, which writes

$$c = \overline{\mathbf{q}}^T \mathbf{L}\,\overline{\mathbf{q}} \tag{3.10}$$

where $\mathbf{L}$ is a diagonal matrix which defines the weights of the Fourier coefficients. The derivatives of c with respect to $\overline{\mathbf{q}},\ \omega, \omega_p$ are written as

$$\frac{\partial c}{\partial \overline{\mathbf{q}}} = 2\,\overline{\mathbf{q}}^T \mathbf{L}, \quad \frac{\partial c}{\partial \omega} = 0, \quad \frac{\partial c}{\partial \omega_p} = 0 \tag{3.11}$$

By substituting Eq. (3.11) into Eq. (3.9), the adjoint variables can be solved. Then the sensitivities are calculated by using Eq. (3.8).

It is worth noticing that the derivation in the thesis originates from the derivation in [P1], where a slightly different formulation was used.

3.3 Optimization examples

In this section, the proposed optimization is applied to tune the amplitude of nonlinear resonance peak of a clamped-clamped beam, and the hardening/softening behavior of nonlinear resonance peak of a three-beam ⊓-shaped frame. In the end, a preliminary study in topology optimization is briefly introduced to inspire future work.

3.3.1 Optimization of nonlinear resonance amplitude [P1]

Nonlinear resonance peak analysis

Consider a clamped-clamped beam sketched in Fig. 3.1. The geometry of initial design is defined by: in-plane width $b = 30$ mm, out-of-plane thickness $t = 10$ mm, and length $L = 433$ mm. The material property is assumed as Young's modulus $E = 205$ Gpa, mass density $\rho = 7800$ kg/m^3. The excitation force is applied at midspan of the beam in the out-of-plane direction. Load levels are selected such that nonlinear resonances can be observed for the initial design. The damping model is introduced by using a damping matrix proportional to the mass matrix, i.e. $\mathbf{C} = \alpha\mathbf{M}$ with $\alpha = 2\xi\omega_1$, where ω_1 denotes the first eigenfrequency of the initial design and the damping ratio ξ is chosen as 0.0044.

The beam is discretized with 100 beam elements with quadratic and cubic nonlinearity arising from midplane stretching and up to sixth-order harmonics are used in the Fourier expansion. For specific formulation of the beam element, the reader can refer to [P1] and (Chen et al., 2001). The primary resonance of the clamped-clamped beam is displayed in Fig. 3.2, where the frequency response (solid lines) is computed using frequency increments for initial steps, and the combination of cubic polynomial predictor and arc-length method for path-following and continuation. The backbone (dashed lines) is computed by using the proposed nonlinear resonance peak analysis in Section 3.1.

As seen in Fig. 3.2, the nonlinear frequency response includes a shift of the resonance frequency, folding of the response curve and multiple solutions. The peak of the resonance shifts towards higher frequencies, which represents hardening

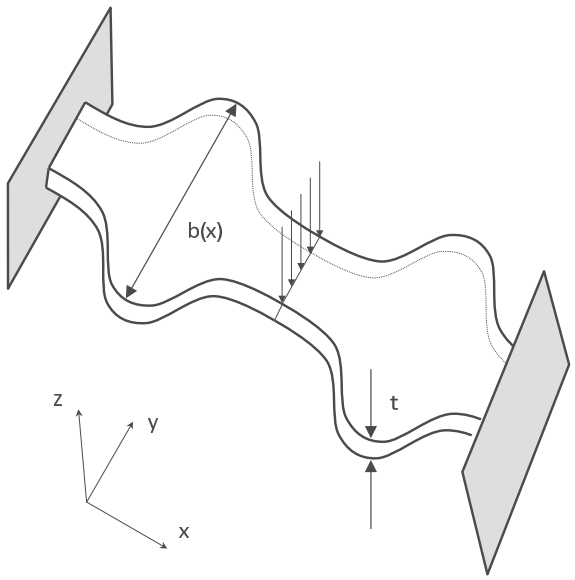

Figure 3.1 A clamped-clamped beam with variable width. Figure taken from [P1].

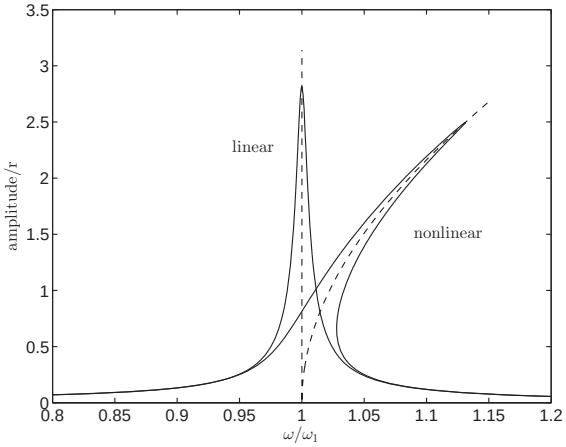

Figure 3.2 Forced vibration of a doubly clamped beam around the first flexural mode. Solid lines denote the frequency-amplitude curves for forced vibration. Dashed lines denote the backbone computed with the phase lag quadrature criterion. Figure taken from [P1].

nonlinearity. In certain frequency ranges there are three solutions for one specific frequency. The top and bottom branches are stable, and the middle branch is unstable. So when the frequency sweeps upwards, the solution jumps to the bottom branch at the peak of the resonance. When the frequency sweeps downwards, the solution jumps to the top branch at the lower folding point. These are all well known phenomena but emphasize the need for an efficient and robust method to predict and subsequently optimize the resonance peak in nonlinear vibration.

Minimize nonlinear resonance peak

The optimization problem is to minimize the peak of the primary resonance by using equation (3.4) with a specific objective function expressed as:

$$c(\mathbf{q}(\rho_e)) = \overline{\mathbf{q}}^T \mathbf{L}\, \overline{\mathbf{q}} = a_{i1}^2 + b_{i1}^2 \tag{3.12}$$

where the index i denotes the degree of freedom corresponding to the lateral deflection at midspan of the beam, a_{i1} and b_{i1} denote the corresponding coefficients of the fundamental harmonic for the lateral displacement, and ω is the frequency of the peak, which is identified using the aforementioned phase lag quadrature criterion and computed along the backbone of the primary resonance. It is noted that the objective function can be simplified to a_{i1}^2 by recalling that $b_{i1} = 0$ in Eq. (3.4).

We bound the width by setting $b_{\text{min}} = 0.1$ mm and $b_{\text{max}} = 100$ mm and specify the volume constraint as $\alpha = 0.3$ which is also set as the volume of the reference beam used as initial design for the optimization. We bound the allowable volume from below and since we are minimizing the amplitude for a fixed

force this ensures that the volume of the final optimized design will match that of the initial reference design. Often design optimization is performed using a linear model and for comparison we will here compare the optimized designs obtained using the nonlinear finite element model with a corresponding linear model. The optimized results are shown in Figure 3.3. The design obtained by using the linear finite element model is independent of the load amplitude and it is seen to have two weak links in the structure where the design variables take their minimum value. In contrast, the optimized design obtained with the nonlinear finite element model shows a dependence on the amplitude of load. For a small amplitude of the load, $f = 60.74$ N, the obtained design is very close to the linear design. However, when we increase the load to a larger amplitude level, $f = 91.11$ N, the two weak links near $x = \frac{1}{4}L$ and $\frac{3}{4}L$ become wider. Thus, even with a limited design freedom that is here dictated by having only a single beam with a fixed thickness, we can see that including the nonlinearities in the optimization procedure has an influence on the nonlinear performance of the optimized designs. This effect is discussed in the end of this section.

The linear and nonlinear frequency-amplitude curves for the two designs are shown in Figure 3.4. Both in linear and nonlinear analysis, the two optimized designs have a resonant peak with an amplitude significantly lower than that of the uniform design. When applying linear vibration analysis, the frequency-amplitude curves for the two optimized designs are seen to overlap. However, based on nonlinear vibration analysis we see a notable difference in the response and the nonlinear optimized design shows a slightly smaller peak amplitude as well as a larger ratio ω/ω_1 for the peak of the primary resonance. A comparison of linear mode shapes of the two optimized structures normalized with respect to mass matrix is shown in Figure 3.4(c). While the mode shapes of two optimized structures only have slightly observable difference, they are quite different from the mode shape of the uniform design.

It is noted that when we minimize the resonant peak, the optimized design based on the nonlinear finite element model has a larger width around $x = \frac{1}{4}L$ and $x = \frac{3}{4}L$, whereas the cross section area vanishes in the optimized design based on the linear finite element model. There is a simple physical interpretation for this phenomenon. Based on the theory of linear vibration, the cross section area would be allowed to vanish at inner points where the material does not contribute to the bending strain energy. In contrast, the bending and stretching deformations are coupled in the nonlinear case. In our example, the bending deformation causes stretching strain energy due to midplane stretching. As shown in Figure 3.5, where ϕ_1 denotes the deformation w for the first linear mode of a doubly clamped beam, the bending strain energy is proportional to $(\frac{\partial^2\phi_1}{\partial x^2})^2$ and the strain energy associated with midplane stretching is proportional to $(\frac{\partial\phi_1}{\partial x})^4$. The strongest midplane stretching effect occurs where $(\frac{\partial\phi_1}{\partial x})^4$ reaches the local maximum and $(\frac{\partial^2\phi_1}{\partial x^2})^2$ reaches the local minimum. So as the load increases, the

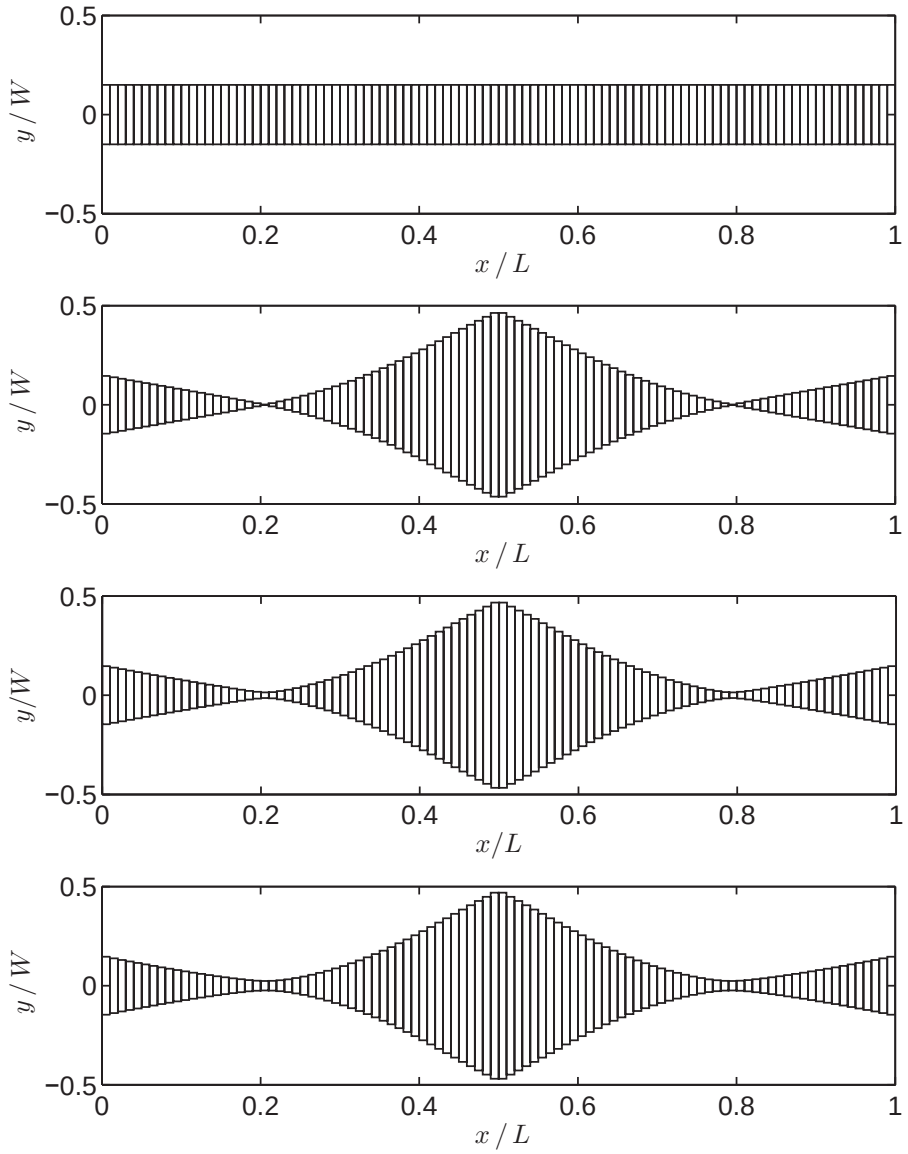

Figure 3.3 A doubly clamped beam with optimized width for minimizing the peak of primary resonance. The sub-figures from top to bottom correspond to uniform width and initial guess, optimized width using linear finite element model, optimized width using nonlinear finite element model and f = 60.74 N, optimized width using nonlinear finite element model and f = 91.11 N. Figure taken from [P1].

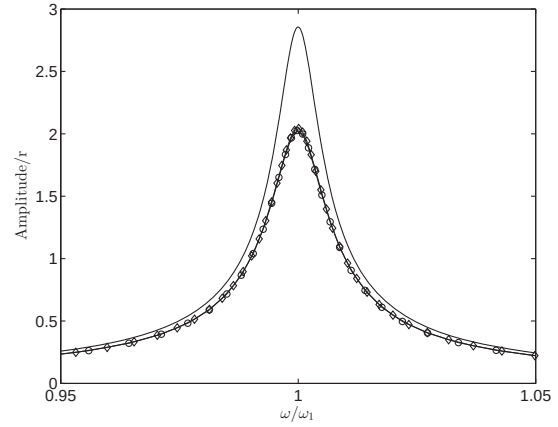

(a)

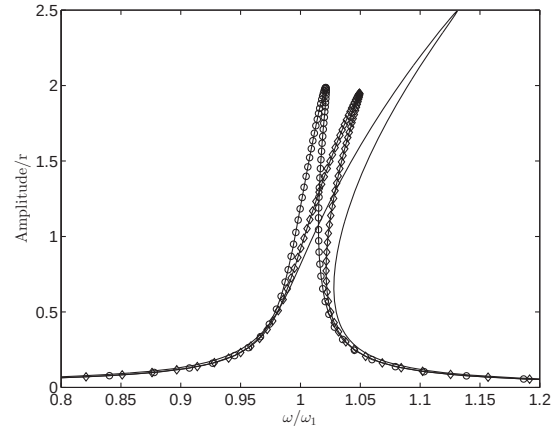

(b)

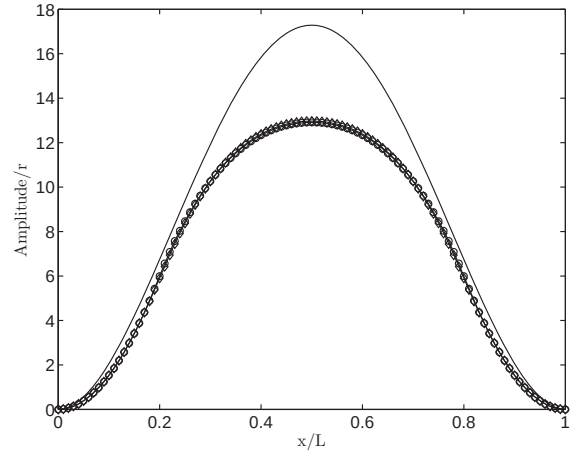

(c)

Figure 3.4 A doubly clamped beam with optimized width for minimizing the peak of primary resonance: '.' uniform width; 'o' optimized width using linear finite element model; '◇' optimized width using nonlinear finite element model and f = 91.11 N: (a) linear analysis; (b) nonlinear analysis; (c) linear modal analysis. Figure taken from [P1].

coupling effect will lead to an increased width around $x = \frac{1}{4}\,L$ and $x = \frac{3}{4}\,L$.

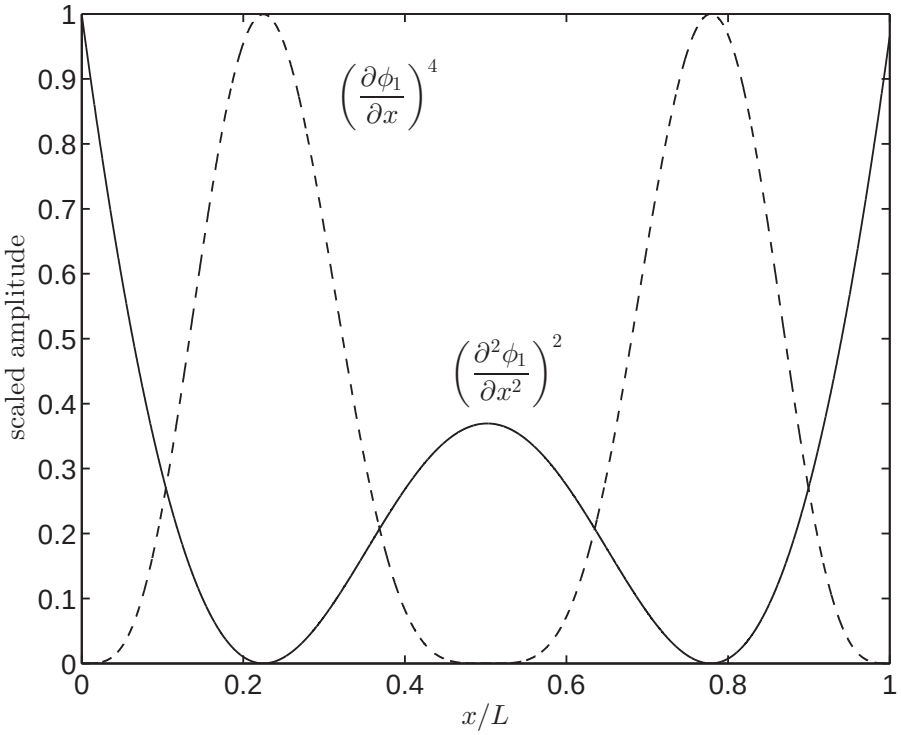

Figure 3.5 Strain energy distribution for the first linear mode. Figure taken from [P1].

3.3.2 Optimization of hardening/softening behavior [P4]

The optimization problem for tuning the hardening/softening behavior of nonlinear resonance peak is formulated as

$$\begin{aligned} &\min_{\rho_e} \ \pm\gamma \\ \text{s.t. : } &\gamma = \frac{\omega}{\omega_p}, \quad (\omega_p^2 \mathbf{M} - \mathbf{K}_L)\boldsymbol{\Phi} = \mathbf{0}, \\ &\omega^2\,\overline{\mathbf{M}}\,\overline{\mathbf{q}} + \omega\,\overline{\mathbf{C}}\,\overline{\mathbf{q}} + \overline{\mathbf{g}} = \overline{\mathbf{f}},\ b_{i1} = 0. \end{aligned} \tag{3.13}$$

where ρ_e is normalized design variable with e denoting the associated element, ω is the nonlinear resonant frequency, ω_p is the eigenfrequency of pth linear normal mode, and γ measures the extent of the hardening or softening nonlinearity. The adjoint sensitivity analysis can be obtained by using Eqs. (3.9) and (3.8). The sensitivities are calculated as

$$\frac{\mathrm{d}c}{\mathrm{d}\rho_e} = \boldsymbol{\lambda}_1^T \left(\omega^2 \frac{\partial \overline{\mathbf{M}}}{\partial \rho_e}\,\overline{\mathbf{q}} + \omega \frac{\partial \overline{\mathbf{C}}}{\partial \rho_e}\,\overline{\mathbf{q}} + \frac{\partial \overline{\mathbf{g}}}{\partial \rho_e} \right) \mp \frac{\omega}{\omega_p^2} \frac{\mathrm{d}\omega_p}{\mathrm{d}\rho_e} \tag{3.14}$$

where the adjoint variable $\boldsymbol{\lambda}_1$ is found from the adjoint equation as

$$\begin{bmatrix} \left(\omega^2\overline{\mathbf{M}}+\omega\overline{\mathbf{C}}+\overline{\mathbf{K}}_T\right)^T & \mathbf{I}_n \\ \left(2\,\omega\,\overline{\mathbf{M}}\,\overline{\mathbf{q}}+\overline{\mathbf{C}}\,\overline{\mathbf{q}}\right)^T & \mathbf{0} \end{bmatrix} \begin{bmatrix} \boldsymbol{\lambda}_1 \\ \lambda_2 \end{bmatrix} = \mp \begin{bmatrix} \mathbf{0} \\ \dfrac{1}{\omega_p} \end{bmatrix} \tag{3.15}$$

In Eq. (3.14), the sensitivity of the eigenfrequency of the pth linear normal mode is required. For simple eigenvalues ω_p^2, it can be obtained as

$$\frac{\mathrm{d}\omega_p}{\mathrm{d}\rho_e} = \frac{1}{2\omega_p}\frac{\mathrm{d}\omega_p^2}{\mathrm{d}\rho_e}, \quad \frac{\mathrm{d}\omega_p^2}{\mathrm{d}\rho_e} = \boldsymbol{\Phi}_p^T\left(\frac{\partial\mathbf{K}_L}{\partial\rho_e} - \omega_p^2\frac{\partial\mathbf{M}}{\partial\rho_e}\right)\boldsymbol{\Phi}_p \tag{3.16}$$

where $\mathbf{K}_L$ is the matrix of linear stiffness, $\boldsymbol{\Phi}_i$ is the eigenvector normalized with respect to mass matrix, i.e. $\boldsymbol{\Phi}_p^T\mathbf{M}\boldsymbol{\Phi}_p = 1$.

For a specific example, consider a three-beam ⊓-shaped frame shown in Fig. 3.6. The beams with uniform cross section are defined by out-of-plane width 30 mm, in-plane thickness 30 mm and a slenderness ratio of 20. The material properties are E=205 GPa, ν=0.3, ρ=7800 kg/m^3. The initial design has a softening resonance around its second linear normal mode. The optimization problem is to minimize the softening behavior and accordingly maximize the hardening behavior, by varying the thickness distribution. This is achieved by using $(-\gamma)$ as the objective function in Eq. (3.13). The design domain is bounded so that the thickness can vary from 20 mm to 40 mm. Besides, the total volume is constrained to not exceed half of the allowed volume and this causes the optimized non-uniform design have the same volume as the initial design.

The optimized frame with non-uniform thickness is shown in Fig. 3.6. The evolution of the backbone during the iterations and comparison of initial backbone and optimized backbone at larger load are shown in Fig. 3.7. It is shown that the backbone was turned from softening behavior to hardening behavior. It is also noticed that the optimized design produces a larger amplitude for the same load level.

3.3.3 One example of topology optimization [P5]

A third example is maximizing the hardening behavior of a thin two-dimensional continuum structure in micro-scale with doubly-clamped boundary condition. An in-plane vertical time-harmonic load is applied at the center node of the structure. The material is Silicon nitride and its mechanical properties are: Young's modulus $E = 241$ GPa, Poisson's ratio $\nu = 0.23$ and mass density 300 kg/m^3. Plane stress conditions are assumed and preliminary results are obtained with a coarse discretization of 40×20 elements.

The initial design is simply the uniform distribution of material in the design domain. The specified load is so small that the relative frequency shift around the

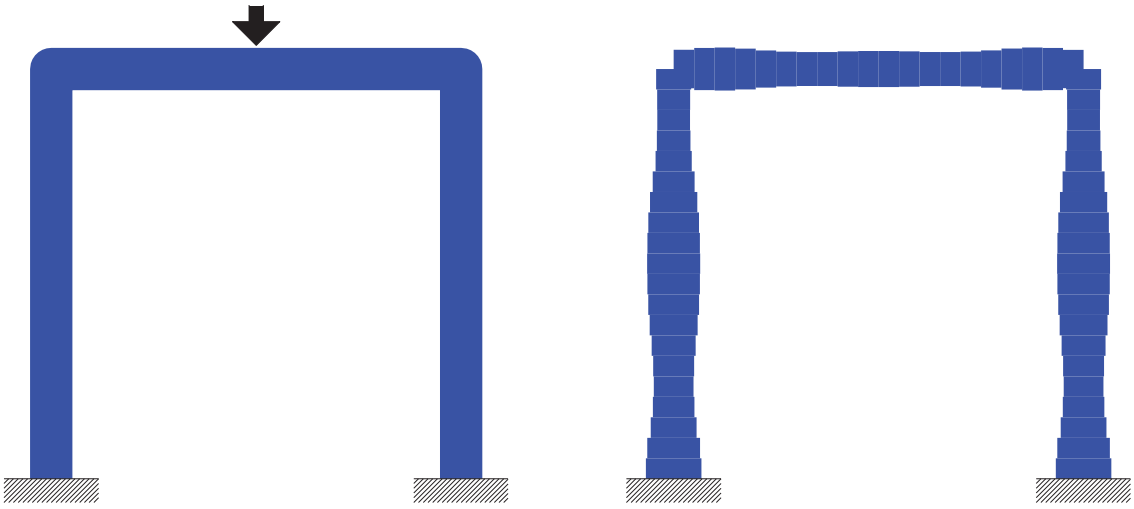

Figure 3.6 Schematic representation of initial design (left) and optimized design (right). Figure taken from [P4].

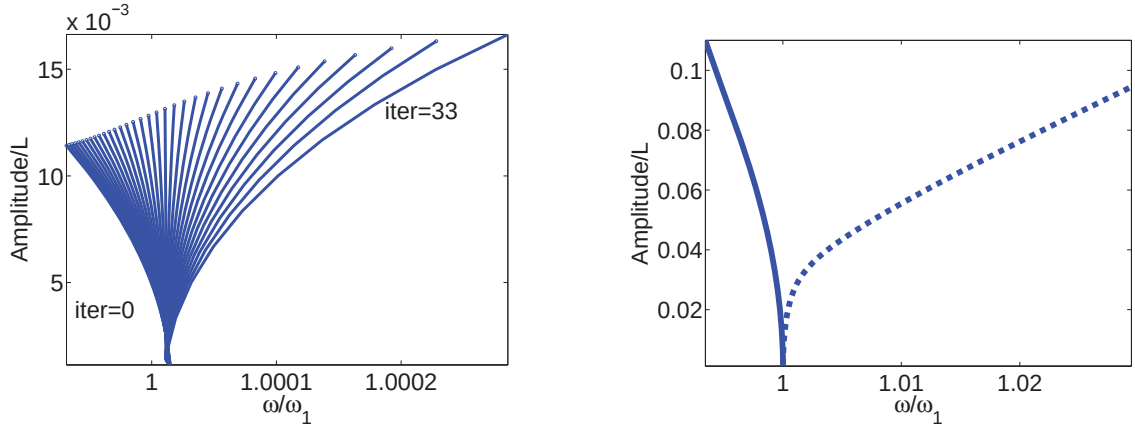

Figure 3.7 Evolution of backbone during iterations (left) and comparison of initial backbone and optimized backbone at larger load (right). Solid line: initial design; dashed line: optimized design. Figure taken from [P4].

first flexural mode is less than 0.04% for the initial design. The objective function is to maximize the relative frequency shift caused by hardening resonance around the first flexural mode, see Eq. (3.13). In the optimized design, the solid structure (black area) is not allowed to fill more than half of the total area of the design domain. The optimized design with a volume constraint is shown in Fig. 3.8. Since it displays weak hinges, an additional constraint on minimal eigenvalue is imposed in order to ensure sufficient structural rigidity. The second optimized design is showed in Fig. 3.8. For both optimized designs, the relative frequency shifts are more than 34%.

A physical interpretation of the optimized structures is that the midplane

stretching plays a key role when four beams are connected to one central mass and two boundaries through eight hinge-like connections. In the designs point-hinges appear as well as gray elements that correspond to intermediate material properties. Further work is currently being undertaken to improve the designs by employing a finer mesh, projection filtering and minimal length control techniques. However, in reality the gray elements may be realized using a weaker material such as polymer. For example, polymeric hinges have been used in the design of micro-mirrors to achieve large deflection at small external forces.

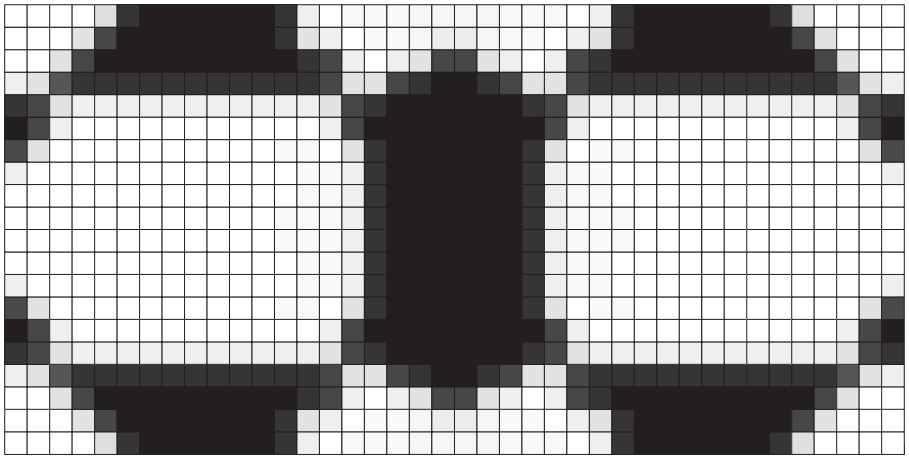

Figure 3.8 Optimized design with constraint on maximal volume. Figure taken from [P5].

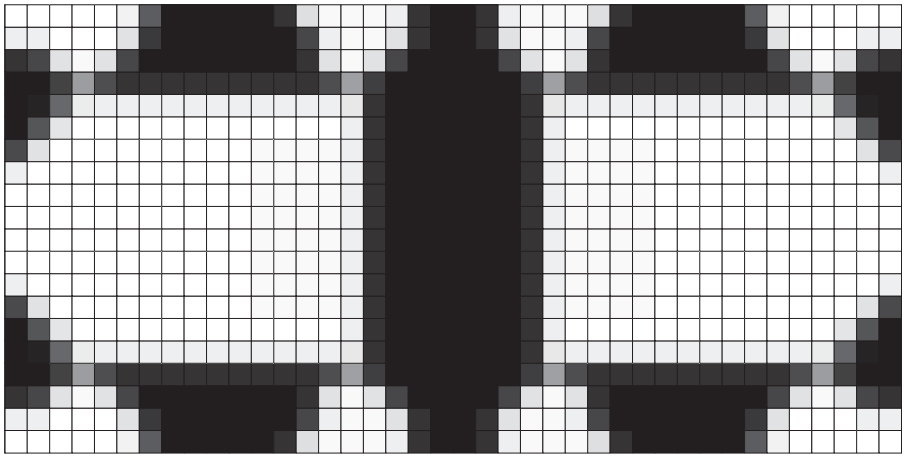

Figure 3.9 Optimized design with constraint on maximal volume and a constraint on minimal eigenvalue. Figure taken from [P5].

Chapter 4
Optimization of superharmonic resonances

In nonlinear dynamics, superharmonic resonances may occur when the excitation frequency ω has a particular relation with the linear eigenfrequency ω_p, i.e. $\omega \approx \gamma\omega_p$, where γ is a constant value. For example, $\gamma = \frac{1}{3}$ corresponds to superharmonic resonance of order-3, where the third-order harmonic in the response can be excited into resonance state. This section presents a method for gradient-based optimization of superharmonic resonances. In the optimization, the value of γ is constant and thereby ω varies with ω_p over optimization iterations. By tracking and tuning the frequency response at this condition, the corresponding superharmonic resonance is effectively optimized.

4.1 Formulation of optimization problem

A general formulation for optimizing the amplitude of the superharmonic resonance can be written as

$$\begin{aligned} \min_{\rho_e} \;& c(\overline{\mathbf{q}}(\rho_e), \omega(\rho_e)) \\ \text{s.t. :} \;& \omega^2 \overline{\mathbf{M}}\, \overline{\mathbf{q}} + \omega\, \overline{\mathbf{C}}\, \overline{\mathbf{q}} + \overline{\mathbf{g}} = \overline{\mathbf{f}}, \\ & \omega = \gamma\, \omega_p \text{ (frequency condition)} \end{aligned} \tag{4.1}$$

where ω is angular frequency of the excitation frequency, ω_p is the eigenfrequency of the pth linear normal mode, and $\omega = \gamma\omega_p$ denotes the frequency condition for a specific superharmonic resonance. In the thesis, two cases including $\gamma = \frac{1}{3}$ and $\gamma = \frac{1}{2}$ are studied, which correspond to superharmonic resonances of order-3 and order-2, respectively.

In the design sensitivity analysis, the adjoint method is used. In the derivation, the objective function can be rewritten in conjunction with the governing equation of the equilibrium state and the frequency condition as

$$c = c(\overline{\mathbf{q}}, \omega) + \boldsymbol{\lambda}_1 \left(\omega^2 \overline{\mathbf{M}}\overline{\mathbf{q}} + \omega \overline{\mathbf{C}}\overline{\mathbf{q}} + \overline{\mathbf{g}} - \overline{\mathbf{f}} \right) + \lambda_2 \left(\omega - \gamma\omega_p \right) \tag{4.2}$$

By differentiating the objective function with respect to the design variables, it

yields

$$\begin{aligned}\frac{\mathrm{d}c}{\mathrm{d}\rho_e} = &\left[\frac{\partial c}{\partial \overline{\mathbf{q}}^T} + \boldsymbol{\lambda}_1^T\left(\omega^2\,\overline{\mathbf{M}} + \omega\,\overline{\mathbf{C}} + \overline{\mathbf{K}}_T\right)\right]\frac{\mathrm{d}\overline{\mathbf{q}}}{\mathrm{d}\rho_e} + \\ &\left[\frac{\partial c}{\partial \omega} + \boldsymbol{\lambda}_1^T\left(2\,\omega\,\overline{\mathbf{M}}\,\overline{\mathbf{q}} + \overline{\mathbf{C}}\,\overline{\mathbf{q}}\right) + \lambda_2\right]\frac{\mathrm{d}\omega}{\mathrm{d}\rho_e} - \gamma\,\lambda_2\,\frac{\mathrm{d}\omega_p}{\mathrm{d}\rho_e} + \\ &\boldsymbol{\lambda}_1^T\left(\omega^2\,\frac{\partial \overline{\mathbf{M}}}{\partial \rho_e}\,\overline{\mathbf{q}} + \omega\,\frac{\partial \overline{\mathbf{C}}}{\partial \rho_e}\,\overline{\mathbf{q}} + \frac{\partial \overline{\mathbf{g}}}{\partial \rho_e}\right)\end{aligned} \tag{4.3}$$

Since the direct computation of $\mathrm{d}\overline{\mathbf{q}}/\mathrm{d}\rho_e$ and $\mathrm{d}\omega/\mathrm{d}\rho_e$ is computationally expensive, it can be avoided by selecting the values of the adjoint variables such that the expressions in the two brackets in front of them become zeros. This leads to the adjoint equation as

$$\begin{aligned}&\frac{\partial c}{\partial \overline{\mathbf{q}}^T} + \boldsymbol{\lambda}_1^T\left(\omega^2\overline{\mathbf{M}} + \omega\overline{\mathbf{C}} + \overline{\mathbf{K}}_T\right) \qquad = 0 \\ &\frac{\partial c}{\partial \omega} \;+ \boldsymbol{\lambda}_1^T\left(2\,\omega\,\overline{\mathbf{M}}\,\overline{\mathbf{q}} + \overline{\mathbf{C}}\,\overline{\mathbf{q}}\right) \qquad + \lambda_2 = 0\end{aligned} \tag{4.4}$$

and the sensitivity of c with respect to ρ_e can be calculated through

$$\frac{\mathrm{d}c}{\mathrm{d}\rho_e} = \boldsymbol{\lambda}_1^T\left(\omega^2\,\frac{\partial \overline{\mathbf{M}}}{\partial \rho_e}\,\overline{\mathbf{q}} + \omega\,\frac{\partial \overline{\mathbf{C}}}{\partial \rho_e}\,\overline{\mathbf{q}} + \frac{\partial \overline{\mathbf{g}}}{\partial \rho_e}\right) - \gamma\lambda_2\frac{\mathrm{d}\omega_p}{\mathrm{d}\rho_e} \tag{4.5}$$

where $\mathrm{d}\omega_p/\mathrm{d}\rho_e$ is expressed in terms of $\mathrm{d}\omega_p^2/\mathrm{d}\rho_e$ as

$$\frac{\mathrm{d}\omega_p}{\mathrm{d}\rho_e} = \frac{1}{2\omega_p}\frac{\mathrm{d}\omega_p^2}{\mathrm{d}\rho_e} \tag{4.6}$$

For the convenience in numerical implementation, the adjoint equation is rewritten with one bordered matrix as

$$\begin{bmatrix}\left(\omega^2\,\overline{\mathbf{M}} + \omega\,\overline{\mathbf{C}} + \overline{\mathbf{K}}_T\right)^T & \mathbf{0} \\ \left(2\,\omega\,\overline{\mathbf{M}}\,\overline{\mathbf{q}} + \overline{\mathbf{C}}\,\overline{\mathbf{q}}\right)^T & 1\end{bmatrix}\begin{bmatrix}\boldsymbol{\lambda}_1 \\ \lambda_2\end{bmatrix} = -\begin{bmatrix}\dfrac{\partial c}{\partial \overline{\mathbf{q}}} \\ \dfrac{\partial c}{\partial \omega}\end{bmatrix} \tag{4.7}$$

In Eq. (4.6), the sensitivity of the eigenvalue of linear system is required. For simple eigenvalues, it is well known that

$$\frac{\mathrm{d}\omega_p^2}{\mathrm{d}\rho_e} = \boldsymbol{\Phi}_p^T\left(\frac{\partial \mathbf{K}_L}{\partial \rho_e} - \omega_p^2\frac{\partial \mathbf{M}}{\partial \rho_e}\right)\boldsymbol{\Phi}_p \tag{4.8}$$

where $\mathbf{K}_L$ is the matrix of linear stiffness, $\boldsymbol{\Phi}_p$ is the eigenvector normalized with respect to mass matrix, i.e. $\boldsymbol{\Phi}_p^T\mathbf{M}\boldsymbol{\Phi}_p = 1$. It is noted that an original derivation was formulated in [P1], where a slightly different formulation was used.

4.2 Optimization examples

4.2.1 Optimization of superharmonic resonance of order-3 [P1]

A frequency-amplitude curve of the clamped-clamped beam sketched in Fig. 3.1 is shown in Fig. 4.1. A higher excitation level than that used for primary resonance is applied to induce the superharmonic resonance. For linear vibration, there is only one fundamental harmonic whereas in the non-linear case there are multiple harmonics. It is seen in Fig. 4.1 that the amplitude of the third harmonic is resonantly excited around $\frac{\omega}{\omega_1} \approx \frac{1}{3}$ and we refer to this as a superharmonic resonance of order-3.

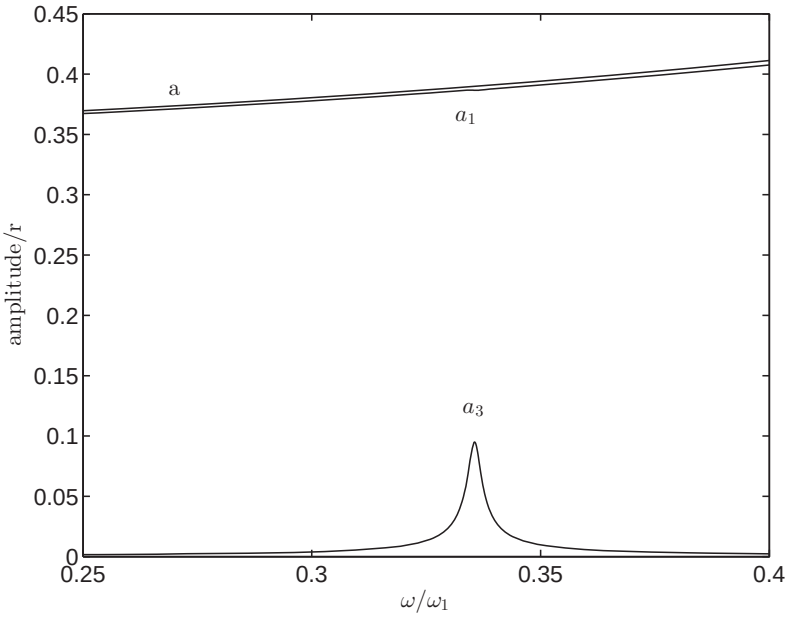

Figure 4.1 Superharmonic resonance of a clamped-clamped beam at $\frac{\omega}{\omega_1} \approx \frac{1}{3}$. "a" denotes the amplitude of the fundamental harmonic in linear vibration; "a_1" and "a_3" denote the amplitudes of first-order and third-order harmonics in nonlinear dynamic response. Figure taken from [P1].

In order to tailor the amplitude of the superharmonic resonance, the optimization problem is formulated as

$$\begin{aligned} \min_{\rho_e}/\max \;\; & c = a_{i3}^2 + b_{i3}^2 \\ \text{s.t.} : \;\; & \omega^2 \overline{\mathbf{M}}\,\overline{\mathbf{q}} + \omega\,\overline{\mathbf{C}}\,\overline{\mathbf{q}} + \overline{\mathbf{g}} = \overline{\mathbf{f}} \\ & \frac{\omega}{\omega_1} = \frac{1}{3} \text{ (frequency condition)} \end{aligned} \tag{4.9}$$

where a_{i3} and b_{i3} are the coefficients of the third harmonic terms $\cos 3\tau$ and $\sin 3\tau$, respectively, the subscript i denotes the reference degree of freedom correspond-

ing to the deflection at midspan of the beam, and ω_1 is the eigenfrequency of the first flexural mode. The optimization is also subjected to the volume constraints using either a minimum or a maximum volume fraction. The design variables, volume fraction and the minimum and maximum width are the same as the optimization of primary resonance.

In the case of an external load given by 607.4 N, the optimized structures for minimizing/maximizing the superharmonic resonance are shown in Fig. 4.2 and 4.3, respectively. The frequency-amplitude curves for the uniform-width design and the optimized designs are compared in Fig. 4.4. It can be seen that the superharmonic resonance is either reduced or increased significantly with the optimized width distribution even though the total volume is unchanged. The effect of modifying the design can also clearly be seen by viewing the structural response in the time domain. Fig. 4.5 shows the periodic response in the time domain for the peak of the frequency-amplitude curve in Fig. 4.4. The design with uniform width distribution produces a slightly distorted signal with higher-order harmonics whereas the optimized designs can either suppress or enhance the higher-order harmonics, respectively.

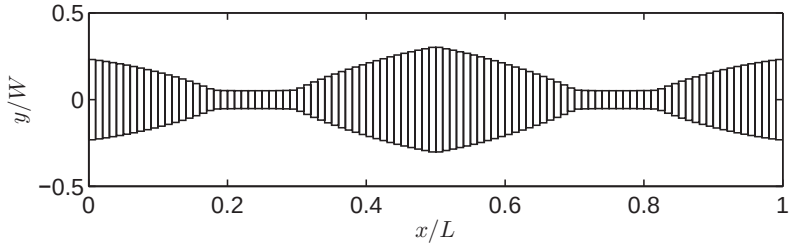

Figure 4.2 A clamped-clamped beam with optimized width for minimizing superharmonic resonance around $\omega_1/3$. Figure taken from [P1].

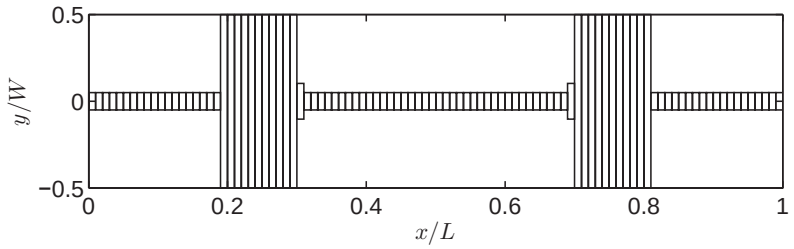

Figure 4.3 A clamped-clamped beam with optimized width for maximizing superharmonic resonance around $\omega_1/3$. Figure taken from [P1].

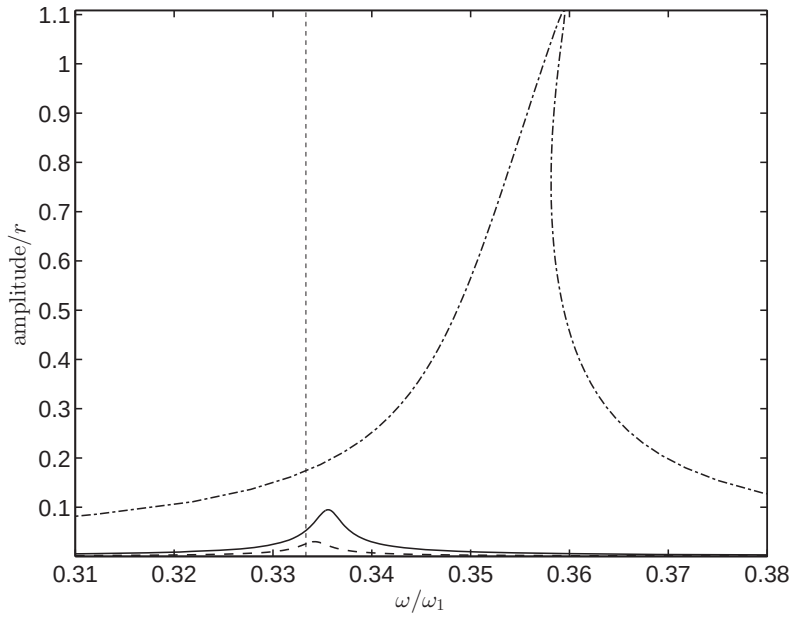

Figure 4.4 Frequency-amplitude curves of superharmonic resonance at $\frac{\omega}{\omega_1} \approx \frac{1}{3}$: solid line: uniform; dashed line: minimized superharmonic resonance; dot dashed line: maximized superharmonic resonance; dotted line: $\frac{\omega}{\omega_1} = \frac{1}{3}$. Figure taken from [P1].

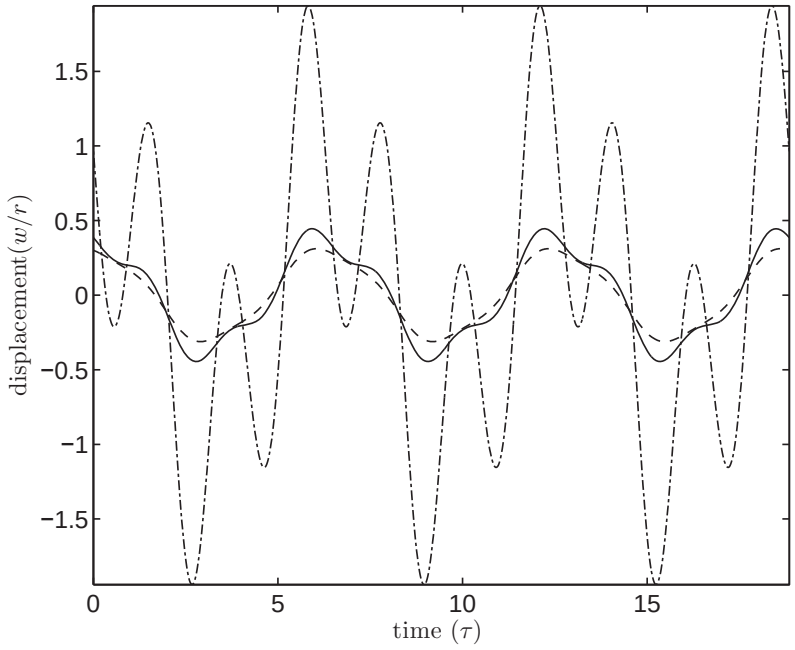

Figure 4.5 The responses for the peak of superharmonic resonance at $\frac{\omega}{\omega_1} \approx \frac{1}{3}$: solid line: uniform; dashed line: minimized superharmonic resonance; dot dashed line: maximized superharmonic resonance. Figure taken from [P1].

4.2.2 Optimization of superharmonic resonance of order-2

In the second example, superharmonic resonance of order-2 is studied. For a specific example, consider the three-beam ⊓-shaped frame structure which has been studied for tuning the hardening/softening behavior in Section 3.3.2. Due to its asymmetric configuration, it possesses significant quadratic nonlinearity. It displays superharmonic resonance of order-2 associated with the second linear normal mode (Fig. 4.9). For convenience, we also refer to its eiegenfrequency as ω_1. The optimization problem is formulated as

$$\begin{aligned} \min_{\rho_e}/\max \;\; & c = a_{i2}^2 + b_{i2}^2 \\ \text{s.t. :} \;\; & \omega^2 \overline{\mathbf{M}}\,\overline{\mathbf{q}} + \omega\,\overline{\mathbf{C}}\,\overline{\mathbf{q}} + \overline{\mathbf{g}} = \overline{\mathbf{f}} \\ & \frac{\omega}{\omega_1} = \frac{1}{2} \text{ (frequency condition)} \end{aligned} \tag{4.10}$$

where a_{i2} and b_{i2} are the coefficients of the second harmonic terms $\cos 2\tau$ and $\sin 2\tau$, respectively, and the subscript i denotes the reference degree of freedom corresponding to the deflection at the mid-span of the horizontal beam. The optimization is also subjected to the volume constraints using either a minimum or a maximum volume fraction. The design variables and the minimum and maximum width are the same as the optimization of primary resonance. The volume fraction is set to 0.5 such that the optimize design has the same volume as that of the initial design.

The optimized designs for minimizing/maximizing the superharmonic resonance are shown in 4.7. Comparisons of periodic responses in time domain and linear modes normalized with respect to mass matrix are displayed in Figs. (4.8) and (4.9). The optimized design with maximized superharmonic resonance presents larger vibration amplitude, and the optimized design with minimized superharmonic resonance presents smaller vibration amplitude.

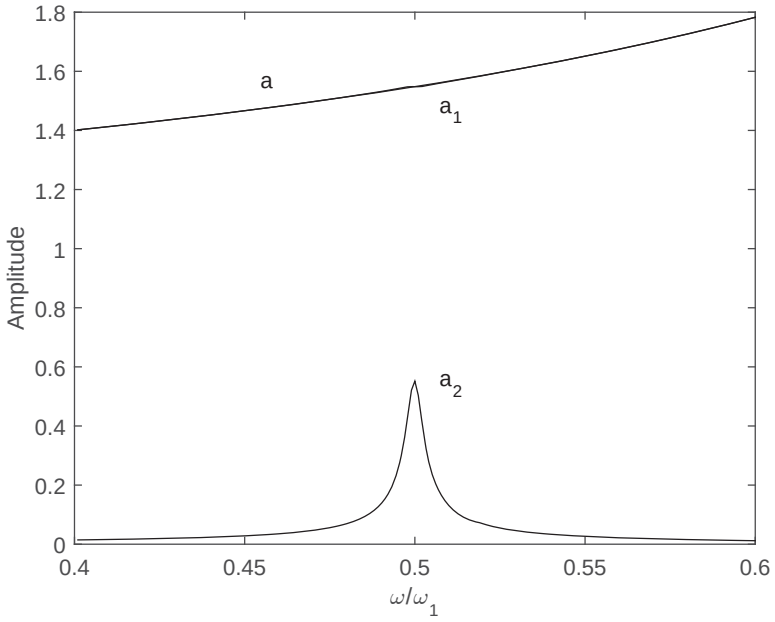

Figure 4.6 Superharmonic resonance of a one-floor frame at $\frac{\omega}{\omega_1} \approx \frac{1}{2}$. "a" denotes the amplitude of the fundamental harmonic in linear vibration; "a_1" and "a_2" denote the amplitudes of first-order and second-order harmonics in nonlinear dynamic response.

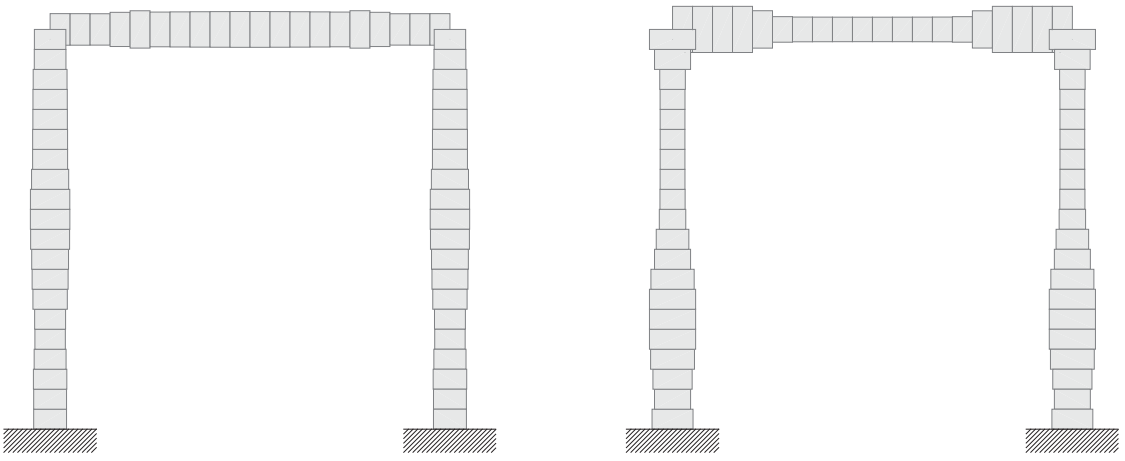

Figure 4.7 Optimized design for minimizing superharmonic resonance (left) and maximizing superharmonic resonance (right).

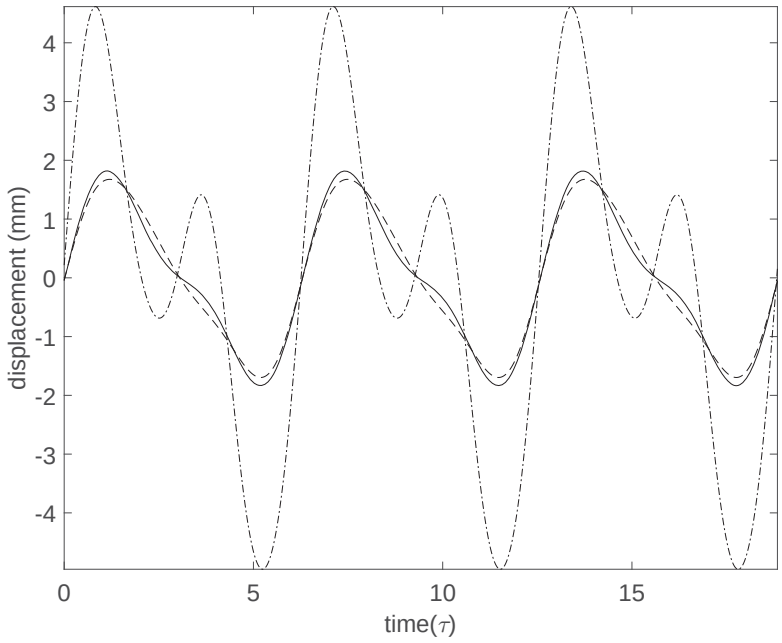

Figure 4.8 A comparison of periodic responses in time domain for uniform design (solid line) and optimized designs for minimizing superharmonic resonance (dashed line) and maximizing superharmonic resonance (dot-dashed line).

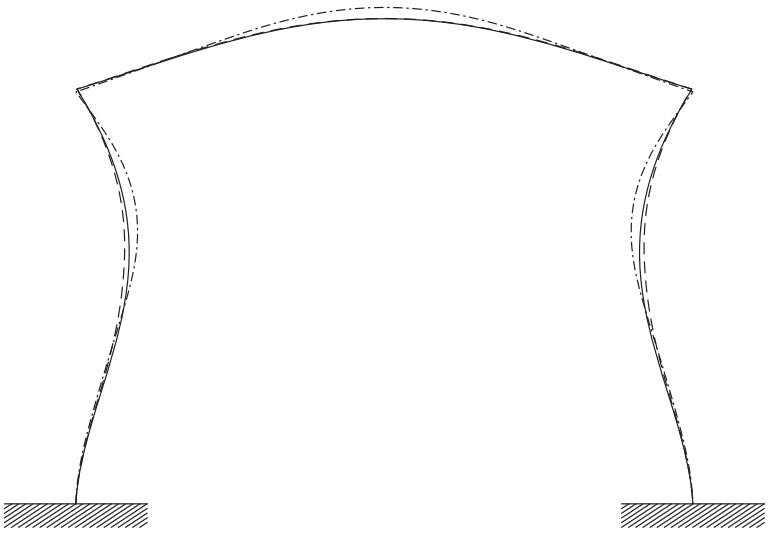

Figure 4.9 A comparison of linear vibration modes normalized with respect to mass matrix for uniform design (solid line) and optimized designs for minimizing superharmonic resonance (dashed line) and maximizing superharmonic resonance (dot-dashed line).

Chapter 5
Optimization of nonlinear normal modes (NNMs)

As a nonlinear analogy of linear normal modes (LNMs), nonlinear normal modes (NNMs) provide a systematic way to study the conservative dynamics of mechanical structures. Based on nonlinear normal modes, this chapter presents an optimization method for tuning the frequency-energy dependence, specifically, the hardening/softening behavior. The optimization problem is formulated in conjunction with a proper normalization of nonlinear normal modes. In the case studies of plane frame structures, the hardening/softening behavior is qualitatively changed by simple manipulation of the structural geometry.

5.1 One example in nonlinear modal analysis

To start with, the concept of nonlinear normal modes is discussed by considering a generic model used in previous study for demonstrating the fundamental properties of nonlinear normal modes (Kerschen et al., 2009). This model is a two-degrees-of-freedom discrete system written as

$$\begin{aligned} \ddot{x}_1 + 2x_1 - x_2 + 0.5x_1^3 &= 0 \\ \ddot{x}_2 + 2x_2 - x_1 &= 0 \end{aligned} \tag{5.1}$$

To compute the nonlinear normal modes, the proposed analysis method in Chapter 2 is applied, and the resulting frequency-energy plot calculated is displayed in Fig. 5.1, where the energy is calculated by using the average kinetic energy over the fundamental period as

$$E_{\text{kin}} = \frac{1}{T}\int_0^T \frac{1}{2}(\dot{\mathbf{q}})^T \mathbf{M}\dot{\mathbf{q}}\,\mathrm{d}t = -\frac{\omega^2}{2}\overline{\mathbf{q}}^T\overline{\mathbf{M}}\overline{\mathbf{q}} \tag{5.2}$$

It is noted that the negative sign in the kinetic energy is because of the definition of $\overline{\mathbf{M}}$. In the analysis, several initial steps can be obtained by incrementally increasing one reference amplitude, e.g., a_{i1}, and then a combination of cubic polynomial predictor and arc-length method is used for robust continuation. As aforementioned in continuation approaches, an alternative to amplitude increment is so-called energy increment, where the kinetic energy E_{kin} is increased in incremental steps, and Eq. (2.16) is solved in conjunction with the incremental form of Eq. (5.2) as

$$-\left(\omega^2\,\overline{\mathbf{q}}^T\,\overline{\mathbf{M}}\right)\Delta\overline{\mathbf{q}} - \left(\omega\,\overline{\mathbf{q}}^T\,\overline{\mathbf{M}}\,\overline{\mathbf{q}}\right)\Delta\omega = E_{\text{kin}} + \frac{\omega^2}{2}\overline{\mathbf{q}}^T\overline{\mathbf{M}}\overline{\mathbf{q}} \tag{5.3}$$

As seen in Fig. 5.1, these nonlinear normal modes can be viewed as continuation of linear normal modes into higher energy level. As the energy level increases, the frequency-energy dependence reveals the hardening behavior. As the energy level continues to increase, the so-called "tongue" occurs, which indicates 1:3 internal resonance. These results agree very well with previous results by using different methods, e.g., shooting method (Kerschen et al., 2009), and complex harmonic balance method (Krack et al., 2013). It is noted that this seemingly simple system has other internal resonances, and additional tongues can be numerically computed. For a comprehensive discussion about the nonlinear normal modes in this system, the reader can refer to (Kerschen et al., 2009).

Hardening/softening behavior

In the following part of this chapter, we restrict our attention to the optimization of nonlinear normal modes with hardening/softening behavior that occurs at a moderately large amplitude. To qualitatively and quantitatively measure the hardening/softening behavior, a quantity related to the relative frequency shift, also known as detuning parameter in nonlinear dynamics, is defined as

$$\gamma = \frac{\omega_{\mathrm{NL}} - \omega_{\mathrm{L}}}{\omega_{\mathrm{L}}} \tag{5.4}$$

where ω_{L} is the linear eigenfrequency of one linear normal mode, and ω_{NL} is the frequency of corresponding nonlinear normal mode at a given reference amplitude. This objective function is inspired by the frequency-amplitude relation derived based on normal form theory, see, e.g., Touzé et al. (2004), written as

$$\omega_{\mathrm{NL}} = \omega_{\mathrm{L}}(1 + \Gamma A^2) \tag{5.5}$$

where Γ is called the effective nonlinear coefficient, A is the amplitude of the single nonlinear normal mode. A comparison of the two equations shows that

$$\gamma = \Gamma A^2 \tag{5.6}$$

Since we use a constant amplitude in the optimization, γ provides a good approximation of the effective nonlinear coefficient. In the following of this section, the optimization problem is formulated and its sensitivity analysis is derived by using the adjoint method.

5.2 Formulation of optimization problem

For general applicability, the objective function is assumed as a function of the frequency and the Fourier coefficients of one nonlinear normal mode so that it is a nonlinear analogy of the optimization of eigenfrequency and eigenvector of one

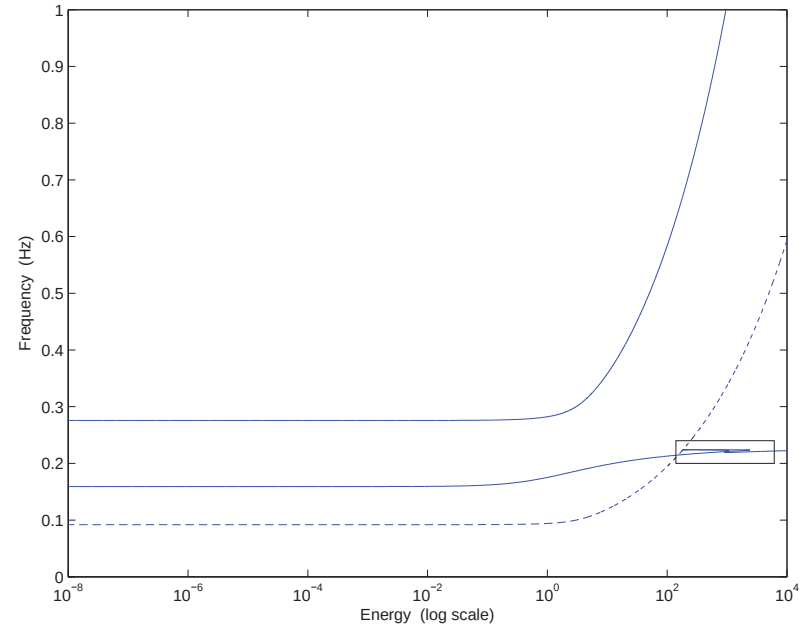

(a)

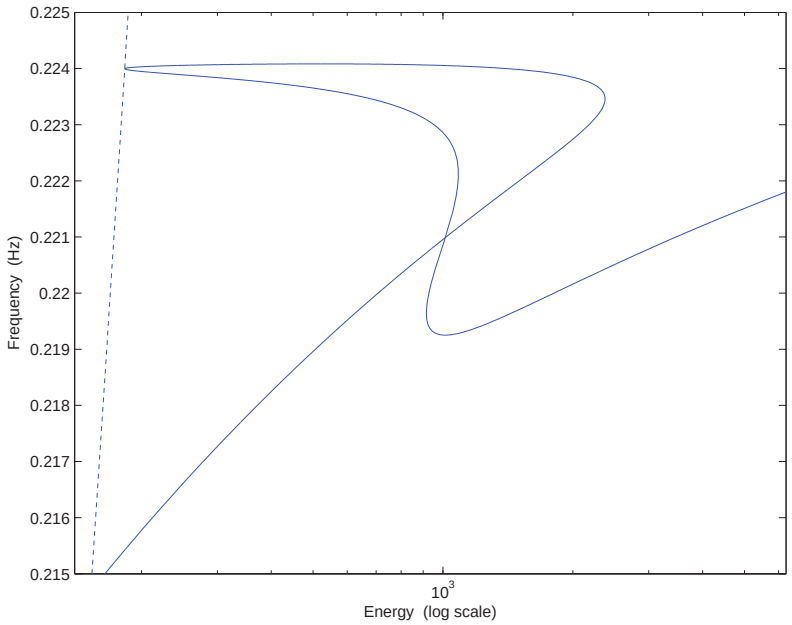

(b)

Figure 5.1 The frequency-energy plot for the nonlinear normal modes of a two-degrees-of-freedom nonlinear systems (a) and zoom of a tongue (b). Solid lines: first nonlinear normal mode (bottom curve) and second nonlinear normal mode (top curve); dashed line: second nonlinear normal mode with its frequency divided by three. Figure taken from [P3].

linear normal mode. Further, the linear eigenfrequency is also included in the objective function because it is used to quantify the hardening/softening behavior in Eq. (5.4). The optimization problem is formulated as

$$\begin{aligned} &\min_{\rho_e} \; c(\omega_p(\rho_e), \omega(\rho_e), \overline{\mathbf{q}}(\rho_e)) \\ \text{s.t. :} \; &\omega_p^2 \mathbf{M}\boldsymbol{\Phi}_p - \mathbf{K}_\mathrm{L}\boldsymbol{\Phi}_p = \mathbf{0}, \quad \boldsymbol{\Phi}_p^T \mathbf{M}\boldsymbol{\Phi}_p = 1, \\ &\omega^2 \overline{\mathbf{M}}\,\overline{\mathbf{q}} + \overline{\mathbf{g}} = \mathbf{0}, \quad \chi(\overline{\mathbf{q}}, \omega) = 0 \end{aligned} \tag{5.7}$$

where $\mathbf{K}_\mathrm{L}$ is the linear stiffness matrix, ω_p and $\boldsymbol{\Phi}_p$ denote eigenfrequency and eigenvector of pth linear normal mode, ω and $\overline{\mathbf{q}}$ denote frequency and amplitudes of the corresponding nonlinear normal mode, and $\rho_e \in [0,\, 1]$ is normalized design variable used in the optimization with $e = 1, \ldots, N_e$ and N_e denoting the number of elements.

Normalization of nonlinear normal mode

It should be noted that the optimization problem is performed based on both linear and nonlinear modal analyses. The linear normal mode is normalized with respect to mass matrix and $\chi(\overline{\mathbf{q}}, \omega) = 0$ represents a normalization of one nonlinear normal mode in the sense that it has a specific energy level or a specific reference amplitude. Mathematically, $\chi(\overline{\mathbf{q}}, \omega) = 0$ constructs a hyper-surface in terms of $(\overline{\mathbf{q}}, \omega)$ so that the nonlinear normal mode can only evolve in this hyper surface during optimization. Further, it is noted that the gradient of the nonlinear normal mode is always normal to this hyper surface, i.e.

$$\frac{\partial \chi(\overline{\mathbf{q}}, \omega)}{\partial \overline{\mathbf{q}}^T} \Delta\overline{\mathbf{q}} + \frac{\partial \chi(\overline{\mathbf{q}}, \omega)}{\partial \omega} \Delta\omega = 0 \tag{5.8}$$

In practice, $\chi(\overline{\mathbf{q}}, \omega)$ can be defined with respect to a specific energy level or a specific amplitude. For a simple amplitude-based normalization, it is written as

$$a_{i1} - a_{i1}^* = 0, \quad \Delta a_{i1} = 0 \tag{5.9}$$

where i is the degree of freedom related to the reference amplitude that characterizes the full motion of the nonlinear normal mode. For some problems (e.g., topology optimization), this characteristic degree of freedom is difficult to be selected in advance. So an energy-based normalization is preferable.

$$-\frac{1}{2}\omega^2 \overline{\mathbf{q}}^T \overline{\mathbf{M}}\,\overline{\mathbf{q}} - E_\mathrm{kin}^* = 0, \quad \left(\omega^2\, \overline{\mathbf{q}}^T\, \overline{\mathbf{M}}\right) \Delta\overline{\mathbf{q}} + \left(\omega\, \overline{\mathbf{q}}^T\, \overline{\mathbf{M}}\,\overline{\mathbf{q}}\right) \Delta\omega = 0. \tag{5.10}$$

Adjoint sensitivity analysis

Below, the sensitivity analysis is derived by using the adjoint method specialized for the optimization of nonlinear normal modes. First, the objective function is augmented with adjoint variables, $\boldsymbol{\lambda}_1$ and λ_2, as

$$c = c(\omega_p, \omega, \overline{\mathbf{q}}) + \boldsymbol{\lambda}_1^T \left(\omega^2 \overline{\mathbf{M}}\, \overline{\mathbf{q}} + \overline{\mathbf{g}}\right) + \lambda_2\, \chi(\overline{\mathbf{q}}, \omega) \tag{5.11}$$

Next, differentiating the two sides of Eq. (5.11) with respect to design variable ρ_e leads to

$$\begin{aligned} \frac{\mathrm{d}c}{\mathrm{d}\rho_e} = &\left[\frac{\partial c}{\partial \overline{\mathbf{q}}^T} + \boldsymbol{\lambda}_1^T \left(\omega^2 \overline{\mathbf{M}} + \overline{\mathbf{K}}_T\right) + \lambda_2 \frac{\partial \chi(\overline{\mathbf{q}}, \omega)}{\partial \overline{\mathbf{q}}^T}\right] \frac{\mathrm{d}\overline{\mathbf{q}}}{\mathrm{d}\rho_e} + \\ &\left[\frac{\partial c}{\partial \omega} + \boldsymbol{\lambda}_1^T \left(2\omega \overline{\mathbf{M}} \overline{\mathbf{q}}\right) + \lambda_2 \frac{\partial \chi(\overline{\mathbf{q}}, \omega)}{\partial \omega}\right] \frac{\mathrm{d}\omega}{\mathrm{d}\rho_e} + \frac{\partial c}{\partial \omega_p} \frac{\mathrm{d}\omega_p}{\mathrm{d}\rho_e} + \\ &\boldsymbol{\lambda}_1^T \left(\omega^2 \frac{\partial \overline{\mathbf{M}}}{\partial \rho_e} \overline{\mathbf{q}} + \frac{\partial \overline{\mathbf{g}}}{\partial \rho_e}\right) \end{aligned} \tag{5.12}$$

Then, the adjoint variables $\boldsymbol{\lambda}_1$ and λ_2 are selected such that the coefficients in the brackets in front of $\frac{\mathrm{d}\overline{\mathbf{q}}}{\mathrm{d}\rho_e}$ and $\frac{\mathrm{d}\omega}{\mathrm{d}\rho_e}$ vanish, which leads to the adjoint equation

$$\begin{aligned} &\frac{\partial c}{\partial \overline{\mathbf{q}}^T} + \boldsymbol{\lambda}_1^T \left(\omega^2 \overline{\mathbf{M}} + \overline{\mathbf{K}}_T\right) + \lambda_2 \frac{\partial \chi(\overline{\mathbf{q}}, \omega)}{\partial \overline{\mathbf{q}}^T} = \mathbf{0} \\ &\frac{\partial c}{\partial \omega} + \boldsymbol{\lambda}_1^T \left(2\omega \overline{\mathbf{M}} \overline{\mathbf{q}}\right) \qquad + \lambda_2 \frac{\partial \chi(\overline{\mathbf{q}}, \omega)}{\partial \omega} = 0 \end{aligned} \tag{5.13}$$

For the convenience in numerical implementation, the adjoint equation is rewritten in matrix form as

$$\begin{bmatrix} \left(\omega^2 \overline{\mathbf{M}} + \overline{\mathbf{K}}_T\right) & \dfrac{\partial \chi(\overline{\mathbf{q}}, \omega)}{\partial \overline{\mathbf{q}}} \\ \left(2\omega \overline{\mathbf{q}}^T \overline{\mathbf{M}}\right) & \dfrac{\partial \chi(\overline{\mathbf{q}}, \omega)}{\partial \omega} \end{bmatrix} \begin{bmatrix} \boldsymbol{\lambda}_1 \\ \lambda_2 \end{bmatrix} = \begin{bmatrix} \dfrac{\partial c}{\partial \overline{\mathbf{q}}} \\ \dfrac{\partial c}{\partial \omega} \end{bmatrix} \tag{5.14}$$

Finally, the sensitivity of c with respect to design variable ρ_e can be computed using the adjoint variable $\boldsymbol{\lambda}_1$ as

$$\frac{\mathrm{d}c}{\mathrm{d}\rho_e} = \boldsymbol{\lambda}_1^T \left(\omega^2 \frac{\partial \overline{\mathbf{M}}}{\partial \rho_e} \overline{\mathbf{q}} + \frac{\partial \overline{\mathbf{g}}}{\partial \rho_e}\right) + \frac{\partial c}{\partial \omega_p} \frac{\mathrm{d}\omega_p}{\mathrm{d}\rho_e} \tag{5.15}$$

It is noted that the adjoint variable λ_2 does not appear in Eq. (5.15), and the sensitivities of the eigenfrequency ω_p are required. Only single modal eigenvalues are encountered and considered here. By using the sensitivity of a single eigenvalue, we have

$$\frac{\mathrm{d}\omega_p}{\mathrm{d}\rho_e} = \frac{1}{2\omega_p} \boldsymbol{\Phi}_p^T \left[\frac{\partial \mathbf{K}_L}{\partial \rho_e} - \omega_p^2 \frac{\partial \mathbf{M}}{\partial \rho_e}\right] \boldsymbol{\Phi}_p \tag{5.16}$$

where the eigenvector is assumed to be normalized with respect to the mass matrix, i.e. $\mathbf{\Phi}_p^T \mathbf{M} \mathbf{\Phi}_p = 1$.

For the objective function defined in Eq. (5.4), its sensitivity analysis can be derived by substituting its differentiations, i.e.

$$\frac{\partial c}{\partial \omega} = \frac{1}{\omega_p}, \quad \frac{\partial c}{\partial \omega_p} = -\frac{\omega}{\omega_p^2}, \quad \frac{\partial c}{\partial \overline{\mathbf{q}}} = \mathbf{0} \tag{5.17}$$

into Eq. (5.14) and solving the adjoint variable $\boldsymbol{\lambda}_1$. Once the adjoint vector $\boldsymbol{\lambda}_1$ is solved, the sensitivities with respect to all design variables can be calculated by using Eq. (5.15). In the optimization, each iteration consists of several steps: computation of nonlinear normal mode, solving the adjoint equation in Eq. (5.14), calculation of sensitivity using Eq. (5.15) and update of design variables using the method of moving asymptotes (MMA) (Svanberg, 1987).

5.3 Optimization examples

In this section, two examples are provided to demonstrate the effectiveness of the proposed procedure. The first example is a one-floor ⊓-shaped frame (Chen et al., 2001), and the second example is an H-shaped frame. In each example, the initial configuration consists of three identical beams with uniform rectangular cross section. In the optimization procedure, the distribution of in-plane thickness is varied to tailor the hardening/softening behavior of a symmetric vibration mode. In finite element discretization, the beam element based on geometrically exact theory is used.

5.3.1 From softening behavior to hardening behavior [P3]

The one-floor frame and one of its linear normal modes are shown in Fig. 5.2. In the initial design, the geometry of each beam is defined by out-of-plane width $b = 30$ mm, in-plane thickness $h = 30$ mm, beam length $L = 180$ mm. The in-plane thickness is allowed to vary between 20 mm and 40 mm. The material properties are fixed with mass density 7800 kg/m^3, Young's modulus $E = 205$ GPa, Poisson's ratio $\nu = 0.3$ and shear modulus $G = E/(2(1+\nu))$. The initial configuration shows a softening behavior. The optimization problem is formulated such that the softening behavior is minimized and thereby the hardening behavior maximized, i.e.

$$\max_{\rho_e} \ \gamma = \frac{\omega_{\mathrm{NL}} - \omega_{\mathrm{L}}}{\omega_{\mathrm{L}}} \tag{5.18}$$

which also are subjected to the additional constraints in Eq. (5.7). Evolution of the frequency-amplitude dependence and the corresponding frequency-energy dependence are shown in Fig. 5.3 and Fig. 5.4. While the initial design is displayed

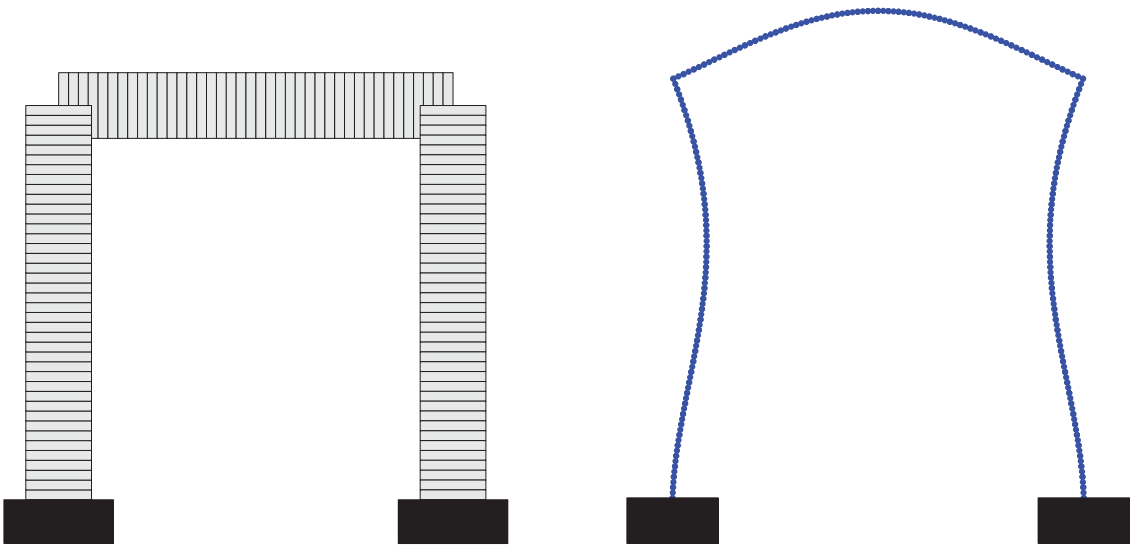

Figure 5.2 One-floor frame structure (left) and one linear normal mode (right). The solid black patches indicate boundary conditions of the structure. Figure taken from [P3].

in Fig. 5.2, one intermediate design and final design are given in Fig. 5.5. It is noted that the hardening/softening behavior of the structure is qualitatively and quantitatively changed smoothly during the optimization iterations. Further, it is noticed that both the frequency of LNM and the frequency of NNM at a given amplitude are decreased continuously. A larger drop in the frequency of LNM than in the frequency of NNM is achieved to yield the hardening behavior. It is observed that the softening behavior is first tuned into mixed hardening/softening behavior, and then tuned into hardening behavior as the optimization iterations proceed. Finally, it is noted that for the NNM at the given amplitude, the system energy stays almost constant when the optimized design has a softening behavior, and increases slightly as the hardening behavior sets in and increases in strength.

In some applications, it will be natural to introduce a constraint on the eigenfrequency of linear normal mode. To demonstrate the effect of this, we introduce a minimum allowable value of the eigenfrequency of linear normal mode and the optimization problem is consequently rewritten as

$$\begin{aligned} &\max_{\rho_e} \ \gamma = \frac{\omega_{\mathrm{NL}} - \omega_{\mathrm{L}}}{\omega_{\mathrm{L}}} \\ &\text{s.t.} : \ \omega_{\mathrm{L}} \geq \omega_{\mathrm{L}}^{*} \end{aligned} \tag{5.19}$$

which is also subjected to the additional constraints in Eq. (5.7). Evolution of the frequency-amplitude dependence and the corresponding frequency-energy dependence are now given in Fig. 5.6 and Fig. 5.7. While the initial design is displayed in Fig. 5.2, one intermediate design and final design are given in Fig.

5.8. For this example we see that the nonlinear behavior is also tuned from softening behavior to hardening behavior. It is found that the frequency of NNM is increased smoothly and significantly, whereas the frequency of LNM changes only slightly and presents a small fluctuation. Further, the energy for the NNMs at the given reference amplitude is slightly reduced for optimized design. The evolution of the energy for these NNMs is similar to the optimization without a constraint on the eigenfrequency of linear normal mode, where the energy is first reduced when softening behavior evolves to mixed softening/hardening behavior, and then increased when mixed softening/hardening behavior evolves to hardening behavior.

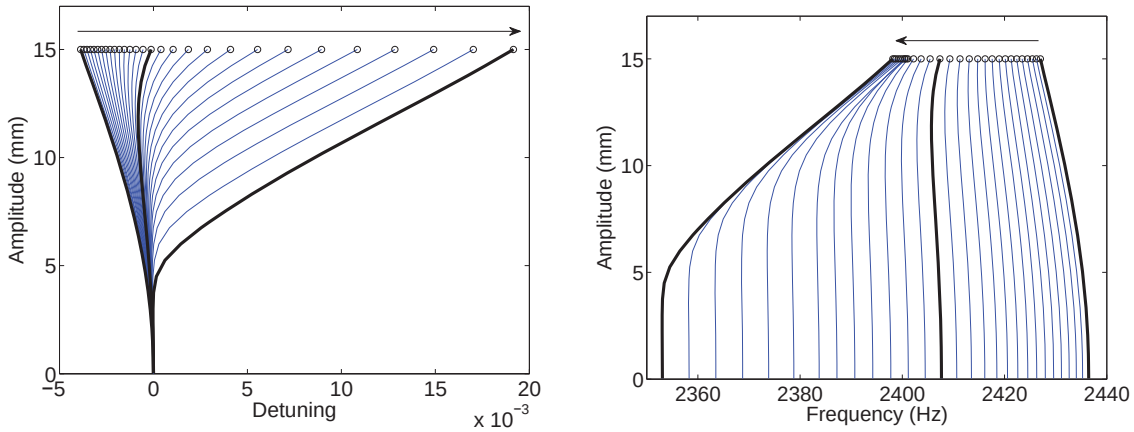

Figure 5.3 Evolution of the detuning-amplitude relation (left) and the frequency-amplitude dependence (right). Thick curves correspond to initial design, optimized design at 15th iteration, and final design. Figure taken from [P3].

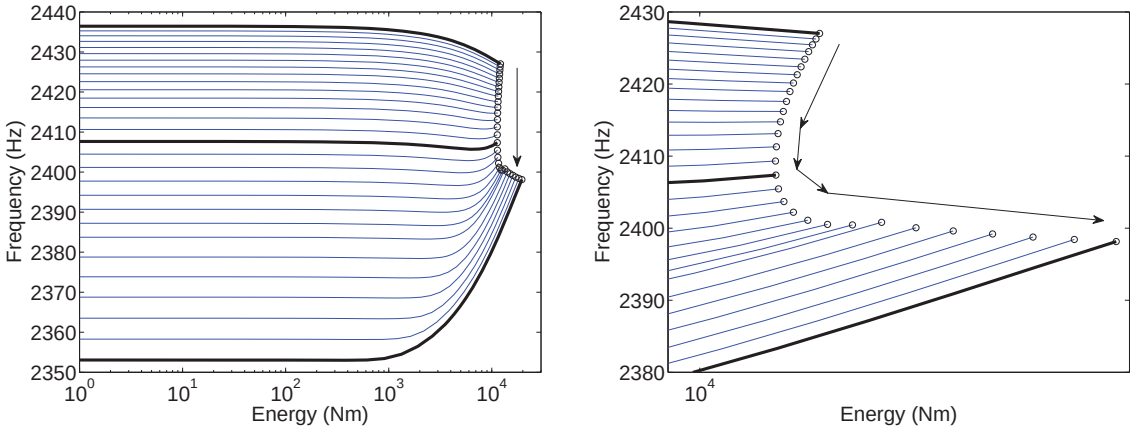

Figure 5.4 Evolution of the frequency-energy relation (left) and the details for NNMs at a given reference amplitude (right).Thick curves correspond to initial design, optimized design at 15th iteration, and final design. Figure taken from [P3].

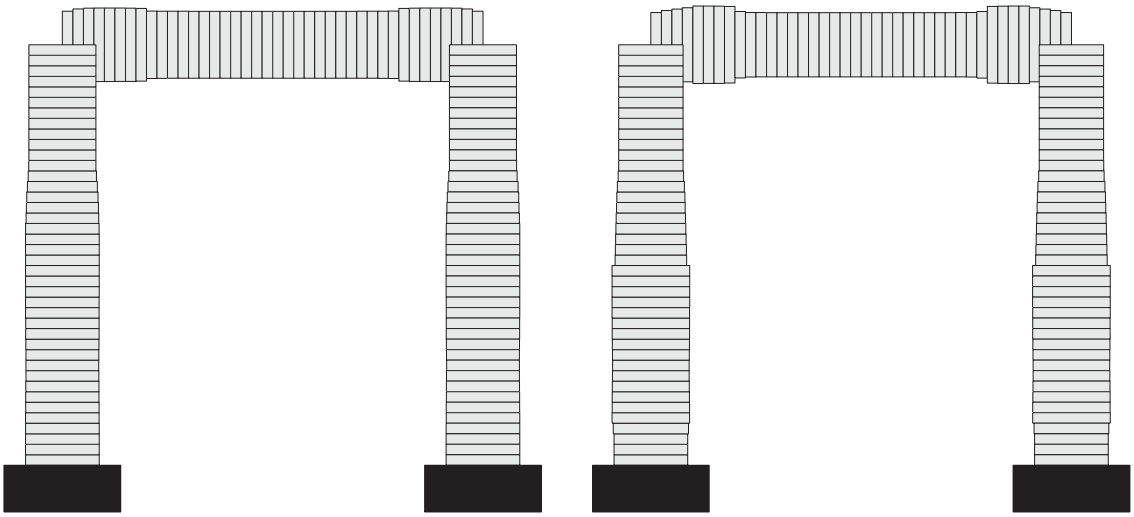

Figure 5.5 Evolution of optimized designs over iterations. (left): 15th iteration; (right): final design. Figure taken from [P3].

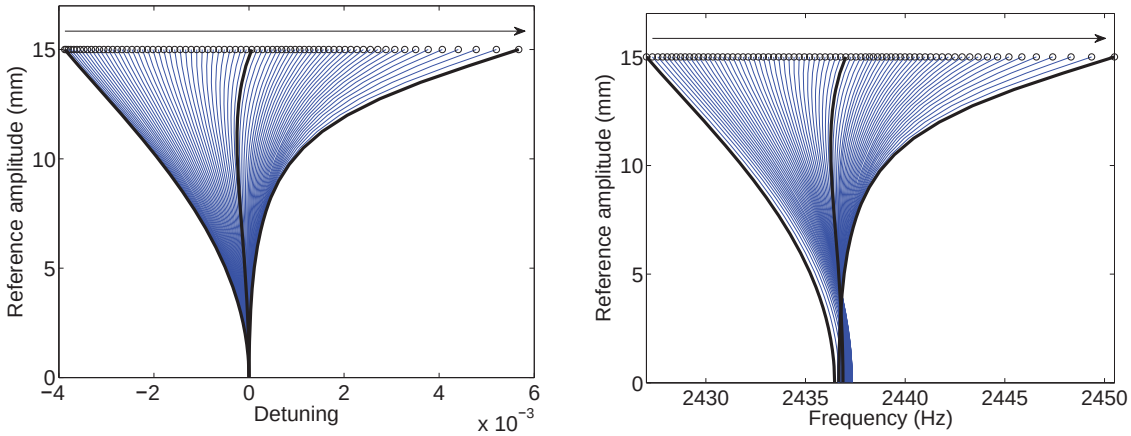

Figure 5.6 Evolution of the detuning-amplitude relation (left) and the frequency-amplitude dependence (right). Thick curves correspond to initial design, optimized design at 40th iteration, and final design. Figure taken from [P3].

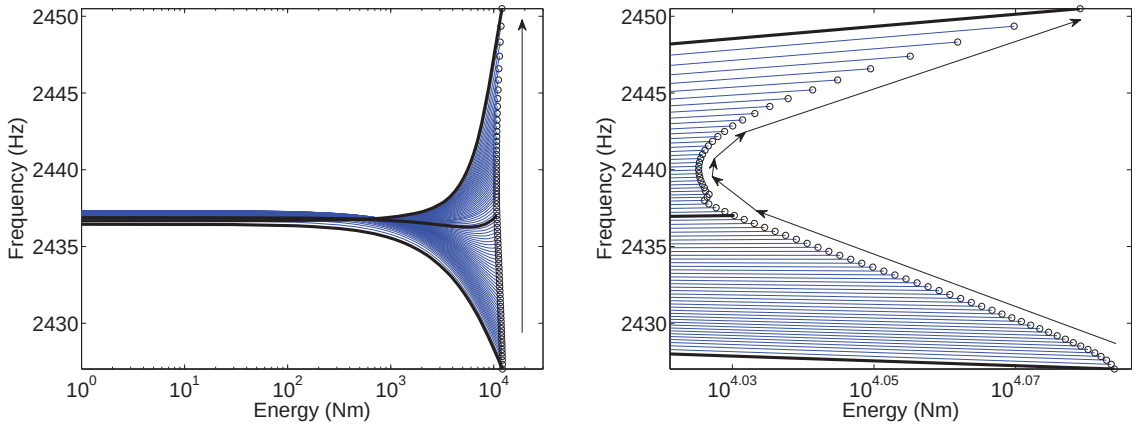

Figure 5.7 Evolution of the frequency-energy relation (left) and the details for NNMs at a given reference amplitude (right). Figure taken from [P3].

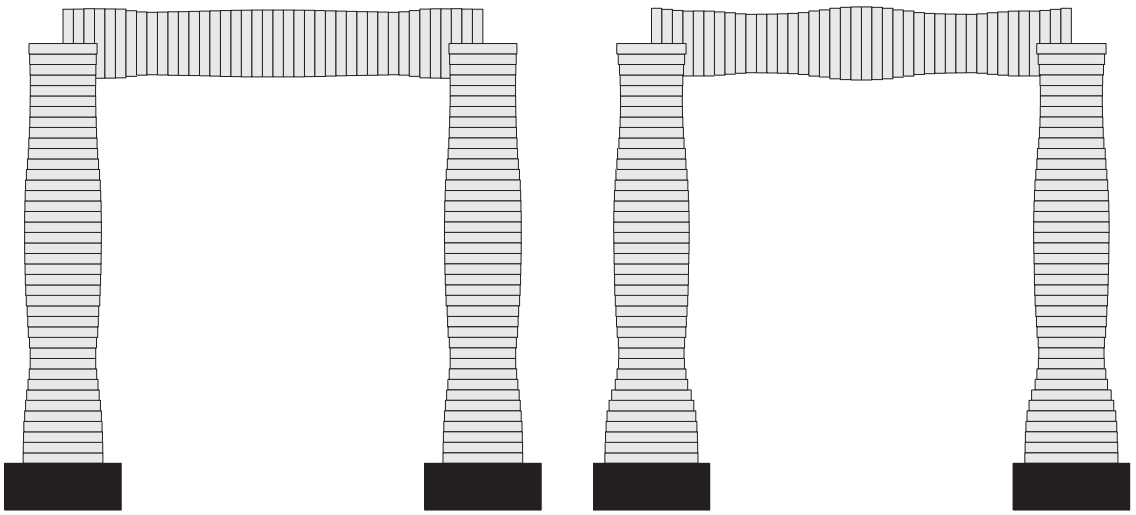

Figure 5.8 Evolution of optimized designs over iterations. (left): 40th iteration; (right): final design. Figure taken from [P3].

5.3.2 From hardening behavior to softening behavior [P3]

In order to demonstrate the conversion from a hardening to a softening nonlinear behavior we choose a slightly different initial configuration that displays a hardening behavior in its original configuration. The H-shaped frame and one of its

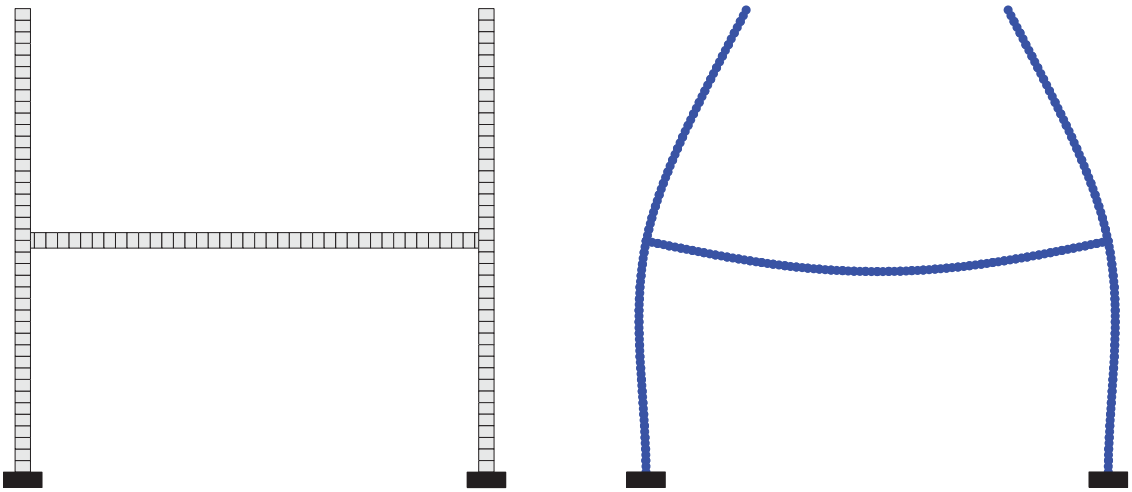

Figure 5.9 One-floor frame structure (left) and one linear normal mode (right). The solid black patches indicate boundary conditions of the structure. Figure taken from [P3].

linear normal modes are shown in Fig. 5.9. In the initial design, the geometry of each beam is defined by out-of-plane width $b = 30$ mm, in-plane thickness $h = 20$ mm, beam length $L = 600$ mm. In the optimization, the maximum in-plane thickness is 40 mm. The material properties are the same as that of the one-floor frame structure. The optimization problem is rewritten as

$$\begin{aligned} &\min_{\rho_e} \ \gamma = \frac{\omega_{\mathrm{NL}} - \omega_{\mathrm{L}}}{\omega_{\mathrm{L}}} \\ &\text{s.t.}: \ \omega_{\mathrm{L}} \leq \omega_{\mathrm{L}}^{*} \end{aligned} \tag{5.20}$$

which also are subjected to the additional constraints in Eq. (5.7). The reference amplitude is defined as the amplitude of the transverse vibration at midspan of the horizontal beam. Evolution of the frequency-amplitude dependence and the corresponding frequency-energy dependence are shown in Fig. 5.10 and Fig. 5.11. The intermediate design corresponding to a straight line in frequency-amplitude plot and the final design with softening behavior are displayed in Fig 5.12. A clear change in the linear normal mode is also observed when comparing the initial design and the final design. The associated linear normal modes are displayed in Fig. 5.13. In the optimized design, the vibration in the two free half-beams is reduced, and the vibration in the horizontal beam is amplified.

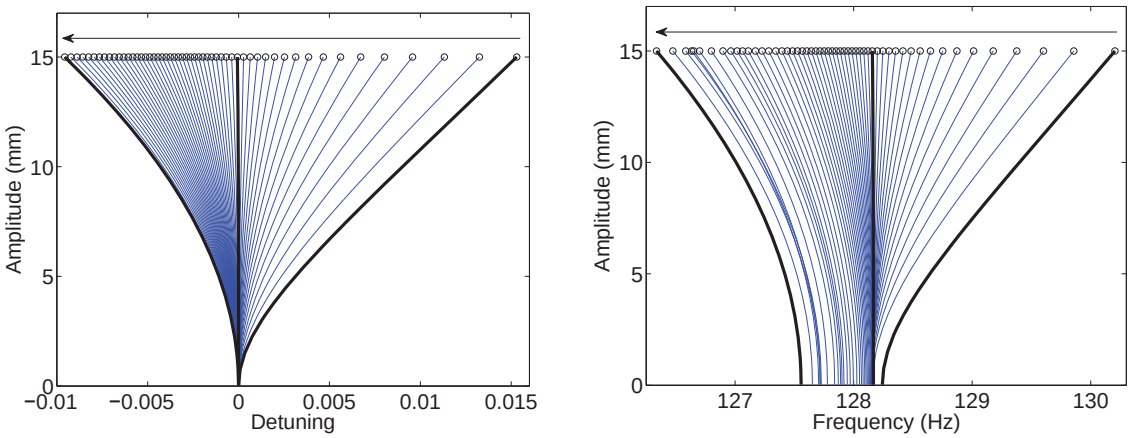

Figure 5.10 Evolution of the detuning-amplitude relation (left) and the frequency-amplitude dependence (right). Thick curves correspond to initial design, optimized design at 14th iteration, and final design. Figure taken from [P3].

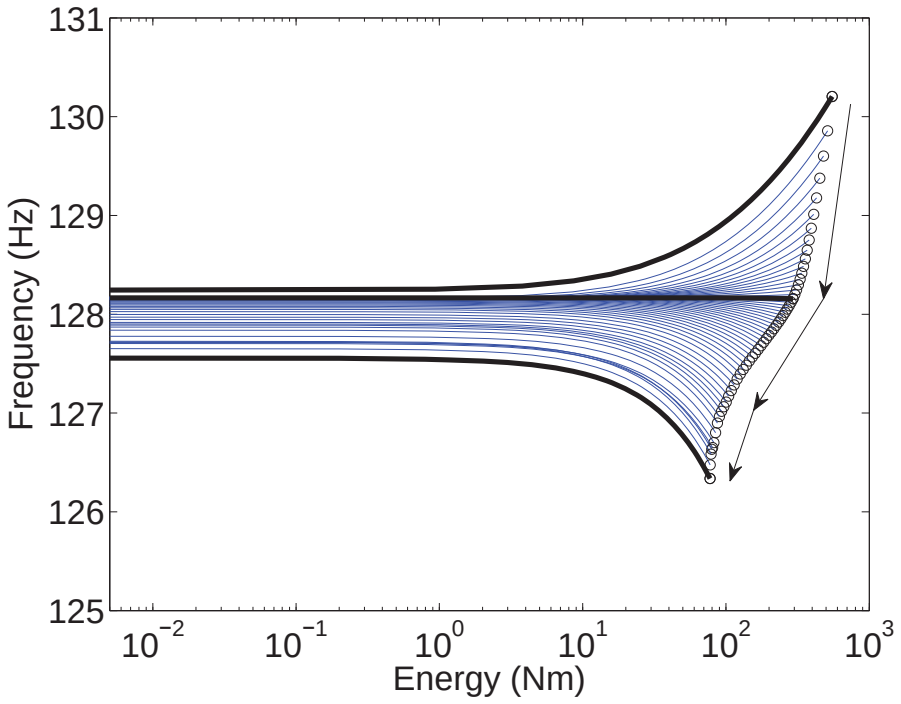

Figure 5.11 Evolution of the frequency-energy relation. The circles represent the NNMs at a given reference amplitude. The thick curves correspond to initial design: optimized design at 14th iteration, and final design. Figure taken from [P3].

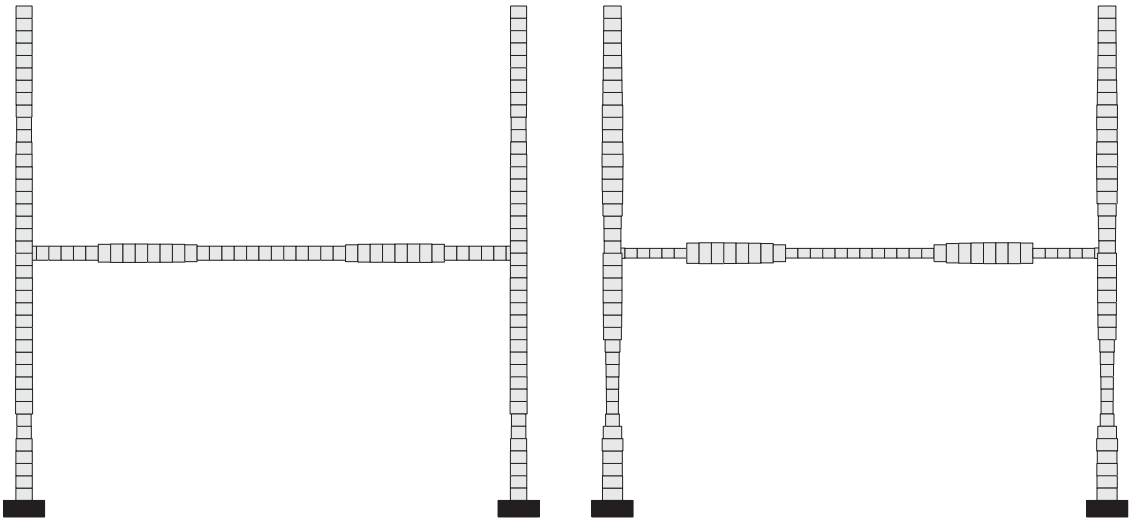

Figure 5.12 Evolution of optimized designs over iterations. (left): 14th iteration; (right): final design. Figure taken from [P3].

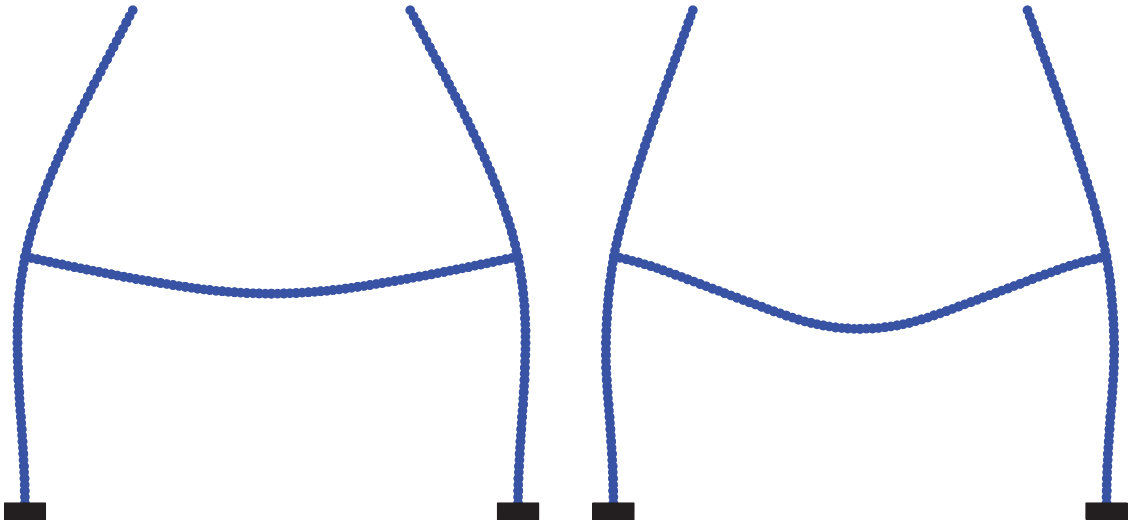

Figure 5.13 Evolution of linear normal mode of optimized design over iterations. (left): 14th iteration; (right): final design.

Chapter 6
Optimization of normal form coefficents

Based on the characterization theory in Chapter 2, a gradient-based optimization is presented in this chapter for optimizing nonlinear modal coupling coefficients and normal form coefficients for a given resonance condition. The optimization problems are formulated for the hardening/softening behavior of a single-mode resonator, and the essential modal coupling effects in a coupled-mode resonator, respectively. Design examples including a clamped-clamped beam with hardening behavior and a T-shaped frequency divider with 2:1 internal resonance are used to demonstrate the proposed optimization procedure.

6.1 Formulation of optimization problem

For general applicability, we consider an objective function that may be an explicit function of the nonlinear coefficients, as well as the eigenvectors and associated eigenfrequencies, and formulate our optimization problem as the following minimization problem:

$$\begin{aligned} \min_{\rho_e} \quad & c(\omega_p, \mathbf{\Phi}_p, \alpha^{(3)}_{ijk}(\mathbf{\Phi}_p), \alpha^{(4)}_{ijkl}(\mathbf{\Phi}_p)) \\ \text{s.t.}: \quad & (\omega_p^2 \mathbf{M} - \mathbf{K}_L)\mathbf{\Phi}_p = 0, \quad p = 1, \ldots, N_m \end{aligned} \tag{6.1}$$

where the subscripts $i,\ j,\ k,\ l = 1, \ldots, N_m$ with N_m denoting the number of linear modes, $\alpha^{(3)}_{ijk}(\mathbf{\Phi}_p)$ and $\alpha^{(4)}_{ijkl}(\mathbf{\Phi}_p)$ are cubic and quartic coefficients in the Hamiltonian $\mathcal{H}$ of the system corresponding to the quadratic and cubic nonlinearity in reduced order model projected on linear modes, ρ_e with $e = 1, \ldots, N_e$ are normalized design variables, and N_e is the number of elements. It can also be subject to additional constraints as discussed later in optimization examples.

The sensitivity analysis is derived by using the adjoint method. To derive the adjoint equation, the objective function is first rewritten with adjoint variables $\boldsymbol{\lambda}_p$ and η_p as

$$c = c(\omega_p, \mathbf{\Phi}_p, \alpha^{(3)}_{ijk}(\mathbf{\Phi}_p), \alpha^{(4)}_{ijkl}(\mathbf{\Phi}_p)) + \sum_{p=1}^{N_m} \left[\boldsymbol{\lambda}_p^T (\omega_p^2 \mathbf{M}\mathbf{\Phi}_p - \mathbf{K}_L \mathbf{\Phi}_p) + \eta_p (\mathbf{\Phi}_p^T \mathbf{M} \mathbf{\Phi}_p - 1) \right] \tag{6.2}$$

where it is noted that the terms in the two sets of parentheses that appear in the appended term both vanish identically. Differentiation of the objective function

with respect to design variable ρ_e is then expressed as

$$\begin{aligned}\frac{\mathrm{d}c}{\mathrm{d}\rho_e} &= \frac{\partial c}{\partial \rho_e} + \sum_{p=1}^{N_m}\left[\frac{\partial c}{\partial \mathbf{\Phi}_p^T}\frac{\mathrm{d}\mathbf{\Phi}_p}{\mathrm{d}\rho_e} + \frac{\partial c}{\partial \omega_p}\frac{\mathrm{d}\omega_p}{\mathrm{d}\rho_e}\right] + \sum_{i=1}^{N_m}\sum_{j=1}^{N_m}\sum_{k=1}^{N_m}\frac{\partial c}{\partial \alpha_{ijk}^{(3)}}\left(\frac{\partial \alpha_{ijk}^{(3)}}{\partial \rho_e} + \sum_{p=1}^{N_m}\frac{\partial \alpha_{ijk}^{(3)}}{\partial \mathbf{\Phi}_p^T}\frac{\mathrm{d}\mathbf{\Phi}_p}{\mathrm{d}\rho_e}\right) \\ &+ \sum_{i=1}^{N_m}\sum_{j=1}^{N_m}\sum_{k=1}^{N_m}\sum_{l=1}^{N_m}\frac{\partial c}{\partial \alpha_{ijkl}^{(4)}}\left(\frac{\partial \alpha_{ijkl}^{(4)}}{\partial \rho_e} + \sum_{p=1}^{N_m}\frac{\partial \alpha_{ijkl}^{(4)}}{\partial \mathbf{\Phi}_p^T}\frac{\mathrm{d}\mathbf{\Phi}_p}{\mathrm{d}\rho_e}\right) + \sum_{p=1}^{N_m}\eta_p\left(2\mathbf{\Phi}_p^T\mathbf{M}\frac{\mathrm{d}\mathbf{\Phi}_p}{\mathrm{d}\rho_e} + \mathbf{\Phi}_p^T\frac{\partial \mathbf{M}}{\partial \rho_e}\mathbf{\Phi}_p\right) \\ &+ \sum_{p=1}^{N_m}\boldsymbol{\lambda}_p^T\left[\left(\omega_p^2\mathbf{M} - \mathbf{K}_L\right)\frac{\mathrm{d}\mathbf{\Phi}_p}{\mathrm{d}\rho_e} + 2\omega_p\mathbf{M}\mathbf{\Phi}_p\frac{\mathrm{d}\omega_p}{\mathrm{d}\rho_e} + \left(\omega_p^2\frac{\partial \mathbf{M}}{\partial \rho_e} - \frac{\partial \mathbf{K}_L}{\partial \rho_e}\right)\mathbf{\Phi}_p\right]\end{aligned} \tag{6.3}$$

Since the direct computation of the sensitivities of eigenvalues and eigenvectors (i.e. $\frac{\mathrm{d}\mathbf{\Phi}_p}{\mathrm{d}\rho_e}$ and $\frac{\mathrm{d}\omega_p}{\mathrm{d}\rho_e}$) is computationally expensive, the adjoint variables are selected such that the coefficients of $\frac{\mathrm{d}\mathbf{\Phi}_p}{\mathrm{d}\rho_e}$ and $\frac{\mathrm{d}\omega_p}{\mathrm{d}\rho_e}$ vanish. This leads to the adjoint equation in terms of $\boldsymbol{\lambda}_p$ and η_p as

$$\begin{aligned}\frac{\mathrm{d}c}{\mathrm{d}\mathbf{\Phi}_p} + \left(\omega_p^2\mathbf{M} - \mathbf{K}_L\right)\boldsymbol{\lambda}_p + \left(2\mathbf{M}\mathbf{\Phi}_p\right)\eta_p &= \mathbf{0} \\ \frac{\partial c}{\partial \omega_p} + \left(2\omega_p\mathbf{\Phi}_p^T\mathbf{M}\right)\boldsymbol{\lambda}_p &= 0\end{aligned} \tag{6.4}$$

where we use the symmetry of $\mathbf{M}$ and $\mathbf{K}_L$, and

$$\frac{\mathrm{d}c}{\mathrm{d}\mathbf{\Phi}_p} = \frac{\partial c}{\partial \mathbf{\Phi}_p} + \sum_{i=1}^{N_m}\sum_{j=1}^{N_m}\sum_{k=1}^{N_m}\frac{\partial c}{\partial \alpha_{ijk}^{(3)}}\frac{\partial \alpha_{ijk}^{(3)}}{\partial \mathbf{\Phi}_p} + \sum_{i=1}^{N_m}\sum_{j=1}^{N_m}\sum_{k=1}^{N_m}\sum_{l=1}^{N_m}\frac{\partial c}{\partial \alpha_{ijkl}^{(4)}}\frac{\partial \alpha_{ijkl}^{(4)}}{\partial \mathbf{\Phi}_p} \tag{6.5}$$

In this case, the sensitivity of the objective function writes

$$\begin{aligned}\frac{\mathrm{d}c}{\mathrm{d}\rho_e} = \frac{\partial c}{\partial \rho_e} &+ \sum_{i=1}^{N_m}\sum_{j=1}^{N_m}\sum_{k=1}^{N_m}\frac{\partial c}{\partial \alpha_{ijk}^{(3)}}\frac{\partial \alpha_{ijk}^{(3)}}{\partial \rho_e} + \sum_{i=1}^{N_m}\sum_{j=1}^{N_m}\sum_{k=1}^{N_m}\sum_{l=1}^{N_m}\frac{\partial c}{\partial \alpha_{ijkl}^{(4)}}\frac{\partial \alpha_{ijkl}^{(4)}}{\partial \rho_e} \\ &+ \sum_{p=1}^{N_m}\left[\boldsymbol{\lambda}_p^T\left(\omega_p^2\frac{\partial \mathbf{M}}{\partial \rho_e} - \frac{\partial \mathbf{K}_L}{\partial \rho_e}\right)\mathbf{\Phi}_p + \eta_p\left(\mathbf{\Phi}_p^T\frac{\partial \mathbf{M}}{\partial \rho_e}\mathbf{\Phi}_p\right)\right]\end{aligned} \tag{6.6}$$

For convenience of computational implementation, the adjoint equations are expressed in matrix form as

$$\begin{bmatrix}\left(\omega_p^2\mathbf{M} - \mathbf{K}_L\right) & \left(2\mathbf{M}\mathbf{\Phi}_p\right) \\ \left(2\omega_p\mathbf{\Phi}_p^T\mathbf{M}\right) & 0\end{bmatrix}\begin{bmatrix}\boldsymbol{\lambda}_p \\ \eta_p\end{bmatrix} = -\begin{bmatrix}\frac{\mathrm{d}c}{\mathrm{d}\mathbf{\Phi}_p} \\ \frac{\partial c}{\partial \omega_p}\end{bmatrix} \tag{6.7}$$

It is noted that in the adjoint equation, $\mathrm{d}c/\mathrm{d}\boldsymbol{\Phi}_p$ is calculated using the Eq. (6.5), and in numerical implementation the quantities $\partial\alpha^{(3)}_{ijk}/\partial\boldsymbol{\Phi}_p$ and $\partial\alpha^{(4)}_{ijkl}/\partial\boldsymbol{\Phi}_p$ in Eq. (6.5) are assembled from the corresponding element-wise quantities $\partial\alpha_{ijk}/\partial\boldsymbol{\Phi}^e_p$ and $\partial\beta_{ijkl}/\partial\boldsymbol{\Phi}^e_p$.

6.1.1 Optimization of a single-mode resonator

In Chapters 3 and 5, hardening/softening behavior is measured by using nonlinear resonance peak and nonlinear normal modes, respectively. The analyses in these studies are based on harmonic balance method, which can handle complex nonlinearity, including polynomial-type nonlinearity and trigonometric nonlinearity. Below, a third method to optimize hardening/softening behavior is proposed based on nonlinear modal coupling coefficients and normal form theory. The new optimization method is especially suitable for mechanical systems with polynomial-type nonlinearity. For general applicability in both symmetric structures (e.g., clamped-clamped beams) and asymmetric structures (e.g., arches or shells), the following derivation includes both quadratic and cubic nonlinear terms.

For a single-mode resonator, its reduced order model based on a single linear mode is written as

$$\ddot{q}_p + \omega_p^2 q_p + g^p_{pp} q_p^2 + h^p_{ppp} q_p^3 = 0 \tag{6.8}$$

with $g^p_{pp} = 3\alpha^{(3)}_{ppp}$ and $h^p_{ppp} = 4\alpha^{(4)}_{pppp}$. The frequency-amplitude relation is derived as

$$\omega_{\mathrm{NL}} = \omega_p(1 + \Gamma\, a^2) \tag{6.9}$$

where a is the amplitude of the corresponding linear mode, and the effective coefficient Γ is

$$\Gamma = \frac{3}{8}\frac{h^p_{ppp}}{\omega_p^2} - \frac{5}{12}\frac{(g^p_{pp})^2}{\omega_p^4} \tag{6.10}$$

A more accurate model for the hardening/softening behavior of general structures can be created with the dynamics projected onto a single nonlinear normal mode and the corresponding equation is then written as

$$\ddot{R}_p + \omega_p^2 R_p + (A^p_{ppp} + h^p_{ppp}) R_p^3 + B^p_{ppp} R_p \dot{R}_p^2 = 0 \tag{6.11}$$

with the new coefficients A^p_{ppp} and B^p_{ppp} given as explicit functions of nonlinear modal coupling coefficients g^l_{ij} and h^l_{ijk}, see Touzé et al. (2004). Based on Eq. (6.11), the frequency-amplitude relation is derived as

$$\omega_{\mathrm{NL}} = \omega_p(1 + \Gamma^* A^2) \tag{6.12}$$

where A is the amplitude of the corresponding nonlinear normal mode in curved, normal coordinates, and the effective coefficient Γ^* is

$$\Gamma^* = \frac{3\,(A^p_{ppp} + h^p_{ppp}) + \omega_p^2\, B^p_{ppp}}{8\,\omega_p^2} \tag{6.13}$$

Note that in this case Γ^* is not only linked to the p^{th} linear mode explicitly through ω_p and h^p_{ppp} and implicitly through g^p_{pp} which is in A^p_{ppp} and B^p_{ppp}, but also linked to other linear modes, whose contributions are taken into account through A^p_{ppp} and B^p_{ppp}.

So the optimization problem for tuning hardening/softening behavior of pth mode can be formulated as

$$\begin{aligned} \min_{\rho_e} \quad & \pm\,|\Gamma^*|\ (\text{or } \pm\,|\Gamma|) \\ \text{s.t. :} \quad & (\omega_p^2\mathbf{M} - \mathbf{K}_L)\mathbf{\Phi}_p = 0 \end{aligned} \tag{6.14}$$

where a plus/minus sign corresponds to cancel/enhance the hardening/softening behavior. Note that without taking the modulus (i.e. absolute value) of Γ^* (or Γ), the hardening/softening behavior may be qualitatively changed, as illustrated in Chapter 5. In practical application, the formulation of Γ^* (or Γ) can be simplified by recognizing the significant coefficients. This is illustrated in the optimization example.

6.1.2 Optimization of a coupled-mode resonator

For a coupled-mode resonator, its operation involves at least two modes with energy transfer among them. It has contributed to developing multi-harmonic atomic force microscopy (Pettit et al., 2015), frequency stabilization (Antonio et al., 2012), passive frequency division (Strachan et al., 2013; Qalandar et al., 2014), and disk resonator gyroscope with self-induced parametric amplification (Nitzan et al., 2015). Below, optimization of the essential modal coupling effect is formulated for a coupled-mode resonator with 2:1 internal resonance, e.g., $\omega_{p_2} \approx 2\omega_{p_1}$. For simplicity, modes p_1 and p_2 are referred to as modes 1 and 2, respectively.

The reduced order dynamic model with its conservative dynamics projected onto two nonlinear normal modes in curved, normal coordinates is written as

$$\begin{aligned} &\ddot{R}_1 + \omega_1^2 R_1 + (g^1_{12} + g^1_{21})R_2R_1 + (A^1_{111} + h^1_{111})R_1^3 + B^1_{111}R_1\dot{R}_1^2 \\ &\quad + \left[(A^1_{212} + A^1_{122} + h^1_{122} + h^1_{212} + h^1_{221})R_2^2 + B^1_{122}\dot{R}_2^2\right] R_1 + \left(B^1_{212}R_2\dot{R}_2\right)\dot{R}_1 = 0 \end{aligned} \tag{6.15}$$

$$\begin{aligned} &\ddot{R}_2 + \omega_2^2 R_2 + g^2_{11}R_1^2 + (A^2_{222} + h^2_{222})R_2^3 + B^2_{222}R_2\dot{R}_2^2 \\ &\quad + \left[(A^2_{112} + A^2_{211} + h^2_{112} + h^2_{121} + h^2_{211})R_1^2 + B^2_{211}\dot{R}_1^2\right] R_2 + \left(B^2_{112}R_1\dot{R}_1\right)\dot{R}_2 = 0 \end{aligned} \tag{6.16}$$

where the explicit expressions of A^p_{ijk} and B^p_{ijk} are given in (Touzé et al., 2004). The key term of interest is that associated with the *essential* modal coupling coefficients g^1_{12}, g^1_{21} and g^2_{11}, since they are the terms in the normal form that describes the resonant nonlinear coupling terms that promote energy exchange between the modes.

These essential modal coupling coefficients can also be observed from the governing equation with its dynamics projected onto two linear modes, which is written as

$$\begin{aligned} \ddot{q}_1 + \omega_1^2 q_1 + (g^1_{12} + g^1_{21}) q_1 q_2 + g^1_{11} q_1^2 + h^1_{111} q_1^3 + \text{others} = f_1(t) \\ \ddot{q}_2 + \omega_2^2 q_2 + g^2_{11}\, q_1^2 + g^2_{22} q_2^2 + h^2_{222} q_2^3 + \text{others} = f_2(t) \end{aligned} \tag{6.17}$$

where the most important coefficients are g^1_{12}, g^1_{21} and g^2_{11}, between which there is an exact relation $g^1_{12} + g^1_{21} = 2g^2_{11}$. The reason for this exact relation is that the coefficients of $q_1 q_2$ and q_1^2 in Eq. (6.17) arise from differentiation of the term $\beta q_1^2 q_2$ in the Hamiltonian $\mathcal{H}$ with respect to q_1 and q_2, where $\beta = \alpha^{(3)}_{112} + \alpha^{(3)}_{121} + \alpha^{(3)}_{211}$.

After recognizing the essential modal coupling term, the optimization problem is formulated as

$$\begin{aligned} \min_{\rho_e} \quad & c = -\left|\alpha^{(3)}_{112} + \alpha^{(3)}_{121} + \alpha^{(3)}_{211}\right| \\ \text{s.t.:} \quad & (\omega_p^2 \mathbf{M} - \mathbf{K}_L)\boldsymbol{\Phi}_p = 0,\ p = 1,\ 2. \\ & |\omega_1/\omega_2 - 1/2| \le \epsilon \end{aligned} \tag{6.18}$$

where ϵ is a tolerance of frequency relation. The sensitivity is computed with Eq. (6.6) written as

$$\frac{\mathrm{d}c}{\mathrm{d}\rho_e} = S \cdot \left(\frac{\partial \alpha^{(3)}_{112}}{\partial \rho_e} + \frac{\partial \alpha^{(3)}_{121}}{\partial \rho_e} + \frac{\partial \alpha^{(3)}_{211}}{\partial \rho_e} \right) + \sum_{p=1}^{2} \left[\boldsymbol{\lambda}_p^T \left(\omega_p^2 \frac{\partial \mathbf{M}}{\partial \rho_e} - \frac{\partial \mathbf{K}_L}{\partial \rho_e} \right) \boldsymbol{\Phi}_p + \eta_p \boldsymbol{\Phi}_p^T \frac{\partial \mathbf{M}}{\partial \rho_e} \boldsymbol{\Phi}_p \right] \tag{6.19}$$

where $S = -\text{sign}\left(\alpha^{(3)}_{112} + \alpha^{(3)}_{121} + \alpha^{(3)}_{211}\right)$. It is noted that there are two groups of adjoint variables, $\boldsymbol{\lambda}_1$ and η_1, $\boldsymbol{\lambda}_2$ and η_2, corresponding to the two vibration modes. These two groups of adjoint variables are solved using adjoint equation in Eq. (6.7) with $p = 1,\ 2$.

6.2 Optimization examples

Two examples are presented. The first is to maximize/minimize the cubic nonlinearity of the fundamental mode in a nonlinear resonator consisting of a clamped-clamped beam, a common element in MEMS applications. The second example shows how one can maximize the essential modal coupling nonlinearity in a T-shaped frame with a 2:1 internal resonance, a structure that has been proposed as a MEMS frequency divider.

6.2.1 Optimization of a clamped-clamped beam [P2]

We find that for the flexural mode of a clamped-clamped beam with geometric nonlinearity from mid-plane stretching, the dominating coefficient is h^p_{ppp} and we can therefore simplify our optimization problem considerably by approximating Γ^* as:

$$\Gamma^* \approx \Gamma = \frac{3}{8}\frac{h^p_{ppp}}{\omega_p^2} = \frac{3}{2}\frac{\alpha^{(4)}_{pppp}}{\omega_p^2} \tag{6.20}$$

where the second simplification holds true since $g^p_{pp} \equiv 0$. Based on the coefficient Γ^* in Eq. (6.20) and omitting the constant factor, the objective function is now selected as

$$\min_{\rho_e} \quad c = \pm\frac{\alpha^{(4)}_{pppp}}{\omega_p^2} \tag{6.21}$$

where a plus/minus sign leads to minimizing/maximizing the hardening behavior respectively. This simplification is possible since we consider the fundamental mode of a clamped-clamped beam, which has a strictly hardening nonlinearity, that is $\alpha^{(4)}_{pppp} > 0$. Substituting the objective function in Eq. (6.21) into Eq. (6.6), its sensitivity with respect to design variables ρ_e is obtained as

$$\frac{\mathrm{d}c}{\mathrm{d}\rho_e} = \pm\frac{1}{\omega_p^2}\frac{\partial\alpha^{(4)}_{pppp}}{\partial\rho_e} + \boldsymbol{\lambda}_p^T\left(\omega_p^2\frac{\partial\mathbf{M}}{\partial\rho_e} - \frac{\partial\mathbf{K}_L}{\partial\rho_e}\right)\boldsymbol{\Phi}_p + \eta_p\boldsymbol{\Phi}_p^T\frac{\partial\mathbf{M}}{\partial\rho_e}\boldsymbol{\Phi}_p \tag{6.22}$$

where the adjoint variables $\boldsymbol{\lambda}_p$ and η_p are solved from adjoint equation in Eq. (6.7) with

$$\frac{\mathrm{d}c}{\mathrm{d}\boldsymbol{\Phi}_p} = \pm\frac{1}{\omega_p^2}\frac{\partial\alpha^{(4)}_{pppp}}{\partial\boldsymbol{\Phi}_p}, \quad \frac{\partial c}{\partial\omega_p} = \mp 2\frac{\alpha^{(4)}_{pppp}}{\omega_p^3} \tag{6.23}$$

and

$$\frac{\partial\alpha^{(4)}_{pppp}}{\partial\boldsymbol{\Phi}^e_p} = \frac{1}{2}\int_{V_e}(\boldsymbol{\Phi}^e_p)^T\left(\mathbf{B}_1(\boldsymbol{\Phi}^e_p)\right)^T\mathbb{C}\left(\mathbf{B}_1(\boldsymbol{\Phi}^e_p)\right)\,dV \tag{6.24}$$

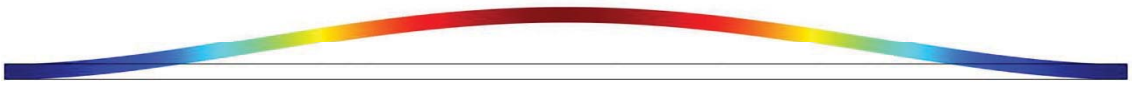

Figure 6.1 Initial design of a clamped-clamped beam and its linear vibration mode. The color represents the vibration amplitude. Figure taken from [P2].

Figure 6.2 Optimized design for maximizing the cubic nonlinearity of a clamped-clamped beam and its linear vibration mode. The color represents the vibration amplitude. Figure taken from [P2].

Figure 6.3 Optimized design for minimizing the cubic nonlinearity of a clamped-clamped beam and its linear vibration mode. The color represents the vibration amplitude.

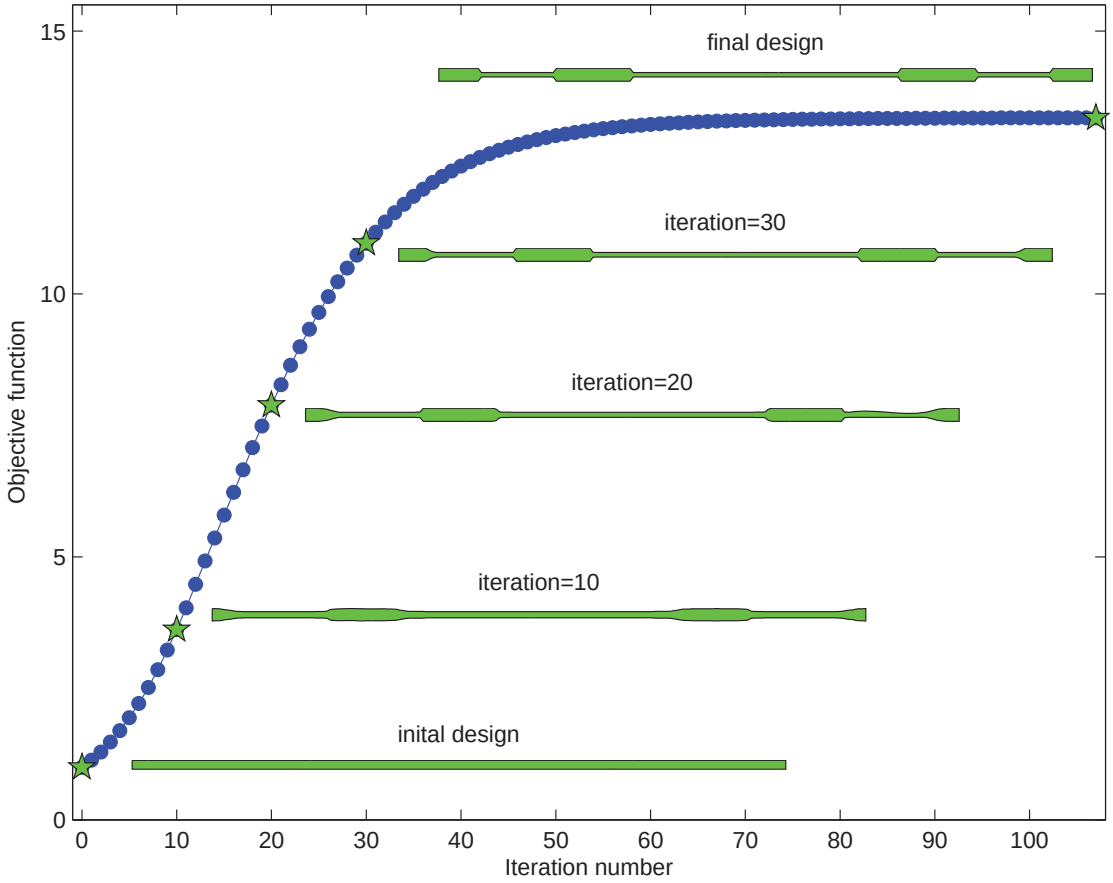

Figure 6.4 Evolution of the objective function and shapes encountered during the optimization process. The vertical axis is the absolute value of the objective function divided by its initial value and the horizontal axis is the iteration number. Figure taken from [P2].

For specific calculations, the beam has a fixed length L of 300 µm and a fixed out-plane width of 20 µm. The initial design has a uniform in-plane thickness of 4 µm, and is discretized with 400 beam elements. During shape optimization the in-plane thickness h is varied to tailor the cubic nonlinearity in the reduced order model. We set $h_{\min}$ =2 µm, and $h_{\max}$ =6 µm. The material properties are assumed for Si, that is, mass density $\rho = 2329\ \mathrm{kg/m^3}$, and Young's modulus $E =$ 170 GPa. The vibration modes of the initial design and two optimized designs are shown in Figs. 6.1–6.3, respectively. Evolution of the objective function and shapes obtained during the evolution are shown in Figs. 6.4 and 6.5. In these optimizations, the objective function is increased by a factor of 13 and reduced by a factor of 4, respectively.

The optimized designs are in accordance with the results in Section 3.3.1, obtained using the incremental harmonic balance method. We found the nonlinear strain energy due to midplane stretching reaches its local maximum around

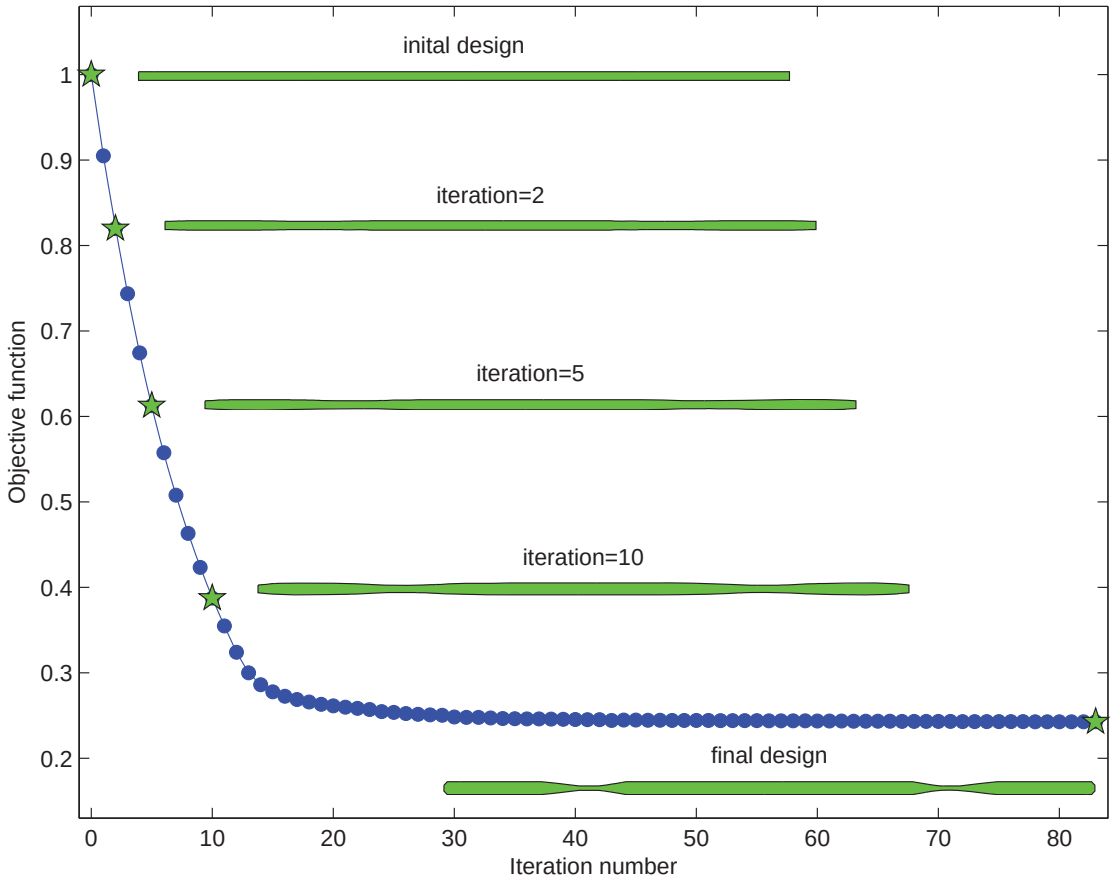

Figure 6.5 Evolution of the objective function and shapes encountered during the optimization process. The vertical axis is the absolute value of the objective function divided by its initial value and the horizontal axis is the iteration number. Figure taken from [P2].

$x = \frac{1}{4}L$ and $x = \frac{3}{4}L$, which is precisely where the optimized structures are altered most significantly relative to their general thickness.

Furthermore, the eigenfrequency of the first flexural mode decreases during optimization of maximizing the cubic nonlinearity, and increases during optimization of minimizing the cubic nonlinearity. This follows from the fact that the structure is made generally thinner when maximizing the nonlinearity, so that the critical sections can be made relatively thick, and the opposite trend occurs when minimizing the nonlinearity.

6.2.2 Optimization of a T-shaped frequency divider [P2]

To demonstrate the optimization procedure for tuning the essential modal coupling term, consider a T-shaped frame structure shown in Fig. 6.6 with 2:1 internal resonance. This example is motivated by a MEMS frequency divider that makes use of internal resonance, for which a general theory is presented by Strachan et al. (2013), and dynamic tests is presented by Qalandar et al. (2014). As seen in Fig. 6.6, the vibration of mode 1 is localized in the vertical beam and the vibration of mode 2 is localized in the horizontal beam. We refer to these modes as localized modes even though the entire structure is generally involved in the modal vibration. The localization of these modes is a desirable feature in frequency divider.

In operation, a harmonic load with frequency close to ω_2 is applied to drive mode 2 into resonance. When the amplitude of mode 2 is sufficiently large, it will induce the vibration of mode 1 due to the parametric pumping. A physical interpretation is that the transverse vibration of the horizontal beam provides an axial force in the vertical beam, which in turn induces transverse motion of the vertical beam when the frequency of the horizontal beam is approximately twice that of the vertical beam.

For a specific example the length of the horizontal beam is taken to be 300 µm and the length of the vertical beam is taken to be 195.5 µm, so that $\omega_2 \approx 2\omega_1$.The lengths of the two beams are fixed during the optimization. The initial in-plane thickness is uniformly 4 µm along both beams, and the in-plane thickness is bounded between 2 µm and 6 µm during the optimization. The material properties are the same as the example in Section 6.2.1. An optimized design and its two important vibration modes are displayed in Fig. 6.7. Evolution of the objective function and optimized designs over iterations are displayed in Fig. 6.8.

Evolution of the eigenfrequencies of linear vibration modes 1 and 2 encountered over iterations of the optimization process is displayed in Fig. 6.9(a). Other measures of interest for this system are (i) the degree of spatial energy localization in the vertical beam of the first vibration mode (note that from symmetry the second vibration mode has perfect localization) and (ii) the effectiveness of the horizontal beam in parametrically pumping the vertical beam in the second mode. The localization of the first mode is measured by the maximum transverse

amplitude of the *horizontal* beam divided by the maximum transverse amplitude of the *vertical* beam. Likewise, the pumping effectiveness of the horizontal beam in the second mode is measured by the ratio of the transverse vibration at the *midspan* of the horizontal beam to the maximum transverse vibration of the same beam, which occurs near the *quarter spans*. The results in Fig. 6.9(b) show that the localization ratio decreases during optimization, which indicates improved localization, and the pumping ratio increases, which indicates enhanced coupling of the two modes.

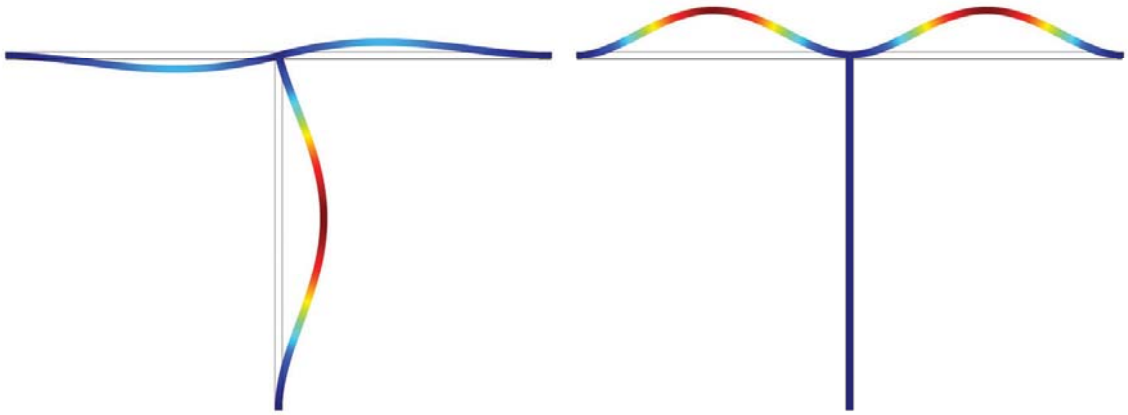

Figure 6.6 Initial design and the two coupled linear vibration modes obtained using COMSOL modal analysis. Left: linear vibration mode 1, right: linear vibration mode 2, and $\omega_2 \approx 2\omega_1$. The color represents the vibration amplitude. Figure taken from [P2].

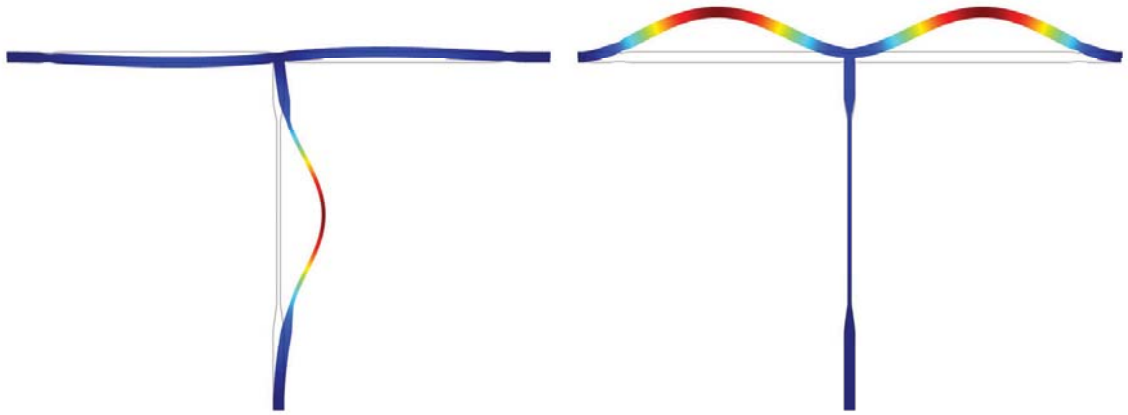

Figure 6.7 Optimized design for maximizing the absolute value of the *essential* modal coupling coefficient and the two coupled linear vibration modes obtained using COMSOL modal analysis. Left: linear vibration mode 1, right: linear vibration mode 2 and $\omega_2 \approx 2\omega_1$. The color represents the vibration amplitude. Figure taken from [P2].

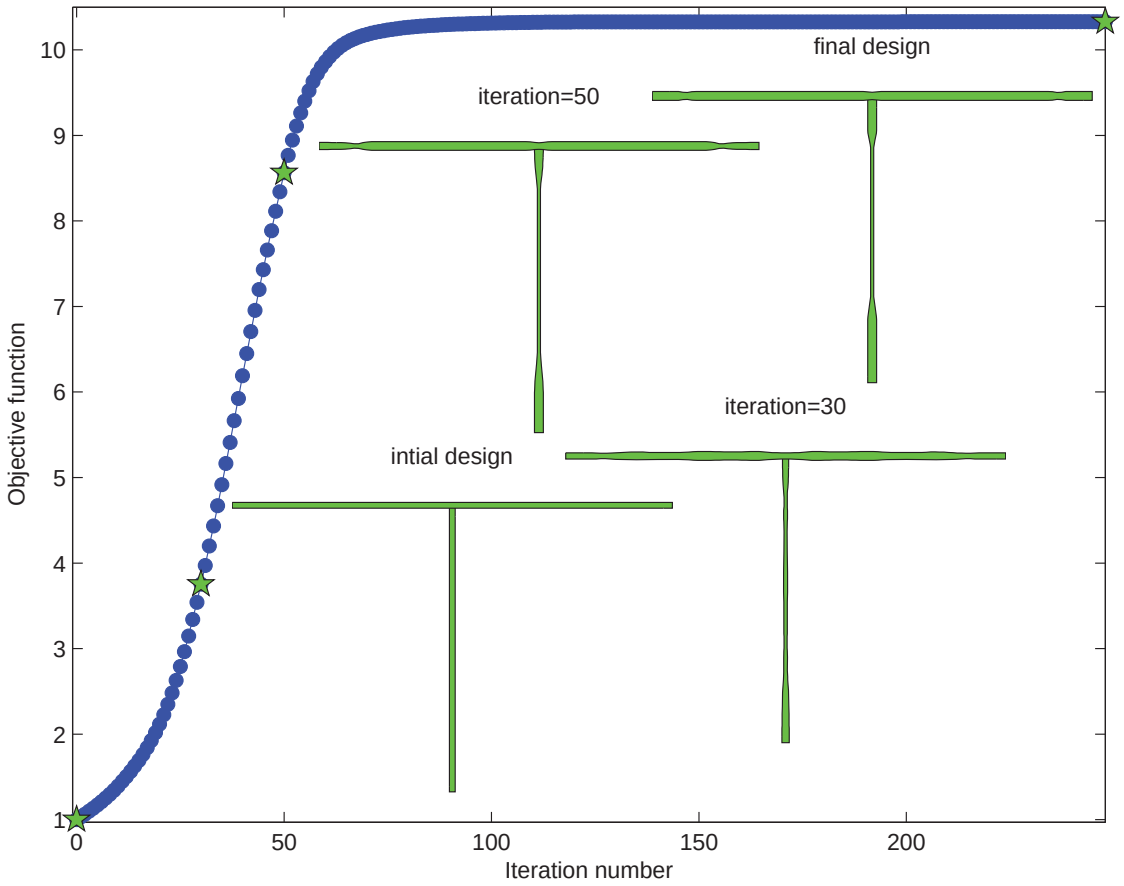

Figure 6.8 Evolution of the objective function and shapes encountered during the optimization process. The vertical axis is the absolute value of the objective function divided by its initial value and the horizontal axis is the iteration number. Figure taken from [P2].

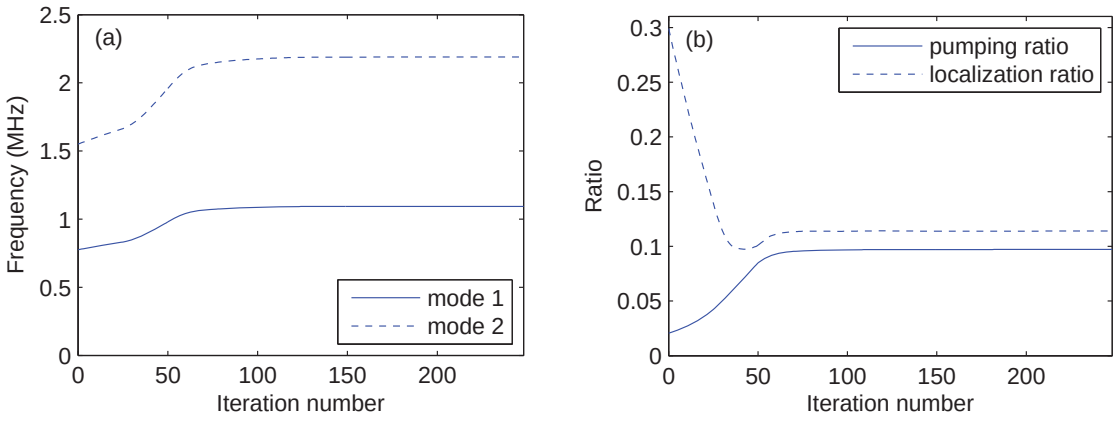

Figure 6.9 (a) Evolution of eigenfrequencies of linear vibration mode 1 and 2 encountered during the optimization process. (b) Evolution of pumping ratio and localization ratio encountered during the optimization process. Figure taken from [P2].

Chapter 7
Dynamic tests of optimized design

This chapter describes the ongoing work on experimental validation of the optimized designs including clamped-clamped beams and T-shaped frequency dividers. We have finished the fabrication of these micro-structures. We expect to validate the effectiveness of the optimization in dynamic tests in near future. The following part of this chapter describes the fabrication process as well as the plan of dynamic tests.

7.1 Fabrication process

For convenience and efficiency, silicon-on-insulator (SOI) wafer is used in the fabrication. SOI wafer consists of a top thin layer of silicon used as device layer, and a bottom thick layer of silicon used as support layer. Between the two silicon layers, there is an insulator layer of silicon dioxide. Based on the thickness of the top layer, SOI wafer is classified into thick film SOI wafer and thin film SOI wafer. In the fabrication, thick film SOI wafer with top layer thickness of 5 µm is used. The targeting structures includes clamped-camped beams and T-shaped frequency dividers. In these micro-mechanical structures, the maximum in-plane thickness of beams is 6 µm. In initial designs the in-plane thickness of each beam is uniformly 4 µm, whereas in the optimized designs the in-plane thickness of beams is bounded between 2 µm and 6 µm.

In the process, these structures is fabricated by using dry etching of silicon and wet etching of silicon dioxide in conjunction with photo-lithography. Dry etching is anisotropic etching and can avoid notching and significant undercutting of the resist pattern. It is essential for achieving the accurate representation of the distribution of in-plane thickness of beams in the optimized structures.

A sequence of the fabrication process is illustrated in Fig. 7.1. To begin with, the wafer is prepared. Then, Hexamethyldisilazane (HDMS) is applied for promoting the adhesion of the photo-resist to the top silicon layer, and then the photo-resist, or simply resist, is covered by spin coating, see Fig. 7.1(a). After soft bake of the wafer, it is exposed to a pattern of intense light and the pattern defined in the mask is transferred to the resist, see Fig. 7.1(b). In photo-lithography, the UV light is used. For positive resist, the resist in the exposed region become soluble in the developer, see Fig. 7.1(c). After developing the pattern of resist, dry etching of silicon is performed, see Fig. 7.1(d), and the targeting structures are defined in the top silicon layer, see Fig. 7.1(g). After dry etching, wet etching of the thin film silicon dioxide is applied by using buffered HF, which is mixture

of a buffering agent such as NH_4F and HF. The time of wet etching is estimated for isotropic etching at least 6 µm silicon dioxide. After wet etching, the targeting structures are released from the underlying support layer, see Fig. 7.1(e). It is noted that the structures are supported by silicon dioxide at the ends of the targeting structures, see Fig. 7.1(h). The supports of the targeting structures are designed to be sufficiently large so that the underlying silicon dioxide can sustain the wet etching. In the end, the resist is stripped by using plasma ashing, see Fig. 7.1(f).

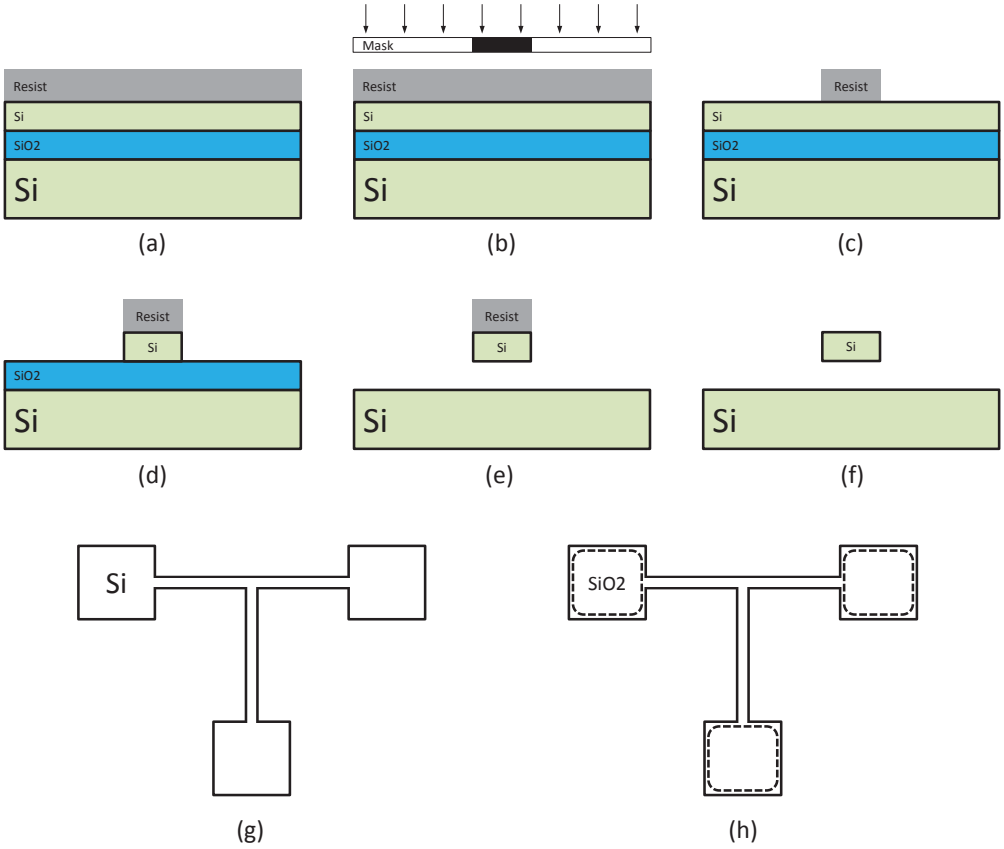

Figure 7.1 Fabrication process of optimized design.

7.2 Dynamic tests

The first consideration in dynamic tests is the approaches for driving actuation and motion detection. Since only geometric nonlinearity is considered in the analysis and optimization, it is preferable to use piezoelectric shaker for base excitation and laser Doppler vibrometer for motion detection. For the out-of-plane motion, it can be detected in a straightforward way by using laser beam. For the

in-plane motion, laser can be guided to the in-plane surfaces by using 45 degrees mirrors built on the chip fabricated with focused iron beam (FIB) milling.

For clamped-clamped beams, the hardening/softening behavior can be characterized in open-loop operation with upward and downward sweeping of excitation frequency. An improved characterization can be achieved in closed-loop operation by using the so-called variable-phase closed-loop test, where the phase between the response and the input is varied in the dynamic test. The variable-phase closed-loop test was originally developed for stable operation of nonlinear resonators beyond the bifurcation point (Lee et al., 2011) and has been increasingly used in characterization of nonlinear resonators (Villanueva et al., 2013; Yang et al., 2014, 2015).

For T-shaped frequency dividers, the interesting quantities are the pumping effectiveness of the second mode and the localization of the first mode, see Section 6.2.2. Another interesting relation is the parametric instability region (Qalandar et al., 2014). We expect that the optimized designs can broaden the instability region and therefore lead to a larger activation region for operation of the frequency divider. Last but not least, experimental characterization of the nonlinear modal coupling coefficients would directly validate the effectiveness of the characterization and the optimization. A fabricated micro-mechanical T-shaped frequency divider with optimized in-plane thickness is shown in Fig. 7.2. This optimized design is obtained by maximizing the essential mode coupling effects (Section 6.2.2) in conjunction with a volume constraint (Dou et al., 2014). The dynamic tests are in progress.

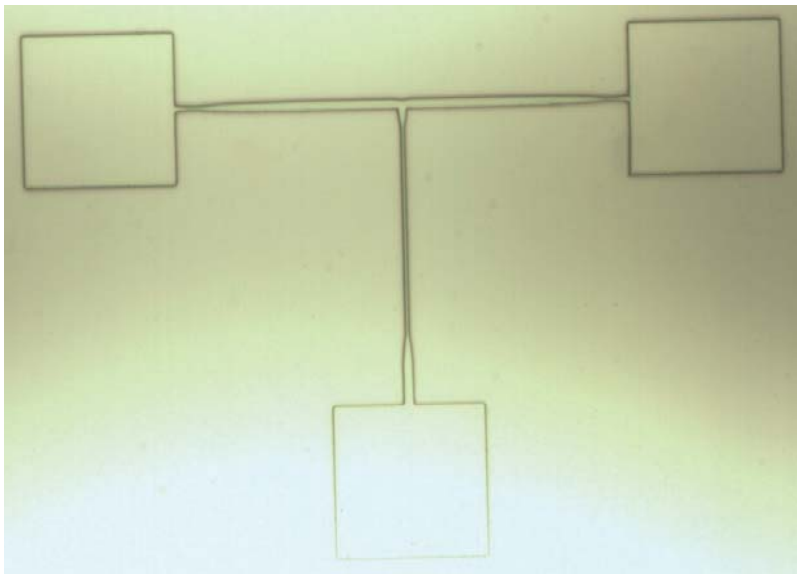

Figure 7.2 Microscope image of a micro-mechanical T-shaped frequency divider with optimized in-plane thickness. The structure spans 300 µm × 200 µm.

Chapter 8
Concluding remarks

8.1 Summary

In this thesis, nonlinear dynamics and nonlinear micro-mechanical resonators are studied from the point of view of gradient-based structural optimization. We have demonstrated that structural optimization is a convenient tool for tuning complex nonlinear dynamics. In some case studies, an order-of-magnitude improvement of the targeted performance is achieved with simple manipulation of the structural geometry. The second major finding in the thesis was the efficient design sensitivity analyses of nonlinear frequency response, nonlinear normal modes and nonlinear modal coupling coefficients. Particularly, these sensitivity analyses are derived by using the adjoint method, which enables their future application in topology optimization. These sensitivity analyses are also useful for solving other inverse problems in nonlinear dynamics.

The thesis starts with a systematic discussion about the modelling, analysis, and characterization of nonlinear dynamics in mechanical systems with geometric nonlinearity. Based on a nonlinear finite element model, three kinds of dynamic features are obtained by using two methods. Nonlinear frequency response and nonlinear normal modes are numerically computed by using the harmonic balance method with higher-order harmonics. Both the classical incremental harmonic balance method and the alternating frequency/time domain method are investigated and reorganized for the convenience in numerical implementation. For characterization of the nonlinearity, nonlinear modal coupling coefficients can be explicitly derived from a nonlinear finite element model. Based on the modal coupling coefficients, normal form linked to nonlinear normal modes can be further derived. It is noted that the harmonic balance method in conjunction with the alternating frequency/time domain method can handle complex nonlinearity, whereas the method of explicit calculation of modal coupling coefficients can handle polynomial-type nonlinearity.

In the optimization, plane frame structures including clamped-clamped beams, $\sqcap$-shaped frames, H-shaped frames and T-shaped frames are used in case studies. In these structures, geometric nonlinearity plays an important role. The nonlinearity gives rise to rich nonlinear dynamics including nonlinear resonance peak with hardening/softening behavior, super-harmonic resonances with a higher-order harmonic in resonance state, and nonlinear modal interactions with internal resonance. Based on the modelling, analysis and characterization, a series of specialized schemes are proposed for tuning the associated nonlinear dynamic responses.

Nonlinear frequency response is a nonlinear analogy of the linear frequency response function. It can take into account structural properties including mass, nonlinear stiffness, dissipation and loads. When the excitation frequency is around the linear eigenfrequency, nonlinear forced resonance could display hardening/-softening behavior with jumping phenomenon because of the existence of multiple solutions. For robustness and efficiency, a nonlinear resonance peak analysis is proposed based on the phase lag quadrature criterion. Examples are offered for tuning the amplitude and the hardening/softening behavior of nonlinear resonance peak.

Besides the primary resonances near linear eigenfrequencies, super-harmonic resonances can also occur in nonlinear mechanical systems. For mechanical systems with cubic nonlinearity, super-harmonic resonance of order-3 may be observed when excitation frequency is around one third of the linear eigenfrequency. In this case the third-order harmonic of the response can be excited into resonance state. Optimization of super-harmonic resonance is performed based on the analysis of nonlinear frequency response at a prescribed frequency condition, i.e., a constant relation between the excitation frequency and the linear eigenfrequency. Two examples are studied including superharmonic resonance of order-3 in a clamped-clamped beam, and superharmonic resonance of order-2 in a $\sqcap$-shaped frame structure. We have shown that the higher-order harmonic in superharmonic resonance can be effectively enhanced or suppressed by using optimized structural shapes.

Nonlinear normal mode is proposed and developed as a nonlinear analogy of linear normal mode. It is calculated based on the mass and the nonlinear stiffness of a nonlinear mechanical system, and reveals the conservative dynamics of the undamped system that underlies the damped one. For nonlinear mechanical systems with low dissipation, nonlinear forced resonance peak is in the neighborhood of nonlinear normal mode. By tuning the hardening/softening behavior of nonlinear normal mode of these systems, the hardening/softening behavior of nonlinear forced resonance can also be tuned. In the design sensitivity analysis of the hardening/softening behavior of nonlinear normal modes, normalization of nonlinear normal modes is performed with respect to the reference amplitude or the energy present in the system, which resembles the normalization of linear eigenvector with respect to the amplitude and the mass matrix. In case studies, we successfully demonstrated that simple manipulation of structural geometry could tune the softening behavior into hardening behavior and vice versa.

Normal form can be viewed as the most simplified model in nonlinear dynamics. It plays a central role in characterization and physical interpretation of nonlinear resonance response. For a nonlinear mechanical system with polynomial-type nonlinearity or approximation of nonlinearity using polynomial functions, the nonlinear modal coupling coefficients can be explicitly derived from its nonlinear finite element model. By using the normal form theory, the normal form linked to nonlinear normal modes can be further derived. It is noted that the non-

linear modal coupling coefficients are explicit functions of the eigenvectors and the eigenvalues of linear normal modes. For a general function of the modal coupling coefficients and the normal form coefficients, the design sensitivity analysis is derived. Optimization examples are given for tuning the hardening/softening behavior of a clamped-clamped beam, and the essential inter-modal coupling effect in a T-shaped frequency divider.

8.2 Future work

This study extends our knowledge of nonlinear dynamics and structural optimization. It also has thrown up many questions in need of further investigation. It is recommended that further research can be undertaken in the following areas.

A limitation of this study is that the major work is based on simple manipulation of structural geometry, which limits the performance of optimized designs. More studies need to be carried out by using topology optimization. The variation of topology may produce novel designs that enable further improvement of the targeted performance.

The second extension of the study is its applications in multi-physics problems. For example, its application in nonlinear micro-mechanical resonators can be refined by using an integrated optimization of geometric nonlinearity, material nonlinearity and electrostatic nonlinearity.

Thirdly, the combination of nonlinear finite element models and the higher-order harmonic balance method can be extended to analysis and optimization of nonlinear waves. This major extension would enable its application in nonlinear acoustic-mechanical resonators, nonlinear periodic structures and nonlinear optical devices.

Last but not least, the study can also be used in system identification and finite element model updating in nonlinear structural dynamics. By minimizing the deviation between simulated and measured nonlinear frequency response and nonlinear normal modes, the uncertain parameters can be iteratively updated and finally identified.

References

Abdel-Rahman, E.M. and Nayfeh, A.H. (2003). Secondary resonances of electrically actuated resonant microsensors. *Journal of Micromechanics and Microengineering*, 13(3):491.

Antonio, D., Zanette, D.H. and López, D. (2012). Frequency stabilization in nonlinear micromechanical oscillators. *Nature communications*, 3:806.

Bendsøe, M.P. and Sigmund, O. (2003). *Topology optimization: theory, methods and applications*. Springer Science & Business Media.

Cameron, T. and Griffin, J. (1989). An alternating frequency/time domain method for calculating the steady-state response of nonlinear dynamic systems. *Journal of applied mechanics*, 56(1):149–154.

Chen, S., Cheung, Y. and Xing, H. (2001). Nonlinear vibration of plane structures by finite element and incremental harmonic balance method. *Nonlinear Dynamics*, 26(1):87–104.

Cheung, Y., Chen, S. and Lau, S. (1990). Application of the incremental harmonic balance method to cubic non-linearity systems. *Journal of Sound and Vibration*, 140(2):273 – 286.

Cho, H., Jeong, B., Yu, M.F., Vakakis, A.F., McFarland, D.M. and Bergman, L.A. (2012a). Nonlinear hardening and softening resonances in micromechanical cantilever-nanotube systems originated from nanoscale geometric nonlinearities. *International Journal of Solids and Structures*, 49(15):2059–2065.

Cho, H., Yu, M.F., Vakakis, A.F., Bergman, L.A. and McFarland, D.M. (2010). Tunable, broadband nonlinear nanomechanical resonator. *Nano letters*, 10(5):1793–1798.

Cho, H., Yu, M.F., Vakakis, A.F., Bergman, L.A. and McFarland, D.M. (2012b). Dynamics of microcantilever integrated with geometric nonlinearity for stable and broadband nonlinear atomic force microscopy. *Surface Science*, 606(17):L74–L78.

Choi, K.K. and Kim, N.H. (2006). *Structural sensitivity analysis and optimization 1: linear systems*. Springer Science & Business Media.

Cook, R.D. et al. (2007). *Concepts and applications of finite element analysis*. John Wiley & Sons.

Dai, X., Miao, X., Sui, L., Zhou, H., Zhao, X. and Ding, G. (2012). Tuning of nonlinear vibration via topology variation and its application in energy harvesting. *Applied Physics Letters*, 100(3):031902.

Detroux, T., Renson, L. and Kerschen, G. (2014). The harmonic balance method for advanced analysis and design of nonlinear mechanical systems. *Nonlinear Dynamics, Volume 2*, pages 19–34.

Detroux, T., Renson, L., Masset, L. and Kerschen, G. (2015). The harmonic balance method for bifurcation analysis of nonlinear mechanical systems. In *SEM IMAC XXXIII A Conference and Exposition on Structural Dynamics*.

Didier, J., Sinou, J.J. and Faverjon, B. (2013). Nonlinear vibrations of a mechanical system with non-regular nonlinearities and uncertainties. *Communications in Nonlinear Science and Numerical Simulation*, 18(11):3250–3270.

Dou, S., Strachan, B., Shaw, S. and Jensen, J. (2014). Characterization and optimal design of nonlinear mems resonators. Poster session presented at Solid-State Sensors, Actuators and Microsystems Workshop, Hilton Head Island, SC, United States.

Dou, S. and Jensen, J.S. (2015). Optimization of nonlinear structural resonance using the incremental harmonic balance method. *Journal of Sound and Vibration*, 334:239 – 254.

Dou, S., Strachan, B.S., Shaw, S.W. and Jensen, J.S. (2015). Structural optimization for nonlinear dynamic response. *To appear in the "A field guide to nonlinearity in structural dynamics" issue of Philosophical Transactions A*.

Elshurafa, A.M., Khirallah, K., Tawfik, H.H., Emira, A., Abdel Aziz, A.K. and Sedky, S.M. (2011). Nonlinear dynamics of spring softening and hardening in folded-mems comb drive resonators. *Microelectromechanical Systems, Journal of*, 20(4):943–958.

Guckenheimer, J. and Holmes, P. (1983). *Nonlinear oscillations, dynamical systems, and bifurcations of vector fields*. Springer-Verlag, New York.

Hajati, A. and Kim, S.G. (2011). Ultra-wide bandwidth piezoelectric energy harvesting. *Applied Physics Letters*, 99(8):083105.

Ishinabe, H., Kobayashi, T., Wang, D.F., Itoh, T. and Maeda, R. (2012). Characterization of super-harmonic effect using piezoelectric film cantilever with a proof mass in the point. In *Nano/Micro Engineered and Molecular Systems (NEMS), 2012 7th IEEE International Conference on*, pages 615–618. IEEE.

Jensen, J.S. and Lazarov, B.S. (2008). Optimization of non-linear mass damper parameters for transient response. In B. Andrievsky and A. Fradkov, editors, *Proceedings of the Sixth EUROMECH Nonlinear Dynamics Conference*.

Jeong, B., Cho, H., Keum, H., Kim, S., McFarland, D.M., Bergman, L.A., King, W.P. and Vakakis, A.F. (2014). Complex nonlinear dynamics in the limit of weak coupling of a system of microcantilevers connected by a geometrically nonlinear tunable nanomembrane. *Nanotechnology*, 25(46):465501.

Kacem, N., Baguet, S., Hentz, S. and Dufour, R. (2012). Pull-in retarding in nonlinear nanoelectromechanical resonators under superharmonic excitation. *Journal of Computational and Nonlinear Dynamics*, 7(2):021011.

Kerschen, G. (2014). *Modal analysis of nonlinear mechanical systems*. Springer.

Kerschen, G., Peeters, M., Golinval, J.C. and Vakakis, A.F. (2009). Nonlinear normal modes, Part I: A useful framework for the structural dynamicist. *Mechanical Systems and Signal Processing*, 23(1):170 – 194.

Kim, Y.I. and Park, G.J. (2010). Nonlinear dynamic response structural optimization using equivalent static loads. *Computer Methods in Applied Mechanics and Engineering*, 199(9-12):660–676.

Krack, M., von Scheidt, L.P. and Wallaschek, J. (2013). A method for nonlinear modal analysis and synthesis: Application to harmonically forced and self-excited mechanical systems. *Journal of Sound and Vibration*, 332(25):6798 – 6814.

Krenk, S. (2009). *Non-linear modeling and analysis of solids and structures*. Cambridge University Press.

LaBryer, A. and Attar, P. (2010). A harmonic balance approach for large-scale problems in nonlinear structural dynamics. *Computers & Structures*, 88(17-18):1002 – 1014.

Lacarbonara, W. and Verlag., A.S. (2013). *Nonlinear structural mechanics : theory, dynamical phenomena and modeling*. Springer.

Lacarbonara, W. and Yabuno, H. (2006). Refined models of elastic beams undergoing large in-plane motions: theory and experiment. *International Journal of Solids and Structures*, 43(17):5066–5084.

Lazarus, A., Thomas, O. and Deü, J.F. (2012). Finite element reduced order models for nonlinear vibrations of piezoelectric layered beams with applications to nems. *Finite Elements in Analysis and Design*, 49(1):35–51.

Lee, H.A. and Park, G.J. (2015). Nonlinear dynamic response topology optimization using the equivalent static loads method. *Computer Methods in Applied Mechanics and Engineering*, 283:956–970.

Lee, H.K., Melamud, R., Chandorkar, S., Salvia, J., Yoneoka, S. and Kenny, T.W. (2011). Stable operation of mems oscillators far above the critical vibration amplitude in the nonlinear regime. *Journal of microelectromechanical systems*, 20(6):1228–1230.

Leung, A.Y.T. (1992). Nonlinear modal analysis of frames by the incremental harmonic-balance method. *Dynamics and Stability of Systems*, 7(1):43–58.

Leung, A.Y.T. and Fung, T.C. (1990). Non-linear steady state vibration and dynamic snap through of shallow arch beams. *Earthquake Engineering & Structural Dynamics*, 19(3):409–430.

Leung, A. and Chui, S. (1995). Non-linear vibration of coupled duffing oscillators by an improved incremental harmonic balance method. *Journal of Sound and Vibration*, 181(4):619 – 633.

Leung, A. and Fung, T. (1989). Non-linear steady state vibration of frames by finite element method. *International journal for numerical methods in engineering*, 28(7):1599–1618.

Lewandowski, R. (1992). Non-linear, steady-state vibration of structures by harmonic balance/finite element method. *Computers & structures*, 44(1):287–296.

Lewandowski, R. (1994). Non-linear free vibrations of beams by the finite element and continuation methods. *Journal of Sound and Vibration*, 170(5):577–593.

Lewandowski, R. (1997). Computational formulation for periodic vibration of geometrically nonlinear structures–part 1: theoretical background. *International journal of solids and structures*, 34(15):1925–1947.

Lifshitz, R. and Cross, M. (2008). Nonlinear dynamics of nanomechanical and micromechanical resonators. *Review of nonlinear dynamics and complexity*, 1:1–52.

Matheny, M., Villanueva, L., Karabalin, R., Sader, J.E. and Roukes, M. (2013). Nonlinear mode-coupling in nanomechanical systems. *Nano letters*, 13(4):1622–1626.

Nayfeh, A.H. and Younis, M.I. (2005). Dynamics of mems resonators under superharmonic and subharmonic excitations. *Journal of Micromechanics and Microengineering*, 15(10):1840.

Nayfeh, A.H. (2000). *Nonlinear interactions*. Wiley.

Nayfeh, A.H., Balachandran, B. and Sons., J.W.. (2004). *Applied nonlinear dynamics : analytical, computational, and experimental methods*. Wiley-VCH Verlag.

Nayfeh, A.H. and Mook, D.T. (1979). *Nonlinear oscillations*. John Wiley & Sons.

Nitzan, S.H., Zega, V., Li, M., Ahn, C.H., Corigliano, A., Kenny, T.W. and Horsley, D.A. (2015). Self-induced parametric amplification arising from nonlinear elastic coupling in a micromechanical resonating disk gyroscope. *Sci. Rep.*, 5:9036.

Olhoff, N. and Du, J. (2014a). Structural topology optimization with respect to eigenfrequencies of vibration. In *Topology Optimization in Structural and Continuum Mechanics*, pages 275–297. Springer.

Olhoff, N. and Du, J. (2014b). Topological design for minimum dynamic compliance of structures under forced vibration. In *Topology Optimization in Structural and Continuum Mechanics*, pages 325–339. Springer.

Pedersen, N.L. (2005). Designing plates for minimum internal resonances. *Structural and Multidisciplinary Optimization*, 30(4):297–307.

Peeters, M., Kerschen, G. and Golinval, J. (2011a). Dynamic testing of nonlinear vibrating structures using nonlinear normal modes. *Journal of Sound and Vibration*, 330(3):486 – 509.

Peeters, M., Kerschen, G. and Golinval, J. (2011b). Modal testing of nonlinear vibrating structures based on nonlinear normal modes: Experimental demonstration. *Mechanical Systems and Signal Processing*, 25(4):1227 – 1247.

Peeters, M., Viguié, R., Sérandour, G., Kerschen, G. and Golinval, J.C. (2009). Nonlinear normal modes, Part II: Toward a practical computation using numerical continuation techniques. *Mechanical Systems and Signal Processing*, 23(1):195 – 216.

Petrov, E.P. (2011). Advanced analysis and optimization of nonlinear resonance vibrations in gas-turbine structures with friction and gaps. *IUTAM Symposium on Emerging Trends in Rotor Dynamics*, 25:297–307.

Pettit, C., Jeong, B., Keum, H., Lee, J., Kim, J., Kim, S., McFarland, D.M., Bergman, L.A., Vakakis, A.F. and Cho, H. (2015). Microcantilever system incorporating internal resonance for multi-harmonic atomic force microscopy. In *Micro Electro Mechanical Systems (MEMS), 2015 28th IEEE International Conference on*, pages 752–755.

Qalandar, K., Strachan, B., Gibson, B., Sharma, M., Ma, A., Shaw, S. and Turner, K. (2014). Frequency division using a micromechanical resonance cascade. *Applied Physics Letters*, 105(24):244103.

Raghothama, A. and Narayanan, S. (1999). Non-linear dynamics of a two-dimensional airfoil by incremental harmonic balance method. *Journal of Sound and Vibration*, 226(3):493–517.

Raghothama, A. and Narayanan, S. (2000). Bifurcation and chaos of an articulated loading platform with piecewise non-linear stiffness using the incremental harmonic balance method. *Ocean Engineering*, 27(10):1087–1107.

Rhoads, J.F., Shaw, S.W. and Turner, K.L. (2010). Nonlinear dynamics and its applications in micro- and nanoresonators. *Journal of Dynamic Systems, Measurement, and Control*, 132(3):034001.

Ribeiro, P. and Petyt, M. (1999). Non-linear vibration of beams with internal resonance by the hierarchical finite-element method. *Journal of Sound and vibration*, 224(4):591–624.

Stanford, B. and Beran, P. (2012). Computational strategies for reliability-based structural optimization of aeroelastic limit cycle oscillations. *Structural and Multidisciplinary Optimization*, 45(1):83–99.

Stanford, B., Beran, P. and Kurdi, M. (2010). Adjoint sensitivities of time-periodic nonlinear structural dynamics via model reduction. *Computers and Structures*, 88(19-20):1110–1123.

Stanford, B., Beran, P., Snyder, R. and Patil, M. (2013). Stability and power optimality in time-periodic flapping wing structures. *Journal of Fluids and Structures*, 38(0):238 – 254.

Strachan, B.S., Shaw, S.W. and Kogan, O. (2013). Subharmonic resonance cascades in a class of coupled resonators. *Journal of Computational and Nonlinear Dynamics*, 8(4):041015.

Svanberg, K. (1987). The method of moving asymptotes—a new method for structural optimization. *International Journal for Numerical Methods in Engineering*, 24(2):359–373.

Thomsen, J.J. (1997). *Vibrations and Stability, Order and Chaos*. McGRAW-HILL.

Thomsen, J.J. (2003). *Vibrations and stability: advanced theory, analysis, and tools*. Springer Science & Business Media.

Tortorelli, D.A. and Michaleris, P. (1994). Design sensitivity analysis: overview and review. *Inverse problems in Engineering*, 1(1):71–105.

Touzé, C., Thomas, O. and Chaigne, A. (2004). Hardening/softening behaviour in non-linear oscillations of structural systems using non-linear normal modes. *Journal of Sound and Vibration*, 273(1):77–101.

Touzé, C. (2014). Normal form theory and nonlinear normal modes: Theoretical settings and applications. In *Modal Analysis of Nonlinear Mechanical Systems*, pages 75–160. Springer.

Touzé, C. and Amabili, M. (2006). Nonlinear normal modes for damped geometrically nonlinear systems: Application to reduced-order modelling of harmonically forced structures. *Journal of sound and vibration*, 298(4):958–981.

Touzé, C., Vidrascu, M. and Chapelle, D. (2014). Direct finite element computation of non-linear modal coupling coefficients for reduced-order shell models. *Computational Mechanics*, 54(2):567–580.

Tripathi, A. and Bajaj, A.K. (2013). Computational synthesis for nonlinear dynamics based design of planar resonant structures. *Journal of Vibration and Acoustics*, 135(5):051031.

Tripathi, A. and Bajaj, A.K. (2014). Design for 1: 2 internal resonances in in-plane vibrations of plates with hyperelastic materials. *Journal of Vibration and Acoustics*, 136(6):061005.

Tsai, T. and Cheng, C. (2013). Structural design for desired eigenfrequencies and mode shapes using topology optimization. *Structural and Multidisciplinary Optimization*, 47(5):673–686.

Villanueva, L., Kenig, E., Karabalin, R., Matheny, M., Lifshitz, R., Cross, M. and Roukes, M. (2013). Surpassing fundamental limits of oscillators using nonlinear resonators. *Physical review letters*, 110(17):177208.

Vyas, A., Peroulis, D. and Bajaj, A.K. (2008). Dynamics of a nonlinear microresonator based on resonantly interacting flexural-torsional modes. *Nonlinear Dynamics*, 54(1-2):31–52.

Vyas, A., Peroulis, D. and Bajaj, A.K. (2009). A microresonator design based on nonlinear 1: 2 internal resonance in flexural structural modes. *Microelectromechanical Systems, Journal of*, 18(3):744–762.

Westra, H., Poot, M., Van der Zant, H. and Venstra, W. (2010). Nonlinear modal interactions in clamped-clamped mechanical resonators. *Physical review letters*, 105(11):117205.

Wiggins, S. (2003). *Introduction to applied nonlinear dynamical systems and chaos*, volume 2. Springer Science & Business Media.

Wriggers, P. (2008). Nonlinear finite element methods.

Yang, Y., Ng, E., Polunin, P., Chen, Y., Strachan, S., Hong, V., Ahn, C.H., Shoshani, O., Shaw, S., Dykman, M. and Kenny, T. (2015). Experimental investigation on mode coupling of bulk mode silicon mems resonators. In *Micro Electro Mechanical Systems (MEMS), 2015 28th IEEE International Conference on*, pages 1008–1011.

Yang, Y., Ng, E.J., Hong, V.A., Ahn, C.H., Chen, Y., Ahadi, E., Dykman, M. and Kenny, T.W. (2014). Measurement of the nonlinear elasticity of doped bulk-mode mems resonators. In M. Allen and M. Mehregany, editors, *Solid-State Sensors, Actuators and Microsystems Workshop*, pages 285–288. Hilton Head Islands, SC, USA.

Yoon, G.H. (2010). Maximizing the fundamental eigenfrequency of geometrically nonlinear structures by topology optimization based on element connectivity parameterization. *Computers and Structures*, 88(1-2):120–133.

Younesian, D., Sadri, M. and Esmailzadeh, E. (2014). Primary and secondary resonance analyses of clamped–clamped micro-beams. *Nonlinear Dynamics*, 76(4):1867–1884.

A Formulation and codes for harmonic balance method

A.1 Precomputed matrices

The explicit expressions of the four precomputed matrices are given as follows:

$$
\begin{aligned}
&\mathbf{H}^{(0)} = \frac{1}{2\pi}\int_0^{2\pi} \mathbf{C}_S^T \mathbf{C}_S'' \, d\tau = \frac{1}{2}\mathbf{diag}([0 \ -1 \ \cdots \ -N_H^2 \ -1 \ \cdots \ -N_H^2]) \\
&\mathbf{H}^{(1)} = \frac{1}{2\pi}\int_0^{2\pi} \mathbf{C}_S^T \mathbf{C}_S' \, d\tau = \begin{bmatrix} 0 & \mathbf{0} & \mathbf{0} \\ \mathbf{0} & \mathbf{0} & \mathbf{c} \\ \mathbf{0} & -\mathbf{c} & \mathbf{0} \end{bmatrix}, \mathbf{c} = \frac{1}{2}\mathbf{diag}([\ 1 \ \cdots \ N_H \ ]) \\
&\mathbf{H}^{(2)} = \frac{1}{2\pi}\int_0^{2\pi} \mathbf{C}_S^T \mathbf{C}_S \, d\tau = \frac{1}{2}\mathbf{diag}([\ 2 \ \ 1 \ \cdots \ 1 \ \ 1 \ \cdots \ 1 \ ]) \\
&\mathbf{H}^{(3)}(m,n,k) = \frac{1}{2\pi}\int_0^{2\pi} \mathbf{C}_S(m)\mathbf{C}_S(n)\mathbf{C}_S(k) \, d\tau, \\
&m,n,k = 1,2,\ldots,2N_H+1
\end{aligned}
\tag{1}
$$

The explicit expression of $\mathbf{H}^{(3)}$ is given as

$$
\begin{aligned}
&\mathbf{H}^{(3)}(1,m,n) = \mathbf{H}^{(3)}(m,1,n) = \mathbf{H}^{(3)}(m,n,1) = \mathbf{H}^{(2)}(m,n), \\
&ccc = \frac{1}{4}[\delta(i-j+k) + \delta(i-j-k) + \delta(i+j+k) + \delta(i+j-k)], \\
&ssc = \frac{1}{4}[\delta(i-j+k) + \delta(i-j-k) - \delta(i+j+k) - \delta(i+j-k)], \\
&\mathbf{H}^{(3)}(i_s,j_s,k_c) = \mathbf{H}^{(3)}(i_s,k_c,j_s) = \mathbf{H}^{(3)}(k_c,i_s,j_s) = ssc, \\
&\mathbf{H}^{(3)}(i_c,j_c,k_c) = ccc, \ \ i,j,k = 1,\ldots,N_H, \ \ m,n = 1,\ldots,2N_H+1, \\
&i_c = i+1, \ \ j_c = j+1, \ \ k_c = k+1, \ \ i_s = i_c + N_H, \ \ j_s = j_c + N_H, \\
&\delta(n) = 1, \text{ if } n = 0; \quad \delta(n) = 0, \text{ if } n \neq 0.
\end{aligned}
\tag{2}
$$

For convenience in numerical implementation, sample codes written in MATLAB are given as follows:

```
% Matlab code for H0, H1, H2 and H3 in Eq. (2.18)
H0 = -diag([0:NH 1:NH].^2)/2;
H1 = (diag(0:NH,NH)-diag(0:NH,-NH))/2;
H2 = eye(2*NH+1)/2; H2(1) = 1;
H3 = zeros(2*NH+1, 2*NH+1, 2*NH+1);
H3(1,:,:) = H2; H3(:,1,:) = H2; H3(:,:,1) = H2;
for i=1:NH
    for j=1:NH
        for k=1:NH
            ccc = sum([i-j+k i-j-k i+j-k i+j+k]==0)/4;
            ssc = sum([i-j+k i-j-k]==0))/4;
            ssc = ssc - sum([i+j-k i+j+k]==0)/4;
            H3(i+1,j+1,k+1) = ccc;
            H3(i+NH+1,j+NH+1,k+1) = ssc;
            H3(i+NH+1,k+1,j+NH+1) = ssc;
            H3(k+1,i+NH+1,j+NH+1) = ssc;
        end
    end
end
```

A.2 Global implementation

In a global implementation of Eq. (2.19), the frequency-domain quantities ($\overline{\mathbf{M}}$, $\overline{\mathbf{C}}$, $\overline{\mathbf{g}}$, $\overline{\mathbf{f}}$ and $\overline{\mathbf{K}}_T$) can be constructed in MATLAB by using "`kron`" and "`reshape`" as follows:

```
% Matlab code for augmentation procedure
% nterm: the number of harmonic terms
% ndofs: the number of degrees of freedom
% neqn: the number of equations
nterm = 2*NH+1; neqn = nterm*ndofs;
Mbar = kron(M,H0); Cbar = kron(C,H1);
% fg is Fourier transform of internal force g
gbar = reshape(H2*reshape(fg,nterm,ndofs),neqn,1);
% ff is Fourier transform of external force f
fbar = reshape(H2*reshape(ff,nterm,ndofs),neqn,1);
Ktbar = zeros(neqn,neqn);
for k=1:nterm
    % fKt is Fourier transform of tangent stiffness Kt
    Ktbar = Ktbar + kron(fKt(:,:,k),H3(:,:,k);
end
```

A.3 Element-wise implementation

For the element-wise implementation of Eq. (2.19) in conjunction with the alternating frequency/time domain method, some sample codes written in MATLAB are given as follows:

```
% NH: the highest order of retained harmonics
% NT: the number of time points
% nedof: the number of DOFs in one element
% nelem: the number of elements
% Qbar: global vector of Fourier coefficients
% edof: the DOFs of one element with the size (1—by—nedof)
% eharm: the harmonics of one element corresponding to edof
NT = 1024; nterm = 2*NH+1; nedof = 8; % Q4 element
for e = 1:nelem
    edof = edofMat(e,1:nedof);
    eharm = zeros(1, nedof*nterm);
    for i=1:nedof
        ih = (i—1)*nterm+(1:nterm);
        eharm(1,ih) = (edof(i)—1)*nterm+(1:nterm)
    end
    Qebar = Qbar(eharm,1);
    Qet = Wifft*Qebar; % Qet = ifftsub(Qe, ntime);
    Ket = zeros(NT, nedof*nedof); get = zeros(NT, nedof)
    for time = 1:NT
        [Ket(time, :), get(time, :)] = FE(Qet(time,:));
    end
    fKe = Wfft * ket; % fKe = fftsub(ket, nharm);
    fge = Wfft * get; % fge = fftsub(get, nharm);
    % mapping relation
    for i=1:nedof
        ih = (i—1)*nterm+(1:nterm);
        gebar(ih,1) =gebar(ih,1) + H2*fge(:,i);
        for j=1:nedof
            jh = (j—1)*nterm+(1:nterm);
            Mebar(ih,jh) = Mebar(ih,jh) + H0*Me(i,j);
            Cebar(ih,jh) = Cebar(ih,jh) + H1*Ce(i,j);
            for k=1:nterm
                ij = (j—1)*nedof+i;
                Kebar(ih,jh) = Kebar(ih,jh) + H3(:,:,k)*fKe(k,ij);
            end
        end
    end
    % assemble
    Mbar(eharm,eharm) = Mbar(eharm,eharm) + Mebar;
    Cbar(eharm,eharm) = Cbar(eharm,eharm) + Cebar;
    Kbar(eharm,eharm) = Kbar(eharm,eharm) + Kebar;
    Gbar(eharm,1) = Gbar(eharm,1) + gebar;
end
```

Publication [P1]

Optimization of nonlinear structural resonance using the incremental harmonic balance method

Journal of Sound and Vibration 334 (2015) 239–254

Contents lists available at ScienceDirect

Journal of Sound and Vibration

journal homepage: www.elsevier.com/locate/jsvi

Optimization of nonlinear structural resonance using the incremental harmonic balance method

Suguang Dou [a,*], Jakob Søndergaard Jensen [a,b]

[a] Department of Mechanical Engineering, Technical University of Denmark, 2800 Kgs. Lyngby, Denmark
[b] Department of Electrical Engineering, Technical University of Denmark, 2800 Kgs. Lyngby, Denmark

ARTICLE INFO

Article history:
Received 5 August 2013
Received in revised form
1 July 2014
Accepted 20 August 2014
Handling Editor: K. Worden
Available online 3 October 2014

ABSTRACT

We present an optimization procedure for tailoring the nonlinear structural resonant response with time-harmonic loads. A nonlinear finite element method is used for modeling beam structures with a geometric nonlinearity and the incremental harmonic balance method is applied for accurate nonlinear vibration analysis. An optimization procedure based on a gradient-based algorithm is developed and we use the adjoint method for efficient computation of design sensitivities. We consider several examples in which we find optimized beam width distributions that minimize or maximize fundamental or super-harmonic resonant responses.

1. Introduction

Nonlinear structural vibrations have drawn increasing attention in fields of energy harvesting devices and vibration-based microelectromechanical systems (MEMS). Rhoads et al. gave a comprehensive review of the application of nonlinear dynamics in Micro- and Nanoresonators concerning theoretical and experimental investigations of modeling, analysis and optimization [1]. A well known phenomenon in nonlinear vibration is the hardening and softening nonlinear effects [2,3]. Midplane stretching of a clamped–clamped beam, for example, results in a hardening nonlinearity that shifts the resonance frequency towards higher values for vibrations with higher amplitude. On one hand, this can undermine the performance of MEMS resonators serving as frequency references and demanding low acceleration sensitivity [4,5]. On the other hand, it can be utilized to develop ultra-wide bandwidth piezoelectric energy harvesting devices [6]. In both cases, incorporating nonlinear effects is an essential part in the design optimization of such structures.

For the computation of the steady-state response of nonlinear structural vibration, the principle of harmonic balance is widely used to develop efficient methods. Lau and Cheung proposed the incremental harmonic balance (IHB) method [7]. Chen et al. combined the IHB and finite element methods to analyze nonlinear vibrations of plane structures [8] whereas Lewandowski presented a general formulation for computing steady-state vibrations of geometrically nonlinear structures by using a harmonic balance and finite element method [9–11]. The classical IHB method is suitable for structural vibration with polynomial nonlinearity, whereas for structural vibration with a more complex nonlinearity, the alternating frequency/time (AFT) domain method proposed by Cameron and Griffin [12] is widely used. The AFT method takes advantage of the

* Corresponding author.
E-mail addresses: sudou@mek.dtu.dk (S. Dou), json@elektro.dtu.dk (J.S. Jensen).

http://dx.doi.org/10.1016/j.jsv.2014.08.023
0022-460X/

convenience of evaluating nonlinear terms in the time domain. Maple et al. proposed an adaptive harmonic balance method for nonlinear time-periodic flows which results in a significant reduction in computational costs [13].

It is well known that harmonic balance methods can be combined with arc-length methods for path following [14–16]. Didier et al. summarized three predictors and three correctors for path following [17]. Beside the arc-length method, Leung and Fung proposed a phase increment method for path following of complicated frequency–amplitude curves [18,19], and Cochelin and Vergez proposed an asymptotic numerical method (ANM) for continuation [20]. Hall et al. presented a high dimensional harmonic balance (HDHB) method [21,22] where, instead of working in the frequency domain, the problem is cast into the time domain. Recently LaBryer and Attar presented a filtered HDHB method for large-scale problems in nonlinear structural dynamics [23] and Didier et al. proposed a stochastic multidimensional harmonic balance method (Stochastic-MHBM) for mechanical systems with non-regular nonlinearities and uncertainties [17]. The IHB method is adopted here because it is easy to implement for systems with quadratic and cubic nonlinearities and does not suffer from the aliasing problems that may occur using the AFT and HDHB methods.

In recent years, the principle of harmonic balance has been used on several occasions together with optimization procedures. Thothadri and Moon presented a nonlinear system identification method, which combined the principle of harmonic balance and bifurcation theory techniques to form a constrained optimization problem [24] and Ahmadian and Jalali used the incremental harmonic balance method and unconstrained optimization to identify nonlinear parameters for modeling bolted lap joints [25]. Coudeyras et al. proposed the constrained harmonic balance method together with finite element model to analyze the squeal of a brake system [26] whereas Liao and Sun used the principle of harmonic balance and the Hill method to form a constrained maximization problem for predicting the maximum vibration amplitude [27]. Here we apply the incremental harmonic balance method in conjunction with a shape optimization procedure to design geometrically nonlinear beam structures.

Shape optimization of beam structures has been considered by many researchers. Olhoff studied shape optimization of a thin, elastic beam with geometrically similar cross sections for maximizing higher order natural frequencies [28]. Olhoff and Parbery investigated shape optimization of vibrating beams and rotating shafts for maximizing the gap between two adjacent natural frequencies [29] and Bendsøe and Olhoff considered shape optimization of beams and rotating shafts for maximizing the distance from a given external excitation frequency or service speed to the nearest natural frequency in order to avoid resonance or whirling instability [30]. Meske et al. presented a new shape optimization method for natural frequency problems based on an optimality criterion, which is implemented in the optimization system TOSCA [31]. Olhoff et al. studied shape optimization of Bernoulli–Euler beams for maximizing the frequency gaps by using finite element method and gradient based optimization, and highlighted the associated periodicity and bandgaps of the optimized beam designs [32]. In the past years, shape optimization has also been a growing topic in the field of energy harvesting. Dietl and Garcia used optimization techniques to find the optimized shape of a beam with non-uniform width to improve the power output [33]. Wickenheiser demonstrated that beams with variable thickness lead to increased harvesting performance [34]. However, shape optimization of beam structures based on nonlinear vibrations with the focus on the nonlinear resonant response has to the authors' knowledge not been considered previously. In related work, Stanford et al. investigated shape optimization of a planar elastic rotating beam with geometric nonlinearities and time-periodic load by use of time marching method, spectral element method and finite difference method with/without model reduction based on proper orthogonal decomposition (POD) modes [35]. In further work, Stanford et al. optimized the stability and the peak power of nonlinear time-periodic flight and structural dynamics of flapping wing structures, where the wing is modeled as a geometrically nonlinear beam structure [36].

In the present paper we focus on developing an accurate and efficient method for optimization of nonlinear structural resonance with time-harmonic loads based on the finite element analysis and the incremental harmonic balance method. We apply the proposed methodology to optimize several featured problems in nonlinear structural vibrations. Firstly, we formulate an optimization problem for the minimum amplitude of nonlinear resonant vibrations valid in the case of synchronous forcing. Secondly, we demonstrate the effectiveness of the methodology in minimizing/maximizing the amplitude of super-harmonic resonances. For all problems, the sensitivities are efficiently computed by the adjoint method and the iterative updates of design variables are found with a gradient-based strategy using a mathematical programming tool [37].

2. Incremental harmonic balance method

We consider the nonlinear structural vibrations of beam structures. The beam is assumed to have a constant thickness t, but a variable width $b(x)$ that we optimize in order to tailor the nonlinear structural response. A schematic of the optimization problem is shown in Fig. 1.

2.1. Nonlinear finite element method

We begin with a geometrically nonlinear beam element with quadratic and cubic nonlinearities arising from midplane stretching [8]. Since our primary interest is to demonstrate the methodology for optimization, large deformations and

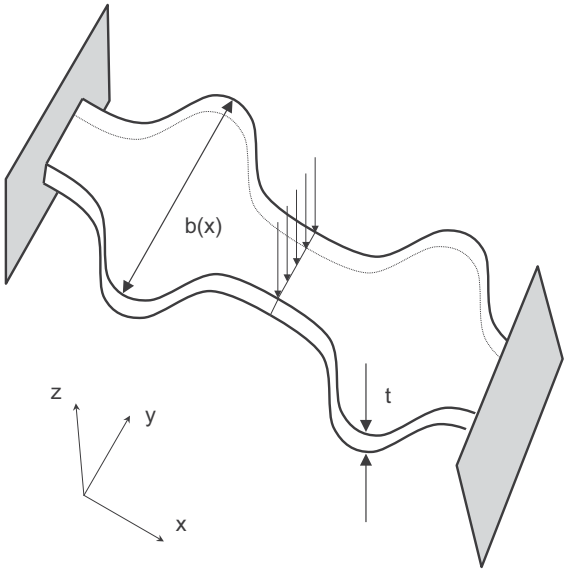

Fig. 1. Schematic diagram of a doubly clamped beam with constant thickness and non-uniform width.

rotation are not taken into account here. The displacement vector is defined as

$$\mathbf{u}(x,t) = [u(x,t)\ w(x,t)]^T \tag{1}$$

where $u(x,t)$ and $w(x,t)$ is the axial and the transverse displacement, respectively, and the axial strain ϵ_0 and curvature κ are defined as

$$\epsilon_0 = \frac{\partial u}{\partial x} + \frac{1}{2}\left(\frac{\partial w}{\partial x}\right)^2, \quad \kappa = \frac{\partial^2 w}{\partial x^2} \tag{2}$$

where the quadratic term in the axial strain represents the effect of the midplane stretching. The nonlinear strain–displacement relation can be expressed as

$$\epsilon = \epsilon_0 + z\kappa \tag{3}$$

where z is the distance of the material particle in the cross section from the midplane. Assume that the stress–strain relation is still linear as

$$\sigma = E\epsilon \tag{4}$$

where E is Young's modulus.

Using Eqs. (1)–(4) and ignoring rotational inertia, we obtain the kinetic energy T, the potential energy U and the work W done by external force and damping force as

$$\begin{aligned} T &= \sum_{e=1}^{N_e} \frac{1}{2}\int_{l_e} \rho A\left(\dot{u}^2 + \dot{w}^2\right)\,\mathrm{d}x \\ U &= \sum_{e=1}^{N_e} \frac{1}{2}\int_{l_e} EA\epsilon_0^2 + EI\kappa^2\,\mathrm{d}x \\ W &= \sum_{e=1}^{N_e} \int_{l_e} \mathbf{u}^T\mathbf{p} - \mu A\mathbf{u}^T\dot{\mathbf{u}}\,\mathrm{d}x \end{aligned} \tag{5}$$

where the external force vector is expressed as

$$\mathbf{p} = [f_u(x,t)\ f_w(x,t)]^T \tag{6}$$

and A is the cross-sectional area, I is the area moment of inertia, ρ is the mass density and μ is a viscous damping coefficient.

We now discretize the beam with a Galerkin finite element procedure by introducing the nodal displacement vectors $\mathbf{u}_e$, $\mathbf{w}_e$ and $\mathbf{q}_e$ associated with the finite element discretization as

$$u = \mathbf{N}^p\mathbf{u}_e, \quad w = \mathbf{N}^b\mathbf{w}_e, \quad \mathbf{u} = \mathbf{N}\mathbf{q}_e \tag{7}$$

where

$$\begin{aligned} &\mathbf{u}_e = [u_i\ u_j]^T, \quad \mathbf{w}_e = [w_i\ \theta_i\ w_j\ \theta_j]^T, \quad \mathbf{q}_e = [\mathbf{u}_e^T\ \mathbf{w}_e^T]^T \\ &\mathbf{N}^p = [N_1\ N_2], \quad \mathbf{N}^b = [N_3\ N_4\ N_5\ N_6], \quad \mathbf{N} = \begin{bmatrix} \mathbf{N}^p & \mathbf{0} \\ \mathbf{0} & \mathbf{N}^b \end{bmatrix} \end{aligned} \tag{8}$$

The shape functions are selected as

$$N_1 = 1-\xi, \quad N_2 = \xi, \quad \xi = x/l_e$$
$$N_3 = 1-3\xi^2+2\xi^3, \quad N_4 = l_e(\xi-2\xi^2+\xi^3)$$
$$N_5 = 3\xi^2-2\xi^3, \quad N_6 = l_e(\xi^3-\xi^2) \tag{9}$$

By substituting Eq. (7) into Eq. (5) and applying Hamilton's principle

$$\int_0^t \delta T - \delta U + \delta W \, \mathrm{d}t = 0, \tag{10}$$

we obtain the global equation of motion for the beam structure as

$$\mathbf{M}\ddot{\mathbf{q}} + \mathbf{C}\dot{\mathbf{q}} + \mathbf{g}(\mathbf{q}) = \mathbf{f} \tag{11}$$

where global matrices, $\mathbf{M}$ and $\mathbf{C}$, and vectors, $\mathbf{g}$ and $\mathbf{f}$, are assembled in the usual finite element way from the local element quantities, $\mathbf{M}_e$, $\mathbf{C}_e$, $\mathbf{g}_e$ and $\mathbf{f}_e$. The element mass matrix $\mathbf{M}_e$ and the damping matrix $\mathbf{C}_e$ are the same as for the linear problem; the element vector $\mathbf{g}_e$ represents the nonlinear elastic force and the vector $\mathbf{f}_e$ denotes the external force. Their specific forms are given as

$$\mathbf{M}_e = \rho A \int_0^{l_e} \mathbf{N}^T\mathbf{N} \, \mathrm{d}x, \quad \mathbf{C}_e = \mu A \int_0^{l_e} \mathbf{N}^T\mathbf{N} \, \mathrm{d}x, \quad \mathbf{f}_e = \int_0^{l_e} \mathbf{N}^T\mathbf{p} \, \mathrm{d}x$$
$$\mathbf{g}_e(\mathbf{q}_e) = \mathbf{K}_0\mathbf{q}_e + \mathbf{f}_{\mathrm{nl}}, \quad \mathbf{K}_0 = \begin{bmatrix} \mathbf{K}_u & \mathbf{0} \\ \mathbf{0} & \mathbf{K}_w \end{bmatrix}, \quad \mathbf{f}_{\mathrm{nl}} = \begin{bmatrix} \mathbf{f}_u(\mathbf{w}_e) \\ \mathbf{f}_w(\mathbf{u}_e, \mathbf{w}_e) \end{bmatrix}$$
$$\mathbf{K}_u = EA \int_0^{l_e} (\mathbf{B}_0^p)^T\mathbf{B}_0^p \, \mathrm{d}x, \quad \mathbf{K}_w = EI \int_0^{l_e} (\mathbf{B}_0^b)^T\mathbf{B}_0^b \, \mathrm{d}x$$
$$\mathbf{f}_u = EA \int_0^{l_e} \frac{1}{2}(\mathbf{B}_0^p)^T(\mathbf{G}\mathbf{w}_e)^2 \, \mathrm{d}x$$
$$\mathbf{f}_w = EA \int_0^{l_e} \mathbf{G}^T(\mathbf{G}\mathbf{w}_e)(\mathbf{B}_0^p\mathbf{u}_e) + \frac{1}{2}\mathbf{G}^T(\mathbf{G}\mathbf{w}_e)^3 \, \mathrm{d}x$$
$$\mathbf{B}_0^p = \frac{\partial \mathbf{N}^p}{\partial x}, \quad \mathbf{B}_0^b = \frac{\partial^2 \mathbf{N}^b}{\partial x^2}, \quad \mathbf{G} = \frac{\partial \mathbf{N}^b}{\partial x} \tag{12}$$

2.2. Incremental harmonic balance method

The derivations in the following can be found in the similar form in reference [8]. Here, we have reorganized the derivations and included details for completeness in combination with the forthcoming sensitivity analysis.

First we introduce a non-dimensional time scale $\tau = \omega t$ and rewrite the equation of motion (11) as

$$\omega^2\mathbf{M}\mathbf{q}'' + \omega\mathbf{C}\mathbf{q}' + \mathbf{g} = \mathbf{f} \tag{13}$$

where the prime ($'$) represents the differentiation with respect to τ.

The IHB method effectively combines a Newton–Raphson procedure with the harmonic balance approach. Most commonly the incremental procedure is applied before the Newton–Raphson procedure. However, in order to highlight the governing equation of the equilibrium state in the frequency domain, we apply the harmonic balance method first. The harmonic balance method starts with the assumption that the external loads and the dynamic response are periodic as

$$f_i = f_{i0} + \sum_{n=1}^{N_H} (f_{in}^c \cos(n\tau) + f_{in}^s \sin(n\tau)) = \mathbf{C}_S\mathcal{F}(f_i)$$
$$q_i = a_{i0} + \sum_{n=1}^{N_H} (a_{in} \cos(n\tau) + b_{in} \sin(n\tau)) = \mathbf{C}_S\mathcal{F}(q_i) \tag{14}$$

where

$$\mathbf{C}_S = [1 \ \cos\tau \ \ldots \ \cos(N_H\tau) \ \sin\tau \ \ldots \ \sin(N_H\tau)] \tag{15}$$

and $\mathcal{F}(\,)$ denotes the coefficient vector of the Fourier series projected on the basis of $\mathbf{C}_S$. For convenience and conciseness, the global displacement vector $\mathbf{q}$ is expressed as

$$\mathbf{q} = \mathbf{S}\overline{\mathbf{q}} \tag{16}$$

where $\overline{\mathbf{q}}$ collects all the coefficients a_{in} and b_{in} in the Fourier expansion, and

$$\mathbf{S} = \mathbf{diag}([\mathbf{C}_S \ \ldots \ \mathbf{C}_S]) \tag{17}$$

The essence of the harmonic balance method is to eliminate the time dimension and reform the differential equation into a set of algebraic equations. Substituting Eq. (14) into Eq. (13), and applying the principle of harmonic balance, one can

obtain a set of nonlinear equations with a_{in} and b_{in} as unknowns. A procedure in matrix format is obtained by substituting Eq. (16) into Eq. (13) and applying the Galerkin method using the left multiplication with $\mathbf{S}^T$ and integration from 0 to 2π. In this case, one can readily obtain a set of equations in matrix form as

$$\omega^2\overline{\mathbf{M}}\overline{\mathbf{q}}+\omega\overline{\mathbf{C}}\overline{\mathbf{q}}+\overline{\mathbf{g}}=\overline{\mathbf{f}} \tag{18}$$

This governing equation can be viewed as a frequency domain representation of the equation of motion in (11). The barred terms $\overline{\mathbf{M}}$, $\overline{\mathbf{C}}$, $\overline{\mathbf{g}}$ and $\overline{\mathbf{f}}$ are given as

$$\overline{\mathbf{M}}=\frac{1}{2\pi}\int_0^{2\pi}\mathbf{S}^T\mathbf{M}\mathbf{S}''\,\mathrm{d}\tau,\quad \overline{\mathbf{g}}=\frac{1}{2\pi}\int_0^{2\pi}\mathbf{S}^T\mathbf{g}\,\mathrm{d}\tau,$$
$$\overline{\mathbf{C}}=\frac{1}{2\pi}\int_0^{2\pi}\mathbf{S}^T\mathbf{C}\mathbf{S}'\,\mathrm{d}\tau,\quad \overline{\mathbf{f}}=\frac{1}{2\pi}\int_0^{2\pi}\mathbf{S}^T\mathbf{f}\,\mathrm{d}\tau \tag{19}$$

The second step of the incremental harmonic balance method is to obtain the incremental equation. Let $\mathbf{q}_0$ and ω_0 denote the amplitudes and the frequency of a known solution respectively. The state in the neighborhood of the known state can be expressed as

$$\mathbf{q}=\mathbf{q}_0+\Delta\mathbf{q},\quad \omega=\omega_0+\Delta\omega \tag{20}$$

Inserting Eq. (20) into Eq. (18) and collecting the first-order incremental terms, we obtain

$$\overline{\mathbf{K}}_{\overline{\mathbf{q}}}\Delta\overline{\mathbf{q}}+\overline{\mathbf{K}}_{\omega}\Delta\omega=\overline{\mathbf{r}} \tag{21}$$

in which

$$\overline{\mathbf{K}}_{\overline{\mathbf{q}}}=\omega_0^2\overline{\mathbf{M}}+\omega_0\overline{\mathbf{C}}+\overline{\mathbf{K}}_T$$
$$\overline{\mathbf{K}}_{\omega}=2\omega_0\overline{\mathbf{M}}\overline{\mathbf{q}}_0+\overline{\mathbf{C}}\overline{\mathbf{q}}_0$$
$$\overline{\mathbf{r}}=\overline{\mathbf{f}}-\omega_0^2\overline{\mathbf{M}}\overline{\mathbf{q}}_0-\omega_0\overline{\mathbf{C}}\overline{\mathbf{q}}_0-\overline{\mathbf{g}} \tag{22}$$

The barred terms $\overline{\mathbf{K}}_T$ are obtained by integration from 0 to 2π and recalling Eq. (16) as

$$\overline{\mathbf{K}}_T=\frac{1}{2\pi}\int_0^{2\pi}\mathbf{S}^T\frac{\partial\mathbf{g}}{\partial\mathbf{q}}\frac{\partial\mathbf{q}}{\partial\overline{\mathbf{q}}}\,\mathrm{d}\tau=\frac{1}{2\pi}\int_0^{2\pi}\mathbf{S}^T\mathbf{K}_T\mathbf{S}\,\mathrm{d}\tau \tag{23}$$

It is noted that the matrix $\mathbf{K}_T$ represents the tangent stiffness matrix, and $\overline{\mathbf{K}}_T$ denotes its counterpart in the frequency domain.

2.3. Numerical implementation

In the finite element formulation, the shape functions for the stretching and bending contributions are not consistent for ϵ_0 in Eq. (2), and this causes a locking problem and an unphysical hardening nonlinearity. To overcome this problem, an average approximation of the axial strain is used [8]. Introduce a constant matrix as

$$\mathbf{K}_g=\int_0^{l_e}\mathbf{G}^T\mathbf{G}\,\mathrm{d}x, \tag{24}$$

where $\mathbf{G}$ is defined in Eq. (12). Then the average value of the axial strain in one beam element is constant as

$$\epsilon_0=\mathbf{B}_0^p\mathbf{u}_e+\frac{1}{2l_e}\mathbf{w}_e^T\mathbf{K}_g\mathbf{w}_e \tag{25}$$

The nonlinear internal forces in Eq. (12) are re-expressed as

$$\mathbf{f}_u=\frac{1}{2}EA(\mathbf{B}_0^p)^T\mathbf{w}_e^T\mathbf{K}_g\mathbf{w}_e$$
$$\mathbf{f}_w=EA\left(\mathbf{B}_0^p\mathbf{u}_e+\frac{1}{2l_e}\mathbf{w}_e^T\mathbf{K}_g\mathbf{w}_e\right)\mathbf{K}_g\mathbf{w}_e=T_0\mathbf{K}_g\mathbf{w}_e \tag{26}$$

where T_0 is the average value of axial force. The specific form of the tangent stiffness matrix $\mathbf{K}_T$ is written in three parts as

$$\mathbf{K}_T=\mathbf{K}_0+\mathbf{K}_L+\mathbf{K}_\sigma \tag{27}$$

where

$$\mathbf{K}_L=\begin{bmatrix}\mathbf{0} & \mathbf{K}_{uw}\\ \mathbf{K}_{wu} & \mathbf{K}_{ww}\end{bmatrix},\quad \mathbf{K}_\sigma=\begin{bmatrix}\mathbf{0} & \mathbf{0}\\ \mathbf{0} & \mathbf{K}_\sigma^b\end{bmatrix}$$
$$\mathbf{K}_{uw}=EA(\mathbf{B}_0^p)^T\mathbf{w}_e^T\mathbf{K}_g,\quad \mathbf{K}_{wu}=\mathbf{K}_{uw}^T$$
$$\mathbf{K}_{ww}=\frac{EA}{l_e}\mathbf{K}_g\mathbf{w}_e\mathbf{w}_e^T\mathbf{K}_g$$

$$\mathbf{K}_\sigma^b = EA\left(\mathbf{B}_0^p\mathbf{u}_e + \frac{1}{2l_e}\mathbf{w}_e^T\mathbf{K}_g\mathbf{w}_e\right)\mathbf{K}_g = T_0\mathbf{K}_g \tag{28}$$

Note that $\mathbf{K}_T$ is symmetric. Symbolic calculations are done for Eqs. (26) and (28), and the coefficients of quadratic and cubic terms are automatically extracted.

To perform the integration in Eqs. (19) and (23) it can be exploited that following matrices can be analytically precomputed:

$$\begin{gathered}
\mathbf{H}^{(0)} = \frac{1}{2\pi}\int_0^{2\pi}\mathbf{C}_S^T\mathbf{C}_S''\,\mathrm{d}\tau = \frac{1}{2}\,\mathbf{diag}\left(\left[0\ -1\ \cdots\ -N_H^2\ -1\ \cdots\ -N_H^2\right]\right)\\
\mathbf{H}^{(1)} = \frac{1}{2\pi}\int_0^{2\pi}\mathbf{C}_S^T\mathbf{C}_S'\,\mathrm{d}\tau = \begin{bmatrix}0 & \mathbf{0} & \mathbf{0}\\ \mathbf{0} & \mathbf{0} & \mathbf{c}\\ \mathbf{0} & -\mathbf{c} & \mathbf{0}\end{bmatrix},\quad \mathbf{c} = \frac{1}{2}\,\mathbf{diag}([1\ \cdots\ N_H])\\
\mathbf{H}^{(2)} = \frac{1}{2\pi}\int_0^{2\pi}\mathbf{C}_S^T\mathbf{C}_S\,\mathrm{d}\tau = \frac{1}{2}\,\mathbf{diag}([2\ 1\ \cdots\ 1\ 1\ \cdots\ 1])\\
\mathbf{H}^{(3)}(m,n,k) = \frac{1}{2\pi}\int_0^{2\pi}\mathbf{C}_S(m)\mathbf{C}_S(n)\mathbf{C}_S(k)\,\mathrm{d}\tau,\\
m,n,k = 1,2,\ldots,2N_H+1
\end{gathered} \tag{29}$$

with the components of $\mathbf{H}^{(3)}$ expressed as

$$\begin{gathered}
\mathbf{H}^{(3)}(1,m,n) = \mathbf{H}^{(3)}(m,1,n) = \mathbf{H}^{(3)}(m,n,1) = \mathbf{H}^{(2)}(m,n),\\
ccc = \frac{1}{4}\left[\delta(i-j+k)+\delta(i-j-k)+\delta(i+j+k)+\delta(i+j-k)\right],\\
ssc = \frac{1}{4}\left[\delta(i-j+k)+\delta(i-j-k)-\delta(i+j+k)-\delta(i+j-k)\right],\\
\mathbf{H}^{(3)}(i_s,j_s,k_c) = \mathbf{H}^{(3)}(i_s,k_c,j_s) = \mathbf{H}^{(3)}(k_c,i_s,j_s) = ssc,\\
\mathbf{H}^{(3)}(i_c,j_c,k_c) = ccc,\quad i,j,k = 1,\ldots,N_H,\quad m,n = 1,\ldots,2N_H+1,\\
i_c = i+1,\quad j_c = j+1,\quad k_c = k+1,\quad i_s = i_c+N_H,\quad j_s = j_c+N_H,\\
\delta(n) = 1,\quad \text{if } n = 0;\quad \delta(n) = 0,\quad \text{if } n \neq 0.
\end{gathered} \tag{30}$$

which saves considerable computational time when performing the iterative analysis. The barred terms in Eqs. (19) and (23) are calculated by using the precomputed matrices as

$$\begin{gathered}
\mathbf{M}(i,j)\longrightarrow\mathbf{M}(i,j)\mathbf{H}^{(0)},\quad \mathbf{C}(i,j)\longrightarrow\mathbf{C}(i,j)\mathbf{H}^{(1)}\\
\mathbf{g}(i)\longrightarrow\mathbf{H}^{(2)}\mathcal{F}(\mathbf{g}(i)),\quad \mathbf{f}(i)\longrightarrow\mathbf{H}^{(2)}\mathcal{F}(\mathbf{f}(i))\\
\mathbf{K}_T(\mathbf{q})(i,j)\longrightarrow\mathbf{H}^{(3)}\ \odot\ \mathcal{F}(\mathbf{K}_T(\mathbf{q})(i,j))
\end{gathered} \tag{31}$$

where the arrow "$\longrightarrow$" represents a map from one entry in the matrix to one block in the augmented matrix, and "$\odot$" represents the dot multiplication of the third dimension of the $\mathbf{H}^{(3)}$ with the vector $\mathcal{F}(\mathbf{K}_T(\mathbf{q})(i,j))$, and yields a two-dimensional matrix.

As for the problem size, the total number of unknown variables equals the product of N_{DOF}, the degrees of freedom of the finite element model, and $(2N_H+1)$, the number of harmonic terms used for each degree of freedom. If the finite element matrices have a band structure, the augmented matrices are sparse matrices with band structure and the bandwidth is $(2N_H+1)$ times that of the finite element matrices. Since only a few iterations are required to find the dynamic equilibrium, it is faster than the time marching method.

2.4. Numerical solution techniques

We adapt the incremental Eq. (21) in several ways to solve Eq. (18). Of primary interest is the frequency-response curve which is reflected in the choice of specifying the increments in the frequency–amplitude space in Eq. (20). For very weakly nonlinear problems and non-resonant states we can apply a simple frequency-increment scheme where $\Delta\omega$ is specified and Eq. (21) is solved for amplitude increments $\Delta\overline{\mathbf{q}}$. However for general path following of the frequency–amplitude curve this technique is not sufficient.

2.4.1. The arc-length method

Here, the arc-length of the frequency–amplitude curve is increased incrementally and terminated when the solution is outside a prescribed region. In Eq. (21), both the frequency increment and amplitude increments are treated as unknowns $\Delta\mathbf{X} = [\Delta\overline{\mathbf{q}}^T\ \Delta\omega]^T$, and a constraint is imposed so as to determine the solution. The arc-length constraint employed is

$$\beta\left(\frac{\omega-\omega_0}{\omega_0}\right)^2 + \left(\frac{\|\,\overline{\mathbf{q}}-\overline{\mathbf{q}}_0\,\|}{\|\,\overline{\mathbf{q}}_0\,\|}\right)^2 = (\Delta s)^2 \tag{32}$$

where β is 1 in the current algorithm. This can be viewed a corrector step. In the predictor step, the cubic extrapolation is used [14]. It should be noted that the predictor can also use the normalization procedure in Eq. (32). Step control is very important for developing a robust and efficient method. The step size is decided according to the ratio between the desirable number N^* and the previous number N_{k-1} of iterations [38] so as $s_{k+1} = N^*/N_k \times s_k$. In practice, the ratio $r = N^*/N_k$ is bounded to achieve smooth change of step size [39]. For small-scale equations, $N^* = 3$ is a desirable value. For large-scale equations, N^* should be larger. A maximum number of iterations $N_{\max}$ is used to make the code robust and efficient. However, the iteration may fail to converge, if the matrix becomes singular and the residual then increases drastically. Besides, the solution may jump to another branch, which can be identified through the length of real step size and the angle between consecutive predictor steps. In cases of no convergence and jumping, the step size is halved until convergence is achieved. The convergence criteria for the arc-length method are $\|\Delta\mathbf{X}\| < \epsilon_{\mathbf{X}}\|\Delta\mathbf{X}_0\|$ and $\|\overline{\mathbf{r}}\| < \epsilon_{\overline{\mathbf{r}}}\|\overline{\mathbf{f}}\|$.

2.4.2. Resonance peak analysis

In order to optimize the peak of primary resonance, a simple criterion is required to identify the peak. In previous work, Petrov defined the resonance peak as the local maximum point with $\partial a/\partial\omega = 0$, where $a = \frac{1}{2}\sqrt{a_{in}^2 + b_{in}^2}$, i and n denote the ith degree of freedom and the nth harmonic, respectively [40]. Likewise, the folding point with $\partial\omega/\partial a = 0$ may also be tracked and optimized. In both schemes, second-order sensitivity analysis is required in optimization. Here in the case of synchronous forcing, we track the resonance peak by using the point whose displacement response has 90° phase lag relative to the harmonic loads, which only requires the first-order sensitivity analysis in optimization. So in addition to the arc-length method we also apply a specialized scheme for resonance peak analysis. For this scheme we increase the external load $\overline{\mathbf{f}}$ in incremental steps with one Fourier coefficient $\overline{\mathbf{q}}(i)$ and its corresponding increment $\Delta\overline{\mathbf{q}}(i)$ constantly fixed to zero in Eq. (21). The load starts from a small value and the initial guess is obtained using least square method or Moore–Penrose pseudo-inverse method with $\omega = \omega_i$ and $\Delta\omega = 0$. For each load increment, the corresponding frequency increment $\Delta\omega$ and the other Fourier coefficient increments $\Delta\overline{\mathbf{q}}(j)$ with $j \neq i$ are then solved iteratively. This provides an efficient way to evaluate the peak of the primary resonance. This scheme provides an efficient way to evaluate the peak of the primary resonance and will be further outlined in the following section.

2.5. Nonlinear vibrations of a uniform beam

In the following a beam with uniform width will be analyzed. This will also be the reference beam used in the optimization procedure. The parameters of this beam are $b = 30$ mm, $h = 10$ mm, $E = 2.05 \times 10^5$ MPa, $\rho = 7.8 \times 10^{-9}$ tonne/mm^3, $A = bh$, $I = (bh^3)/12$, $r = \sqrt{I/A}$, $L = 150r$. The damping model is introduced in Eq. (5) and leads to a damping matrix proportional to the mass matrix, i.e. $\mathbf{C} = \alpha\mathbf{M}$, with $\alpha = \mu/\rho$. Assuming $\alpha = 2\xi\omega_1$, then the damping coefficient μ is given by $\mu = 2\rho\xi\omega_1$, where ω_1 is the first eigenvalue of the initial design of a doubly clamped beam and the damping ratio ξ is chosen as 0.004. Note that r is the radius of gyration of the cross section area and the amplitudes in the following results are scaled with $1/r$. Two load cases are considered including weak excitation with $f = 15EIr/L^3$ and a higher excitation level with $f = 200EIr/L^3$. The location and the direction of the excitation force are shown in Fig. 1.

Here the beam is discretized with 100 elements and up to sixth-order harmonics are used in the Fourier expansion. The primary resonance of this beam with doubly clamped boundary condition is shown in Fig. 2. Weak excitation with $f = 15EIr/L^3$ is used and the frequency–amplitude curve is computed using frequency increments as initial steps and the arc-length method as the path-following steps. As seen in the figure, the nonlinear response includes a shift of the resonance frequency, folding of the response curve, jumping phenomena and multiple solutions. The peak of the resonance shifts

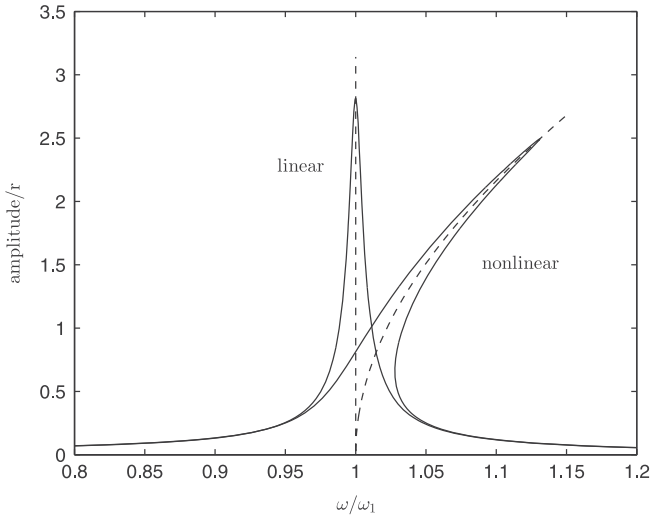

Fig. 2. Forced vibration of a doubly clamped beam around the first natural frequency ω_1. Solid lines denote the frequency–amplitude curves for forced vibration. Dashed lines denote the backbone computed with the phase lag quadrature criterion.

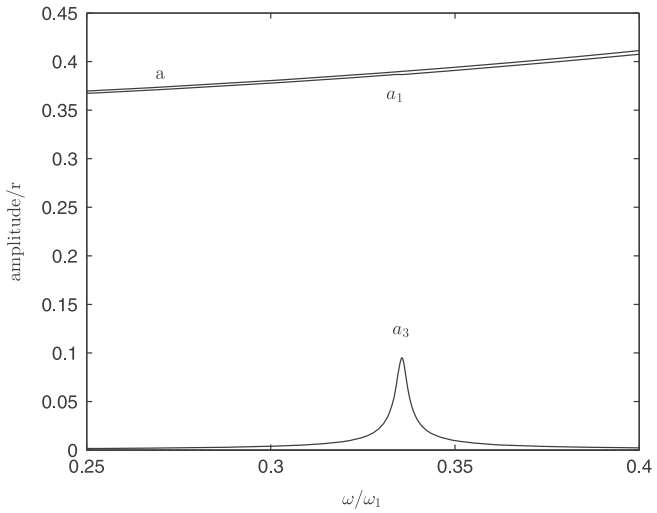

Fig. 3. Superharmonic resonance of a doubly clamped beam near $\omega_1/3$. a denotes the amplitude of the fundamental harmonic in linear vibration. a_1 and a_3 denote the amplitudes of the first-order and third-order harmonics in nonlinear vibration respectively.

towards higher frequencies, which represents hardening nonlinearity. In certain frequency ranges there are three solutions for one specific frequency. The top and bottom branches are stable, and the middle branch is unstable. So when the frequency sweeps upwards, the solution jumps to the bottom branch at the peak of the resonance. When the frequency sweeps downwards, the solution jumps to the top branch at the folding point. These are all well known phenomena which emphasize the need for an efficient and robust method to predict and subsequently optimize the resonance peak in nonlinear vibration.

In the following we outline a simple and efficient method to predict the peak of the resonance based on the backbone of the primary resonance shown in Fig. 2. The backbone is obtained by path following of the resonant state with a phase lag of 90° in the fundamental harmonic relative to the external excitation. This idea originates in the phase-lag quadrature criterion: for a structure with well separated modes, when it vibrates close to the peak of primary resonance, the periodic response of displacement crosses a phase lag of 90° with respect to the excitation. Peeters and Kerschen et al. have theoretically and experimentally demonstrated that the phase-lag quadrature criterion used in linear vibration can be generalized to nonlinear vibrations [41,42]. A physical interpretation is that the external load compensates for the damping force. For nonlinear vibrations, the phase-lag criterion can be defined for each harmonic and when the periodic load is written as a sine series

$$f_i = \sum_{n=1}^{N_H} f_{in}^s \ \sin(n\tau) \tag{33}$$

the nonlinear response fulfilling the phase lag quadrature criterion is

$$q_i = \sum_{n=1}^{N_H} a_{in} \ \cos(n\tau) \tag{34}$$

In this case, all the coefficients b_{in} of sine terms become zero. In our analysis, only b_{i1} of the fundamental harmonic is zero, i.e.

$$b_{i1} = 0 \tag{35}$$

and the increments of the other Fourier coefficients and the frequency are found by the incremental scheme. Note that the assumption that the phase lag between displacements and excitation is 90° at the resonance is valid only in the case when all forces are synchronous.

The superharmonic resonance of this beam with doubly clamped boundary conditions is shown in Fig. 3 with higher excitation level ($f = 200EIr/L^3$) used to induce the superharmonic resonance. For linear vibrations, there is only one fundamental harmonic whereas in the nonlinear case there are multiple harmonics. It is seen clearly that the amplitude of the third harmonic is resonantly excited and we refer to this as a superharmonic resonance. In the following part, we also propose an optimization scheme to optimize the amplitude of the superharmonic resonance.

3. Optimization problem

Our optimization problem is to minimize (or alternatively maximize) the response amplitude for primary and superharmonic resonances by optimizing the width distribution of the beam. The optimization problems for primary and superharmonic resonances are formulated in slightly different ways as follows.

3.1. Optimization of primary resonance

Based on the phase-lag quadrature criterion and by assuming that the external excitation is a pure sine function, a specific formulation for minimizing the amplitude of the peak of primary resonance is written as

$$\begin{aligned} \min_{\rho_e} \quad & c = \overline{\mathbf{q}}^T \mathbf{L} \overline{\mathbf{q}} \\ \text{s.t.} \quad & b_{i1} = 0, \\ & \omega^2 \overline{\mathbf{M}} \overline{\mathbf{q}} + \omega \overline{\mathbf{C}} \overline{\mathbf{q}} + \overline{\mathbf{g}} = \overline{\mathbf{f}}, \\ & \sum_{e=1}^{N_e} b_e \le \alpha N_e b_{\max}, \\ & b_e = b_{\min} + \rho_e (b_{\max} - b_{\min}), \\ & 0 \le \rho_e \le 1. \end{aligned} \tag{36}$$

where $\mathbf{L}$ is a diagonal matrix with unit entries that define which components of $\overline{\mathbf{q}}$ that are considered, ρ_e $(e = 1, \ldots, N_e)$ are the design variables that are used to control the width of each beam element b_e, and α defines a volume constraint by specifying a maximum allowable design volume fraction of the total admissible design domain $N_e b_{\max}$ (where the constant beam thickness t has been omitted in the formulas). As we will explain in the subsequent examples it makes sense to specify a minimum volume for some optimization problems.

With ω determined from the phase-lag quadrature criterion we need to modify the general equations slightly. We write governing equation of the peak of the primary resonance as

$$\omega^2 \overline{\overline{\mathbf{M}}}\, \overline{\overline{\mathbf{q}}} + \omega \overline{\overline{\mathbf{C}}}\, \overline{\overline{\mathbf{q}}} + \overline{\overline{\mathbf{g}}} = \overline{\overline{\mathbf{f}}} - (\omega^2 \overline{\mathbf{M}}_j \overline{\mathbf{q}}_j + \omega \overline{\mathbf{C}}_j \overline{\mathbf{q}}_j) \tag{37}$$

where $\overline{\overline{\mathbf{M}}}$ is the same as $\overline{\mathbf{M}}$ except that the jth column $\overline{\mathbf{M}}_j$ is taken out, $\overline{\overline{\mathbf{C}}}$ is the same as $\overline{\mathbf{C}}$ except that the jth column $\overline{\mathbf{C}}_j$ is taken out, $\overline{\overline{\mathbf{q}}}$ is the same as $\overline{\mathbf{q}}$ except that the jth component $\overline{\mathbf{q}}_j$ is taken out, and $\overline{\mathbf{q}}_j = b_{i1} = 0$. The incremental form used in the computation is

$$(\omega^2 \overline{\overline{\mathbf{M}}} + \omega \overline{\overline{\mathbf{C}}} + \overline{\overline{\mathbf{K}}}_T) \Delta \overline{\overline{\mathbf{q}}} + (2\omega \overline{\mathbf{M}} \overline{\mathbf{q}} + \overline{\mathbf{C}} \overline{\mathbf{q}}) \Delta \omega = \overline{\overline{\mathbf{f}}} - (\omega^2 \overline{\mathbf{M}} \overline{\mathbf{q}} + \omega \overline{\mathbf{C}} \overline{\mathbf{q}} + \overline{\mathbf{g}}) \tag{38}$$

where $\overline{\overline{\mathbf{K}}}_T$ is the same as $\overline{\mathbf{K}}_T$ except that the jth column is taken out. The sensitivity of $\overline{\overline{\mathbf{q}}}$ with respect to ρ_e can be found through

$$\left[\omega^2 \overline{\overline{\mathbf{M}}} + \omega \overline{\overline{\mathbf{C}}} + \overline{\overline{\mathbf{K}}}_T \;\; 2\omega \overline{\mathbf{M}} \overline{\mathbf{q}} + \overline{\mathbf{C}} \overline{\mathbf{q}} \right] \begin{bmatrix} \frac{\mathrm{d}\overline{\overline{\mathbf{q}}}}{\mathrm{d}\rho_e} \\ \frac{\mathrm{d}\omega}{\mathrm{d}\rho_e} \end{bmatrix} = - \left(\omega^2 \frac{\partial \overline{\mathbf{M}}}{\partial \rho_e} \overline{\mathbf{q}} + \omega \frac{\partial \overline{\mathbf{C}}}{\partial \rho_e} \overline{\mathbf{q}} + \frac{\partial \overline{\mathbf{g}}}{\partial \rho_e} \right) \tag{39}$$

and the sensitivity of c with respect to ρ_e can then be expressed as

$$\frac{\mathrm{d}c}{\mathrm{d}\rho_e} = 2\boldsymbol{\lambda}^T \left(\omega^2 \frac{\partial \overline{\mathbf{M}}}{\partial \rho_e} \overline{\mathbf{q}} + \omega \frac{\partial \overline{\mathbf{C}}}{\partial \rho_e} \overline{\mathbf{q}} + \frac{\partial \overline{\mathbf{g}}}{\partial \rho_e} \right) \tag{40}$$

with the following adjoint equation:

$$[\omega^2 \overline{\overline{\mathbf{M}}} + \omega \overline{\overline{\mathbf{C}}} + \overline{\overline{\mathbf{K}}}_T \;\; 2\omega \overline{\mathbf{M}} \overline{\mathbf{q}} + \overline{\mathbf{C}} \overline{\mathbf{q}}]^T \boldsymbol{\lambda} = -\mathbf{L}_1 [\overline{\overline{\mathbf{q}}}^T \;\; \omega]^T \tag{41}$$

where $\mathbf{L}_1$ is defined so as $\overline{\mathbf{q}}^T \mathbf{L} \overline{\mathbf{q}} = [\overline{\overline{\mathbf{q}}}^T \;\; \omega] \mathbf{L}_1 [\overline{\overline{\mathbf{q}}}^T \;\; \omega]^T$.

3.2. Optimization of superharmonic resonance

In optimization of superharmonic resonances, we find that it is effective to optimize the resonance peak by controlling the responses at $\omega = \gamma \omega_i$, where ω_i is the ith eigenvalue, γ is a selected constant value that corresponds to superharmonic resonances. The optimization problem is now formulated as

$$\begin{aligned} \min_{\rho_e} \quad & c = \overline{\mathbf{q}}^T \mathbf{L} \overline{\mathbf{q}} \\ \text{s.t.} \quad & \omega = \gamma \omega_i \end{aligned} \tag{42}$$

subjected also to the additional constraints from Eq. (36) (except $b_{i1} = 0$).

The sensitivity of the objective function w.r.t. our design variables can be derived through direct differentiation or an adjoint approach using Lagrange multipliers. For an efficient implementation with a large number of design variables we adhere to the latter approach and rewrite the objective function with a Lagrange multiplier as

$$c = \overline{\mathbf{q}}^T \mathbf{L} \overline{\mathbf{q}} + 2\boldsymbol{\lambda}^T (\omega^2 \overline{\mathbf{M}} \overline{\mathbf{q}} + \omega \overline{\mathbf{C}} \overline{\mathbf{q}} + \overline{\mathbf{g}}) \tag{43}$$

Note that the Lagrange multiplier can take an arbitrary value. The sensitivity of c with respect to ρ_e can now be written as

$$\frac{\mathrm{d}c}{\mathrm{d}\rho_e}=2\overline{\mathbf{q}}^T\mathbf{L}\,\frac{\mathrm{d}\overline{\mathbf{q}}}{\mathrm{d}\rho_e}+2\boldsymbol{\lambda}^T\begin{bmatrix}\omega^2\frac{\partial\overline{\mathbf{M}}}{\partial\rho_e}\overline{\mathbf{q}}+\omega\frac{\partial\overline{\mathbf{C}}}{\partial\rho_e}\overline{\mathbf{q}}+\frac{\partial\overline{\mathbf{g}}}{\partial\rho_e}\\ +\left(\omega^2\overline{\mathbf{M}}+\omega\overline{\mathbf{C}}+\overline{\mathbf{K}}_T\right)\frac{\mathrm{d}\overline{\mathbf{q}}}{\mathrm{d}\rho_e}\\ +\left(2\omega\overline{\mathbf{M}}\overline{\mathbf{q}}+\overline{\mathbf{C}}\overline{\mathbf{q}}\right)\frac{\mathrm{d}\omega}{\mathrm{d}\rho_e}\end{bmatrix} \tag{44}$$

where it should be noted that we include the excitation frequency ω, which generally is design dependent since ω_i changes with the design. Since it is computationally expensive to compute the term $\mathrm{d}\overline{\mathbf{q}}/\mathrm{d}\rho_e$, the value of $\boldsymbol{\lambda}$ is chosen in a way so as to eliminate $\mathrm{d}\overline{\mathbf{q}}/\mathrm{d}\rho_e$ from Eq. (44). This leads to the following condition for $\boldsymbol{\lambda}$:

$$2\boldsymbol{\lambda}^T(\omega^2\overline{\mathbf{M}}+\omega\overline{\mathbf{C}}+\overline{\mathbf{K}}_T)+2\overline{\mathbf{q}}^T\mathbf{L}=0 \tag{45}$$

As a result, the sensitivity of c with respect to design variables ρ_e is

$$\frac{\mathrm{d}c}{\mathrm{d}\rho_e}=2\boldsymbol{\lambda}^T\left[\omega^2\frac{\partial\overline{\mathbf{M}}}{\partial\rho_e}\overline{\mathbf{q}}+\omega\frac{\partial\overline{\mathbf{C}}}{\partial\rho_e}\overline{\mathbf{q}}+\frac{\partial\overline{\mathbf{g}}}{\partial\rho_e}+\left(2\omega\overline{\mathbf{M}}\overline{\mathbf{q}}+\overline{\mathbf{C}}\overline{\mathbf{q}}\right)\frac{\mathrm{d}\omega}{\mathrm{d}\rho_e}\right] \tag{46}$$

and the adjoint equation is found as

$$(\omega^2\overline{\mathbf{M}}+\omega\overline{\mathbf{C}}+\overline{\mathbf{K}}_T)\boldsymbol{\lambda}=-\mathbf{L}\overline{\mathbf{q}} \tag{47}$$

In Eq. (46), the sensitivity of frequency ω w.r.t. the design variable ρ_e has not yet been derived. Recalling that $\omega=\gamma\omega_i$ we obtain

$$\frac{\mathrm{d}\omega}{\mathrm{d}\rho_e}=\frac{\gamma}{2\omega_i}\frac{\mathrm{d}\omega_i^2}{\mathrm{d}\rho_e} \tag{48}$$

where the eigenvalue ω_i is found from a standard eigenvalue problem as

$$(\mathbf{K}-\omega_i^2\mathbf{M})\boldsymbol{\Phi}_i=0 \tag{49}$$

and the sensitivity $\mathrm{d}\omega_i^2/\mathrm{d}\rho_e$ of a single modal eigenvalue is well known as

$$\frac{\mathrm{d}\omega_i^2}{\mathrm{d}\rho_e}=\boldsymbol{\Phi}_i^T\left[\frac{\partial\mathbf{K}}{\partial\rho_e}-\omega_i^2\frac{\partial\mathbf{M}}{\partial\rho_e}\right]\boldsymbol{\Phi}_i \tag{50}$$

where the eigenvector is assumed to be normalized with respect to the mass matrix, i.e. $\boldsymbol{\Phi}_i^T\mathbf{M}\boldsymbol{\Phi}_i=1$. Otherwise, the right-hand side of Eq. (50) should be divided by $\boldsymbol{\Phi}_i^T\mathbf{M}\boldsymbol{\Phi}_i$. Only the case of simple eigenvalue is considered here whereas for the case of multiple eigenvalues we refer to [43–45]. The sensitivities computed by the adjoint method have been verified by comparison with results from finite difference calculations.

Based on the results of the nonlinear vibration analysis we compute the sensitivities and we then obtain an update of the design variables by the use of the mathematical programming software MMA [46]. This constitutes an optimization iteration and the iterative procedure is repeated until design variables and objective function converge to a prescribed tolerance.

We should point out that during the optimization procedure we keep the damping coefficient μ constant. This implies that smaller eigenvalues ω_i lead to a larger modal damping ratio $\xi_i=\mu/(2\rho\omega_i)$, which might bias the optimization procedure is the damping is not sufficiently small.

4. Optimization examples

4.1. Optimization of the peak of primary resonance

As the first optimization problem we aim to minimize the peak of the primary resonance by using Eq. (36). The general objective function is expressed as

$$c(\rho_e,\omega(\rho_e))=\overline{\mathbf{q}}^T\mathbf{L}\overline{\mathbf{q}}=a_{i1}^2+b_{i1}^2 \tag{51}$$

where the index i denotes the degree of freedom corresponding to the lateral deflection at mid-span of the beam, $a_{i\,1}$ and $b_{i\,1}$ denote the corresponding coefficients of the fundamental harmonic for the lateral displacement, and ω is the frequency of the peak, which is identified using the aforementioned phase lag quadrature criterion and computed along the backbone of the primary resonance.

We bound the width by setting $b_{\min}=0.1$ and $b_{\max}=100$ and specify the volume constraint as $\alpha=0.3$ which is also set as the volume of the reference beam used as initial design for the optimization. We bound the allowable volume from below and since we are *minimizing* the amplitude for a fixed force this ensures that the volume of the final optimized design will match that of the initial reference design. Other parameters of the beam are listed in Section 2.5.

Often design optimization is performed using a linear model and for comparison we will here compare the optimized designs obtained using the nonlinear finite element model with a corresponding linear model. For the linear model we optimize for the response at the linear fundamental frequency $\omega_1(\rho_e)$ using the general formulation in Eq. (42) (with $\gamma=1$)

and the sensitivities found from Eqs. (46) and (47). The optimized results are shown in Fig. 4. The design obtained by using the linear finite element model is independent of the load amplitude and it is seen to have two weak links in the structure where the design variables take their minimum value. In contrast, the optimized design obtained with the nonlinear finite element model shows a dependence on the amplitude of load. For a small amplitude of the load, $f = 10EIr/L^3$, the obtained design is very close to the linear design. However, when we increase the load to a larger amplitude level, $f = 15EIr/L^3$, the two weak links near $x = \frac{1}{4}L$ and $\frac{3}{4}L$ become wider. This effect is discussed in more detail in Section 5.

The linear and nonlinear frequency–amplitude curves for the two designs are shown in Fig. 5. Both in linear and nonlinear analyses, the two optimized designs have a resonant peak with an amplitude significantly lower than that of the uniform design. When applying linear vibration analysis, the frequency–amplitude curves for the two optimized designs are seen to overlap. However, based on the nonlinear vibration analysis we see a notable difference in the response and the nonlinear optimized design shows a slightly smaller peak amplitude as well as a larger ratio ω/ω_1 for the peak of the primary resonance. A comparison of linear mode shapes of the two optimized structures normalized with respect to mass matrix is shown in Fig. 5(c). While the mode shapes of two optimized structures only have slightly observable difference, they are quite different from the mode shape of the uniform design.

Thus, even with a limited design freedom that is here dictated by having only a single beam with a fixed thickness, we can see that including the nonlinearities in the optimization procedure has an influence on the nonlinear performance of the optimized designs. In the next examples we will optimize the inherent nonlinear phenomenon of superharmonic resonance.

4.2. Optimization of superharmonic resonance

In this case, we consider two optimization problems by using Eq. (42). The first one is to minimize the superharmonic resonance with a fixed load amplitude without increasing the amount of material in the beam. The second will be to maximize the superharmonic resonance also for a fixed load amplitude but without reducing the amount of material.

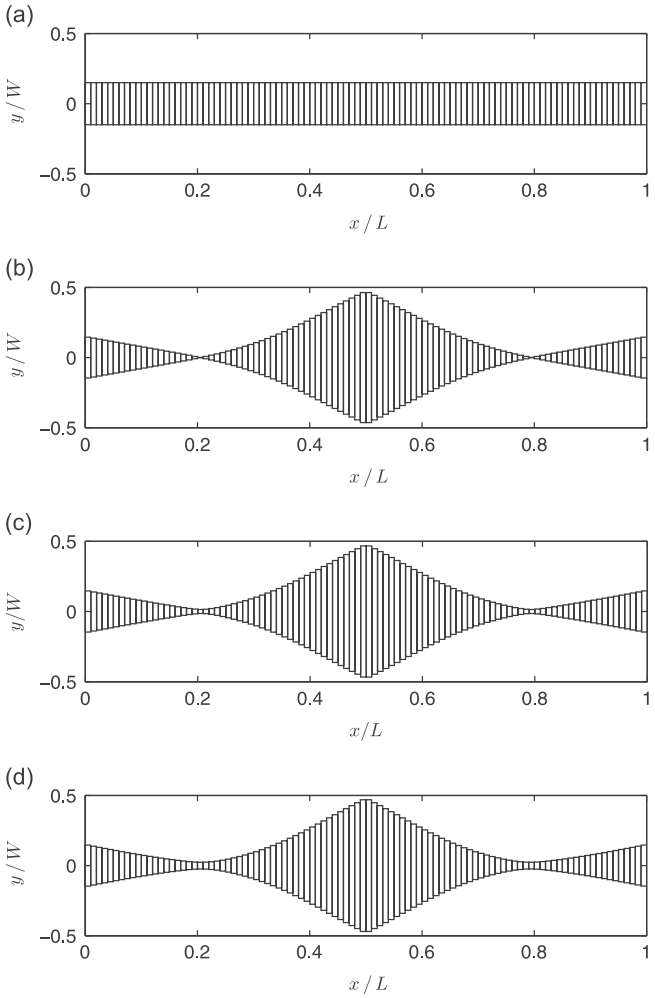

Fig. 4. A doubly clamped beam with optimized width for minimizing the peak of primary resonance: (a) uniform width and initial guess; (b) optimized width using linear finite element model; (c) optimized width using nonlinear finite element model and $f = 60.74$ N; (d) optimized width using nonlinear finite element model and $f = 91.11$ N.

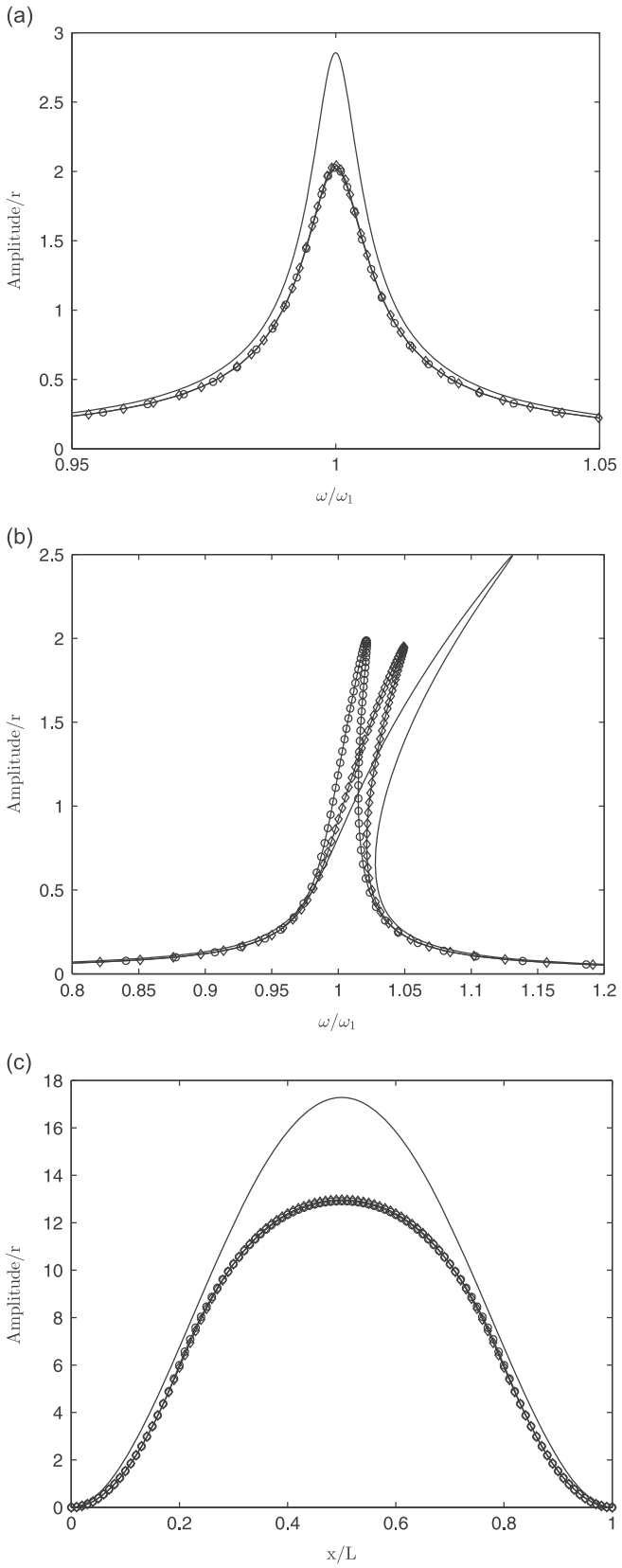

Fig. 5. A doubly clamped beam with optimized width for minimizing the peak of primary resonance: '.' uniform width; 'o' optimized width using linear finite element model; '⋄' optimized width using nonlinear finite element model and $f = 91.11$ N: (a) linear analysis; (b) nonlinear analysis; (c) linear modal analysis.

Considering the superharmonic resonance, the objective function is selected as

$$c(\rho_e, \omega_1(\rho_e)/3) = \overline{\mathbf{q}}^T \mathbf{L} \overline{\mathbf{q}} = a_{i3}^2 + b_{i3}^2 \tag{52}$$

where $a_{i\ 3}$ and $b_{i\ 3}$ are the coefficients of the third harmonic terms $\cos 3\tau$ and $\sin 3\tau$, respectively and the subscript i denotes the degree of freedom corresponding to the deflection w at the mid-span of the beam.

The optimization problem is then changed to

$$\min_{\rho_e}/\max \quad c = a_{i3}^2 + b_{i3}^2$$
$$\text{s.t.} \quad \omega = \frac{1}{3}\omega_1 \tag{53}$$

subjected also to the additional constraints from Eq. (36) (except $b_{i1} = 0$) using either a minimum or a maximum volume fraction. Here, ω_1 is the 1st eigenvalue so that $\omega = \frac{1}{3}\omega_1$ corresponds to a frequency close to the first superharmonic resonance. The allowable volume is $\alpha = 0.3$. The initial structure is a beam with uniform width and a bottom limit of the width set to $b_{\min} = 10$.

In the case of an external load given by 607.4 N we obtain the optimized structure shown in Fig. 6. The frequency–amplitude curves for the uniform-width design and the optimized design are compared in Fig. 9. It can be seen that the superharmonic resonance is reduced significantly with the optimized width distribution even though the total volume is unchanged. The effect of modifying the design can clearly be seen by viewing the structural response in the time domain. Fig. 10 shows the periodic response in the time domain for the peak of the frequency–amplitude curve in Fig. 9. The design with uniform width distribution produces a distorted signal with higher harmonics whereas the design with optimized width reduces the higher-order harmonics effectively.

Next we aim to maximize the superharmonic resonant response. We pose this as a minimization problem with $1/c$ as the objective. The volume constraint is set as $\alpha = 0.3$ but we now bound the volume from above. The initial design, the bottom limit of the width and the external load are the same as for the minimization problem solved above. The optimized structure is shown in Fig. 7 and the evolution of the objective during the optimization iterations for both optimization problems is shown in Fig. 8. The frequency–amplitude curves for uniform and optimized designs are shown in Fig. 9. The time-domain response that corresponds to the peak of the frequency–amplitude curve is shown in Fig. 10 and we see here that the response at the mid-span of the beam is dominated by the third-order harmonic for this optimized design.

5. Discussion

Numerical experience shows that it is important to select necessary and sufficient harmonics in the Fourier expansion. A general guideline about completeness and balance ability was given by Leung and Fung [19]. For the sake of completeness, the second- and third-order harmonics are essential for the case of quadratic and cubic nonlinearities. Particularly, the second-order harmonic is necessary for describing the longitudinal motion of stretching. For the sake of balance ability, all harmonics up to and including the sixth order are included in the Fourier expansion here. Additionally it should be mentioned that the number of elements should be sufficient to predict the modes around the highest frequency in the Fourier expansion.

It is noted that when we minimize the resonant peak, the optimized design based on the nonlinear finite element model has a larger width around $x = \frac{1}{4}L$ and $x = \frac{3}{4}L$, whereas the cross section area vanishes in the optimized design based on the linear finite element model. There is a simple physical interpretation for this phenomenon. Based on the theory of linear

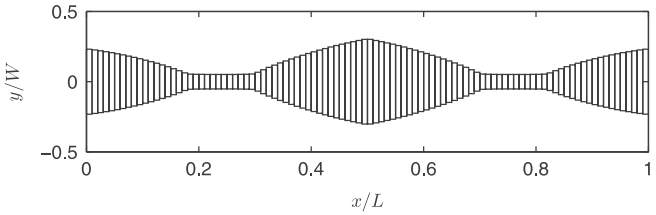

Fig. 6. A doubly clamped beam with optimized width for minimizing superharmonic resonance around $\omega_1/3$.

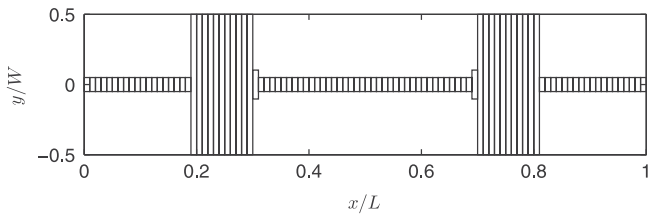

Fig. 7. A doubly clamped beam with optimized width for maximizing superharmonic resonance around $\omega_1/3$.

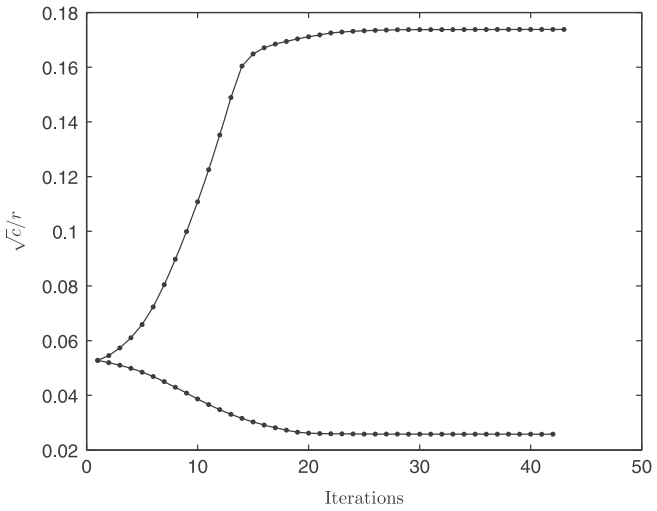

Fig. 8. Iteration history of the objective during optimization.

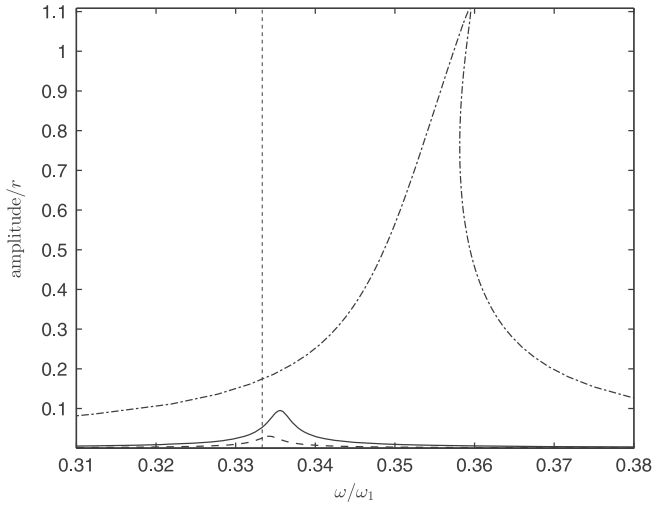

Fig. 9. Frequency–amplitude curves of superharmonic resonance around $\omega_1/3$: solid line: uniform; dashed line: minimized superharmonic resonance; dot dashed line: maximized superharmonic resonance; dotted line: $\omega/\omega_1 = \frac{1}{3}$.

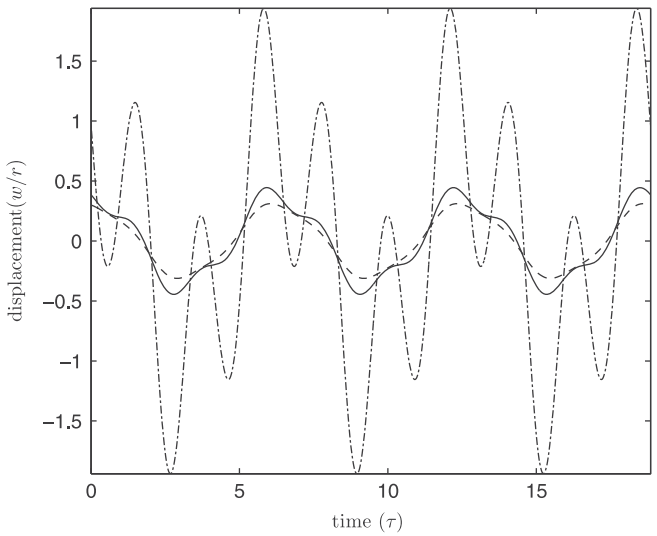

Fig. 10. The responses for the peak of superharmonic resonance around $\omega_1/3$: solid line: uniform; dashed line: minimized superharmonic resonance; dot dashed line: maximized superharmonic resonance.

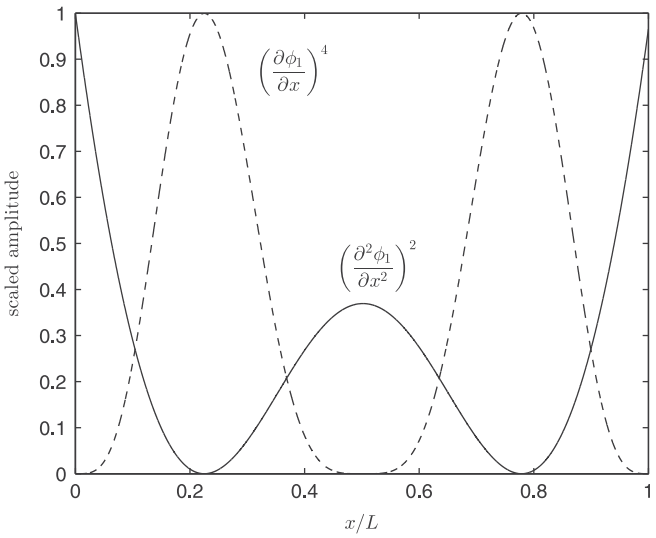

Fig. 11. Strain energy distribution for the first linear mode.

vibration, the cross section area would be allowed to vanish at inner points where the material does not contribute to the bending strain energy. In contrast, the bending and stretching deformations are coupled in the nonlinear case. In our example, the bending deformation causes stretching strain energy due to midplane stretching. As shown in Fig. 11, where ϕ_1 denotes the deformation w for the first linear mode of a doubly clamped beam, the bending strain energy is proportional to $(\partial^2\phi_1/\partial x^2)^2$ and the strain energy associated with midplane stretching is proportional to $(\partial\phi_1/\partial x)^4$. The strongest midplane stretching effect occurs where $(\partial\phi_1/\partial x)^4$ reaches the local maximum and $(\partial^2\phi_1/\partial x^2)^2$ reaches the local minimum. So as the load increases, the coupling effect will lead to an increased width around $x=\frac{1}{4}L$ and $x=\frac{3}{4}L$.

6. Conclusion

A methodology here is proposed for optimizing the nonlinear forced response of geometrically nonlinear beam structures with quadratic and cubic nonlinearities. The nonlinear vibration analysis is performed via the combination of the finite element method and the incremental harmonic balance method. Design sensitivities are derived from the nonlinear response using an adjoint approach and we solve the optimization problem using a gradient-based approach with the mathematical programming tool MMA. We include examples that demonstrate the effectiveness of the proposed methodology. By minimizing the amplitude of the primary resonance we demonstrate the effect of including the nonlinearity in the optimization procedure, although the difference in the final response is not very large. However, it is noted that the optimization based on the nonlinear finite element model leads to a more robust design without the weak links that are found in the linear design. In the case of optimizing the superharmonic resonance, it is necessary to employ the nonlinear finite element model. In this case we see a significant effect on the structural response when we either minimize or maximize the contribution from the third-order harmonic.

This methodology has shown a promising ability in optimizing the design of the nonlinear dynamic response of beam structures and may find applications for vibration-based energy harvesting and MEMS structures by taking into account their nonlinear performance. The work can be extended to general finite element models by using the alternating frequency/time domain method. Future work includes optimization of frame structures and 2D continuum structure based on the geometrically nonlinear finite element analysis.

Acknowledgments

This project was supported by ERC Starting Grant 279529 INNODYN. The authors also thank Krister Svanberg in Royal Institute of Technology (KTH), Sweden, for the permission to use MMA and Ole Sigmund for valuable comments and suggestions.

References

[1] J.F. Rhoads, S.W. Shaw, K.L. Turner, Nonlinear dynamics and its applications in micro- and nanoresonators, *Journal of Dynamic Systems, Measurement, and Control* 132 (2010) 034001.
[2] J. J. Thomsen, Vibrations and Stability: Advanced Theory, Analysis, and Tools (2nd ed., revised), Springer-Verlag, Berlin Heidelberg, 2003.
[3] W. Lacarbonara, H. Yabuno, Refined models of elastic beams undergoing large in-plane motions: *theory and experiment*, *International Journal of Solids and Structures* 43 (2006) 5066–5084.
[4] K. Wojciechowski, R. Olsson, M. Baker, J. Wittwer, *Low Vibration Sensitivity mems Resonators*, 2007, pp. 1220–1224.

[5] R. Mestrom, R. Fey, K. Phan, H. Nijmeijer, Simulations and experiments of hardening and softening resonances in a clamped-clamped beam mems resonator, *Sensors and Actuators A: Physical* 162 (2010) 225–234.
[6] A. Hajati, S.-G. Kim, Ultra-wide bandwidth piezoelectric energy harvesting, *Applied Physics Letters* 99 (2011) 083105.
[7] S.L. Lau, Y.K. Cheung, Amplitude incremental variational principle for nonlinear vibration of elastic systems, *Journal of Applied Mechanics* 48 (1981) 959–964.
[8] S.H. Chen, Y.K. Cheung, H.X. Xing, Nonlinear vibration of plane structures by finite element and incremental harmonic balance method, *Nonlinear Dynamics* 26 (2001) 87–104.
[9] R. Lewandowski, Non-linear, steady-state vibration of structures by harmonic balance/finite element method, *Computers & Structures* 44 (1992) 287–296. (Special issue: WCCM II).
[10] R. Lewandowski, Computational formulation for periodic vibration of geometrically nonlinear structures—Part 1: *theoretical background*, *International Journal of Solids and Structures* 34 (1997) 1925–1947.
[11] R. Lewandowski, Computational formulation for periodic vibration of geometrically nonlinear structures—Part 2: *numerical strategy and examples*, *International Journal of Solids and Structures* 34 (1997) 1949–1964.
[12] T. Cameron, J. Griffin, An alternating frequency/time domain method for calculating the steady-state response of nonlinear dynamic systems, *Journal of Applied Mechanics* 56 (1989) 149–154.
[13] R.C. Maple, P.I. King, P.D. Orkwis, J.M. Wolff, Adaptive harmonic balance method for nonlinear time-periodic flows, *Journal of Computational Physics* 193 (2004) 620–641.
[14] Y. Cheung, S. Chen, S. Lau, Application of the incremental harmonic balance method to cubic non-linearity systems, *Journal of Sound and Vibration* 140 (1990) 273–286.
[15] A. Leung, S. Chui, Non-linear vibration of coupled duffing oscillators by an improved incremental harmonic balance method, *Journal of Sound and Vibration* 181 (1995) 619–633.
[16] A. Raghothama, S. Narayanan, Bifurcation and chaos in geared rotor bearing system by incremental harmonic balance method, *Journal of Sound and Vibration* 226 (1999) 469–492.
[17] J. Didier, J.-J. Sinou, B. Faverjon, Nonlinear vibrations of a mechanical system with non-regular nonlinearities and uncertainties, *Communications in Nonlinear Science and Numerical Simulation* 18 (2013) 3250–3270.
[18] A.Y.T. Leung, T.C. Fung, Phase increment analysis of damped duffing oscillators, *International Journal for Numerical Methods in Engineering* 28 (1989) 193–209.
[19] A.Y.T. Leung, T.C. Fung, Non-linear steady state vibration of frames by finite element method, *International Journal for Numerical Methods in Engineering* 28 (1989) 1599–1618.
[20] B. Cochelin, C. Vergez, A high order purely frequency-based harmonic balance formulation for continuation of periodic solutions, *Journal of Sound and Vibration* 324 (2009) 243–262.
[21] J. Thomas, E. Dowell, K. Hall, Nonlinear inviscid aerodynamic effects on transonic divergence, flutter, and limit-cycle oscillations, *AIAA Journal* 40 (2002) 638–646.
[22] K. Hall, J. Thomas, W. Clark, Computation of unsteady nonlinear flows in cascades using a harmonic balance technique, *AIAA Journal* 40 (2002) 879–886.
[23] A. LaBryer, P. Attar, A harmonic balance approach for large-scale problems in nonlinear structural dynamics, *Computers & Structures* 88 (2010) 1002–1014.
[24] M. Thothadri, F.C. Moon, Nonlinear system identification of systems with periodic limit-cycle response, *Nonlinear Dynamics* 39 (2005) 63–77.
[25] H. Ahmadian, H. Jalali, Generic element formulation for modelling bolted lap joints, *Mechanical Systems and Signal Processing* 21 (2007) 2318–2334.
[26] N. Coudeyras, J.-J. Sinou, S. Nacivet, A new treatment for predicting the self-excited vibrations of nonlinear systems with frictional interfaces: *the constrained harmonic balance method, with application to disc brake squeal*, *Journal of Sound and Vibration* 319 (2009) 1175–1199.
[27] H. Liao, W. Sun, A new method for predicting the maximum vibration amplitude of periodic solution of non-linear system, *Nonlinear Dynamics* (2012) 1–14.
[28] N. Olhoff, Optimization of vibrating beams with respect to higher order natural frequencies, *Journal of Structural Mechanics* 4 (1976) 87–122.
[29] N. Olhoff, R. Parbery, Designing vibrating beams and rotating shafts for maximum difference between adjacent natural frequencies, *International Journal of Solids and Structures* 20 (1984) 63–75.
[30] M.P. Bendsøe, N. Olhoff, A method of design against vibration resonance of beams and shafts, *Optimal Control Applications and Methods* 6 (1985) 191–200.
[31] R. Meske, B. Lauber, E. Schnack, A new optimality criteria method for shape optimization of natural frequency problems, *Structural and Multidisciplinary Optimization* 31 (2006) 295–310.
[32] N. Olhoff, B. Niu, G. Cheng, Optimum design of band-gap beam structures, *International Journal of Solids and Structures* 49 (2012) 3158–3169.
[33] S. Paquin, Y. St-Amant, Improving the performance of a piezoelectric energy harvester using a variable thickness beam, *Smart Materials and Structures* 19 (2010) 105020.
[34] J.M. Dietl, E. Garcia, Beam shape optimization for power harvesting, *Journal of Intelligent Material Systems and Structures* 21 (2010) 633–646.
[35] B. Stanford, P. Beran, M. Kurdi, Adjoint sensitivities of time-periodic nonlinear structural dynamics via model reduction, *Computers and Structures* 88 (2010) 1110–1123.
[36] B. Stanford, P. Beran, R. Snyder, M. Patil, Stability and power optimality in time-periodic flapping wing structures, *Journal of Fluids and Structures* 38 (2013) 238–254.
[37] M.P. Bendsøe, O. Sigmund, *Topology Optimization: Theory, Methods and Applications*, Springer, Berlin Heidelberg, 2003.
[38] M. Crisfield, A fast incremental/iterative solution procedure that handles 'snap-through', *Computers & Structures* 13 (1981) 55–62.
[39] M. Peeters, R. Viguié, G. Sérandour, G. Kerschen, J.C. Golinval, Nonlinear normal modes, Part ii: *toward a practical computation using numerical continuation techniques*, *Mechanical Systems and Signal Processing* 23 (2009) 195–216.
[40] E.P. Petrov, Advanced analysis and optimization of nonlinear resonance vibrations in gas-turbine structures with friction and gaps, *IUTAM Symposium on Emerging Trends in Rotor Dynamics*, Vol. 25, 2011, pp. 297–307.
[41] M. Peeters, G. Kerschen, J. Golinval, Modal testing of nonlinear vibrating structures based on nonlinear normal modes: *experimental demonstration*, *Mechanical Systems and Signal Processing* 25 (2011) 1227–1247.
[42] M. Peeters, G. Kerschen, J. Golinval, Dynamic testing of nonlinear vibrating structures using nonlinear normal modes, *Journal of Sound and Vibration* 330 (2011) 486–509.
[43] A.P. Seyranian, Sensitivity analysis of multiple eigenvalues, *Journal of Structural Mechanics* 21 (1993) 261–284.
[44] A. Seyranian, E. Lund, N. Olhoff, Multiple eigenvalues in structural optimization problems, *Structural Optimization* 8 (1994) 207–227.
[45] J. Du, N. Olhoff, Topological design of freely vibrating continuum structures for maximum values of simple and multiple eigenfrequencies and frequency gaps, *Structural and Multidisciplinary Optimization* 34 (2007) 91–110.
[46] K. Svanberg, The method of moving asymptotes—a new method for structural optimization, *International Journal for Numerical Methods in Engineering* 24 (1987) 359–373.

Publication [P2]

Structural optimization for nonlinear dynamic response

PROCEEDINGS OF THE ROYAL SOCIETY A

rspa.royalsocietypublishing.org

Research

Article submitted to journal

Subject Areas:
mechanical engineering, microsystems, computational mechanics

Keywords:
shape optimization, adjoint method, normal form, internal resonance, nonlinear normal mode

Author for correspondence:
Steven W. Shaw
e-mail: shawsw@msu.edu

Royal Society Publishing
Informing the science of the future

Structural optimization for nonlinear dynamic response

Suguang Dou[1], B. Scott Strachan[2,3], Steven W. Shaw[2,4], Jakob S. Jensen[1,5]

[1]Department of Mechanical Engineering, Technical University of Denmark
[2]Department of Mechanical Engineering, Michigan State University
[3]Department of Electrical and Computer Engineering, Michigan State University
[4]Department of Physics and Astronomy, Michigan State University
[5]Department of Electrical Engineering, Technical University of Denmark

Much is known about the nonlinear resonant response of mechanical systems, but methods for the systematic design of structures that optimize aspects of these responses have received little attention. Progress in this area is particularly important in the area of micro-systems, where nonlinear resonant behaviour is being used for a variety of applications in sensing and signal conditioning. In this work we describe a computational method that provides a systematic means for manipulating and optimizing features of nonlinear resonant responses of mechanical structures that are described by a single vibrating mode, or by a pair of internally resonant modes. The approach combines techniques from nonlinear dynamics, computational mechanics, and optimization, and it allows one to relate the geometric and material properties of structural elements to terms in the normal form for a given resonance condition, thereby providing a means for tailoring its nonlinear response. The method is applied to the fundamental nonlinear resonance of a clamped-clamped beam and to the coupled mode response of a frame structure, and the results show that one can modify essential normal form coefficients by an order of magnitude by relatively simple changes in the shape of these elements. We expect the proposed approach, and its extensions, to be useful for the design of systems used for fundamental studies of nonlinear behaviour as well as for the development of commercial devices that exploit nonlinear behaviour.

1. Introduction

The nonlinear resonant behaviour of structures is quite well understood for the case of single-mode resonance and for nonlinear interactions between a few modes. The phenomena associated with these resonances include amplitude-dependent natural frequencies, instabilities and bifurcations, coexistence of multiple steady-states, etc. There are abundant analytical and simulation studies on these topics, and plenty of experimental evidence to support the validity of simple models for describing these phenomena. In many applications these behaviours are viewed as curiosities, generally to be avoided.

However, recent advances in the fields of non-linear micro- and nano-resonators [1] have contributed to the development of new MEMS devices that utilize nonlinear dynamics, e.g. the hardening and softening behaviour of individual modes and energy transfer between modes, for applications, including energy harvesting [2], atomic force microscopy [3], mass detection [4], inertial sensing [5], passive frequency division [6], and frequency stabilization [7]. In most previous studies, devices have been designed that demonstrate the behaviour of interest, but more recently researchers have started to explore the possibility of tailoring systems for targeted responses. For single-mode resonators, tuning the nonlinear resonances with hardening and softening behaviour is considered by Cho et al. [8], where the orientation of a nano-tube connecting two cantilever structures was changed to obtain hardening or softening behaviour, and Dai et al. [9], where the impact of topology variation on the hardening behaviour was investigated in dynamic tests of an energy harvesting device. For coupled-mode resonators with internal resonances, Tripathi and Bajaj [10] presented a procedure to synthesize families of structures with two commensurable natural frequencies (such as 1:2 or 1:3 relations). In contrast, Pedersen investigated structural optimization for minimizing the possibility of internal resonance by avoiding integer relations between the frequencies [11].To the authors' knowledge, structural manipulation and optimization of the essential nonlinear effects that capture the energy transfer between coupled modes has not been reported. These effects are naturally described by the normal form associated with a given resonance condition [12], in which the coefficients of particular nonlinear terms dictate the behaviour at the given resonance; we refer to these as the *essential* nonlinearities of the system. The key to optimizing nonlinear resonant responses is in the manipulation of these coefficients by structural modifications.

Gradient-based structural optimization is a powerful tool in design optimization. In previous research, it has been applied in nonlinear structural dynamics to optimize the amplitude of transient responses [13,14], periodic responses [15,16], and also eigenfrequencies of deformed structures with geometrical nonlinearities [17]. For a clamped-clamped beam, optimal shape design associated with nonlinear frequency responses, including primary resonances and super-harmonic resonances, was studied by Dou and Jensen [18] using the incremental harmonic balance method. Another related work is the optimal shape design of comb fingers for electrostatic forces as investigated by Ye et al. [19], which produced combinations of linear, quadratic, and cubic driving-force profiles. Shaped comb drives have been fabricated, tested, and widely used in many applications, including tunable resonators [20] and large-displacement parametric resonators [21].

Here a gradient-based optimization method is presented that allows one to tailor the nonlinearities associated with certain nonlinear resonances for a given resonator configuration. First, the coefficients associated with the *essential* nonlinearity for a given resonance are explicitly derived from nonlinear finite element models; this involves finite element discretization, explicit modal expansion, and distillation of the normal form coefficients. Then, the quantity that captures the *essential* nonlinearity in the reduced order model is manipulated by structural optimization. For example, the hardening and softening behaviour associated with the first flexural mode of a clamped-clamped beam is captured by the coefficient of a certain cubic term in a single-mode reduced order model, while for internal resonances the main nonlinearity is a nonlinear modal coupling term that promotes energy exchange between modes.

For a micro-resonator with complex geometry, characterization based on nonlinear finite element models offers a powerful tool to derive reduced order models. This procedure has been investigated for the analysis of nonlinear vibration of piezoelectric layered beams with applications to NEMS [22]. A more general theory for finite element models with geometric nonlinearity was provided by Touzé et al. [23] with applications to reduced-order models by using "Mixed Interpolation of Tensorial Components" (MITC) shell elements. Here we adopt this method for characterization of nonlinear resonators, which is applicable at macro and micro scales. Our focus is on nonlinearities arising from finite deformation kinematics of structures, but the methodology can be adapted to other situations for which forces can be described in terms of a potential, such as electrostatic loads, and for which the material nonlinearity, i.e., a nonlinear stress-strain relation, is expressed in terms of polynomial functions.

The article is organized as follows. First, the characterization theory is introduced in Section 2, where the coefficients for nonlinear stiffness and nonlinear modal coupling, for both the Hamiltonian and the reduced order differential equation model, are explicitly derived from the finite element model. Continuing in section 2, the sensitivity of the nonlinear modal coupling coefficients and the general optimization problem are formulated. Examples are given in section 3 and section 4 provides some discussion, conclusions, and directions for future work.

2. Analysis and optimization

(a) Characterization theory

In order to demonstrate the methodology we consider systems for which the dominant nonlinear effects arise from non-inertial conservative effects and we neglect the nonlinear inertial terms that might be important in, for example, cantilevered structures. This includes planar frame structures for which mid-plane stretching is the primary nonlinearity. For convenience in implementation, the derivation is formulated in matrix-vector form instead of tensor form. The full set of coefficients for individual mode nonlinear stiffness and for nonlinear modal coupling are first derived for the Hamiltonian of the system, and then the attendant essential coefficients in the reduced-order model are obtained in a straightforward manner.

The characterization theory is derived for general finite element models with quadratic and cubic nonlinearities arising from nonlinear strain-displacement relations. With the finite element discretization of the continuous structure, the Hamiltonian for the system, i.e. the sum of kinetic energy T and potential energy U, can be expressed as

$$\mathcal{H} = T + U = \frac{1}{2}\dot{\mathbf{u}}^T\mathbf{M}\dot{\mathbf{u}} + \sum_{e=1}^{N_e}\frac{1}{2}\int_{V_e}\boldsymbol{\epsilon}^T\boldsymbol{\sigma}\; dV \tag{2.1}$$

where $\mathbf{M}$ is the mass matrix of the finite element model, $\mathbf{u}$ is the global vector of nodal displacements, $\boldsymbol{\epsilon}$ and $\boldsymbol{\sigma}$ are element-wise vectors of strain and stress components, respectively, and V_e indicates that the volume integration is performed within the element e. Assuming a linear strain-stress relation, the potential energy U can be written as

$$U = \sum_{e=1}^{N_e}\frac{1}{2}\int_{V_e}\boldsymbol{\epsilon}^T\boldsymbol{\sigma}\; dV = \sum_{e=1}^{N_e}\frac{1}{2}\int_{V_e}\boldsymbol{\epsilon}^T\mathbb{C}\,\boldsymbol{\epsilon}\; dV \tag{2.2}$$

where $\mathbb{C}$ is a symmetric constitutive matrix. We may now divide the strain into a linear and nonlinear part as

$$\boldsymbol{\epsilon} = \mathbf{B}_0\,\mathbf{u}^e + \frac{1}{2}\,\mathbf{B}_1(\mathbf{u}^e)\,\mathbf{u}^e \tag{2.3}$$

where $\mathbf{B}_0$ is the linear strain-displacement matrix and $\mathbf{B}_1(\mathbf{u}^e)$ is a function of the element-wise vector of nodal displacements $\mathbf{u}^e$. Substituting Eq. (2.3) into Eq. (2.2) and using the symmetry of $\mathbb{C}$, the potential energy U can be divided into three parts, representing its expansion at leading

orders, as

$$U^{(2)} = \sum_{e=1}^{N_e} \frac{1}{2} \int_{V_e} (\mathbf{u}^e)^T \, \mathbf{B}_0^T \, \mathbb{C} \, \mathbf{B}_0 \, \mathbf{u}^e \, dV,$$
$$U^{(3)} = \sum_{e=1}^{N_e} \frac{1}{2} \int_{V_e} (\mathbf{u}^e)^T \, \mathbf{B}_0^T \, \mathbb{C} \, (\mathbf{B}_1(\mathbf{u}^e)) \, \mathbf{u}^e \, dV \tag{2.4}$$
$$U^{(4)} = \sum_{e=1}^{N_e} \frac{1}{8} \int_{V_e} (\mathbf{u}^e)^T \, (\mathbf{B}_1(\mathbf{u}^e))^T \, \mathbb{C} \, (\mathbf{B}_1(\mathbf{u}^e)) \, \mathbf{u}^e \, dV$$

The first step in setting up the modal equations is to solve the corresponding linear eigen-problem

$$(\omega^2 \, \mathbf{M} - \mathbf{K}) \boldsymbol{\Phi} = \mathbf{0} \tag{2.5}$$

where $\mathbf{K}$ is the linear stiffness matrix of the finite element model, to yield a set of modal frequencies and mode shapes $(\omega_p, \ \boldsymbol{\Phi}_p)$; these are normalized w.r.t. $\mathbf{M}$ such that $\boldsymbol{\Phi}_p^T \mathbf{M} \boldsymbol{\Phi}_p = 1$ and $\boldsymbol{\Phi}_p^T \mathbf{K} \boldsymbol{\Phi}_p = \omega_p^2$. We then express the displacements as a superposition of N_m linear modes as

$$\mathbf{u}^e = \sum_{p=1}^{N_m} q_p \, \boldsymbol{\Phi}_p^e \tag{2.6}$$

where q_p are the modal coordinates and $\boldsymbol{\Phi}_p^e$ are the element-wise mode shape vectors extracted from the global vector. Substituting Eq. (2.6) into Eq. (2.4), we obtain the strain energy expressed in terms of mode shapes and modal coordinates as

$$U^{(2)} = \sum_{i=1}^{N_m} \sum_{j=1}^{N_m} \alpha_{ij}^{(2)} \, q_i \, q_j,$$
$$U^{(3)} = \sum_{i=1}^{N_m} \sum_{j=1}^{N_m} \sum_{k=1}^{N_m} \alpha_{ijk}^{(3)} \, q_i \, q_j \, q_k \tag{2.7}$$
$$U^{(4)} = \sum_{i=1}^{N_m} \sum_{j=1}^{N_m} \sum_{k=1}^{N_m} \sum_{l=1}^{N_m} \alpha_{ijkl}^{(4)} \, q_i \, q_j \, q_k \, q_l$$

where the linear modal coupling coefficients $\alpha_{ij}^{(2)}$ and the non-linear modal coupling coefficients, $\alpha_{ijk}^{(3)}$ and $\alpha_{ijkl}^{(4)}$, are explicitly expressed as

$$\alpha_{ij}^{(2)} = \sum_{e=1}^{N_e} \frac{1}{2} \int_{V_e} (\boldsymbol{\Phi}_i^e)^T \, \mathbf{B}_0^T \, \mathbb{C} \, \mathbf{B}_0 \, \boldsymbol{\Phi}_j^e \, dV$$
$$\alpha_{ijk}^{(3)} = \sum_{e=1}^{N_e} \frac{1}{2} \int_{V_e} (\boldsymbol{\Phi}_i^e)^T \, \mathbf{B}_0^T \, \mathbb{C} \left(\mathbf{B}_1(\boldsymbol{\Phi}_j^e) \right) \boldsymbol{\Phi}_k^e \, dV \tag{2.8}$$
$$\alpha_{ijkl}^{(4)} = \sum_{e=1}^{N_e} \frac{1}{8} \int_{V_e} (\boldsymbol{\Phi}_i^e)^T \, \left(\mathbf{B}_1(\boldsymbol{\Phi}_j^e) \right)^T \, \mathbb{C} \, (\mathbf{B}_1(\boldsymbol{\Phi}_k^e)) \, \boldsymbol{\Phi}_l^e \, dV$$

Since we use the linear eigenmodes normalized with respect to the mass matrix, we have $\alpha_{ij}^{(2)} = 0$ for $i \neq j$ and $\alpha_{ii}^{(2)} = \omega_i^2/2$. With these modal coupling coefficients, we can now write the Hamiltonian for the system in Eq. (2.1) in modal coordinates (q_i, p_i) (where $p_i = \dot{q}_i$) as

$$\mathcal{H} = \sum_{i=1}^{N_m} \left(\frac{1}{2} p_i^2 + \frac{1}{2} \omega_i^2 q_i^2 \right) + \sum_{i=1}^{N_m} \sum_{j=1}^{N_m} \sum_{k=1}^{N_m} \alpha_{ijk}^{(3)} \, q_i \, q_j \, q_k + \sum_{i=1}^{N_m} \sum_{j=1}^{N_m} \sum_{k=1}^{N_m} \sum_{l=1}^{N_m} \alpha_{ijkl}^{(4)} \, q_i \, q_j \, q_k \, q_l \tag{2.9}$$

where the relation $\frac{1}{2}\, p_i^2 = \frac{1}{2}(p_i\Phi_i)^T\mathbf{M}(p_i\Phi_i)$ has been used. With the Hamiltonian of the system, it is straightforward to derive a set of ordinary differential equations in modal coordinates as

$$\ddot{q}_p + 2\xi_p\omega_p\dot{q}_p + \omega_p^2 q_p + \sum_{i=1}^{N_m}\sum_{j=1}^{N_m} g_{ij}^p\; q_i\, q_j + \sum_{i=1}^{N_m}\sum_{j=1}^{N_m}\sum_{k=1}^{N_m} h_{ijk}^p\; q_i\, q_j\, q_k = f_p(t) \tag{2.10}$$

where $p = 1, \ldots, N_m$, q_p is the modal coordinate corresponding to $\boldsymbol{\Phi}_p$, and we have introduced the modal force f_p obtained from a projection of the load vector $\mathbf{f}$ in the full finite element model onto the p^{th} mode, i.e., $f_p = \boldsymbol{\Phi}_p^T\mathbf{f}$, as well as modal damping ratios (damping as a ratio of critical damping) expressed as ξ_p. The modal coupling coefficients g_{ij}^p and h_{ijk}^p are

$$\begin{aligned} g_{ij}^p &= \alpha_{pij}^{(3)} + \alpha_{ipj}^{(3)} + \alpha_{ijp}^{(3)} \\ h_{ijk}^p &= \alpha_{pijk}^{(4)} + \alpha_{ipjk}^{(4)} + \alpha_{ijpk}^{(4)} + \alpha_{ijkp}^{(4)} \end{aligned} \tag{2.11}$$

It is noted that the differential equation representation of Eq. (2.10) with the modal coupling coefficients in Eq. (2.11) is equivalent to the formulation obtained using the principle of virtual work in previous studies [23].

It is well known that a large number of linear modes may be required to accurately describe the behaviour of nonlinear resonators. On the other hand, the hardening/softening behaviour of a single-mode resonator is well predicted by a single second-order governing equation with its dynamics projected onto a single nonlinear normal mode. This advanced reduced order model is achieved by using normal form theory, linked to nonlinear normal modes, as described in [24, 25]. Using the theory of normal forms, our modal coordinates (q_p, p_p) can be transformed into the curved, normal coordinates (R_p, S_p) (where $S_p = \dot{R}_p$) through a nonlinear transformation of coordinates, written in general form as

$$\begin{aligned} q_p &= R_p + \mathcal{P}_p(R_i, S_j) \\ p_p &= S_p + \mathcal{Q}_p(R_i, S_j) \end{aligned} \tag{2.12}$$

For details, the reader is referred to [24,25]. For clarity, the reduced order model and the corresponding nonlinear modal coupling coefficients in the curved coordinates of the nonlinear normal modes are further discussed in the examples for a single-mode resonator and a coupled-mode resonator with internal resonance.

In this work we apply the framework to structures modelled by beam elements [18]. However, it should be noted that the characterization and optimization procedure in this paper works independent of the choice of elements.

(b) Optimization and sensitivity analysis

In this section we present the general formulation for optimizing an objective function that depends on non-linear coefficients of interest for a given model. For example, we can maximize/minimize the hardening behaviour in a clamped-clamped beam by maximizing/minimizing the coefficient of the cubic non-linearity.

For generality, we consider an objective function c that may be an explicit function of the nonlinear coefficients, as well as the eigenvectors and associated eigenvalues, and formulate our optimization problem as the following minimization problem:

$$\begin{aligned} \min_{\rho_e} \quad & c(\omega_p, \boldsymbol{\Phi}_p, \alpha_{ijk}^{(3)}(\boldsymbol{\Phi}_p), \alpha_{ijkl}^{(4)}(\boldsymbol{\Phi}_p)) \\ \text{subject to (s.t.):} \quad & h_e = h_{\min} + \rho_e(h_{\max} - h_{\min}) \quad \text{(element-wise beam thickness)} \\ & 0 \le \rho_e \le 1 \qquad\qquad\qquad\quad \text{(normalized design variable)} \end{aligned} \tag{2.13}$$

where the subscripts $i,\ j,\ k,\ l,\ p = 1, \ldots, N_m$. The optimization problem is subjected to a set of constraints associated with the beam shape parametrization: h_e is the thickness of a beam

element which is bounded by $[h_{\min},\ h_{\max}]$ in the optimization and ρ_e is the normalized design variable bounded between 0 and 1. In practice, the lower bound $h_{\min}$ is dictated by fabrication tolerances, and the upper bound $h_{\max}$ is used to keep the beam relatively slender. For coupled -mode resonators, such as the one treated in the second example of this paper, we impose an additional constraint such that the ratio of two associated eigenvalues stays in a sufficiently small neighbourhood of $n_1\omega_{p_1} = n_2\omega_{p_2}$, where, for internal resonance conditions, n_1 and n_2 are selected integers and p_1 and p_2 are the orders of the two modes of interest.

For efficient structural optimization we will use a gradient-based approach. The sensitivity of the objective function can be calculated by using direct differentiation [26,27], but a more efficient approach for many design variables is the adjoint method [28] where we merely need to solve N_m groups of adjoint equations. To derive the adjoint equation, the objective function is first rewritten with adjoint variables $\boldsymbol{\lambda}_p$ and η_p as

$$c = c(\omega_p, \boldsymbol{\Phi}_p, \alpha^{(3)}_{ijk}(\boldsymbol{\Phi}_p), \alpha^{(4)}_{ijkl}(\boldsymbol{\Phi}_p)) + \sum_{p=1}^{N_m} \left[\boldsymbol{\lambda}_p^T(\omega_p^2\mathbf{M}\boldsymbol{\Phi}_p - \mathbf{K}\boldsymbol{\Phi}_p) + \eta_p(\boldsymbol{\Phi}_p^T\mathbf{M}\boldsymbol{\Phi}_p - 1)\right] \tag{2.14}$$

where it is noted that the terms in the two sets of parentheses that appear in the appended term both vanish identically. Differentiation of the objective function with respect to design variable ρ_e is then expressed as

$$\begin{aligned}\frac{\mathrm{d}c}{\mathrm{d}\rho_e} = {} & \frac{\partial c}{\partial \rho_e} + \sum_{p=1}^{N_m}\left[\frac{\partial c}{\partial \boldsymbol{\Phi}_p^T}\frac{\mathrm{d}\boldsymbol{\Phi}_p}{\mathrm{d}\rho_e} + \frac{\partial c}{\partial \omega_p}\frac{\mathrm{d}\omega_p}{\mathrm{d}\rho_e}\right] + \sum_{i=1}^{N_m}\sum_{j=1}^{N_m}\sum_{k=1}^{N_m}\frac{\partial c}{\partial \alpha^{(3)}_{ijk}}\left(\frac{\partial \alpha^{(3)}_{ijk}}{\partial \rho_e} + \sum_{p=1}^{N_m}\frac{\partial \alpha^{(3)}_{ijk}}{\partial \boldsymbol{\Phi}_p^T}\frac{\mathrm{d}\boldsymbol{\Phi}_p}{\mathrm{d}\rho_e}\right) \\ & + \sum_{i=1}^{N_m}\sum_{j=1}^{N_m}\sum_{k=1}^{N_m}\sum_{l=1}^{N_m}\frac{\partial c}{\partial \alpha^{(4)}_{ijkl}}\left(\frac{\partial \alpha^{(4)}_{ijkl}}{\partial \rho_e} + \sum_{p=1}^{N_m}\frac{\partial \alpha^{(4)}_{ijkl}}{\partial \boldsymbol{\Phi}_p^T}\frac{\mathrm{d}\boldsymbol{\Phi}_p}{\mathrm{d}\rho_e}\right) + \sum_{p=1}^{N_m}\eta_p\left(2\boldsymbol{\Phi}_p^T\mathbf{M}\frac{\mathrm{d}\boldsymbol{\Phi}_p}{\mathrm{d}\rho_e} + \boldsymbol{\Phi}_p^T\frac{\partial \mathbf{M}}{\partial \rho_e}\boldsymbol{\Phi}_p\right) \\ & + \sum_{p=1}^{N_m}\boldsymbol{\lambda}_p^T\left[\left(\omega_p^2\mathbf{M} - \mathbf{K}\right)\frac{\mathrm{d}\boldsymbol{\Phi}_p}{\mathrm{d}\rho_e} + 2\omega_p\mathbf{M}\boldsymbol{\Phi}_p\frac{\mathrm{d}\omega_p}{\mathrm{d}\rho_e} + \left(\omega_p^2\frac{\partial \mathbf{M}}{\partial \rho_e} - \frac{\partial \mathbf{K}}{\partial \rho_e}\right)\boldsymbol{\Phi}_p\right]\end{aligned} \tag{2.15}$$

Since the direct computation of $\frac{\mathrm{d}\boldsymbol{\Phi}_p}{\mathrm{d}\rho_e}$ and $\frac{\mathrm{d}\omega_p}{\mathrm{d}\rho_e}$ is computationally expensive, the adjoint variables are selected such that the coefficients of $\frac{\mathrm{d}\boldsymbol{\Phi}_p}{\mathrm{d}\rho_e}$ and $\frac{\mathrm{d}\omega_p}{\mathrm{d}\rho_e}$ vanish. This leads to the adjoint equations in terms of $\boldsymbol{\lambda}_p$ and η_p as

$$\frac{\mathrm{d}c}{\mathrm{d}\boldsymbol{\Phi}_p} + \left(\omega_p^2\mathbf{M} - \mathbf{K}\right)\boldsymbol{\lambda}_p + \left(2\mathbf{M}\boldsymbol{\Phi}_p\right)\eta_p = \mathbf{0} \tag{2.16}$$

$$\frac{\partial c}{\partial \omega_p} + \left(2\omega_p\boldsymbol{\Phi}_p^T\mathbf{M}\right)\boldsymbol{\lambda}_p = 0 \tag{2.17}$$

where we use the symmetry of $\mathbf{M}$ and $\mathbf{K}$, and

$$\frac{\mathrm{d}c}{\mathrm{d}\boldsymbol{\Phi}_p} = \frac{\partial c}{\partial \boldsymbol{\Phi}_p} + \sum_{i=1}^{N_m}\sum_{j=1}^{N_m}\sum_{k=1}^{N_m}\frac{\partial c}{\partial \alpha^{(3)}_{ijk}}\frac{\partial \alpha^{(3)}_{ijk}}{\partial \boldsymbol{\Phi}_p} + \sum_{i=1}^{N_m}\sum_{j=1}^{N_m}\sum_{k=1}^{N_m}\sum_{l=1}^{N_m}\frac{\partial c}{\partial \alpha^{(4)}_{ijkl}}\frac{\partial \alpha^{(4)}_{ijkl}}{\partial \boldsymbol{\Phi}_p} \tag{2.18}$$

In this case, the sensitivity of the objective function writes

$$\begin{aligned}\frac{\mathrm{d}c}{\mathrm{d}\rho_e} = {} & \frac{\partial c}{\partial \rho_e} + \sum_{i=1}^{N_m}\sum_{j=1}^{N_m}\sum_{k=1}^{N_m}\frac{\partial c}{\partial \alpha^{(3)}_{ijk}}\frac{\partial \alpha^{(3)}_{ijk}}{\partial \rho_e} + \sum_{i=1}^{N_m}\sum_{j=1}^{N_m}\sum_{k=1}^{N_m}\sum_{l=1}^{N_m}\frac{\partial c}{\partial \alpha^{(4)}_{ijkl}}\frac{\partial \alpha^{(4)}_{ijkl}}{\partial \rho_e} \\ & + \sum_{p=1}^{N_m}\left[\boldsymbol{\lambda}_p^T\left(\omega_p^2\frac{\partial \mathbf{M}}{\partial \rho_e} - \frac{\partial \mathbf{K}}{\partial \rho_e}\right)\boldsymbol{\Phi}_p + \eta_p\left(\boldsymbol{\Phi}_p^T\frac{\partial \mathbf{M}}{\partial \rho_e}\boldsymbol{\Phi}_p\right)\right]\end{aligned} \tag{2.19}$$

It is noted that the two quantities $\frac{\partial \alpha^{(3)}_{ijk}}{\partial \boldsymbol{\Phi}_p}$ and $\frac{\partial \alpha^{(4)}_{ijkl}}{\partial \boldsymbol{\Phi}_p}$ are assembled from the corresponding element-wise quantities $\frac{\partial \alpha_{ijk}}{\partial \boldsymbol{\Phi}^{(e)}_p}$ and $\frac{\partial \beta_{ijkl}}{\partial \boldsymbol{\Phi}^{(e)}_p}$. For convenience of computational implementation, the adjoint equations are expressed in matrix form as

$$\begin{bmatrix} \left(\omega_p^2\mathbf{M}-\mathbf{K}\right) & \left(2\mathbf{M}\boldsymbol{\Phi}_p\right) \\ \left(2\omega_p\boldsymbol{\Phi}_p^T\mathbf{M}\right) & 0 \end{bmatrix} \begin{bmatrix} \boldsymbol{\lambda}_p \\ \eta_p \end{bmatrix} = - \begin{bmatrix} \frac{\mathrm{d}c}{\mathrm{d}\boldsymbol{\Phi}_p} \\ \frac{\partial c}{\partial \omega_p} \end{bmatrix} \tag{2.20}$$

Based on the objective function and calculated sensitivities, the update of design variables is performed using the mathematical optimization tool called the method of moving asymtotes (MMA) [29], which solves a series of convex approximating subproblems. The algorithm has proven efficient for large-scale structural optimization. A new system analysis is then performed with the updated design variables. These steps are repeated until the design variables no longer change within some prescribed small tolerance.To summarize the procedure, a flow chart of the proposed optimization is displayed in Fig. 1. We now demonstrate the approach with examples.

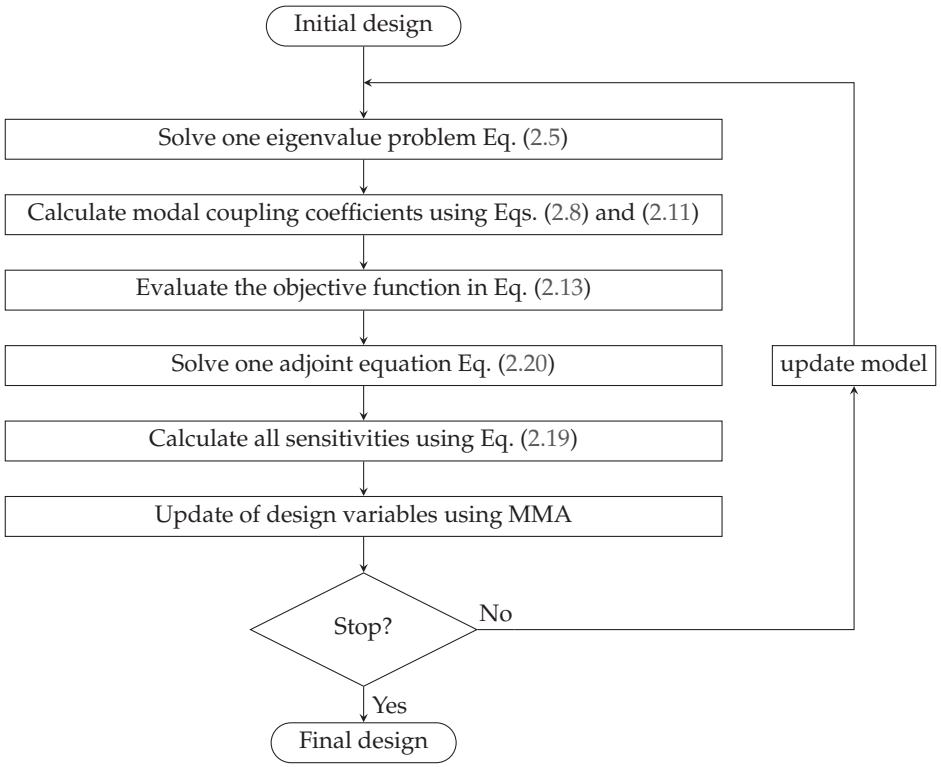

Figure 1. A flow chart of the proposed structural optimization for nonlinear dynamic response.

3. Examples

Two examples are presented. The first is to maximize/minimize the cubic nonlinearity of the fundamental mode in a nonlinear resonator consisting of a clamped-clamped beam, a common element in MEMS applications. The second example shows how one can maximize the essential modal coupling nonlinearity in a T-bar frame with a 2:1 internal resonance, a structure that has been proposed as a MEMS frequency divider.

(a) Single-mode resonator

Figure 2. Initial design of a clamped-clamped beam and its linear vibration mode. The color in online version indicates the vibration amplitude.

Figure 3. Optimized design for maximizing the cubic nonlinearity of a clamped-clamped beam and its linear vibration mode. The color in online version indicates the vibration amplitude.

Figure 4. Optimized design for minimizing the cubic nonlinearity of a clamped-clamped beam and its linear vibration mode. The color in online version indicates the vibration amplitude.

A crucial feature of a nonlinear resonator is the hardening and softening behaviour associated with a given vibration mode. For a lightly damped single-mode resonator, we will focus on the hardening and softening behaviour of its free responses, i.e., without damping and external loads. This problem has been investigated from a structural dynamics/finite element perspective; see, for example, [24]. For its applicability in general structures, including symmetric structures like clamped-clamped beams and asymmetric structures like arches or shells, the model development includes both quadratic and cubic terms. For single-mode resonator, the reduced order model based on a single linear mode is written as

$$\ddot{q}_p + \omega_p^2 q_p + g_{pp}^p q_p^2 + h_{ppp}^p q_p^3 = 0 \tag{3.1}$$

with $g_{pp}^p = 3\alpha_{ppp}^{(3)}$ and $h_{ppp}^p = 4\alpha_{pppp}^{(4)}$. The frequency-amplitude relation is derived as

$$\omega_{\mathrm{NL}} = \omega_p(1 + \Gamma\, a^2) \tag{3.2}$$

where a is the amplitude of the corresponding linear mode, and the effective coefficient Γ is

$$\Gamma = \frac{3}{8}\frac{h_{ppp}^p}{\omega_p^2} - \frac{5}{12}\frac{(g_{pp}^p)^2}{\omega_p^4} \tag{3.3}$$

A more accurate model for the hardening/softening behaviour of these structures can be created with the dynamics projected onto a single nonlinear normal mode and the corresponding

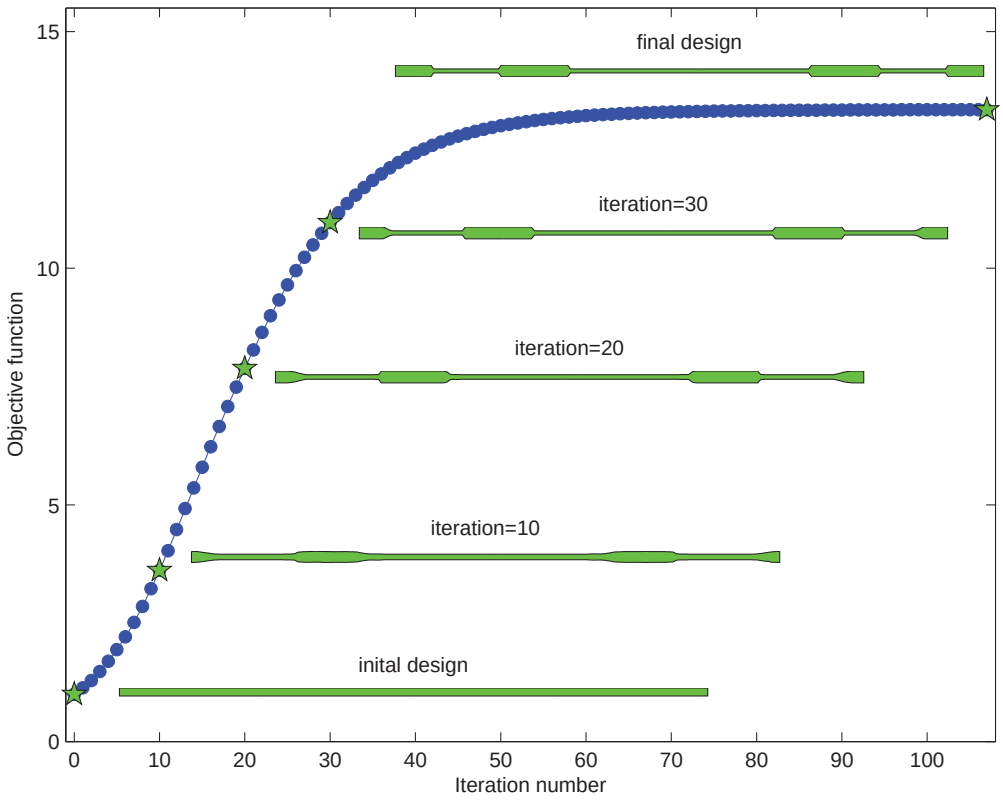

Figure 5. Evolution of the objective function and shapes encountered during the optimization process. The vertical axis is the absolute value of the objective function divided by its initial value and the horizontal axis is the iteration number.

equation is then written as

$$\ddot{R}_p + \omega_p^2 R_p + (A^p_{ppp} + h^p_{ppp}) R_p^3 + B^p_{ppp} R_p \dot{R}_p^2 = 0 \tag{3.4}$$

with the new coefficients A^p_{ppp} and B^p_{ppp} given as explicit functions of nonlinear modal coupling coefficients g^l_{ij} and h^l_{ijk}, [24]. Based on Eq. (3.4), the frequency-amplitude relation is derived as

$$\omega_{\mathrm{NL}} = \omega_p (1 + \Gamma^* A^2) \tag{3.5}$$

where A is the amplitude of the corresponding nonlinear normal mode in curved, normal coordinates, and the effective coefficient Γ^* is

$$\Gamma^* = \frac{3\,(A^p_{ppp} + h^p_{ppp}) + \omega_p^2\, B^p_{ppp}}{8\,\omega_p^2} \tag{3.6}$$

as approximated by averaging methods. Note that in this case Γ^* is not only linked to the p^{th} linear mode explicitly through ω_p and h^p_{ppp} and implicitly through g^p_{pp} which is in A^p_{ppp} and B^p_{ppp}, but also linked to other linear modes, whose contributions are taken into account through A^p_{ppp} and B^p_{ppp}.

We find that for the flexural mode of a clamped-clamped beam with geometric nonlinearity from mid-plane stretching, the dominating coefficient is h^p_{ppp} and we can therefore simplify our

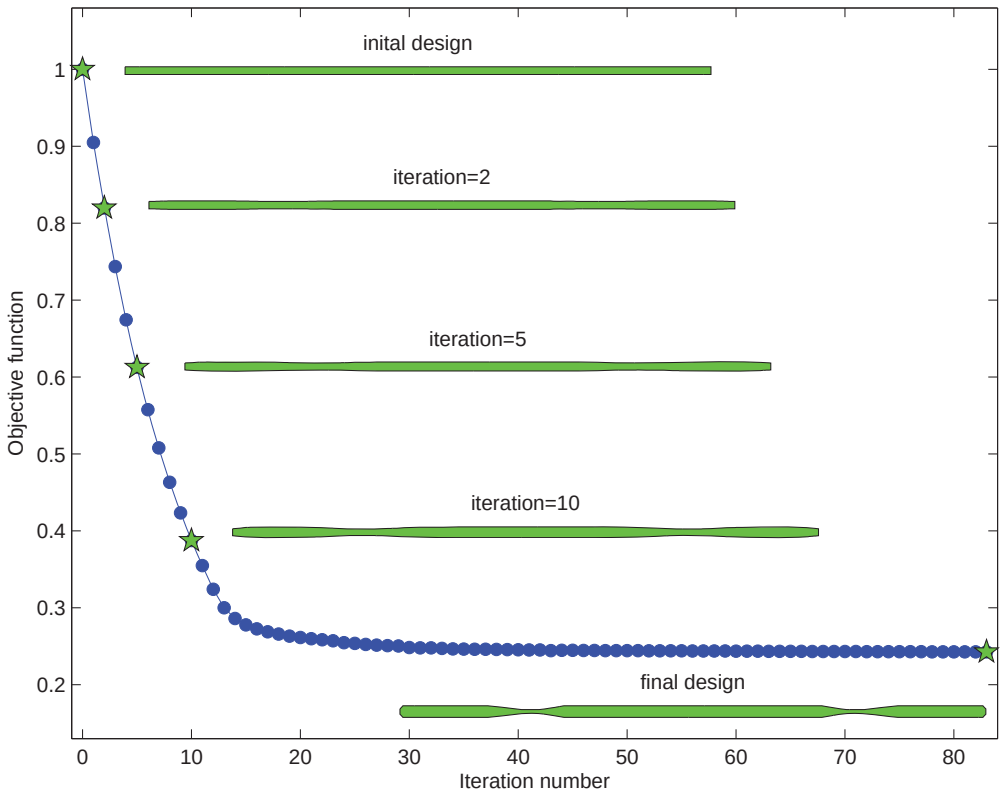

Figure 6. Evolution of the objective function and shapes encountered during the optimization process. The vertical axis is the absolute value of the objective function divided by its initial value and the horizontal axis is the iteration number.

optimization problem considerably by approximating Γ^* as:

$$\Gamma^* \approx \Gamma = \frac{3}{8}\frac{h^p_{ppp}}{\omega_p^2} = \frac{3}{2}\frac{\alpha^{(4)}_{pppp}}{\omega_p^2} \tag{3.7}$$

since $g^p_{pp} \equiv 0$, due to the symmetry. Based on the coefficient Γ^* in Eq. (3.7) and omitting the constant factor, the objective function is now selected as

$$\min_{\rho_e} \quad c = \pm\frac{\alpha^{(4)}_{pppp}}{\omega_p^2} \tag{3.8}$$

where the plus/minus sign corresponds to minimizing/maximizing the hardening behaviour, respectively. This simplification is possible since we consider the fundamental mode of a clamped-clamped beam, which has a strictly hardening nonlinearity, that is $\alpha^{(4)}_{pppp} > 0$. Substituting the objective function c in Eq. (3.8) into Eq. (2.19), its sensitivity with respect to design variables ρ_e is obtained as

$$\frac{\mathrm{d}c}{\mathrm{d}\rho_e} = \pm\frac{1}{\omega_p^2}\frac{\partial\alpha^{(4)}_{pppp}}{\partial\rho_e} + \boldsymbol{\lambda}_p^T\left(\omega_p^2\frac{\partial\mathbf{M}}{\partial\rho_e} - \frac{\partial\mathbf{K}}{\partial\rho_e}\right)\boldsymbol{\Phi}_p + \eta_p\boldsymbol{\Phi}_p^T\frac{\partial\mathbf{M}}{\partial\rho_e}\boldsymbol{\Phi}_p \tag{3.9}$$

with adjoint variables $\boldsymbol{\lambda}_p$ and η_p solved from adjoint equation in Eq. (2.20) with

$$\frac{\mathrm{d}c}{\mathrm{d}\boldsymbol{\Phi}_p} = \pm\frac{1}{\omega_p^2}\frac{\partial\alpha^{(4)}_{pppp}}{\partial\boldsymbol{\Phi}_p}, \quad \frac{\partial c}{\partial\omega_p} = \mp 2\frac{\alpha^{(4)}_{pppp}}{\omega_p^3} \tag{3.10}$$

where

$$\frac{\partial \alpha^{(4)}_{pppp}}{\partial \boldsymbol{\Phi}^e_p} = \frac{1}{2}\int_{V_e} (\boldsymbol{\Phi}^e_p)^T \left(\mathbf{B}_1(\boldsymbol{\Phi}^e_p)\right)^T \mathbb{C} \left(\mathbf{B}_1(\boldsymbol{\Phi}^e_p)\right) dV \tag{3.11}$$

The beam has a fixed length L of 300 µm and a fixed out-plane width of 20 µm. The initial design has a uniform in-plane thickness of 4 µm, and is discretized with 400 beam elements as described in [18]. During shape optimization the in-plane thickness h is varied to tailor the cubic nonlinearity in the reduced order model. We set $h_{\min}$ =2 µm, and $h_{\max}$ =6 µm. The material properties are assumed for Si, that is, mass density $\rho = 2329\ \mathrm{kg/m^3}$, and Young's modulus $E = 170$ GPa. The vibration modes of the initial design and two optimized designs are shown in Fig. 2, Fig. 3 and Fig. 4, respectively. Evolution of the objective function and shapes obtained during the evolution are shown in Fig. 5 and Fig. 6. In these optimizations, the objective function is increased by a factor of 13 and reduced by a factor of 4, respectively. The optimized designs are in accordance with the results in [18], obtained using the incremental harmonic balance method, where we found the nonlinear strain energy due to midplane stretching reaches its local maximum around $x = \frac{1}{4}L$ and $x = \frac{3}{4}L$, which is precisely where the optimized structures are altered most significantly relative to their general thickness. Furthermore, the eigenfrequency of the first flexural mode decreases during optimization of maximizing the cubic nonlinearity, and increases during optimization of minimizing the cubic nonlinearity. This follows from the fact that the structure is made generally thinner when maximizing the nonlinearity, so that the critical sections can be made relatively thick, and the opposite trend occurs when minimizing the nonlinearity. It should be emphasized that, no guarantee can be made that the obtained designs are global optima and the found solutions will in general depend on the chosen initial design. However, repeated optimization runs reveal that the formulation is quite robust and we believe only a marginal improvement in performance could be possibly found with another design.

(b) Coupled-mode resonator with internal resonance

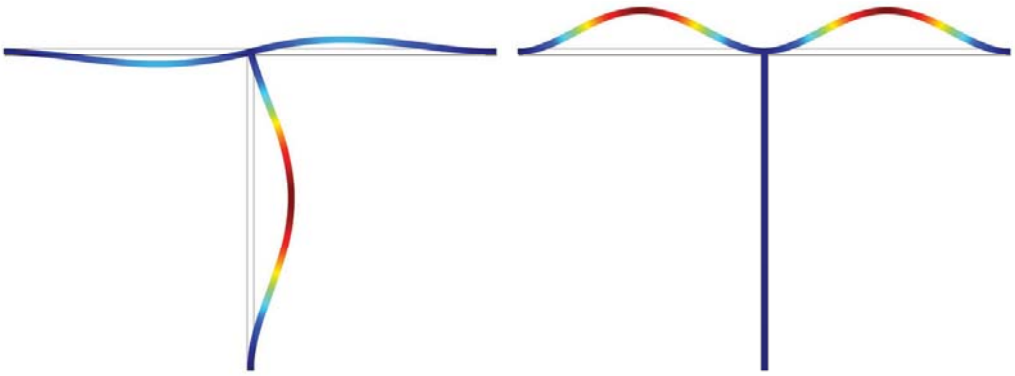

Figure 7. Initial design and the two coupled linear vibration modes obtained using COMSOL modal analysis. Left: linear vibration mode 1, right: linear vibration mode 2, and $\omega_2 \approx 2\omega_1$. The color in online version indicates the vibration amplitude.

We present an example of two-to-one internal resonance for which the normal form has a single important inter-modal coupling term. This example is motivated by a MEMS frequency divider that makes use of internal resonance, for which a general theory is presented in [6]. The structure considered is also similar to other proposed MEMS devices developed for filtering [30, 31]. In these structures two vibrational modes can exchange energy during free vibration. For convenience, we will refer to modes p_1 and p_2 as modes 1 and 2, respectively, in our discussion.

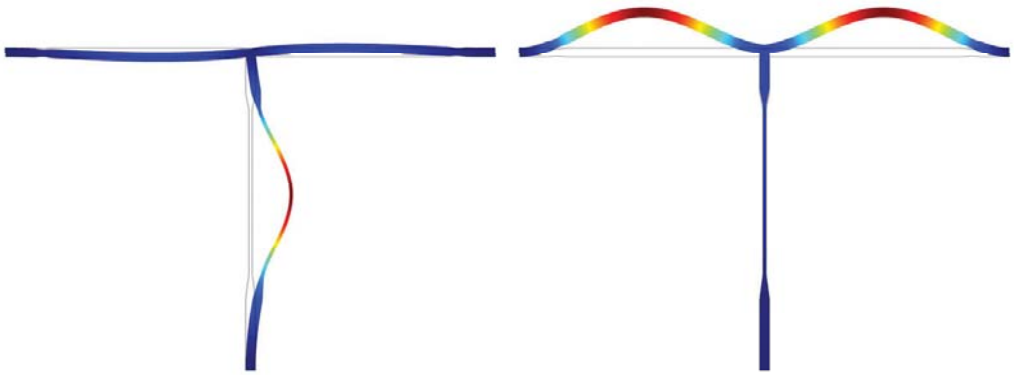

Figure 8. Optimized design for maximizing the absolute value of the *essential* modal coupling coefficient and the two coupled linear vibration modes obtained using COMSOL modal analysis. Left: linear vibration mode 1, right: linear vibration mode 2 and $\omega_2 \approx 2\omega_1$. The color in online version indicates the vibration amplitude.

The divider device consists of two localized modes with $\omega_{p_2} \approx 2\omega_{p_1}$, which provides a division by two in frequency, as measured in mode 1, when mode 2 is driven near its resonance. The term "localized mode" indicates that the dominant vibration associated with the mode occurs in a localized part of the structure, even though the entire structure is generally involved in the modal vibration. For instance, for the T-bar structure shown in Fig. 7, the vibration of mode 1 is localized in the vertical beam and the vibration of mode 2 is localized in the horizontal beam. In operation, a harmonic load with frequency close to ω_2 is applied to drive mode 2 into resonance. When the amplitude of mode 2 is sufficiently large, it will induce the vibration of mode 1 due to the parametric pumping, wherein the transverse vibration of the horizontal beam provides an axial force in the vertical beam, which in turn induces transverse motion of the vertical beam when the frequency of the horizontal beam is approximately twice that of the vertical beam. The response of the structure is governed by a model in which these two modes are coupled through resonant terms. In application, n such elements are linked to achieve division by 2^n; division by eight has been experimentally achieved [32]. The reduced order dynamic model with its conservative dynamics projected onto two nonlinear normal modes in curved, normal coordinates is written as

$$\begin{aligned}&\ddot{R}_1 + \omega_1^2 R_1 + (g_{12}^1 + g_{21}^1) R_2 R_1 + (A_{111}^1 + h_{111}^1) R_1^3 + B_{111}^1 R_1 \dot{R}_1^2 \\ &\quad + \left[(A_{212}^1 + A_{122}^1 + h_{122}^1 + h_{212}^1 + h_{221}^1) R_2^2 + B_{122}^1 \dot{R}_2^2 \right] R_1 + \left(B_{212}^1 R_2 \dot{R}_2 \right) \dot{R}_1 = 0 \end{aligned} \tag{3.12}$$

$$\begin{aligned}&\ddot{R}_2 + \omega_2^2 R_2 + g_{11}^2 R_1^2 + (A_{222}^2 + h_{222}^2) R_2^3 + B_{222}^2 R_2 \dot{R}_2^2 \\ &\quad + \left[(A_{112}^2 + A_{211}^2 + h_{112}^2 + h_{121}^2 + h_{211}^2) R_1^2 + B_{211}^2 \dot{R}_1^2 \right] R_2 + \left(B_{112}^2 R_1 \dot{R}_1 \right) \dot{R}_2 = 0 \end{aligned} \tag{3.13}$$

where the explicit expressions of A_{ijk}^p and B_{ijk}^p are given in [24]. The key term of interest is that associated with the *essential* modal coupling coefficients g_{12}^1, g_{21}^1 and g_{11}^2, since they are the terms in the normal form that describes the resonant nonlinear coupling terms that promote energy exchange between the modes. These modal coupling coefficients can also be observed from the governing equation with its dynamics projected onto two linear modes, which is written as

$$\begin{aligned} \ddot{q}_1 + \omega_1^2 q_1 + (g_{12}^1 + g_{21}^1) q_1 q_2 + g_{11}^1 q_1^2 + h_{111}^1 q_1^3 + \text{others} &= f_1(t) \\ \ddot{q}_2 + \omega_2^2 q_2 + g_{11}^2 q_1^2 + g_{22}^2 q_2^2 + h_{222}^2 q_2^3 + \text{others} &= f_2(t) \end{aligned} \tag{3.14}$$

where the most important coefficients are g_{12}^1, g_{21}^1 and g_{11}^2, between which there is an exact relation $g_{12}^1 + g_{21}^1 = 2g_{11}^2$. The reason for this exact relation is that the coefficients of $q_1 q_2$ and q_1^2 in Eq. (3.14) arise from differentiation of the term $\beta q_1^2 q_2$ in the Hamiltonian $\mathcal{H}$ with respect to q_1 and

q_2, where $\beta = \alpha^{(3)}_{112} + \alpha^{(3)}_{121} + \alpha^{(3)}_{211}$. In fact, this example is particularly attractive for demonstrating the present approach since energy exchange between the modes can be described (to leading order) by this single nonlinear term. Also, as observed in the equation for q_1 in the reduced order model, β is essentially the amplitude of the parametric excitation provided to mode 1 from mode 2, given by $2\beta_1 q_2 q_1$, and is therefore related to the stability region of the linear parametric resonance of q_1. The q_1^2 term in the equation for q_2 captures the back-coupling of the driven mode onto the driving mode, as required for passive coupling, which is beneficial in frequency dividers [32]. The combined effect of this coupling is the possibility of energy transfer between the modes when there is a two-to-one internal resonance.

The optimization problem for this resonance is therefore formulated as

$$\begin{aligned} \min_{\rho_e} \quad & c = -\left|\alpha^{(3)}_{112} + \alpha^{(3)}_{121} + \alpha^{(3)}_{211}\right| \\ \text{s.t.} \quad & |\omega_1/\omega_2 - 1/2| \leq \epsilon \end{aligned} \tag{3.15}$$

where $\epsilon = 0.001$ and additional constraints are imposed as in Eq. (2.13). The sensitivity is computed with Eq. (2.19) written as

$$\frac{\mathrm{d}c}{\mathrm{d}\rho_e} = S \cdot \left(\frac{\partial \alpha^{(3)}_{112}}{\partial \rho_e} + \frac{\partial \alpha^{(3)}_{121}}{\partial \rho_e} + \frac{\partial \alpha^{(3)}_{211}}{\partial \rho_e}\right) + \sum_{p=1}^{2}\left[\boldsymbol{\lambda}_p^T\left(\omega_p^2 \frac{\partial \mathbf{M}}{\partial \rho_e} - \frac{\partial \mathbf{K}}{\partial \rho_e}\right)\boldsymbol{\Phi}_p + \eta_p \boldsymbol{\Phi}_p^T \frac{\partial \mathbf{M}}{\partial \rho_e}\boldsymbol{\Phi}_p\right] \tag{3.16}$$

where $S = -\mathrm{sign}\left(\alpha^{(3)}_{112} + \alpha^{(3)}_{121} + \alpha^{(3)}_{211}\right)$. It is noted that there are two groups of adjoint variables, $\boldsymbol{\lambda}_1$ and η_1, $\boldsymbol{\lambda}_2$ and η_2, corresponding to the two vibration modes. These two groups of adjoint variables are solved using adjoint equation in Eq. (2.20) with $p = 1,\ 2$.

For a specific example the length of the horizontal beam is taken to be 300 µm and the length of the vertical beam is taken to be 195.5 µm, so that $\omega_2 \approx 2\omega_1$.The lengths of the two beams are fixed during the optimization. The initial in-plane thickness is uniformly 4 µm along both beams, and the in-plane thickness is bounded between 2 µm and 6 µm during the optimization. The material properties are the same as in example 1. An optimized design and its two important vibration modes are displayed in Fig. 8. Evolution of the objective function and optimized designs over iterations are displayed in Fig. 9.

In order to demonstrate the effects of tuning and optimizing the coupling nonlinearity in this example, we carry out simulations of the structure for different shapes encountered during the optimization iteration process. With this internal resonance and zero damping, free vibrations of the system will exhibit energy exchange between the modes in a beating type response, whose features depend crucially on the magnitude of the coupling coefficient and the initial conditions, as well as the other system parameters. For each structural shape and initial amplitude of the starting mode, the exchange of energy has a particular beat period; this period will be shorter for higher starting amplitudes and for larger values of the coupling coefficient, since both these effects enhance the nonlinear modal coupling. The left panel of Figure 10 shows a typical response obtained from the finite element model of the final (optimized) shape, obtained by initiating the response using the second linear mode at a moderate amplitude. The right panel of Figure 10 shows the normalized beat period for several values of the initial energy for three different designs, that is, for three different values of the coupling coefficient. The predicted trends are evident as both the coupling coefficient and initial amplitude are varied. Note that it would be also worthwhile to compare results from the finite element model with simulations and analysis of the reduced two mode model, but this requires a more detailed study of the effects of all nonlinear coefficients that vary during the optimization process.

Evolution of the eigenfrequencies of linear vibration modes 1 and 2 encountered over iterations of the optimization process is displayed in Fig. 11(a). Other measures of interest for this system are (i) the degree of spatial energy localization in the vertical beam of the first vibration mode (note that from symmetry the second vibration mode has perfect localization) and (ii) the effectiveness of the horizontal beam in parametrically pumping the vertical beam in the second mode. The

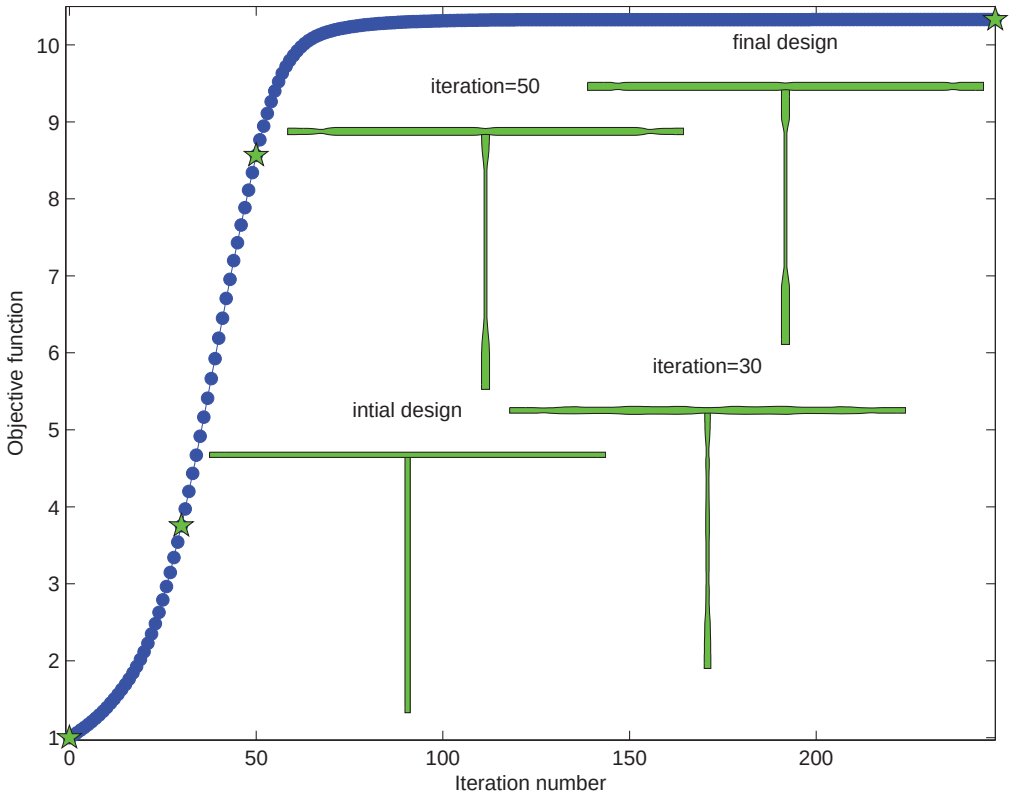

Figure 9. Evolution of the objective function and shapes encountered during the optimization process. The vertical axis is the absolute value of the objective function divided by its initial value and the horizontal axis is the iteration number.

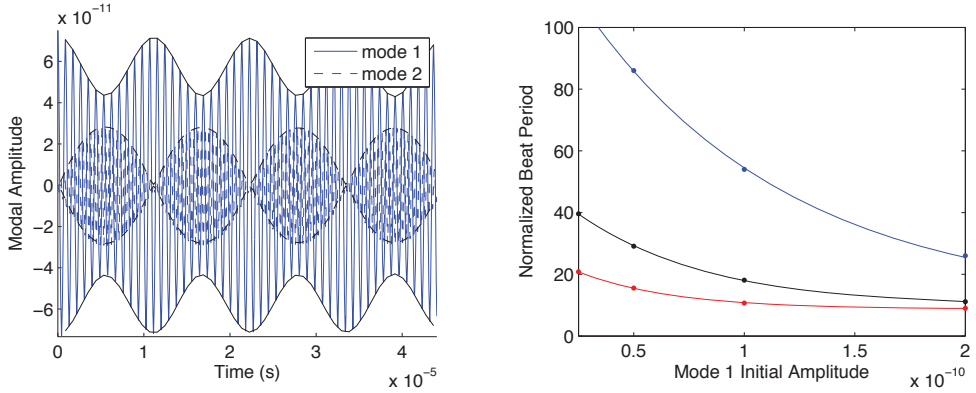

Figure 10. Left: Typical time simulation with added envelope curves showing beats, for the final design with initial first mode amplitude of 7.5×10^{-11} (using eigenvectors normalized by the mass matrix). Right: Data points and fitted exponential curves for the beat period, normalized by the period of the first linear mode, versus the initial amplitude of the first mode, for designs corresponding to iteration numbers 0 (initial design, top curve), 30 (middle curve), and 250 (final design, bottom curve).

localization of the first mode is measured by the maximum transverse amplitude of the horizontal beam divided by the maximum transverse amplitude of the vertical beam. Likewise, the pumping effectiveness of the horizontal beam in the second mode is measured by the ratio of the transverse vibration at the midspan of the horizontal beam to the maximum transverse vibration of the same beam, which occurs near the quarter spans. The results in Fig. 11(b) show that the localization ratio decreases during optimization, which indicates improved localization, and the pumping ratio increases, which indicates enhanced coupling of the two modes. The intuition of the optimized design is that the axial deformation along the vertical beam increases with a larger end mass and a thinner cross section, both of them occur in the optimized design.w

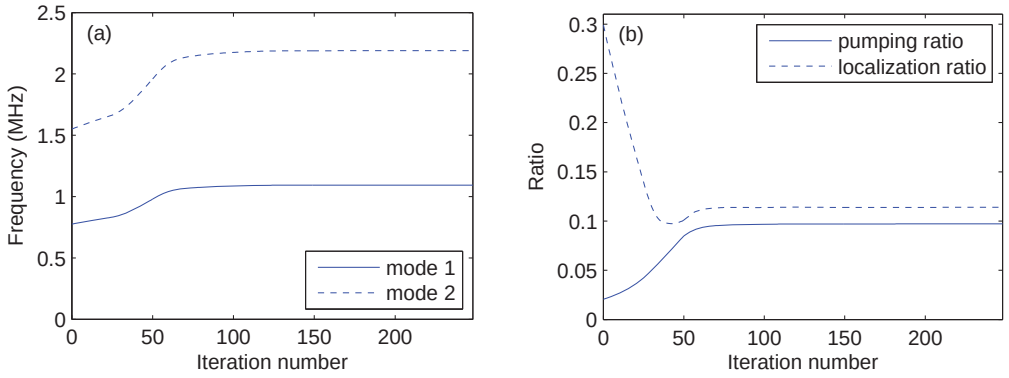

Figure 11. (a) Evolution of eigenfrequencies of linear vibration mode 1 and 2 encountered during the optimization process. (b) Evolution of pumping ratio and localization ratio encountered during the optimization process.

4. Conclusions

A systematic procedure is proposed for characterization and optimal design of nonlinear resonators from finite element models. The method makes use of a means of computing terms in normal forms from nonlinear finite element models and uses sensitivities to update design parameters to vary a given objective function, subject to constraints. The proposed procedure is demonstrated on the optimization of the nonlinear modal stiffness of a single-mode resonator and the optimization of an essential inter-mode coupling term in a resonator with two internally resonant modes. It is shown that quite simple shape alterations can provide significant changes in these nonlinear effects. Thus, this approach offers an important tool for the development of structures with desired nonlinear behaviour, which has particular applicability in micro-systems. Of course, these nonlinear features have a significant effect on the forced response of the system, and this is where most applications will benefit from tailoring the nonlinear response of the system. Also, it is interesting to note that by minimizing the nonlinearity in a single mode structure, one can achieve a larger range of vibration amplitudes over which the system behaves according to a linear model; this may be of significant benefit in applications where one wishes to maximize the linear dynamic range of the device, for example, in frequency sources (oscillators) in which resonating elements are employed in a feedback loop to generate a periodic signal.

Current efforts are focused on experimentally verifying the approach and applying it to specific devices for frequency generation and conversion. Also, although only planar structures with geometrically stiffness nonlinearities are considered in the paper, it is possible to extend the methods to include material nonlinearities, inertial nonlinearities, nonlinear electrostatic forces, and three dimensional physics; these are especially simple for effects that can be modeled by a potential. One can also allow for more variability in structural shapes, for example, by allowing

beam lengths to change, and one can impose additional frequency constraints, which could be important in applications. In addition, varying the shape of the structure changes all coefficients in the reduced two mode model, and these in turn affect the response, so more specific applications may require the use of objective functions that depend on several nonlinear coefficients. Also, while shape optimization is considered here, the philosophy of the present approach can also be applied using topology optimization, which may offer more elaborate structural configurations with better results than can be achieved by shape optimization. Work along these lines for structural models based on hyperelastic materials has recently been reported [33].

Acknowledgements

This project was supported by ERC Starting Grant 279529 INNODYN, US NSF Grant #1234067, and DARPA-MTO-DEFYS. Special thanks to O. Shoshani, K. Turner, D. Czaplewski, D. Lopez, T. Kenny, and C. Touzé for inspiring applications and useful discussions. S. Dou thanks Otto Mønsteds Fond and Thomas B. Thriges Fond for supporting his research stay in Michigan State University in 2014.

Appendix

The linear and nonlinear formulation of the beam element used here can be found in the article [18]. Its nonlinear modal coupling coefficients in the Hamiltonian $\mathcal{H}$ can be written as

$$\alpha^{(3)}_{ijk} = \sum_{e=1}^{N_e} \frac{EA}{2} \left(\mathbf{B}_0^p \mathbf{u}_i^e\right) \left((\mathbf{w}_j^e)^T \mathbf{K}_g \mathbf{w}_k^e\right)$$

$$\alpha^{(4)}_{ijkl} = \sum_{e=1}^{N_e} \frac{EA}{8L} \left((\mathbf{w}_i^e)^T \mathbf{K}_g \mathbf{w}_j^e\right) \left((\mathbf{w}_k^e)^T \mathbf{K}_g \mathbf{w}_l^e\right)$$

where E is Young's modulus, A is cross section area, $\mathbf{u}^e$(the longitudinal displacements) and $\mathbf{w}^e$(the transverse displacements) are obtained from the element-wise eigenvector $\boldsymbol{\Phi}^e$ projected onto the element coordinates, the subscripts i, j and k indicate the order of the eigenvector, and with L denoting the element length $\mathbf{B}_0^p$ and $\mathbf{K}_g$ are expressed as

$$\mathbf{B}_0^p = \begin{bmatrix} -1/L & 1/L \end{bmatrix}, \quad \mathbf{K}_g = \frac{1}{30L} \begin{bmatrix} 36 & 3L & -36 & 3L \\ 3L & 4L^2 & -3L & -L^2 \\ -36 & -3L & 36 & -3L \\ 3L & -L^2 & -3L & 4L^2 \end{bmatrix}$$

References

1. J. F. Rhoads, S. W. Shaw, and K. L. Turner, "Nonlinear dynamics and its applications in micro- and nanoresonators," *Journal of Dynamic Systems, Measurement, and Control*, vol. 132, no. 3, p. 034001, 2010.
2. S. P. Beeby, R. N. Torah, M. J. Tudor, P. Glynne-Jones, T. O'Donnell, C. R. Saha, and S. Roy, "A micro electromagnetic generator for vibration energy harvesting," *Journal of Micromechanics and Microengineering*, vol. 17, no. 7, pp. 1257–1265, 2007.
3. B. Jeong, H. Cho, M.-F. Yu, A. F. Vakakis, D. M. McFarland, and L. A. Bergman, "Modeling and measurement of geometrically nonlinear damping in a microcantilever-nanotube system," *ACS Nano*, vol. 7, no. 10, pp. 8547–8553, 2013.
4. W. Zhang, R. Baskaran, and K. L. Turner, "Effect of cubic nonlinearity on auto-parametrically amplified resonant mems mass sensor," *Sensors and Actuators A: Physical*, vol. 102, no. 1-2, pp. 139 – 150, 2002.
5. L. A. Oropeza-Ramos, C. B. Burgner, and K. L. Turner, "Robust micro-rate sensor actuated by parametric resonance," *Sensors and Actuators A: Physical*, vol. 152, no. 1, pp. 80–87, 2009.
6. B. S. Strachan, S. W. Shaw, and O. Kogan, "Subharmonic resonance cascades in a class of coupled resonators," *Journal of Computational and Nonlinear Dynamics*, vol. 8, no. 4, p. 041015, 2013.

7. D. Antonio, D. H. Zanette, and D. Lopez, "Frequency stabilization in nonlinear micromechanical oscillators," *Nat Commun*, vol. 3, p. 806, May 2012.
8. H. Cho, B. Jeong, M.-F. Yu, A. F. Vakakis, D. M. McFarland, and L. A. Bergman, "Nonlinear hardening and softening resonances in micromechanical cantilever-nanotube systems originated from nanoscale geometric nonlinearities," *International Journal of Solids and Structures*, vol. 49, no. 15-16, pp. 2059 – 2065, 2012.
9. X. Dai, X. Miao, L. Sui, H. Zhou, X. Zhao, and G. Ding, "Tuning of nonlinear vibration via topology variation and its application in energy harvesting," *Appl. Phys. Lett.*, vol. 100, JAN 16 2012.
10. A. Tripathi and A. K. Bajaj, "Computational synthesis for nonlinear dynamics based design of planar resonant structures," *Journal of Vibration and Acoustics*, vol. 135, no. 5, p. 051031, 2013.
11. N. L. Pedersen, "Designing plates for minimum internal resonances," *Structural and Multidisciplinary Optimization*, vol. 30, no. 4, pp. 297–307, 2005.
12. J. Guckenheimer and P. Holmes, *Nonlinear oscillations, dynamical systems, and bifurcations of vector fields*.
    New York Springer Verlag, 1983.
13. J. S. Jensen and B. S. Lazarov, "Optimization of non-linear mass damper parameters for transient response," in *Proceedings of the Sixth EUROMECH Nonlinear Dynamics Conference* (B. Andrievsky and A. Fradkov, eds.), 2008.
14. Y.-I. Kim and G.-J. Park, "Nonlinear dynamic response structural optimization using equivalent static loads," *Computer Methods in Applied Mechanics and Engineering*, vol. 199, no. 9-12, pp. 660–676, 2010.
15. B. Stanford, P. Beran, and M. Kurdi, "Adjoint sensitivities of time-periodic nonlinear structural dynamics via model reduction," *Computers and Structures*, vol. 88, no. 19-20, pp. 1110–1123, 2010.
16. E. P. Petrov, "Advanced analysis and optimization of nonlinear resonance vibrations in gas-turbine structures with friction and gaps," *IUTAM Symposium on Emerging Trends in Rotor Dynamics*, vol. 25, pp. 297–307, 2011.
17. G. H. Yoon, "Maximizing the fundamental eigenfrequency of geometrically nonlinear structures by topology optimization based on element connectivity parameterization," *Computers and Structures*, vol. 88, no. 1-2, pp. 120–133, 2010.
18. S. Dou and J. S. Jensen, "Optimization of nonlinear structural resonance using the incremental harmonic balance method," *Journal of Sound and Vibration*, vol. 334, pp. 239 – 254, 2015.
19. W. Ye, S. Mukherjee, and N. MacDonald, "Optimal shape design of an electrostatic comb drive in microelectromechanical systems," *Journal of Microelectromechanical Systems*, vol. 7, no. 1, pp. 16–26, 1998.
20. B. Jensen, S. Mutlu, S. Miller, K. Kurabayashi, and J. Allen, "Shaped comb fingers for tailored electromechanical restoring force," *Journal of Microelectromechanical Systems*, vol. 12, no. 3, pp. 373–383, 2003.
21. C. Guo and G. K. Fedder, "A quadratic-shaped-finger comb parametric resonator," *Journal of Micromechanics and Microengineering*, vol. 23, no. 9, p. 095007, 2013.
22. A. Lazarus, O. Thomas, and J. F. Deue, "Finite element reduced order models for nonlinear vibrations of piezoelectric layered beams with applications to nems," *Finite Elements in Analysis and Design*, vol. 49, no. 1, pp. 35–51, 2012.
23. C. Touzé, M. Vidrascu, and D. Chapelle, "Direct finite element computation of non-linear modal coupling coefficients for reduced-order shell models," *Computational Mechanics*, pp. 1–14, 2014.
24. C. Touzé, O. Thomas, and A. Chaigne, "Hardening/softening behaviour in non-linear oscillations of structural systems using non-linear normal modes," *Journal of Sound and Vibration*, vol. 273, no. 1, pp. 77–101, 2004.
25. C. Touzé and M. Amabili, "Nonlinear normal modes for damped geometrically nonlinear systems: Application to reduced-order modelling of harmonically forced structures," *Journal of Sound and Vibration*, vol. 298, no. 4-5, pp. 958–981, 2006.
26. N. L. Pedersen, "Design of cantilever probes for atomic force microscopy (afm)," *Engineering Optimization*, vol. 32, no. 3, pp. 373–392, 2000.
27. L. Li, Y. Hu, and X. Wang, "Design sensitivity and hessian matrix of generalized eigenproblems," *Mechanical Systems and Signal Processing*, vol. 43, no. 1-2, pp. 272–294, 2014.
28. D. A. Tortorelli and P. Michaleris, "Design sensitivity analysis: overview and review," *Inverse problems in Engineering*, vol. 1, no. 1, pp. 71–105, 1994.

29. K. Svanberg, "The method of moving asymptotes—a new method for structural optimization," *International Journal for Numerical Methods in Engineering*, vol. 24, no. 2, pp. 359–373, 1987.
30. A. Vyas, D. Peroulis, and A. K. Bajaj, "Dynamics of a nonlinear microresonator based on resonantly interacting flexural-torsional modes," *Nonlinear Dynamics*, vol. 54, no. 1-2, pp. 31–52, 2008.
31. A. Vyas, D. Peroulis, and A. K. Bajaj, "A microresonator design based on nonlinear 1: 2 internal resonance in flexural structural modes," *Microelectromechanical Systems, Journal of*, vol. 18, no. 3, pp. 744–762, 2009.
32. K. Qalandar, B. Strachan, B. Gibson, M. Sharma, A. Ma, S. Shaw, and K. Turner, "Frequency division using a micromechanical resonance cascade," *Applied Physics Letters*, vol. 105, no. 24, p. 244103, 2014.
33. A. Tripathi and A. K. Bajaj, "Design for 1: 2 internal resonances in in-plane vibrations of plates with hyperelastic materials," *Journal of Vibration and Acoustics*, vol. 136, no. 6, p. 061005, 2014.

Publication [P3]

Optimization of hardening/softening behavior of plane frame structures using nonlinear normal modes

Optimization of hardening/softening behavior of plane frame structures using nonlinear normal modes

Suguang Dou, Jakob Søndergaard Jensen

Abstract

Novel devices that exploit essential nonlinear behavior such as hardening/softening and inter-modal coupling effects are increasingly used in engineering and fundamental studies. Based on nonlinear normal modes, this paper presents a gradient-based structural optimization for tailoring the hardening/softening behavior of nonlinear mechanical systems. In the iterative optimization, one iteration consists of calculation of nonlinear normal modes, solving an adjoint equation system, calculation of sensitivities with solved adjoint variables, and an update of design variables. Examples involving plane frame structures are presented where the hardening/softening behavior is qualitatively and quantitatively tuned by simple changes in the geometry of these structures.

Keywords: finite element, structural optimization, nonlinear normal mode, harmonic balance, adjoint method, hardening/softening behavior

1 Introduction

Linear normal modes (LNMs) play a significant role in design optimization of mechanical components for their dynamic response. When applied to nonlinear mechanical systems, this may lead to sub-optimal designs because of the unresolved nonlinear behaviors such as frequency-energy dependence and internal resonances.Moreover, a variety of novel applications that exploit these essentially nonlinear behaviors are increasingly used, e.g. in engineering for vibration mitigation [1, 2, 3], and particularly in nonlinear micromechanical and nanomechanical resonators for energy harvesting [4], frequency stabilization [5, 6], frequency division [7], etc. For a comprehensive review of nonlinear micro- and nanoresonators, the reader may consult [8, 9]. Since structural

optimization of these inherently nonlinear devices cannot be fully achieved using linear structural dynamics, it is of considerable value to develop efficient techniques for structural optimization based on nonlinear structural dynamics.

As a nonlinear analog of LNMs, nonlinear normal modes (NNMs) provides a systematic way to investigate the nonlinear behavior in nonlinear structural dynamics, particularly frequency-energy dependence and modal interactions [10]. The resulting NNMs also provide valuable insight into the damped system. For example, the temporal evolution of the instantaneous frequencies in free decay responses follows NNMs of the undamped system. Based on this feature, free decay tests in conjunction with continuous wavelet transform have been used in experimental analysis of NNMs [11]. Further, the nonlinear forced resonances are in the neighborhood of NNMs. This feature is of practical importance in engineering design, e.g., dynamic tests of NNMs in forced vibrations [12] and efficient optimization of nonlinear resonance peak [13, 14, 15]. Computation of NNMs using numerical methods [16], particularly harmonic balance method [17, 18, 19], is especially attractive for their abilities to be combined with nonlinear finite element models, which facilitate element-based design parameterization of structural geometry and further application of advanced structural optimization (e.g., shape optimization, topology optimization) [20]. In previous study, based on normal form linked to NNM [21, 22] , we studied structural optimization of hardening/softening behavior [23], where the analysis and optimization is limited to mechanical systems with polynomial-type nonlinearity.

For general applicability, nonlinear normal modes can be numerically computed using harmonic balance method [13] in conjunction with the alternating frequency/time domain method (AFT) [24], which has the ability to handle complex nonlinearity. Based on the resulting NNMs, we propose a gradient-based structural optimization formulation for tailoring hardening/softening behavior of nonlinear mechanical systems. For a relatively comprehensive review of the hardening/softening behavior, the reader can refer to [22, 25]. Examples involving plane frame structures are used to demonstrate that both quantitative and qualitative tuning of hardening/softening behavior (e.g. from softening behavior to hardening behavior, and vice versa) can be achieved by a simple manipulation of the structural geometry. In the analysis, these structures are modeled by using beam element based on the geometrically exact theory [26, 27], which does not make any approximation of the trigonometric functions arising in kinematics and hence can be used for vibrations with large in-plane motion. Since NNM is a nonlinear analogy of LNM, the proposed optimization methodology can also be viewed as an extension of the optimization of eigenvalue problems in linear structural

dynamics (e.g., eigenvalues and eigenvectors) [28, 29, 30, 31].

The article is organized as follows. First, computation of NNM using incremental harmonic balance (IHB) in conjunction with the alternating frequency/time domain method is presented in section 2. In section 3, a general optimization problem for tuning NNM with hardening/softening behavior and its sensitivity analysis are formulated. Optimization examples for tailoring the hardening/softening behavior of plane frame structures are presented in section 4 and conclusions are drawn in section 5.

2 Nonlinear modal analysis

An ideal starting point in numerical computation of NNM is continuation of periodic responses in the neighborhood of a LNM. In this case, the NNM reduces to a LNM when the vibration amplitude is sufficiently small. In computation of the NNM for plane frame structures, IHB is applied to a nonlinear finite element model. In contrast to the time marching method widely used in nonlinear structural dynamics, IHB is an efficient way to compute the time-periodic response by describing it into Fourier series and solving a set of nonlinear algebraic equations in terms of the Fourier coefficients and the frequency. In the continuation, with a given initial guess or the responses in previous steps, the unknown response in the neighborhood is first predicted and then iteratively corrected.

2.1 Harmonic balance method

The equation of motion of a discretized undamped mechanical system (e.g., a nonlinear finite element model without dissipation and load) is assumed as

$$\mathbf{M}\ddot{\mathbf{q}}(t) + \mathbf{g}(\mathbf{q}(t)) = \mathbf{0} \tag{1}$$

where $\mathbf{q}(t)$ denotes time-periodic response to be solved, $\mathbf{M}$ is the symmetric and positive definite mass matrix, and $\mathbf{g}(\mathbf{q})$ denotes the nonlinear stiffness force. Further, the differentiation of $\mathbf{g}(\mathbf{q})$ with respect to $\mathbf{q}$, denoted as $\mathbf{K}(\mathbf{q})$, is the symmetric tangent stiffness matrix.

First, a new time scale τ is introduced as $\tau = \omega t$, where $\omega = 2\pi/T$ and T is the fundamental period of the response. So the equation of motion in Eq. (1) can be rewritten as

$$\omega^2 \mathbf{M}\mathbf{q}''(\tau) + \mathbf{g}(\mathbf{q}(\tau)) = \mathbf{0} \tag{2}$$

where the prime indicates the differentiation with respect to the new time scale τ. It is noted that with the new time scale, the fundamental period

of the system response is normalized to 2π. Then the system response is expanded into Fourier series. For the displacement of one degree of freedom, e.g. $q_i(\tau)$, its Fourier series is expressed as

$$q_i(\tau) = a_{i0} + \sum_{n=1}^{N_H} \left(a_{in}\cos(n\tau) + b_{in}\sin(n\tau)\right) \tag{3}$$

where i denotes the ith degree of freedom in the finite element model, n denotes the nth-order harmonic, N_H is the highest order of retained harmonics. In matrix form, Eq. (3) is written as

$$q_i(\tau) = \mathbf{s}\,\overline{\mathbf{q}}_i \tag{4}$$

where $\mathbf{s}$ and $\overline{\mathbf{q}}_i$ represent the bases and the retained Fourier coefficients of $q_i(\tau)$, definied as

$$\begin{aligned} \mathbf{s} &= \begin{bmatrix} 1 & \cos\tau & \dots & \cos(_{N_H}\tau) & \sin\tau & \dots & \sin(_{N_H}\tau) \end{bmatrix} \\ \overline{\mathbf{q}}_i &= \begin{bmatrix} a_{i0} & a_{i1} & \dots & a_{iN_H} & b_{i1} & \dots & b_{iN_H} \end{bmatrix}^T \end{aligned} \tag{5}$$

Based on the Fourier series of the displacement of one degree of freedom, the Fourier series of the displacements of all degrees of freedom are now written as

$$\mathbf{q}(\tau) = \mathbf{S}\,\overline{\mathbf{q}} \tag{6}$$

where $\mathbf{S}$ denotes a set of Fourier basis and $\overline{\mathbf{q}}$ collects the corresponding Fourier coefficients of the displacements of all degrees of freedom, i.e.

$$\mathbf{S} = \mathbf{diag}\left(\begin{bmatrix}\mathbf{s} & \dots & \mathbf{s}\end{bmatrix}\right), \quad \overline{\mathbf{q}} = \begin{bmatrix}\overline{\mathbf{q}}_1^T & \dots & \overline{\mathbf{q}}_{N_D}^T\end{bmatrix}^T \tag{7}$$

and N_D denotes the number of degrees of freedom of the finite element model.

To determine the Fourier coefficients and the frequency of the response, the Galerkin method is applied to the ordinary differential equation in Eq. (2). By substituting Eq. (6) into Eq. (2), multiplying Eq. (2) with $\mathbf{S}^T$ and performing integration with respect to τ on $[0,\ 2\pi]$, one algebraic equation system is obtained as

$$\omega^2\,\overline{\mathbf{M}}\,\overline{\mathbf{q}} + \overline{\mathbf{g}} = \mathbf{0} \tag{8}$$

where the barred terms $\overline{\mathbf{M}}$ and $\overline{\mathbf{g}}$ are given as

$$\overline{\mathbf{M}} = \frac{1}{2\pi}\int_0^{2\pi} \mathbf{S}^T\mathbf{M}\mathbf{S}''\,\mathrm{d}\tau, \quad \overline{\mathbf{g}} = \frac{1}{2\pi}\int_0^{2\pi} \mathbf{S}^T\mathbf{g}(\mathbf{q}(\tau))\,\mathrm{d}\tau \tag{9}$$

It is noted that Eq. (8) can be viewed as the frequency-domain counterpart of the equation of motion in Eq. (1), and $\overline{\mathbf{M}}$ and $\overline{\mathbf{g}}$ can be interpreted as the frequency-domain counterparts of $\mathbf{M}$ and $\mathbf{g}$, respectively.

Since the algebraic equation system in Eq. (8) is nonlinear, we use an iterative Newton-Raphson method to solve it. This requires the incremental form of Eq. (8), which is written as

$$\left(\omega^2\,\overline{\mathbf{M}}+\overline{\mathbf{K}}\right)\Delta\overline{\mathbf{q}}+\left(2\omega\overline{\mathbf{M}}\,\overline{\mathbf{q}}\right)\Delta\omega=-\left(\omega^2\,\overline{\mathbf{M}}\,\overline{\mathbf{q}}+\overline{\mathbf{g}}\right) \tag{10}$$

where $\overline{\mathbf{K}}$ is the frequency-domain counterpart of the tangent stiffness matrix $\mathbf{K}$, and this relation is derived as

$$\overline{\mathbf{K}}=\frac{1}{2\pi}\int_0^{2\pi}\mathbf{S}^T\frac{\partial\mathbf{g}(\mathbf{q}(\tau))}{\partial\mathbf{q}(\tau)}\frac{\partial\mathbf{q}(\tau)}{\partial\overline{\mathbf{q}}}\,\mathrm{d}\tau=\frac{1}{2\pi}\int_0^{2\pi}\mathbf{S}^T\mathbf{K}(\mathbf{q}(\tau))\mathbf{S}\,\mathrm{d}\tau \tag{11}$$

2.2 Numerical implementation

Due to the time-periodic feature of the system response $\mathbf{q}(\tau)$, the displacement-dependent nonlinear stiffness force $\mathbf{g}(\tau)$ and the tangent stiffness matrix $\mathbf{K}(\tau)$ are also time-periodic. Hence, the entries in the nonlinear stiffness force and tangent stiffness matrix can also be written into Fourier series as

$$\begin{aligned}
g_i(\tau)&=a_{i0}^{\mathrm{g}}+\sum_{n=1}^{N_H}\left(a_{in}^{\mathrm{g}}\cos(n\tau)+b_{in}^{\mathrm{g}}\sin(n\tau)\right)\\
K_{ij}(\tau)&=a_{ij0}^{\mathrm{K}}+\sum_{n=1}^{N_H}\left(a_{ijn}^{\mathrm{K}}\cos(n\tau)+b_{ijn}^{\mathrm{K}}\sin(n\tau)\right)
\end{aligned} \tag{12}$$

where $i,\,j=1,\ldots,N_{\mathrm{D}}$. In our numerical implementation, the Fourier coefficients of $g_i(\tau)$ and $K_{ij}(\tau)$ are evaluated and collected in vector form denoted as

$$\begin{aligned}
\overline{\mathbf{g}}_i&=\begin{bmatrix}a_{i0}^{\mathrm{g}} & a_{i1}^{\mathrm{g}} & \ldots & a_{iN_H}^{\mathrm{g}} & b_{i0}^{\mathrm{g}} & \ldots & b_{iN_H}^{\mathrm{g}}\end{bmatrix}^T\\
\overline{\mathbf{k}}_{ij}&=\begin{bmatrix}a_{ij0}^{\mathrm{K}} & a_{ij1}^{\mathrm{K}} & \ldots & a_{ijN_H}^{\mathrm{K}} & b_{ij0}^{\mathrm{K}} & \ldots & b_{ijN_H}^{\mathrm{K}}\end{bmatrix}^T
\end{aligned} \tag{13}$$

After evaluating the Fourier coefficients for all entries in the nonlinear stiffness force and tangent stiffness matrix, the resulting vectors are used to construct $\overline{\mathbf{g}}$ and $\overline{\mathbf{K}}$. Finally, the frequency-domain governing equation Eq. (8) is solved by using its incremental form Eq. (10) using continuation methods. The remaining part of this subsection discusses the approach for evaluating $\mathcal{F}(g_i(\tau))$ and $\mathcal{F}(K_{ij}(\tau))$, how to construct the barred quantities $\overline{\mathbf{g}}$, $\overline{\mathbf{K}}$ and $\overline{\mathbf{M}}$, and how to perform continuation of the time-periodic response.

Evaluation of general nonlinearity

For a polynomial-type nonlinearity (e.g., q_i^2), the Fourier coefficients can directly be evaluated based on the Fourier coefficients of the system response (e.g., q_i). This can be done by substituting the Fourier expansion of the response into the nonlinear expression and expanding the terms into a new Fourier series, see [32, 33, 13]. For general applicability and convenience in implementation, the alternating frequency/time domain method is used in this paper and applied for a "geometrically exact" beam element involving trigonometric nonlinearities.

In the first step, the response described with the Fourier coefficients in the initial structural configuration or previous step/iteration is transferred into the time domain by evaluating Eq. (3) at a series of time points: $\tau_n = 2\pi(n-1)/N_T$ where $n = 1, \ldots, N_T$, N_T denotes the number of time points. Note, that $\tau = 2\pi$ is not included in the time points. With the given Fourier coefficients of $\overline{\mathbf{q}}_i$, its time-domain representation is calculated as

$$\widetilde{\mathbf{q}}_i = \mathbf{W}_{\text{ifft}}\ \overline{\mathbf{q}}_i \tag{14}$$

where $\widetilde{\mathbf{q}}_i$ represents a discretized time sequence of $q_i(\tau)$, and $\mathbf{W}_{\text{ifft}}$ is a two-dimensional matrix of size N_T-by-$(2N_H+1)$, defined as

$$\mathbf{W}_{\text{ifft}} = \begin{bmatrix} 1 & \cos\tau_1 & \ldots & \cos(N_H\tau_1) & \sin\tau_1 & \ldots & \sin(N_H\tau_1) \\ \vdots & \vdots & & \vdots & \vdots & & \vdots \\ 1 & \cos\tau_{N_T} & \ldots & \cos(N_H\tau_{N_T}) & \sin\tau_{N_T} & \ldots & \sin(N_H\tau_{N_T}) \end{bmatrix} \tag{15}$$

In the second step, the nonlinear stiffness force and tangent stiffness matrix for the displacements are generated at each of the N_T time points. As a result, N_T nonlinear stiffness force vectors and N_T tangent stiffness matrices are generated. For each entry in the nonlinear stiffness and tangent stiffness matrix, N_{T} values appear, each set forming a time sequence. For clarity, the time sequences of $g_i(\tau)$ and $K_{ij}(\tau)$ are denoted as $\widetilde{\mathbf{g}}_i$ and $\widetilde{\mathbf{k}}_{ij}$.

In the last step, the retained Fourier coefficients of the time sequences of $\widetilde{\mathbf{g}}_i$ and $\widetilde{\mathbf{k}}_{ij}$ are evaluated as

$$\overline{\mathbf{g}}_i = \mathbf{W}_{\text{fft}}\,\widetilde{\mathbf{g}}_i, \quad \overline{\mathbf{k}}_{ij} = \mathbf{W}_{\text{fft}}\,\widetilde{\mathbf{k}}_{ij} \tag{16}$$

where the Fourier transform matrix $\mathbf{W}_{\text{fft}}$ is a two-dimensional matrix with the size of $(2N_H+1)$-by-N_T, defined as

$$\mathbf{W}_{\text{fft}} = \frac{2}{N}\begin{bmatrix} \frac{1}{2} & \cos\tau_1 & \ldots & \cos(N_H\tau_1) & \sin\tau_1 & \ldots & \sin(N_H\tau_1) \\ \vdots & \vdots & & \vdots & \vdots & & \vdots \\ \frac{1}{2} & \cos\tau_{N_T} & \ldots & \cos(N_H\tau_{N_T}) & \sin\tau_{N_T} & \ldots & \sin(N_H\tau_{N_T}) \end{bmatrix}^T \tag{17}$$

The use of $\mathbf{W}_{\text{ifft}}$ and $\mathbf{W}_{\text{fft}}$ is convenient and simple when N_T is small. For large value of N_T, the first and third steps can be equivalently implemented by performing a fast Fourier tansform (FFT). The overall procedure is further illustrated in Fig. 1.

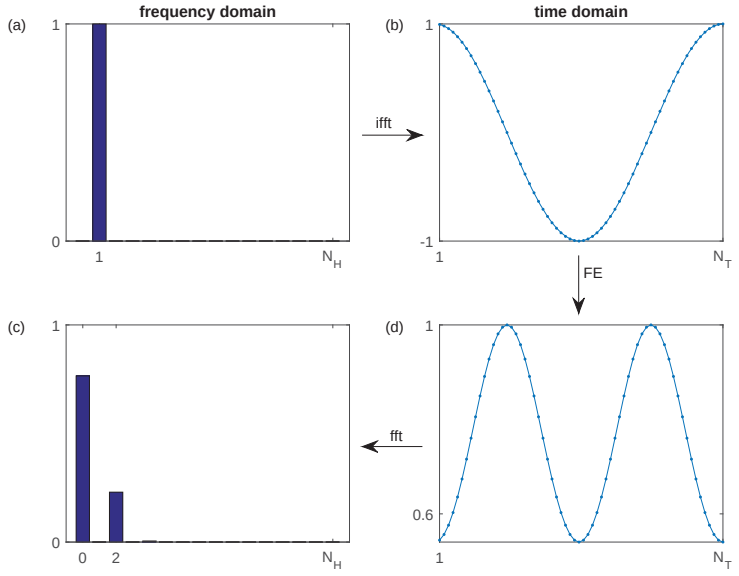

Figure 1: Illustration of the alternating frequency/time domain method for evaluation of the Fourier coefficients of general nonlinearity. (a) the spectrum of system response in frequency domain. (b) the time sequence of system response in time domain. (c) the time sequence of a nonlinear function in time domain. (d) the spectrum of the nonlinear function in frequency domain.

Construction of barred terms

After evaluation of the Fourier coefficients of nonlinearities, the barred terms in the frequency-domain governing equation Eq. (8) and their incremental form Eq. (10) are constructed through

$$\overline{\mathbf{M}} = \left\{ \mathbf{H}^{(0)} M_{ij} \right\}, \ \overline{\mathbf{g}} = \left\{ \mathbf{H}^{(2)} \, \overline{\mathbf{g}}_i \right\}, \ \overline{\mathbf{K}} = \left\{ \sum_l \mathbf{H}_l^{(3)} \, \overline{\mathbf{k}}_{ij}(l) \right\} \tag{18}$$

$\mathbf{H}^{(0)}$ and $\mathbf{H}^{(2)}$ are two-dimensional matrices, $\mathbf{H}_l^{(3)}$ is the lth two-dimensional matrix extracted from a three-dimensional matrix $\mathbf{H}^{(3)}$ with l denoting the third dimension and $\overline{\mathbf{k}}_{ij}(l)$ is the lth entry of $\overline{\mathbf{k}}_{ij}$. The three matrices $\mathbf{H}^{(0)}$,

$\mathbf{H}^{(2)}$ and $\mathbf{H}^{(3)}$ are originally defined in [13] as

$$\begin{aligned}
&\mathbf{H}^{(0)} = \frac{1}{2\pi}\int_0^{2\pi} \mathbf{s}^T\mathbf{s}''\,\mathrm{d}\tau, \quad \mathbf{H}^{(2)} = \frac{1}{2\pi}\int_0^{2\pi} \mathbf{s}^T\mathbf{s}\,\mathrm{d}\tau \\
&\mathbf{H}^{(3)}(m,n,l) = \frac{1}{2\pi}\int_0^{2\pi} \mathbf{s}(m)\,\mathbf{s}(n)\,\mathbf{s}(l)\,\mathrm{d}\tau \\
&l,m,n = 1,\ldots,2N_{\mathrm{H}}+1.
\end{aligned} \tag{19}$$

It is noted that these three matrices depend only on the Fourier basis in Eq. (5), and can therefore be pre-computed. For the explicit expressions, the reader can refer to [13]. For clarity, $\overline{\mathbf{M}}$, $\overline{\mathbf{g}}$ and $\overline{\mathbf{K}}$ in Eq. (18) can also be written as

$$\begin{aligned}
\overline{\mathbf{M}} &= \begin{bmatrix} \mathbf{H}^{(0)}\mathbf{M}_{11} & \cdots & \mathbf{H}^{(0)}\mathbf{M}_{1d} \\ \vdots & \ddots & \vdots \\ \mathbf{H}^{(0)}\mathbf{M}_{d1} & \cdots & \mathbf{H}^{(0)}\mathbf{M}_{dd} \end{bmatrix}, \quad \overline{\mathbf{g}} = \begin{bmatrix} \mathbf{H}^{(2)}\overline{\mathbf{g}}_1 \\ \vdots \\ \vdots \\ \mathbf{H}^{(2)}\overline{\mathbf{g}}_d \end{bmatrix} \\
\overline{\mathbf{K}} &= \begin{bmatrix} \sum_l \mathbf{H}_l^{(3)}\,\overline{\mathbf{k}}_{11}(l) & \cdots & \cdots & \sum_l \mathbf{H}_l^{(3)}\,\overline{\mathbf{k}}_{1d}(l) \\ \vdots & \ddots & & \vdots \\ \sum_l \mathbf{H}_l^{(3)}\,\overline{\mathbf{k}}_{d1}(l) & \cdots & \cdots & \sum_l \mathbf{H}_l^{(3)}\,\overline{\mathbf{k}}_{dd}(l) \end{bmatrix}
\end{aligned} \tag{20}$$

where the subscript d denotes the number of degrees of freedom.

Continuation approaches

We apply two continuation strategies to construct the periodic responses. The simple one is continuation with respect to amplitude or energy, and the more advanced one is a pseudo-arclength method with adaptive steps.

In the so-called amplitude increment approach, one Fourier coefficient, e.g. a_{i1}, is increased in incremental steps. When the value of a_{i1} is given, Δa_{i1} is zero in Eq. (10), and the other Fourier coefficients and the frequency can be solved by using the Newton-Raphson method to minimize the residue. This procedure is convenient to compute NNMs at a moderately large amplitude with hardening/softening behavior. For some applications, it may be difficult to select the characteristic Fourier coefficient. In this case, an energy increment approach can be performed, which is further discussed later.

As the system energy increases, internally resonant NNMs may appear as "tongues" in the frequency-energy plot. In this case, the fixed-step increment method will fail at the turning points. To robustly pass these turning points,

a combination of a cubic polynomial predictor and the arclength method as corrector with adaptive steps can be employed [34, 35, 13].

For further stability analysis and bifurcation switching, the reader can refer to [35, 36, 37].

2.3 Example in nonlinear modal analysis

To validate the effectiveness of the proposed analysis method, we apply it to a generic model that demonstrates the fundamental properties of NNMs. The two-degrees-of-freedom discrete system is written as

$$\begin{aligned} \ddot{x}_1 + 2x_1 - x_2 + 0.5x_1^3 &= 0 \\ \ddot{x}_2 + 2x_2 - x_1 &= 0 \end{aligned} \tag{21}$$

The frequency-energy plot calculated using the method in this paper is displayed in Fig. 2, where the energy is calculated by using the average kinetic energy over the fundamental period as

$$E_{\text{kin}} = \frac{1}{T}\int_0^T \frac{1}{2}(\dot{\mathbf{q}})^T \mathbf{M}\dot{\mathbf{q}}\,\mathrm{d}t = -\frac{\omega^2}{2}\overline{\mathbf{q}}^T\overline{\mathbf{M}}\overline{\mathbf{q}} \tag{22}$$

It is noted that the negative sign is because of the definition of $\overline{\mathbf{M}}$. The frequency-energy dependence and the "tongue" which indicates 1:3 internal resonance agree very well with previous results obtained by using different methods, e.g. shooting method [10] and complex harmonic balance method [18]. In the analysis, the amplitude increment is used for initial steps, and then the arc-length method with a cubic extrapolation is used for robust continuation. As mentioned previously, an alternative to using active increments in reference amplitude is using active increments in the system energy, where the kinetic energy E_{kin} is increased in incremental steps, and Eq. (10) is solved in conjunction with the incremental form of Eq. (22) as

$$-\left(\omega^2\,\overline{\mathbf{q}}^T\,\overline{\mathbf{M}}\right)\Delta\overline{\mathbf{q}} - \left(\omega\,\overline{\mathbf{q}}^T\,\overline{\mathbf{M}}\,\overline{\mathbf{q}}\right)\Delta\omega = E_{\text{kin}} + \frac{\omega^2}{2}\overline{\mathbf{q}}^T\overline{\mathbf{M}}\overline{\mathbf{q}} \tag{23}$$

3 Tailoring hardening/softening behavior

While nonlinear structural dynamics has been investigated in the view of structural optimization [38, 39, 40, 41, 42, 43], the hardening/softening behavior of mechanical systems has received little attention w.r.t. structural

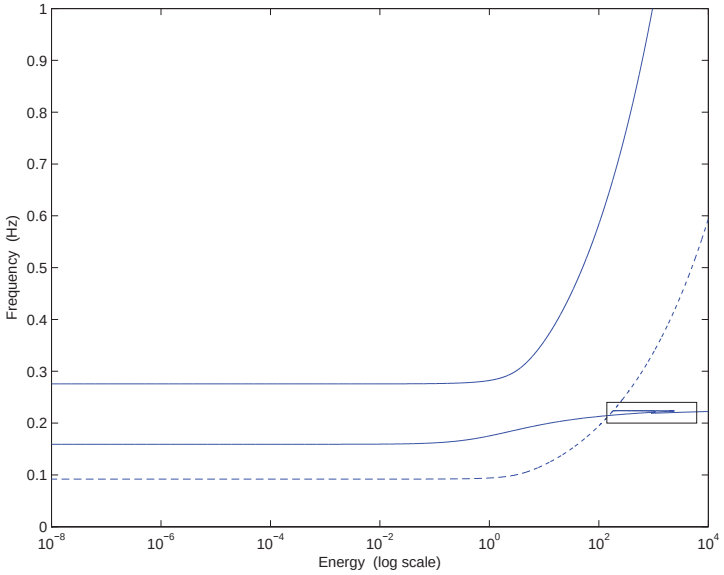

(a)

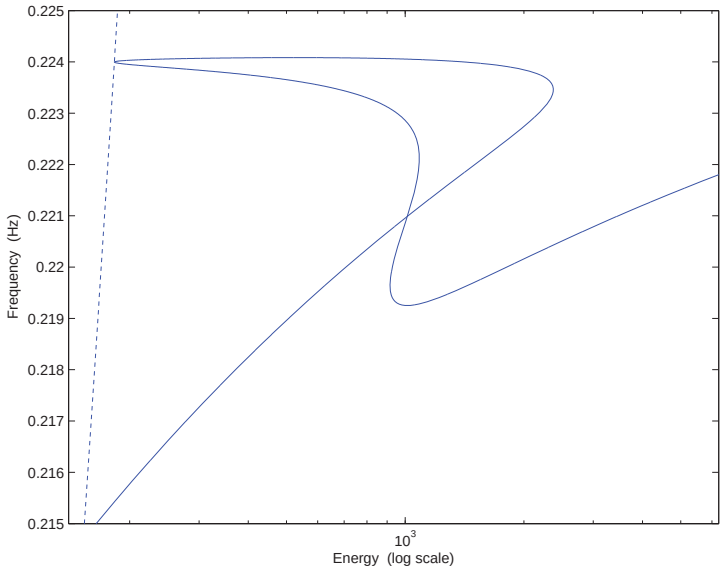

(b)

Figure 2: The frequency-energy plot for the NNMs of a two-DOFs nonlinear systems (a) and zoom of a tongue (b). Solid lines: first NNM (top) and second NNM (bottom); dashed line: second NNM with ifs frequency divided by three.

optimization. Since this is a fundamental feature of nonlinear dynamic systems and is of great importance for the performance of nonlinear micromechanical and nanomechanical resonators, exploring ways to tailor the hardening/softening behavior has drawn significant interests recently [44, 45, 46, 47, 48].

It is noted that the hardening/softening behavior in NNM traces back to the most straightforward definition of NNM, known as Rosenberg's definition [49, 50, 51]. According to this definition, a NNM is a vibration in union of the mechanical system, i.e. a synchronous oscillation where all material points of the structure reach the maximum displacements and pass through the initial configuration simultaneously, and which motion, consequently, can be described in terms of the motion of a single reference material point [10]. In the following part of this paper, the amplitude of the single reference material point is referred to as the reference amplitude.

To qualitatively and quantitatively measure the hardening/softening behavior, a quantity related to the relative frequency shift, also known as the detuning parameter in nonlinear dynamics, is defined as

$$\gamma = \frac{\omega_{\mathrm{NL}} - \omega_{\mathrm{L}}}{\omega_{\mathrm{L}}} \tag{24}$$

where ω_{L} is the eigenfrequency of one LNM, and ω_{NL} is the frequency of the corresponding NNM at a specific reference amplitude (or energy level). This objective function is inspired by the frequency-amplitude relation derived based on normal form theory [22] as

$$\omega_{\mathrm{NL}} = \omega_{\mathrm{L}}(1 + \Gamma A^2) \tag{25}$$

where Γ is known as the effective nonlinear coefficient, A is the amplitude of the single nonlinear normal mode. A comparison of the two equations shows that

$$\gamma = \Gamma A^2 \tag{26}$$

Since we use a constant amplitude in the optimization, γ provides a good approximation of the effective nonlinear coefficient. In the following of this section, the optimization problem is formulated and the sensitivity of γ w.r.t. the design variables is derived by using adjoint method.

3.1 Formulation of optimization problems

To demonstrate the proposed optimization procedure, we consider shape optimization of plane frame structures with geometric nonlinearity. The idea is to qualitatively and quantitatively tailor the hardening/softening behavior

by manipulating the geometry of these structures. In the optimization, the structures are discretized with three-node beam elements based on a geometrically exact theory [26, 27], and the design variables are chosen to be the in-plane thickness of all beam elements, i.e. h_e with $e = 1, \ldots, N_e$, where N_e is the number of elements.

For generality, the objective function is assumed to be a function of the amplitudes and the frequency of a NNM so that it can be considered a nonlinear analogy of the optimization of the mode shape and eigenvalue for a LNM. Furthermore, the eigenfrequency of the LNM is also included in the objective function because it is used to quantify the hardening/softening behavior in Eq. (24). The mathematical formulation of the optimization problem is written as

$$\begin{aligned} &\min_{\rho_e} \; c(\omega_i, \omega, \overline{\mathbf{q}}) \\ \text{s.t. :} \;\; &\mathbf{K}_{\mathrm{L}}\boldsymbol{\Phi}_i = \omega_i^2 \mathbf{M}\boldsymbol{\Phi}_i, \quad \boldsymbol{\Phi}_i^T \mathbf{M}\boldsymbol{\Phi}_i = 1, \\ &\omega^2 \overline{\mathbf{M}}\, \overline{\mathbf{q}} + \overline{\mathbf{g}} = 0, \quad \chi(\overline{\mathbf{q}}, \omega) = 0, \\ &h_e = \; h_{min} + \rho_e (h_{max} - h_{min}) \end{aligned} \tag{27}$$

where $\mathbf{K}_{\mathrm{L}}$ is the linear stiffness matrix, $\boldsymbol{\Phi}_i$ and ω_i denote the mode shape and the eigenfrequency of the ith LNM, $\overline{\mathbf{q}}$ and ω denote the amplitudes and the frequency of the corresponding NNM, $h_{\min}$ is minimum thickness, $h_{\min}$ is maximum thickness, h_e is element thickness, and ρ_e is design variable used in the optimization with $e = 1, \ldots, N_e$.

It should be noted that the optimization problem is performed based on both linear and nonlinear modal analyses. The LNMs are normalized with respect to the mass matrix and $\chi(\overline{\mathbf{q}}, \omega) = 0$ represents a normalization of a NNM in the sense that it has a specific energy level or a specific reference amplitude. Mathematically, $\chi(\overline{\mathbf{q}}, \omega) = 0$ constructs a hypersurface in terms of $(\overline{\mathbf{q}}, \omega)$ so that the NNM is constrained to evolve in this hypersurface during the optimization. Further, it is noted that the gradient of the NNM is always normal to this hypersurface, i.e.

$$\frac{\partial \chi(\overline{\mathbf{q}}, \omega)}{\partial \overline{\mathbf{q}}^T} \Delta \overline{\mathbf{q}} + \frac{\partial \chi(\overline{\mathbf{q}}, \omega)}{\partial \omega} \Delta \omega = 0 \tag{28}$$

In practice, $\chi(\overline{\mathbf{q}}, \omega)$ can be defined with respect to a specific energy level or a specific amplitude of the aforementioned single reference point.For a simple amplitude-based normalization, it is written as

$$a_{i1} - a_{i1}^* = 0, \quad \Delta a_{i1} = 0 \tag{29}$$

where i is the degree of freedom related to the reference amplitude that characterizes the full motion of the NNM. For some problems, this degree of freedom is difficult to select in advance and in this case an energy-based normalization is preferable.

$$-\frac{1}{2}\omega^2 \overline{\mathbf{q}}^T \overline{\mathbf{M}}\, \overline{\mathbf{q}} - E^*_{\text{kin}} = 0, \quad \left(\omega^2\, \overline{\mathbf{q}}^T\, \overline{\mathbf{M}}\right) \Delta\overline{\mathbf{q}} + \left(\omega\, \overline{\mathbf{q}}^T\, \overline{\mathbf{M}}\, \overline{\mathbf{q}}\right) \Delta\omega = 0. \tag{30}$$

3.2 Adjoint sensitivity analysis

For efficient computation of sensitivity, the adjoint method is used. For arbitrary values of adjoint variables $\boldsymbol{\lambda}_1$ and λ_2, the objective function can be written as

$$c = c + \boldsymbol{\lambda}_1^T \left(\omega^2\, \overline{\mathbf{M}}\, \overline{\mathbf{q}} + \overline{\mathbf{g}}\right) + \lambda_2\ \chi(\overline{\mathbf{q}}, \omega) \tag{31}$$

Differentiating the two sides of Eq. (31) with respect to a design variable ρ_e leads to

$$\begin{aligned} \frac{\mathrm{d}c}{\mathrm{d}\rho_e} = &\left[\frac{\partial c}{\partial \overline{\mathbf{q}}^T} + \boldsymbol{\lambda}_1^T \left(\omega^2 \overline{\mathbf{M}} + \overline{\mathbf{K}}\right) + \lambda_2 \frac{\partial \chi(\overline{\mathbf{q}}, \omega)}{\partial \overline{\mathbf{q}}^T}\right] \frac{\mathrm{d}\overline{\mathbf{q}}}{\mathrm{d}\rho_e} + \\ &\left[\frac{\partial c}{\partial \omega} + \boldsymbol{\lambda}_1^T \left(2\omega \overline{\mathbf{M}} \overline{\mathbf{q}}\right) + \lambda_2 \frac{\partial \chi(\overline{\mathbf{q}}, \omega)}{\partial \omega}\right] \frac{\mathrm{d}\omega}{\mathrm{d}\rho_e} + \frac{\partial c}{\partial \omega_i} \frac{\mathrm{d}\omega_i}{\mathrm{d}\rho_e} + \\ &\boldsymbol{\lambda}_1^T \left(\omega^2 \frac{\partial \overline{\mathbf{M}}}{\partial \rho_e} \overline{\mathbf{q}} + \frac{\partial \overline{\mathbf{g}}}{\partial \rho_e}\right) \end{aligned} \tag{32}$$

In the adjoint method, the adjoint variables $\boldsymbol{\lambda}_1$ and λ_2 are selected such that the coefficients in the brackets in front of $\frac{\mathrm{d}\overline{\mathbf{q}}}{\mathrm{d}\rho_e}$ and $\frac{\mathrm{d}\omega}{\mathrm{d}\rho_e}$ vanish. This leads to the adjoint equations

$$\begin{aligned} &\frac{\partial c}{\partial \overline{\mathbf{q}}^T} + \boldsymbol{\lambda}_1^T \left(\omega^2 \overline{\mathbf{M}} + \overline{\mathbf{K}}\right) + \lambda_2 \frac{\partial \chi(\overline{\mathbf{q}}, \omega)}{\partial \overline{\mathbf{q}}^T} = \mathbf{0} \\ &\frac{\partial c}{\partial \omega} + \boldsymbol{\lambda}_1^T \left(2\omega \overline{\mathbf{M}} \overline{\mathbf{q}}\right) + \lambda_2 \frac{\partial \chi(\overline{\mathbf{q}}, \omega)}{\partial \omega} = 0 \end{aligned} \tag{33}$$

To facilitate the numerical implementation, the adjoint equations are rewritten in matrix form as

$$\begin{bmatrix} \left(\omega^2 \overline{\mathbf{M}} + \overline{\mathbf{K}}\right) & \dfrac{\partial \chi(\overline{\mathbf{q}},\, \omega)}{\partial \overline{\mathbf{q}}} \\ \left(2\omega \overline{\mathbf{q}}^T \overline{\mathbf{M}}\right) & \dfrac{\partial \chi(\overline{\mathbf{q}},\, \omega)}{\partial \omega} \end{bmatrix} \begin{bmatrix} \boldsymbol{\lambda}_1 \\ \lambda_2 \end{bmatrix} = \begin{bmatrix} \dfrac{\partial c}{\partial \overline{\mathbf{q}}} \\ \dfrac{\partial c}{\partial \omega} \end{bmatrix} \tag{34}$$

Then the sensitivity of c with respect to design variable ρ_e can be computed using the adjoint variable $\boldsymbol{\lambda}_1$ as

$$\frac{\mathrm{d}c}{\mathrm{d}\rho_e} = \boldsymbol{\lambda}_1^T \left(\omega^2 \frac{\partial \overline{\mathbf{M}}}{\partial \rho_e} \overline{\mathbf{q}} + \frac{\partial \overline{\mathbf{g}}}{\partial \rho_e}\right) + \frac{\partial c}{\partial \omega_i} \frac{\mathrm{d}\omega_i}{\mathrm{d}\rho_e} \tag{35}$$

It is noted that the adjoint variable λ_2 does not appear explicitly in Eq. (35), but the sensitivity of frequency ω_i with respect to the design variable ρ_e is required. By using the sensitivity of a single eigenvalue ω_i^2, we have

$$\frac{\mathrm{d}\omega_i}{\mathrm{d}\rho_e} = \frac{1}{2\omega_i} \boldsymbol{\Phi}_i^T \left[\frac{\partial \mathbf{K}_L}{\partial \rho_e} - \omega_i^2 \frac{\partial \mathbf{M}}{\partial \rho_e} \right] \boldsymbol{\Phi}_i \tag{36}$$

when the eigenvector is assumed to be normalized with respect to the mass matrix, i.e. $\boldsymbol{\Phi}_i^T \mathbf{M} \boldsymbol{\Phi}_i = 1$. Only single eigenvalues are encountered and considered here. For sensitivity analysis of multiple eigenvalues, the reader can refer to [52, 53, 31].

Each iteration of the optimization procedure involves the computation of NNM, solving the adjoint equation in Eq. (34), the calculation of sensitivities using Eq. (35) and finally an update of the design variables. For the latter we apply the mathematical programming toolbox MMA (Method of Moving Asymptotes) [54]. For the objective function defined in Eq. (24), its differentiations are

$$\frac{\partial c}{\partial \omega} = \frac{1}{\omega_i}, \quad \frac{\partial c}{\partial \omega_i} = -\frac{\omega}{\omega_i^2}, \quad \frac{\partial c}{\partial \overline{\mathbf{q}}} = \mathbf{0} \tag{37}$$

By substituting Eq. (37) into Eq. (34), we can compute the adjoint variable $\boldsymbol{\lambda}_1$ and can then calculate the sensitivities using Eq. (35).

4 Examples in plane frame structures

In this section, two examples are provided to demonstrate the effectiveness of the proposed procedure. The first example is a one-floor frame [55, 56], and the second example is an "H"-shaped frame. In each example, the initial configuration consists of three identical beams with uniform rectangular cross sections. In the optimization procedure, the distribution of in-plane thickness is varied to tailor the hardening/softening behavior of a symmetric vibration mode.

4.1 One-floor frame

The one-floor frame and one of its linear vibration modes are shown in Fig. 3. In the initial design, the geometry of each beam is defined by out-of-plane width $b = 30$ mm, in-plane thickness $h = 30$ mm, beam length $L = 180$ mm. The in-plane thickness is allowed to vary between 20 mm and 40 mm. The material properties are fixed with mass density 7800 kg/m^3, Young's modulus $E = 205$ GPa, Poisson's ratio $\nu = 0.3$ and shear modulus $G = E/(2(1+\nu))$.

The initial configuration shows a softening behavior. The optimization problem is formulated such that the softening behavior is minimized and thereby the hardening behavior maximized, i.e.

$$\max_{\rho_e} \ \gamma = \frac{\omega_{\mathrm{NL}} - \omega_{\mathrm{L}}}{\omega_{\mathrm{L}}} \tag{38}$$

which also are subjected to the additional constraints in Eq. (27). Evolution of the frequency-amplitude dependence and the corresponding frequency-energy dependence are shown in Fig. 4 and Fig. 5. The initial design is displayed in Fig. 3, and one intermediate design and final design are given in Fig. 6. It is noted that the hardening/softening behavior of the structure is qualitatively and quantitatively changed smoothly during the optimization iterations. Further, it is noticed that both the frequency of LNM and the frequency of NNM at a given amplitude are decreased continuously. A larger drop in the frequency of LNM than in the frequency of NNM is achieved to yield the hardening behavior. It is observed that the softening behavior is first tuned into mixed hardening/softening behavior, and then tuned into hardening behavior as the optimization iterations proceed. Finally, it is noted that for the NNM at the given amplitude, the system energy stays almost constant when the optimized design has a softening behavior, and increases slightly as the hardening behavior sets in and increases in strength.

In some applications, it will be natural to introduce a constraint on the eigenfrequency ω_{L} of the LNM. To demonstrate the effect of this, we introduce a minimum allowable value of the eigenfrequency ω_{L} and the optimization problem is consequently rewritten as

$$\begin{aligned} &\max_{\rho_e} \ \gamma = \frac{\omega_{\mathrm{NL}} - \omega_{\mathrm{L}}}{\omega_{\mathrm{L}}} \\ &\text{s.t. :} \ \ \omega_{\mathrm{L}} \geq \omega_{\mathrm{L}}^{*} \end{aligned} \tag{39}$$

which is also subjected to the additional constraints in Eq. (27). Evolution of the frequency-amplitude dependence and the corresponding frequency-energy dependence are now given in Fig. 7 and Fig. 8. While the initial design is displayed in Fig. 3, one intermediate design and final design are given in Fig. 9. For this example we see that the nonlinear behavior is also tuned from softening to hardening. It is found that the frequency of NNM is increased smoothly and significantly, whereas the frequency of LNM changes only slightly and presents a small fluctuation. Further, the energy for the NNMs at the given reference amplitude is slightly reduced for the optimized design. The evolution of the energy for these NNMs is similar to the optimization without a constraint on the eigenfrequency ω_{L}, where

the energy is first reduced when softening behavior evolves to mixed softening/hardening behavior, and then increased when mixed softening/hardening behavior evolves to hardening behavior.

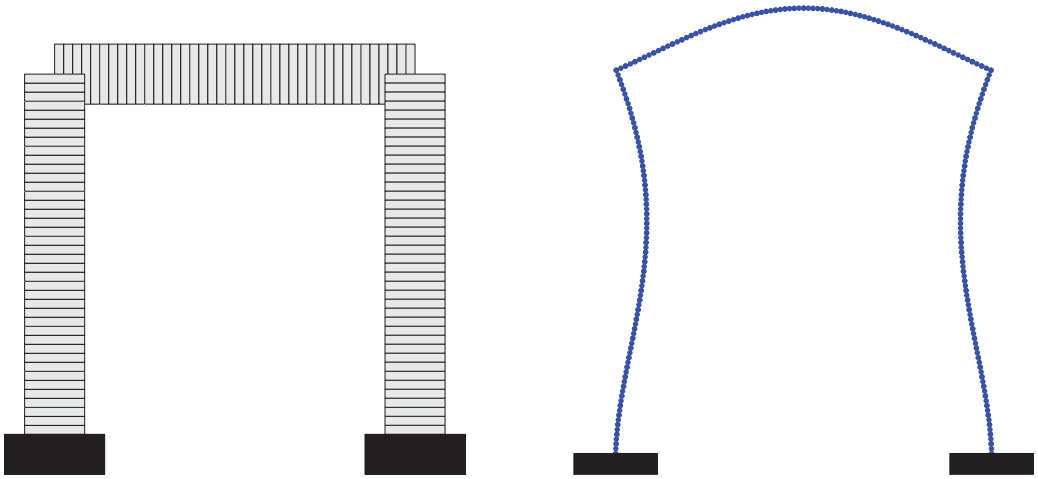

Figure 3: One-floor frame structure (left) and one linear vibration mode (right). The solid black patches indicate boundary conditions of the structure.

4.2 "H"-shaped frame

In order to demonstrate the conversion from a hardening to a softening nonlinear behavior we choose a slightly different initial configuration that displays a hardening behavior in its original configuration. The "H"-shaped frame and one of its linear vibration mode are shown in Fig. 10. In the initial design, the geometry of each beam is defined by out-of-plane width $b = 30$ mm, in-plane thickness $h = 20$ mm, beam length $L = 600$ mm. In the optimization, the maximum in-plane thickness is 40 mm. The material properties are the same as that of the one-floor frame structure. The optimization problem is written as

$$\begin{aligned} \min_{\rho_e} \ & \gamma = \frac{\omega_{\mathrm{NL}} - \omega_{\mathrm{L}}}{\omega_{\mathrm{L}}} \\ \text{s.t.} : \ & \omega_{\mathrm{L}} \leq \omega_{\mathrm{L}}^{*} \end{aligned} \tag{40}$$

which also are subjected to the additional constraints in Eq. (27). Evolution of the frequency-amplitude dependence and the corresponding frequency-energy dependence are shown in Fig. 11 and Fig. 12. The intermediate

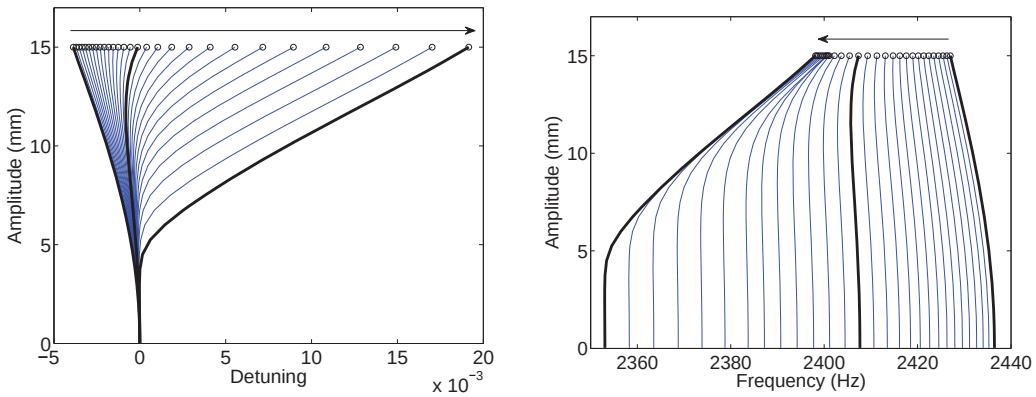

Figure 4: Evolution of the detuning-amplitude relation (left) and the frequency-amplitude dependence (right). Thick curves correspond to initial design, optimized design at 15th iteration, and final design.

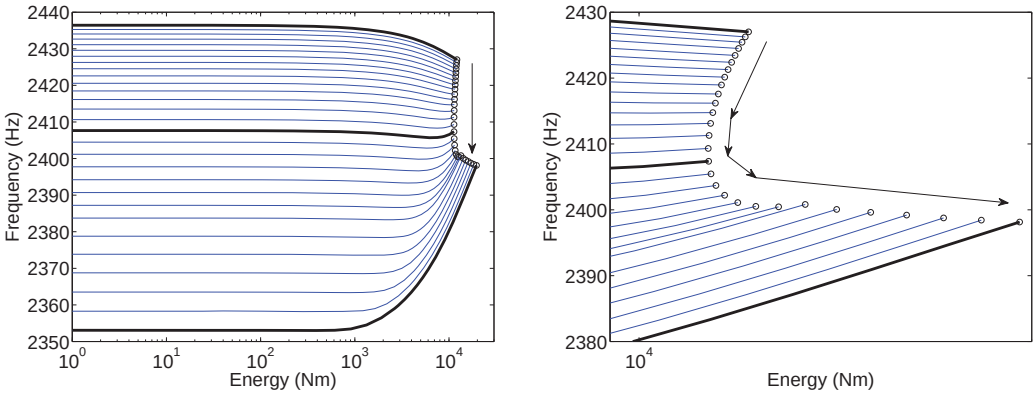

Figure 5: Evolution of the frequency-energy relation (left) and the details for NNMs at a given reference amplitude (right).Thick curves correspond to initial design, optimized design at 15th iteration, and final design.

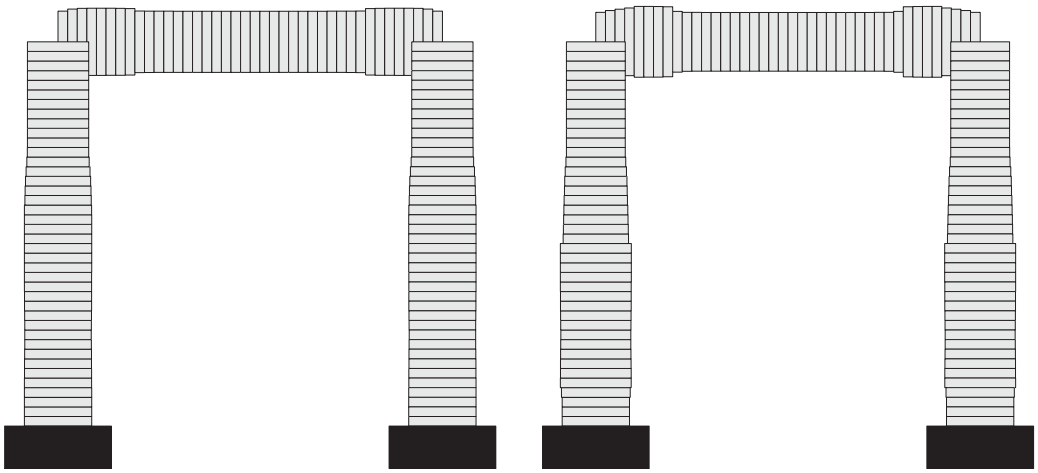

Figure 6: Evolution of optimized designs over iterations. (left): 15th iteration; (right): final design.

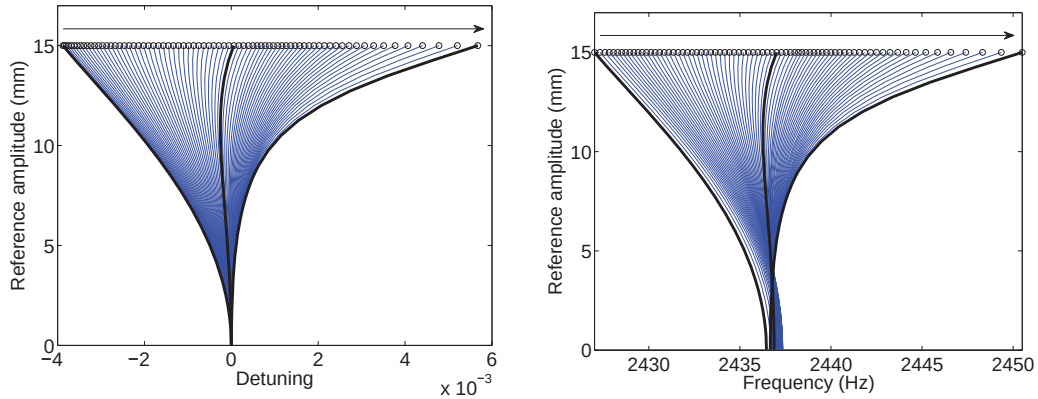

Figure 7: Evolution of the detuning-amplitude relation (left) and the frequency-amplitude dependence (right). Thick curves correspond to initial design, optimized design at 40th iteration, and final design.

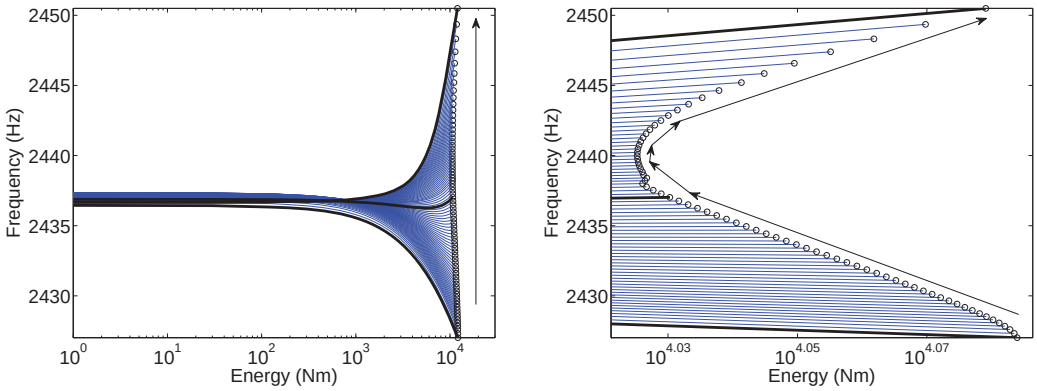

Figure 8: Evolution of the frequency-energy relation (left) and the details for NNMs at a given reference amplitude (right).

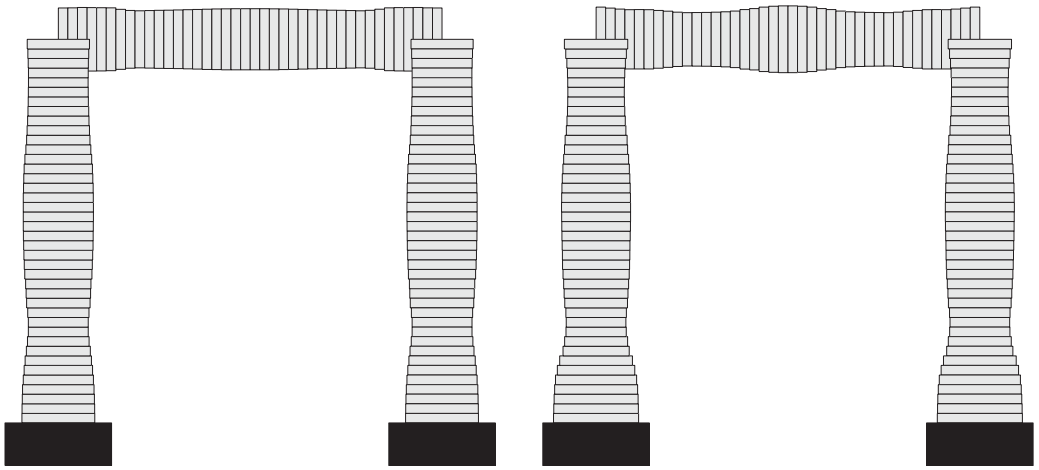

Figure 9: Evolution of optimized designs over iterations. (left): 40th iteration; (right): final design.

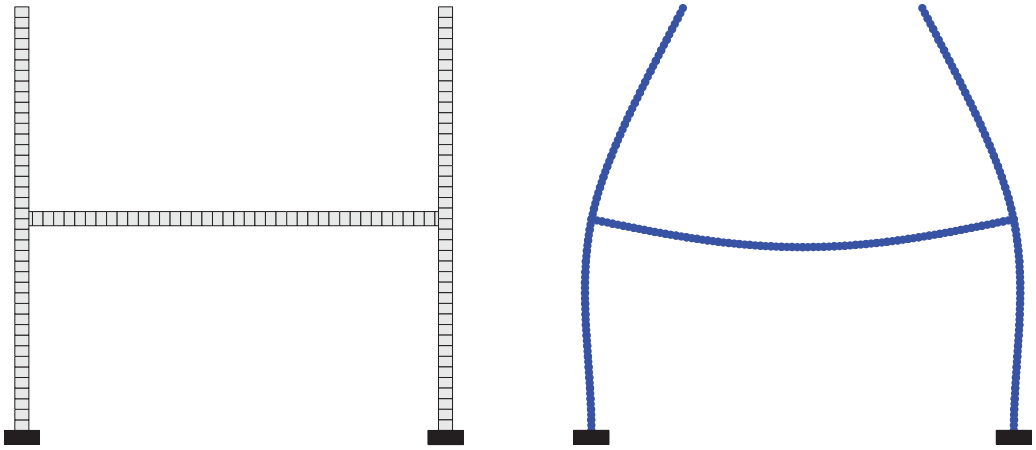

Figure 10: One-floor frame structure (left) and one linear vibration mode (right). The solid black patches indicate boundary conditions of the structure.

design corresponding to a straight line in frequency-amplitude plot and the final design with softening behavior are displayed in Fig 13. A clear change in the linear vibration mode is also observed when comparing the initial design and the final design. The linear vibration modes are displayed in Fig. 14. In the optimized design, the vibration in the two free half-beams is reduced, and the vibration in the horizontal beam is amplified.

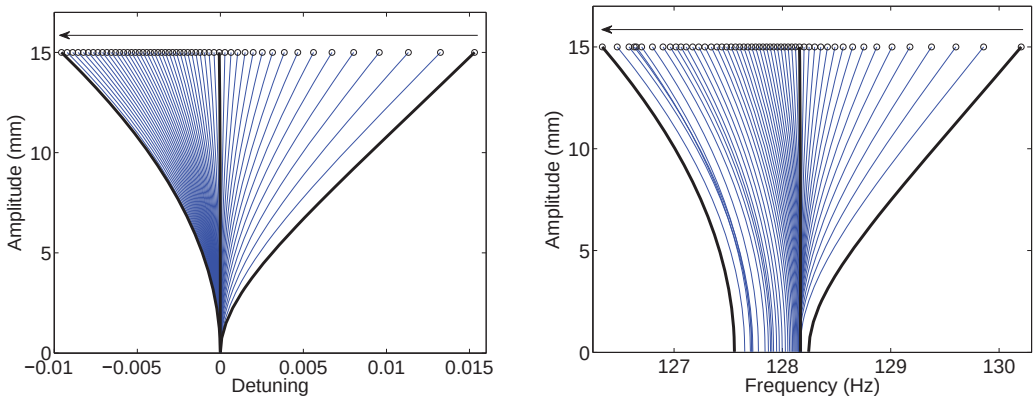

Figure 11: Evolution of the detuning-amplitude relation (left) and the frequency-amplitude dependence (right). Thick curves correspond to initial design, optimized design at 14th iteration, and final design.

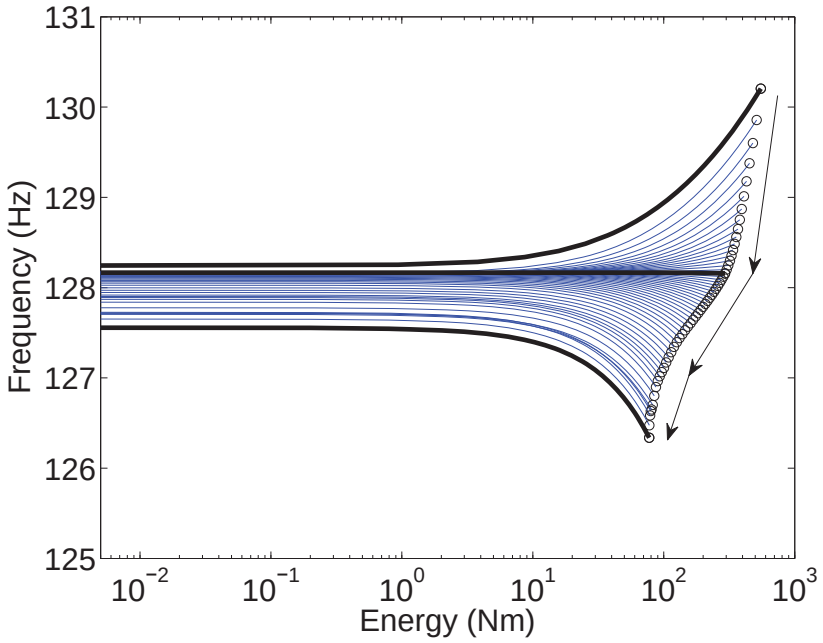

Figure 12: Evolution of the frequency-energy relation. The circles represent the NNMs at a given reference amplitude. The thick curves correspond to initial design: optimized design at 14th iteration, and final design.

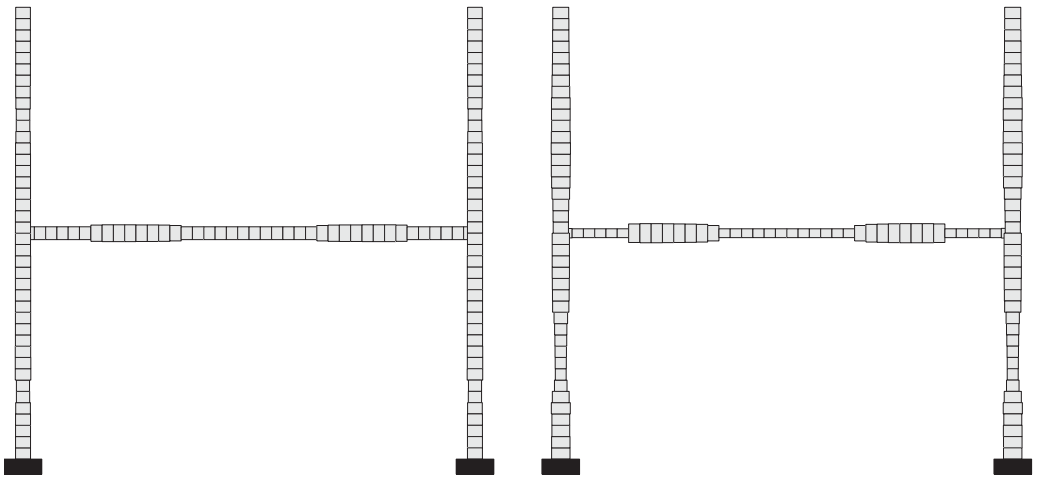

Figure 13: Evolution of optimized designs over iterations. (left): 14th iteration; (right): final design.

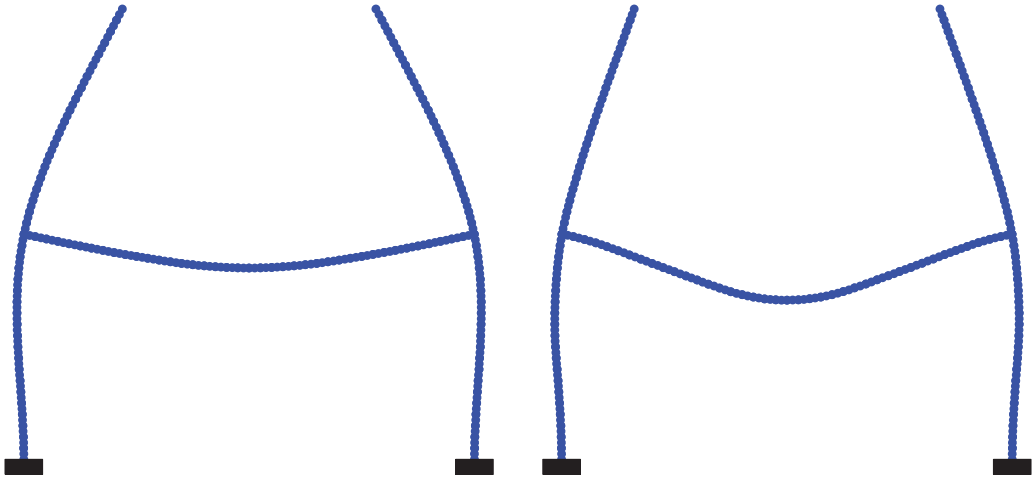

Figure 14: Evolution of linear vibration mode of optimized design over iterations. (left): 14th iteration; (right): final design.

5 Conclusions

We present an efficient procedure for gradient-based structural optimization of the hardening/softening behavior using nonlinear normal modes. The analysis is performed using the framework of the incremental harmonic balance method in conjunction with the alternating frequency/time domain method. In the optimization, each iteration consists of calculation of nonlinear normal modes, evaluation of hardening/softening behavior, solving an adjoint equation, calculation of sensitivities with solved adjoint variables, and an update of design variables using a mathematical programming toolbox. Examples involving plane frame structures are offered to demonstrate that the hardening/softening behavior can be qualitatively and quantitatively changed by using the proposed methodology. Future work would be its applications in multi-physics problems and topology optimization. Addtionally, the sensitivity analysis of nonlinear normal modes can also be used for updating uncertain parameters in a nonlinear finite element model by matching measured and simulated nonlinear normal modes.

Acknowledgement

This project was supported by ERC Starting Grant 279529 INNODYN. Special thanks to Gaëtan Kerschen for the inspiring CISM course on modal analysis of nonlinear mechanical systems in 2012.

References

[1] E. Gourdon, N. A. Alexander, C. A. Taylor, C. H. Lamarque, and S. Pernot, "Nonlinear energy pumping under transient forcing with strongly nonlinear coupling: Theoretical and experimental results," *Journal of sound and vibration*, vol. 300, no. 3, pp. 522–551, 2007.

[2] F. Nucera, F. L. Iacono, D. McFarland, L. Bergman, and A. Vakakis, "Application of broadband nonlinear targeted energy transfers for seismic mitigation of a shear frame: Experimental results," *Journal of sound and vibration*, vol. 313, no. 1, pp. 57–76, 2008.

[3] R. Bellet, B. Cochelin, P. Herzog, and P.-O. Mattei, "Experimental study of targeted energy transfer from an acoustic system to a nonlinear membrane absorber," *Journal of Sound and Vibration*, vol. 329, no. 14, pp. 2768–2791, 2010.

[4] S. P. Beeby, R. Torah, M. Tudor, P. Glynne-Jones, T. O'Donnell, C. Saha, and S. Roy, "A micro electromagnetic generator for vibration energy harvesting," *Journal of Micromechanics and microengineering*, vol. 17, no. 7, p. 1257, 2007.

[5] D. Antonio, D. H. Zanette, and D. López, "Frequency stabilization in nonlinear micromechanical oscillators," *Nature communications*, vol. 3, p. 806, 2012.

[6] L. Villanueva, E. Kenig, R. Karabalin, M. Matheny, R. Lifshitz, M. Cross, and M. Roukes, "Surpassing fundamental limits of oscillators using nonlinear resonators," *Physical review letters*, vol. 110, no. 17, p. 177208, 2013.

[7] K. Qalandar, B. Strachan, B. Gibson, M. Sharma, A. Ma, S. Shaw, and K. Turner, "Frequency division using a micromechanical resonance cascade," *Applied Physics Letters*, vol. 105, no. 24, p. 244103, 2014.

[8] R. Lifshitz and M. Cross, "Nonlinear dynamics of nanomechanical and micromechanical resonators," *Review of nonlinear dynamics and complexity*, vol. 1, pp. 1–52, 2008.

[9] J. F. Rhoads, S. W. Shaw, and K. L. Turner, "Nonlinear dynamics and its applications in micro-and nanoresonators," *Journal of Dynamic Systems, Measurement, and Control*, vol. 132, no. 3, p. 034001, 2010.

[10] G. Kerschen, M. Peeters, J. C. Golinval, and A. F. Vakakis, "Nonlinear normal modes, Part I: A useful framework for the structural dynamicist," *Mechanical Systems and Signal Processing*, vol. 23, no. 1, pp. 170 – 194, 2009.

[11] M. Peeters, G. Kerschen, and J. Golinval, "Dynamic testing of nonlinear vibrating structures using nonlinear normal modes," *Journal of Sound and Vibration*, vol. 330, no. 3, pp. 486 – 509, 2011.

[12] M. Peeters, G. Kerschen, and J. Golinval, "Modal testing of nonlinear vibrating structures based on nonlinear normal modes: Experimental demonstration," *Mechanical Systems and Signal Processing*, vol. 25, no. 4, pp. 1227 – 1247, 2011.

[13] S. Dou and J. S. Jensen, "Optimization of nonlinear structural resonance using the incremental harmonic balance method," *Journal of Sound and Vibration*, vol. 334, pp. 239 – 254, 2015.

[14] S. Dou and J. S. Jensen, "Optimal design of hardening and softening resonances of plane frame structures," in *8th European Nonlinear Dynamics Conference*, 2014.

[15] S. Dou and J. S. Jensen, "Analytical sensitivity analysis and topology optimization of nonlinear resonant structures with hardening and softening behavior," in *17th US National Congress on Theoretical and Applied Mechanics*, 2014.

[16] M. Peeters, R. Viguié, G. Sérandour, G. Kerschen, and J.-C. Golinval, "Nonlinear normal modes, Part II: Toward a practical computation using numerical continuation techniques," *Mechanical Systems and Signal Processing*, vol. 23, no. 1, pp. 195 – 216, 2009.

[17] B. Cochelin and C. Vergez, "A high order purely frequency-based harmonic balance formulation for continuation of periodic solutions," *Journal of sound and vibration*, vol. 324, no. 1, pp. 243–262, 2009.

[18] M. Krack, L. P. von Scheidt, and J. Wallaschek, "A method for nonlinear modal analysis and synthesis: Application to harmonically forced and self-excited mechanical systems," *Journal of Sound and Vibration*, vol. 332, no. 25, pp. 6798 – 6814, 2013.

[19] T. Detroux, L. Renson, and G. Kerschen, "The harmonic balance method for advanced analysis and design of nonlinear mechanical systems," *Nonlinear Dynamics, Volume 2*, pp. 19–34, 2014.

[20] M. P. Bendsøe and O. Sigmund, *Topology optimization: theory, methods and applications*. Springer Science & Business Media, 2003.

[21] C. Touzé, M. Vidrascu, and D. Chapelle, "Direct finite element computation of non-linear modal coupling coefficients for reduced-order shell models," *Computational Mechanics*, vol. 54, no. 2, pp. 567–580, 2014.

[22] C. Touzé, O. Thomas, and A. Chaigne, "Hardening/softening behaviour in non-linear oscillations of structural systems using non-linear normal modes," *Journal of Sound and Vibration*, vol. 273, no. 1, pp. 77–101, 2004.

[23] S. Dou, B. S. Strachan, S. W. Shaw, and J. S. Jensen, "Structural optimization for nonlinear dynamic response," 2015. Accepted for journal publication.

[24] T. M. Cameron and J. H. Griffin, "An alternating frequency/time domain method for calculating the steady-state response of nonlinear dynamic systems," *Journal of Applied Mechanics*, vol. 56, pp. 149–154, Mar. 1989.

[25] C. Touzé and M. Amabili, "Nonlinear normal modes for damped geometrically nonlinear systems: Application to reduced-order modelling of harmonically forced structures," *Journal of sound and vibration*, vol. 298, no. 4, pp. 958–981, 2006.

[26] E. Reissner, "On one-dimensional finite-strain beam theory: the plane problem," *Zeitschrift für angewandte Mathematik und Physik ZAMP*, vol. 23, no. 5, pp. 795–804, 1972.

[27] P. Wriggers, "Nonlinear finite element methods," 2008.

[28] N. L. Pedersen, "Maximization of eigenvalues using topology optimization," *Structural and multidisciplinary optimization*, vol. 20, no. 1, pp. 2–11, 2000.

[29] N. L. Pedersen, "Design of cantilever probes for atomic force microscopy (afm)," *Engineering Optimization*, vol. 32, no. 3, pp. 373–392, 2000.

[30] L. Li, Y. Hu, and X. Wang, "Design sensitivity and hessian matrix of generalized eigenproblems," *Mechanical Systems and Signal Processing*, vol. 43, no. 1-2, pp. 272–294, 2014.

[31] N. Olhoff and J. Du, "Structural topology optimization with respect to eigenfrequencies of vibration," in *Topology Optimization in Structural and Continuum Mechanics*, pp. 275–297, Springer, 2014.

[32] A. Raghothama and S. Narayanan, "Bifurcation and chaos of an articulated loading platform with piecewise non-linear stiffness using the incremental harmonic balance method," *Ocean Engineering*, vol. 27, no. 10, pp. 1087–1107, 2000.

[33] M. Krack, L. Panning-von Scheidt, and J. Wallaschek, "A high-order harmonic balance method for systems with distinct states," *Journal of Sound and Vibration*, vol. 332, no. 21, pp. 5476–5488, 2013.

[34] Y. Cheung, S. Chen, and S. Lau, "Application of the incremental harmonic balance method to cubic non-linearity systems," *Journal of Sound and Vibration*, vol. 140, no. 2, pp. 273 – 286, 1990.

[35] A. Leung and S. Chui, "Non-linear vibration of coupled duffing oscillators by an improved incremental harmonic balance method," *Journal of Sound and Vibration*, vol. 181, no. 4, pp. 619 – 633, 1995.

[36] A. Lazarus and O. Thomas, "A harmonic-based method for computing the stability of periodic solutions of dynamical systems," *Comptes Rendus Mécanique*, vol. 338, no. 9, pp. 510–517, 2010.

[37] T. Detroux, L. Renson, L. Masset, and G. Kerschen, "The harmonic balance method for bifurcation analysis of nonlinear mechanical systems," in *SEM IMAC XXXIII A Conference and Exposition on Structural Dynamics*, 2015.

[38] N. L. Pedersen, "Designing plates for minimum internal resonances," *Structural and Multidisciplinary Optimization*, vol. 30, no. 4, pp. 297–307, 2005.

[39] J. S. Jensen and B. S. Lazarov, "Optimization of non-linear mass damper parameters for transient response," in *Proceedings of the Sixth EUROMECH Nonlinear Dynamics Conference* (B. Andrievsky and A. Fradkov, eds.), 2008.

[40] Y.-I. Kim and G.-J. Park, "Nonlinear dynamic response structural optimization using equivalent static loads," *Computer Methods in Applied Mechanics and Engineering*, vol. 199, no. 9-12, pp. 660–676, 2010.

[41] E. P. Petrov, "Advanced analysis and optimization of nonlinear resonance vibrations in gas-turbine structures with friction and gaps," *IUTAM Symposium on Emerging Trends in Rotor Dynamics*, vol. 25, pp. 297–307, 2011.

[42] B. Stanford, P. Beran, and M. Kurdi, "Adjoint sensitivities of time-periodic nonlinear structural dynamics via model reduction," *Computers and Structures*, vol. 88, no. 19-20, pp. 1110–1123, 2010.

[43] A. Tripathi and A. K. Bajaj, "Computational synthesis for nonlinear dynamics based design of planar resonant structures," *Journal of Vibration and Acoustics*, vol. 135, no. 5, p. 051031, 2013.

[44] L. Shao, M. Palaniapan, and W. Tan, "The nonlinearity cancellation phenomenon in micromechanical resonators," *Journal of Micromechanics and Microengineering*, vol. 18, no. 6, p. 065014, 2008.

[45] N. Kacem and S. Hentz, "Bifurcation topology tuning of a mixed behavior in nonlinear micromechanical resonators," *Applied Physics Letters*, vol. 95, no. 18, p. 183104, 2009.

[46] H. Cho, B. Jeong, M.-F. Yu, A. F. Vakakis, D. M. McFarland, and L. A. Bergman, "Nonlinear hardening and softening resonances in micromechanical cantilever-nanotube systems originated from nanoscale geometric nonlinearities," *International Journal of Solids and Structures*, vol. 49, no. 15, pp. 2059–2065, 2012.

[47] X. Dai, X. Miao, L. Sui, H. Zhou, X. Zhao, and G. Ding, "Tuning of nonlinear vibration via topology variation and its application in energy harvesting," *Applied Physics Letters*, vol. 100, no. 3, p. 031902, 2012.

[48] S. Azizi, M. R. Ghazavi, G. Rezazadeh, I. Ahmadian, and C. Cetinkaya, "Tuning the primary resonances of a micro resonator, using piezoelectric actuation," *Nonlinear Dynamics*, vol. 76, no. 1, pp. 839–852, 2014.

[49] R. M. Rosenberg, "Normal modes of nonlinear dual-mode systems," *Journal of Applied Mechanics*, vol. 27, no. 2, pp. 263–268, 1960.

[50] R. M. Rosenberg, "The normal modes of nonlinear n-degree-of-freedom systems," *Journal of applied Mechanics*, vol. 29, no. 1, pp. 7–14, 1962.

[51] R. Rosenberg, "On nonlinear vibrations of systems with many degrees of freedom," *Advances in applied mechanics*, vol. 9, pp. 155–242, 1966.

[52] A. P. Seyranian, E. Lund, and N. Olhoff, "Multiple eigenvalues in structural optimization problems," *Structural optimization*, vol. 8, no. 4, pp. 207–227, 1994.

[53] J. Du and N. Olhoff, "Topological design of freely vibrating continuum structures for maximum values of simple and multiple eigenfrequencies and frequency gaps," *Structural and Multidisciplinary Optimization*, vol. 34, no. 2, pp. 91–110, 2007.

[54] K. Svanberg, "The method of moving asymptotes—a new method for structural optimization," *International Journal for Numerical Methods in Engineering*, vol. 24, no. 2, pp. 359–373, 1987.

[55] A. Leung and T. Fung, "Non-linear steady state vibration of frames by finite element method," *International journal for numerical methods in engineering*, vol. 28, no. 7, pp. 1599–1618, 1989.

[56] S. Chen, Y. Cheung, and H. Xing, "Nonlinear vibration of plane structures by finite element and incremental harmonic balance method," *Nonlinear Dynamics*, vol. 26, no. 1, pp. 87–104, 2001.

Publication [P4]

Optimal design of hardening and softening resonances of plane frame structures

Optimal design of hardening and softening resonances of plane frame structures

Suguang Dou[1], Jakob Søndergaard Jensen[1,2]

1 Department of Mechanical Engineering, Technical University of Denmark, Kgs. Lyngby, Denmark
2 Department of Electrical Engineering, Technical University of Denmark, Kgs. Lyngby, Denmark

Summary. Nonlinear vibrations have shown many promising applications in the fields of micro- and nano-resonators. One well known phenomenon is the hardening/softening resonances. Here a structural optimization method is applied to tailor the hardening/softening nonlinearity of plane frame structures. A finite element model based on a geometrically exact beam element is used in the computational procedure and the design parameterization is facilitated by a variable thickness distribution. Sensitivities of the resonant amplitude and frequency of hardening/softening resonances with respect to design variables are calculated using the adjoint method. Examples are provided to demonstrate the possibility for controlling the hardening/softening behavior. Currently an extension to topology optimization of 2D continuum structure is in progress.

Introduction

Nonlinear vibrations have shown many promising applications in the fields of micro- and nano-resonators [1]. Also, the hardening and softening nonlinear resonances can be used to broaden the bandwidth of energy harvesters [2]. Among these researches, Cho et al. theoretically and experimentally showed that a micro-mechanical cantilever could display either hardening or softening resonance by controlling the geometric nonlinearity originating from a nanotube [3], and Dai et al. experimentally demonstrated that topological variation of an energy harvesting device could tune the bandwidth of hardening resonances [4]. Based on a topology optimization methodology [5], a systematic procedure for tailoring the hardening and softening nonlinear resonances is proposed.

Methods

A systematic optimization procedure is realized through design iterations using a nonlinear finite element model, nonlinear vibration analysis, sensitive analysis and gradient-based design updates.

Finite element model

The model of plane frame structure is implemented using the nonlinear beam element based on geometric exact beam theory [6], which takes into account large displacement, large rotation, shear deformation and rotational inertia. The current configuration of beam element is described as $\mathbf{x} = [x_0 + u\ v\ \varphi]^T$, where x_0 is the initial configuration in the axial direction, u is the displacement in axial direction, v is the deflection, and φ is the rotation angle. The strain-displacement relation is derived using the principle of virtual work leading to the following strain measures for the axial strain ϵ, the shear strain γ and the curvature κ:

$$\epsilon = (1 + \frac{du}{dx_0})\cos\varphi + \frac{dv}{dx_0}\sin\varphi - 1, \quad \gamma = \frac{dv}{dx_0}\cos\varphi - (1 + \frac{du}{dx_0})\sin\varphi, \quad \kappa = \frac{d\varphi}{dx_0} \tag{1}$$

In the finite element model the tangent stiffness matrix and internal force vector are derived based on the strain-displacement relations. The mass matrix is derived in a consistent manner taking into account rotational inertia. A damping matrix proportional to mass matrix and stiffness matrix is included as well. Both two-node and three-node beam elements are considered.

Nonlinear vibration analysis

Nonlinear vibration analysis of the hardening and softening resonances is carried out by the Alternating Frequency/Time (AFT) domain method [7]. The AFT method is similar to the classical Incremental Harmonic Balance (IHB) method in the sense that all the governing equations are built and solved in the frequency domain. The primary difference is that AFT method transfers the responses solved in frequency domain to time domain, evaluates nonlinear terms (in this case in tangent stiffness and internal force) in time domain, and then transfers these nonlinear terms back to frequency domain which facilitates the treatment of the $\sin$ and $\cos$ nonlinear terms. Additionally, an advantage of the AFT method is that it can work interactively with general finite element codes and therefore can be added to the existing finite element codes as an extension.

Optimization formulation

Based on the results of the analysis, the sensitivities of the hardening and softening resonances with respect to the structural design variables are derived and calculated using the adjoint method, and gradient-based optimization is used to update the design variables [5]. The updated design is used in a new iteration and the procedure is repeated until a termination criterion is satisfied. For shape optimization of the frame structure, the optimization formulation to tailor the hardening

and softening nonlinear resonances can be written as

$$\begin{aligned} &\min_{\rho_e} \ \pm\gamma \\ \text{s.t. :}\ &\gamma = \frac{\omega^*}{\omega_L}, \quad \mathbf{K}_L\mathbf{\Phi} = \omega_L^2\mathbf{M}\mathbf{\Phi}, \quad (\omega^*)^2\bar{\mathbf{M}}\bar{\mathbf{q}} + (\omega^*)\bar{\mathbf{C}}\bar{\mathbf{q}} + \bar{\mathbf{g}} = \bar{\mathbf{f}}, \quad b_{i1} = 0, \\ &\sum_{e=1}^{N_e} h_e \le \alpha N_e h_{max}, \quad h_e = h_{min} + \rho_e(h_{max} - h_{min}), \quad 0 \le \rho_e \le 1. \end{aligned} \tag{2}$$

where ω^* is the nonlinear resonant frequency at specified load, ω_L is the linear resonant frequency, γ measures the extent of the hardening or softening nonlinearity, $h_e(e = 1, \ldots, N_e)$ are the thicknesses of beam elements, $\rho_e(e = 1, \ldots, N_e)$ are design variables used in the optimization and α represents a maximum allowable volume of the optimized beam. Note that b_{i1} is the coefficient of one sinusoidal term and $b_{i1} = 0$ is related to the phase lag quadrature criterion [8]. The barred matrices and vectors are in the frequency domain and can be found in [9]. ms with uniform cross sections with width 30 mm, thickness 30 mm and a slenderness ratio of 20. The material properties are $E = 2.05 \times 10^5 \mathrm{MPa}, \nu = 0.3, \rho = 7800 \mathrm{kg/m}^3$. The initial design has a softening resonance around the second linear vibration mode. The optimization problem is then to maximize the ratio γ by varying the thickness distribution. The design domain is bounded so that the thickness can vary from 20 mm to 40 mm. Besides, the total volume is constrained to not exceed half of the allowed volume and this causes the optimized non-uniform design have the same volume as the initial design. The optimized frame with non-uniform thickness, the evolution of the backbone during the iterations and comparison of initial backbone and optimized backbone at larger load are shown in Figure 1, which illustrates that the resonance has been turned from softening to hardening by optimizing the thickness distribution of the three beams.

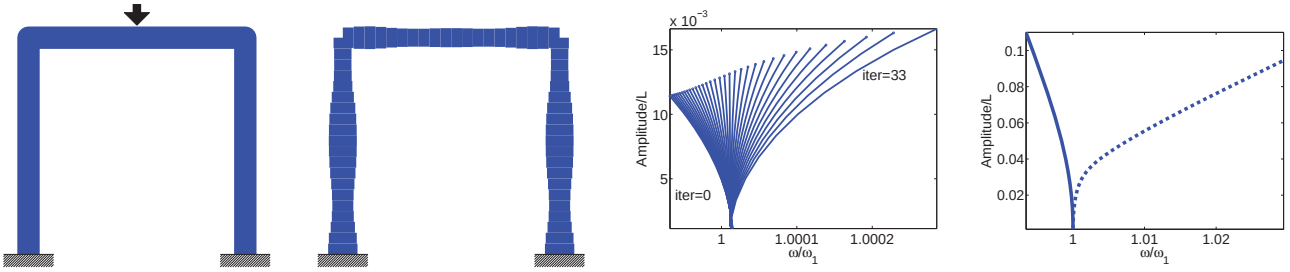

(a) (b) (c) (d)

Figure 1: (a) Optimization problem, (b) optimized design, (c) evolution of backbone during iterations and (d) comparison of initial backbone and optimized backbone at larger load. solid line: initial design; dashed line: optimized design.

Conclusions

A systematic procedure is proposed to optimize the nonlinear resonances with hardening and softening behavior by using structural optimization to tune the geometric nonlinearity. Examples are given to demonstrate the effectiveness of the proposed procedure. This procedure can be applied to complex frame structures. Furthermore, the procedure can integrate other nonlinearities and other demands such as the desired frequency range in the optimization. The work is currently being extended to 2D continuum structures. The work was supported by the ERC starting grant INNODYN.

References

[1] Rhoads J. F., Shaw S. W., and Turner K. L. (2010) Nonlinear Dynamics and Its Applications in Micro- and Nanoresonators. *Journal of Dynamic Systems, Measurement, and Control* **132**:034001.

[2] Hajati A., Kim S. G. (2010) Ultra-wide bandwidth piezoelectric energy harvesting. *Applied Physics Letters* **99**:083105.

[3] Cho H., Jeong B., Yu M. F., Vakakis A. F., McFarland D. M., and Bergman L. A. (2012) Nonlinear hardening and softening resonances in micromechanical cantilever-nanotube systems originated from nanoscale geometric nonlinearities. *International Journal of Solids and Structures* **49**:2059-2065.

[4] Dai X., Miao X., Sui L., Zhou H., Zhao X., and Ding G. (2012) Tuning of nonlinear vibration via topology variation and its application in energy harvesting. *Applied Physics Letters* **100**:031902.

[5] Bendsøe M. P., Sigmund O. (2003) Topology Optimization: Theory, Methods and Applications. Springer.

[6] Wriggers P. (2008) Nonlinear finite element methods. Springer.

[7] Cameron T. M., Griffin J. H. (1989) An Alternating Frequency/Time Domain Method for Calculating the Steady-State Response of Nonlinear Dynamic Systems *Journal of Applied Mechanics* **56**:149-154.

[8] Peeters M., Kerschen G., and Golinval J. C. (2011) Modal testing of nonlinear vibrating structures based on nonlinear normal modes: Experimental demonstration. *Mechanical Systems and Signal Processing* **25**:1227-1247.

[9] Dou S., Jensen J. S. (2013). Optimization of nonlinear structural resonance using the incremental harmonic balance method. Submitted.

Publication [P5]

Analytical sensitivity analysis and topology optimization of nonlinear resonant structures with hardening and softening behavior

17th U.S. National Congress on Theoretical and Applied Mechanics
Michigan State University, June 15-20, 2014

Abstract: D-02-507

Analytical sensitivity analysis and topology optimization of nonlinear resonant structures with hardening and softening behavior

Suguang Dou, Dept. Mechanical Eng., Technical University of Denmark, sudou@mek.dtu.dk
Jakob Jensen, Dept. Electrical Eng., Technical University of Denmark, json@elektro.dtu.dk

With the increasing applications of nonlinear resonant structures [1], researchers are interested in controlling the hardening and softening behavior [2]. We present a systematic procedure for topology optimization of nonlinear resonant structures with hardening and softening behavior. The combination of the finite element method (FEM) and alternating frequency/time domain method (AFT) is used to compute the nonlinear vibrational response. The finite element model facilitates an element-density-based parameterization for topology optimization [3] and the alternating frequency/time domain method takes advantage of the ease in evaluating complex nonlinearities in time domain [4].

Mechanical structures that possess geometrical nonlinearities are used to demonstrate the applicability and efficiency of the proposed procedure, and is here illustrated using 2D continuum structures. Two kinds of optimization problems are considered, including bandwidth problems and dynamic compliance problems. For bandwidth problems, the relative and absolute frequency shifts of resonance peaks caused by hardening and softening behavior are optimized. For dynamic compliance problems we consider point vibration amplitudes and total energy levels of the structure as optimization objectives. In order to speed up the computations we apply analytical sensitivity analysis [5] instead of the commonly applied finite difference approximation. For large FE models this leads to computational savings on up to several orders of magnitude. The optimization problem for relative frequency shift can be formulated as:

$$\begin{aligned} &\min_{x_e} \ \pm\gamma \\ \text{s.t. :}\ &\gamma = \frac{\omega^* - \omega_L}{\omega_L}, \quad \mathbf{K}_L\Phi = \omega_L^2\mathbf{M}\Phi, \quad (\omega^*)^2\bar{\mathbf{M}}\bar{\mathbf{q}} + (\omega^*)\bar{\mathbf{C}}\bar{\mathbf{q}} + \bar{\mathbf{g}} = \bar{\mathbf{f}}, \quad b_{i1} = 0, \\ &E_e = E_{\min} + (x_e)^p(E - E_{\min}), \quad \rho_e = \rho_{\min} + (x_e)^q(\rho - \rho_{\min}), \\ &\sum_{e=1}^{N_e} x_e \le \alpha N_e, \quad 0 \le x_e \le 1. \end{aligned} \tag{1}$$

where ω^* is the nonlinear resonant frequency at the specified load, ω_L is the linear resonant frequency, γ measures the extent of hardening and softening behavior, E_e and ρ_e are interpolated Young's modulus and mass density of each element, p and q are integers with typical values 3 and 1, $x_e (e = 1,\ldots,N_e)$ are design variables and α represents a maximum allowable volume fraction. Note that b_{i1} is the coefficient of one sinusoidal term and the condition $b_{i1} = 0$ is related to the phase lag quadrature criterion [6]. The barred matrices and vectors are in the frequency domain and can be found in [5].

Example Consider a thin 2D continuum structure in micro-scale with doubly-clamped boundary condition. An in-plane vertical time-harmonic load is applied at the center node of the structure. The material is Silicon nitride and its mechanical properties are: Young's modulus $E = 241$ GPa, Poisson's ratio $\nu = 0.23$ and mass density 300 kg/m^3. Plane stress conditions are assumed and preliminary results are obtained

with a coarse discretization of 40×20 elements. The initial design is simply the uniform distribution of material in the design domain. The specified load is so small that the relative frequency shift around the first flexural mode is less than 0.04% for the initial design. The objective function is to maximize the relative frequency shift caused by hardening resonance around the first flexural mode. In the optimized design, the solid structure (black area) is not allowed to fill more than half of the total area of the design domain. The second optimized design is obtained by imposing an additional constraint on minimal eigenvalue in order to ensure sufficient structural rigidity.

For both optimized designs shown in Figure 1, the relative frequency shifts are more than 34%. A physical interpretation of the optimized structures is that the midplane stretching plays a key role when four beams are connected to one central mass and two boundaries through eight hinge-like connections. In the designs point-hinges appear as well as gray elements that correspond to intermediate material properties. Further work is currently being undertaken to improve the designs by employing a finer mesh, projection filtering and minimal length control techniques. However, in reality the gray elements may be realized using a weaker material such as polymer. For example, polymeric hinges have been used in the design of micro-mirrors to achieve large deflection at small external forces.

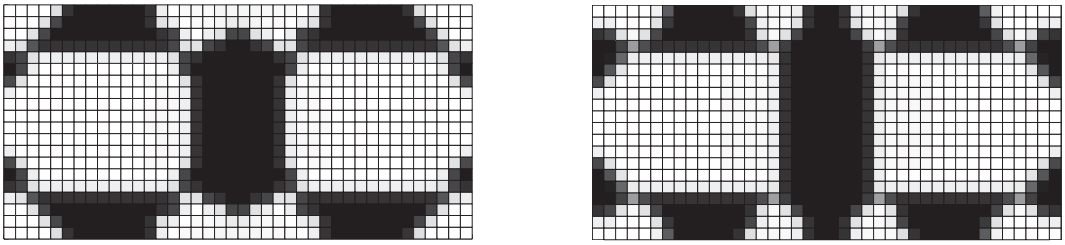

Figure 1. Optimized design with constraint on maximal volume (left) and an additional constraint on minimal eigenvalue (right)

Conclusion A systematic procedure is proposed for optimization of nonlinear resonant structures with hardening and softening behavior by tailoring the geometric nonlinearity. The combination of analytical sensitivity analysis and the topology optimization procedure is shown to be a promising tool in design of nonlinear micro- and nano-resonators.

References

[1] Jeffrey F. Rhoads, Steven W. Shaw, and Kimberly L. Turner. Nonlinear dynamics and its applications in micro- and nanoresonators. *Journal of Dynamic Systems, Measurement, and Control*, 132(3):034001, 2010.

[2] Hanna Cho, Bongwon Jeong, Min-Feng Yu, Alexander F. Vakakis, D. Michael McFarland, and Lawrence A. Bergman. Nonlinear hardening and softening resonances in micromechanical cantilever-nanotube systems originated from nanoscale geometric nonlinearities. *International Journal of Solids and Structures*, 49(15–16):2059 – 2065, 2012.

[3] Martin P. Bendsøe and Ole Sigmund. *Topology Optimization: Theory, Methods and Applications*. Springer, 2003.

[4] T. M. Cameron and J. H. Griffin. An alternating frequency/time domain method for calculating the steady-state response of nonlinear dynamic systems. *Journal of Applied Mechanics*, 56(1):149–154, March 1989.

[5] Suguang Dou and Jakob S. Jensen. Optimization of nonlinear structural resonance using the incremental harmonic balance method. 2013. Submitted.

[6] M. Peeters, G. Kerschen, and J.C. Golinval. Modal testing of nonlinear vibrating structures based on nonlinear normal modes: Experimental demonstration. *Mechanical Systems and Signal Processing*, 25(4):1227 – 1247, 2011.

DTU Mechanical Engineering
Section of Solid Mechanics
Technical University of Denmark

Nils Koppels Allé, Bld. 404
DK- 2800 Kgs. Lyngby
Denmark
Phone (+45) 4525 4250
Fax (+45) 4593 1475
www.mek.dtu.dk
ISBN: 978-87-7475-415-2

DCAMM
Danish Center for Applied Mathematics and Mechanics

Nils Koppels Allé, Bld. 404
DK-2800 Kgs. Lyngby
Denmark
Phone (+45) 4525 4250
Fax (+45) 4593 1475
www.dcamm.dk
ISSN: 0903-1685